TELLURIUM ATTENUATION OF KESTERITE BAND GAP FOR IMPROVED PHOTOVOLTAIC EFFICIENCY.

A THESIS

By

Kelechi Chiemezie Nwambaekwe

(BTech. Industrial Chemistry (FUTO), BSc. Honours Chemical Science (UWC))

In fulfillment of the requirement for the degree of

Magister Scientiae in Chemical science

Faculty of Sciences, University of the Western Cape

Bellville, Cape Town, South Africa

Supervisors: Prof. Emmanuel I. Iwuoha and Dr. Milua Masikini

MARCH, 2019.

ABSTRACT

Tellurium is a member of the chalcogen group in the periodic table and is known to be a better semiconductor material when compared to sulfur and selenium. By introducing tellurium into the kesterite structure there would be an improvement in the semiconducting property of the kesterite material. This research focused on incorporating tellurium into kesterite structure in order to reduce its band-gap thereby improving its light absorption and ultimately lead to a more efficient photovoltaic effect. For a typical synthesis, kesterite nanoparticles were synthesized by anion hot injection process which involved the injection of the anion precursor comprising of sulfur, selenium and tellurium in diethylene glycol into a solution containing the cation precursor which are copper (II) chloride, Zinc chloride and tin (II) chloride which are dissolved in diethylene glycol. The synthesized nanoparticles were copper zinc tin sulfide (CZTS), copper zinc tin sulfide selenide telluride (CZTSSeTe) and copper zinc tin sulfide telluride (CZTSTe). Morphological characterization of the synthesized nanoparticles was carried out by high-resolution scanning electron microscopy (HRSEM) and high-resolution transmission electron microscopy (HRTEM) to obtain the shape of the surface and internal structure of the nanoparticles respectively. The micrograph obtained from HRSEM shows that all synthesized nanoparticles had a flower-like surface appearance which is a common morphology obtained for non-vacuum synthesized kesterite nanoparticles. The micrograph obtained from TEM showed that all nanoparticles were agglomerated and had a black surface covering which attributable to the solvent used during synthesis, washing and centrifugation. The internal structure of the synthesized nanoparticles was obtained through small angle x-ray scattering (SAXS) plot of the shapes. The shape obtained for the nanoparticles were core shell hollow sphere for CZTS, core shell dumb-bell for CZTSSeTe and solid sphere for CZTSTe. The particle size of the synthesized materials was evaluated using small-angle X-ray scattering (SAXS) plot of the size distribution giving

particle size distribution of the CZTS nanoparticle as 10 nm with a large size of 90 nm which is attributed to agglomeration of the nanoparticles, the particle size distribution of CZTSSeTe nanoparticles as 15 nm with a large size distribution of 105nm attributed to agglomeration of the nanoparticles and the size distribution for CZTSTe nanoparticles as 36 nm. Surface conditioning of the nanoparticles was obtained through Fourier transform infra-red spectroscopy (FTIR). The spectrum obtained can be compared to the spectrum of the solvents used during synthesis and washing as the nanoparticles structure doesn't have organic compounds. The functional group and the region of bands showed similarity with the spectrum of the solvents used. The slight shift in the vibrational bands of these functional group shows the formation of new compounds which are coordinated to the solvents. The presence of the functional group from the solvents shows that the solvents were not totally removed during washing after synthesis. This does not pose any problem as they are easily removed by annealing during device production. X-ray diffraction spectroscopy XRD was used to determine the kesterite phase of the nanoparticles as well as determine the crystal size of the nanoparticles. The XRD result confirms the presence of the kesterite phase in all synthesized nanoparticles with. The crystal size obtained from XRD was 11 nm for CZTS, 15 nm for CZTSSeTe and 31 nm for CZTSTe which agrees with the particle size obtained from SAXS. The optical property of the synthesized kesterite nanoparticles was obtained from ultraviolet–visible spectroscopy (UV-Vis). The optical band-gap of the nanoparticles was extrapolated from the data of the UV-Vis characterization and was deduced using Tauc-plot. The band-gap obtained for the three synthesized kesterite nanoparticles are 1.73 eV, 1.62 eV and 1.06 eV for CZTS, CZTSTe and CZTSSeTe in that order. The reduced bandgap observed for CZTSTe and CZTSSeTe are attributable to the semiconductive property of tellurium as well as selenium when compared to sulfur in CZTS. The electrochemical activity of the nanoparticles was evaluated through cyclic voltammetry (CV), square-wave

voltammetry (SWV) as well as electrochemical impedance spectroscopy (EIS). The CV plots shows that CZTSTe with a higher value for its anodic and cathodic peak currents was more conductive than CZTS and CZTSSeTe in that order. The rate of diffusion of the nanoparticles was determined from the data plotted from observed peak current values against square root of scan rate. From the result obtained CZTSTe (0.0036 cm^2/s, 0.00271 cm^2/s) diffused faster to the electrode surface than CZTS (0.00276 cm^2/s, 0.00232 cm^2/s) and CZTSSeTe (0.00117 cm^2/s, 0.00105 cm^2/s) in that order. EIS result obtained for the nanoparticles showed that CZTSTe had the lowest R_{ct} value (3.9 kΩ) which confirms the high cathodic and anodic peak obtained in CV of the nanoparticle and hence its better conductivity than the other nanoparticles where the R_{ct} value for CZTS was (9.8 kΩ) and R_{ct} value for CZTSSeTe. was (67.9 kΩ and 15.9 kΩ). The electrochemical behaviour observed in the nanoparticles shows that with a lower ratio of tellurium as in the case of CZTSTe when compared to sulfur gave an improved electrochemical behaviour but with addition of tellurium and selenium sharing same ratio with sulfur in the case of CZTSSeTe, the material became highly resistive. This resistive behaviour is due to metallic (cation) repulsion occurring in the structure of the nanoparticles as selenium and tellurium tend to act more metallic. With kesterite having more metallic elements; copper, zinc and tin, the addition of tellurium and selenium adds to like-charge repulsion in the structure thereby leading to the material being more resistive. Sulfur which is more electronegative does not have enough ratio to balance out the electropositive charge of the other constituent elements. The I-V curve of the nanoparticles as well as that of the fabricated device was evaluated. The efficiency obtained for the nanoparticles are 0.00244% for CZTS, 0.00116 % for CZTSSeTe and 0.00345%. for CZTSTe. The efficiency obtained for the nanoparticles followed the same trend observed in the electrochemical characterizations. The Photovoltaic cell for the prepared kesterite device had efficiencies of 0.00429 % for CZTS and 0.008351 % for CZTSTe. CZTSTe with the higher efficiency

proves that addition of small ratio of tellurium into the kesterite structure will improve the efficiency of kesterite solar cell device.

GRAPHICAL REPRESENTATION:

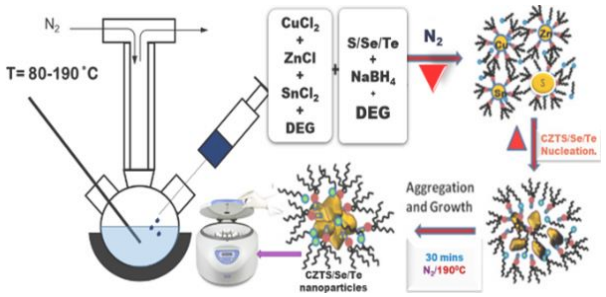

Synthesis of CZTS/Se/Te nanoparticles

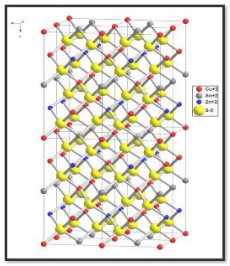

CZTS/Se/Te nanoparticles ink

1. Spin coating
2. Drying at 200 ˚C
3. Repeating
4. Annealing at 400 ˚C for 1.5hr

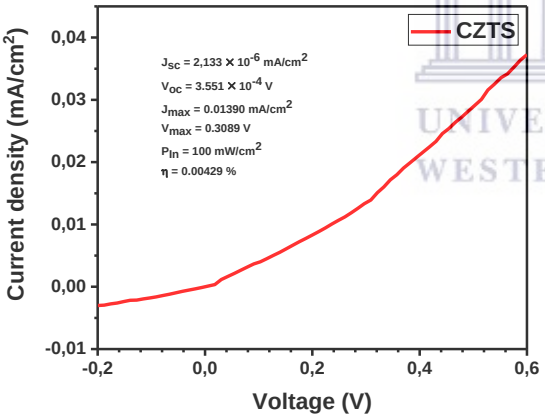

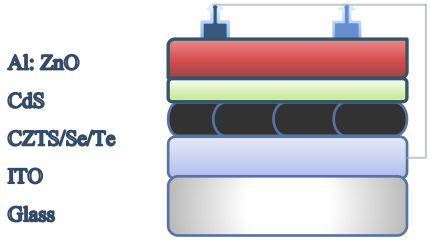

Glass/ITO/Kesterite/CdS/Al: ZnO/Ag PV cell.

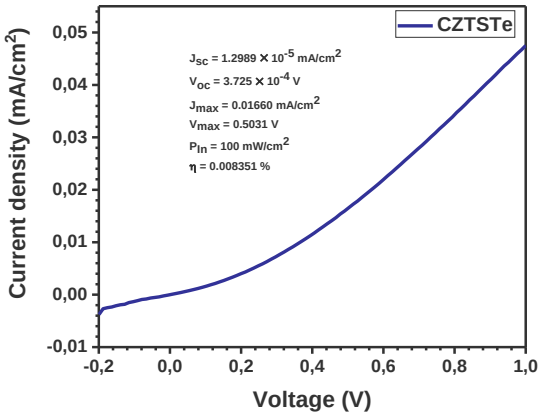

J-V Curve of the kesterite PV cell showing Power conversion efficiency of the devices.

DECLARATION

I, hereby declare that "*Tellurium attenuation of kesterite band-gap for improved photovoltaic efficiency*" is the result of my own work that was done by me under the supervision of Prof. Emmanuel Iwuoha and co-supervision of Dr. Milua Masikini, and that it has not been previously submitted for any degree or examination in any other university or higher education; and that all the sources and quotations have been indicated and acknowledged by complete references.

Kelechi Nwambaekwe March 2019

Signed …… Date ……

DEDICATION

This work is dedicated to my family; Mr. Michael Nwambaekwe (Father), Mrs. Abigail Nwambaekwe (Mother), Mrs. Amarachi Agughasi (sister), Mr. Ikechi Nwambaekwe (brother), Mrs. Ijeoma Ukandu (sister), Mrs. Ozioma Eziefula (sister), Mrs. Ebere Obiokoye (sister), Ms. Uchenna Nwambaekwe (sister), Mr. Lawrence Njoku (brother) and Ms. Rachel Uzoamaka (sister) for their moral support, prayers and love throughout this process.

ACKNOWLEDGEMENTS

First and foremost, I would like to thank the Almighty God for giving me the strength and wisdom to complete this project. Lord I thank you; I could not have made it on my own.

I would like to express my sincere gratitude to my supervisor Prof. Emmanuel Iwuoha for the opportunity he has granted me to advance my career and to have this opportunity to better myself. I have been exposed to far better ways to understand and appreciate science and be tenacious towards a great course. I would like to thank him for his guidance, encouragement and support throughout the study. Thank you very much.

I would like to thank my co-supervisor Dr. Milua Masikini for his support, guidance, immeasurable help and significant inputs during difficult times. I would love to thank you specially for coming back to make sure I completed my work and this degree after experiencing a very tragic loss, I am very grateful. I would say I have gained another father in you. This project couldn't have been a success without you. Thank you very much.

I would like to specially thank Dr. Theresa Onwordi and Dr. Chinwe Ikpo for their motherly role to me since I started this journey. They have become my biggest support and always reliable. I am very grateful. Also, to Dr. Paul Eze and Dr. Olanrewaju Fatoba for their advice and encouragement.

Special thanks to everyone in the University of the Western Cape Sensor Laboratories (SensorLab) family for making SensorLab a pleasant environment for learning. I would want to thank Dr. A. Baleg for his immeasurable advice during the fabrication process of the PV cells which was a very crucial point in this work, Dr. Christopher Sunday for his advice and contribution to me on understanding the principles of cyclic and square-wave voltammetry and to Dr. Lindsay for his deep explanation of electrochemical impedance spectroscopy. It

was fun and inspiring working with you guys. God bless each and every one of you who was willing to help.

I am grateful for the financial support, help and encouragement extended to me by family, friends and my in-laws especially Engr. Chidiebere Ukandu and Mrs. Ijeoma Ukandu who have been a rock and strong support in so many ways to me and also to Pharm. Chika and Mrs. Amarachi Agughasi for all the help and support extended to me.

I would like to thank my friends especially Nompumelelo Mathebula for her constant check in on me and also for the intelligent conversations we always had. To Thando Juqu and Victor Manele for being reliable, jovial and kind friends and for being my GREAT south African brothers. To Ebere Mbilitam for her friendship and encouragements, to Nelia Sanga and Zandile for being great darlings and graceful friends. To Kevin Tambwe for always taking me very cool pictures, great laugh moments and his contribution during the fabrication process, to Ebuka Onyeije and Caleb Nwafor for their friendship and care and to Samkeliso Ndzimandze and Xolane Mandlazi.

I would also love to acknowledge and thank my school sisters and brothers Al Farao, Andisiwe, Anne, Onyinyechi, Penny, Rabelani, Sazi, Sixolile and Sodiq for their support, encouragement, inputs and grace.

I would like to extend my sincere gratitude to my mother Mrs. Abigail Nwambaekwe, for her constant encouragement and involvement throughout this process, she has been a dependable and biggest support I have. To my father Mr. Michael Nwambaekwe and brothers Ikechi Nwambaekwe and Lawrence Njoku, for their support and encouragement as well and my sisters who have also been calling especially Ozioma Eziefula, Uchenna Nwambaekwe and Ebere Obiokoye encouraging me when I feel down. I am very grateful for all the support, understanding, patience, prayers, encouragement, and care when I needed them most. Thank

you very much and may the Almighty God continue to bless you abundantly in every aspect of your lives and keep you safe at all times.

KEYWORDS

Auxiliary phases (secondary phases)

Chalcogens

Copper zinc tin sulfide

Copper zinc tin sulfide selenide telluride

Copper zinc tin sulfide telluride

Cushion (Buffer)

Cyclic voltammetry

Energy

Kesterite

Nebulous

Optical band-gap

Photovoltaic cell

Ultra-violet visible spectroscopy

ACRONYMS AND ABBREVIATIONS

CV	Cyclic Voltammetry
CZTS	Copper zinc tin sulfide
CZTSSeTe	Copper zinc tin sulfide selenide telluride
CZTSTe	Copper zinc tin sulfide telluride
DEG	Diethylene glycol
EIS	Electrochemical Impedance Spectroscopy
EDX	Energy Dispersive Spectroscopy
E_p	Peak potential
E_{pa}	Anodic peak potential
E_{pc}	Cathodic peak potential
FF	Fill-Factor
FTIR	Fourier Transform Infra-Red Spectroscopy
HRSEM	High Resolution Scanning Electron Microscopy
HRTEM	High Resolution Transmission Electron Microscopy
I_{pa}	Anodic Peak current
I_{pc}	Cathodic peak current
I_{sc}	Short-circuit current
J_{max}	Maximum current density

J_{sc}	Short-circuit current density
PCE	Power Conversion Efficiencies
P_{in}	Power input
P_{max}	Maximum power output
SAXS	Small-Angle X-ray Scattering
TGA	Thermogravimetric Analysis
UV-vis	Ultraviolet-visible Spectroscopy
V_{max}	Maximum voltage
V_{oc}	Open-circuit voltage
XRD	X-ray Diffraction Spectroscopy
η	Power conversion efficiency.

TABLE OF CONTENTS

TABLE OF CONTENTS

LIST OF FIGURES

LIST OF TABLES

CHAPTER 1

INTRODUCTION

1.1 BACKGROUND

The short supply of diverse energy sources has throughout the years become a noteworthy issue on the planet. This is in part due to the uneven distribution of energy sources on the planet, explosive growing populace, the ascent in the way of life and monetary advancement. The world's essential energy utilization throughout the decade has been demanding, with an increasing high usage reported to reach 13,647 Mtoe (million tonnes oil equivalent) [1-5]. Majority of the electrical power of the world has been created by consuming petroleum derivatives, for example, oil, coal and flammable gas. This has a downside as petroleum derivatives are a non-sustainable source of energy which implies that they will run out [6]. In spite of being constrained in supply, they are a major contributor of CO_2 into the environment, which is an issue as carbon dioxide is the fundamental source of global warming [7-12].

The focus after some time has been moved towards discovering new sources of energy tosupplant non-renewable energy sources, in order to provide for the increasing demand for energy and furthermore decrease natural contamination (pollution). In accomplishing this, sustainable sources of energy which incorporate and not restricted to sunlight based (solar), wind, hydropower, biogas and geothermal provide an ideal hope for the confinements of the world's energy sources and in the meantime tend to the issue of environmental (climate) change. At a time, nuclear energy plants were surveyed and found to possibly address the world's energy demand having contributed around 13.5% of world's energy produced as recorded in 2008 [13] and decreased to 11 % in 2018 [14]. Nuclear energy was utilized as it has the smallest ozone depleting gas emission over entire

fuel cycles, unwavering quality and typically gave low-cost energy. It was accepted to be the most suitable option in contrast to non-renewable energy source, however this great potential suffered a colossal setback due to the Fukushima atomic catastrophe in Japan, which was caused by a seismic tremor and tidal wave in March 2011, raising worldwide inquiries and protection from the utilization of nuclear innovations up till now [15-20]. More concern was brought up in light of the way that, nuclear waste requires capable handling and must be carefully secured and disposed of. As the world moved away from nuclear energy, it became clear renewable source of energy is the way forward. Of all the sustainable energy source, the solar energy has caught most attention. Solar energy among other sustainable energy sources is most abundant and promising source as a result of its capacity to provide for the world's energy use. The solar energy reaching the earth's surface in one hour is relatively equivalent to the world's total energy use in one year [21-24]. Improvement of frameworks and gadgets that can harness the solar energy and convert it to valuable energy has turned into an undeniably fascinating pattern as of late. Energy conversion of solar energy can be accomplished through two strategies (a) Photothermal frameworks and (b) Photovoltaic (PV) frameworks. While Photothermal frameworks convert solar energy into thermal energy which can be changed over to different types of energy, photovoltaic frameworks convert solar energy specifically into electrical energy through solar cells. The photovoltaic framework has seen a huge increment in capacity all around, for the most part the main focal point of researchers. It has turned into the quickest developing ventures worldwide with a yearly development rate somewhere in the range of 40% and 90%, the aggregate Photovoltaic (PV) creation expanded nearly by two orders of magnitude [25-28].

The wafer-based silicon solar cells out of other PV innovations earned around 85% market shares in 2011 and still predominant today. As its energy change proficiency hasn't

expanded as of late and the confinements of not having lessened cost; logical research and interests have gone into concentrating on thin-film solar cells because of its high decreased cost, less handling time, monolithic integration of cells, higher level of computerization and adaptability when contrasted with wafer-based silicon solar cell [29-31]. By and by, Cadmium Telluride (CdTe) and $CuIn_xGa_{1-x}Se_2$ (CIGS) are the two thriving advances for thin film solar cells (TFSCs). The two advances have shown high device performance with the record efficiencies of 19.6% (CdTe) and 20.4% (CIGS) [32]. CdTe solar cells have been popularized by First Solar with a module proficiency of more than 10%, while CIGS solar cells are presently beginning to move into production in industrial scale. In any case, the two innovations have pragmatic constraints: CdTe includes the utilization of poisonous cadmium Cd and is hence impeding to the earth (toxic), while CIGS contain uncommon (rare) metals - In and Ga and these elements significantly confine the production scale of such cells [33]. These restrictions raise a pressing need to discover substitute materials for thin-film solar cells (TFSCs) which comprise of earth-inexhaustible and low poisonous quality elements.

Cu_2ZnSnS_4 (CZTS, copper zinc tin sulfide) kesterite is a developing absorber material for TFSCs. It has a crystal structure like that of CIGS where (In) and Ga are substituted by Zn and Sn. CZTS has great optical properties for photovoltaic applications: (i) ideal band gap for solar cells of 1.5 eV and (ii) huge absorption coefficient in excess of 104 cm^{-1}. It is vital to bring up that CZTS contains all earth-abundant elements in contrast to CIGS and CdTe. The earth crust contains 50 ppm Cu, 75 ppm Zn, 2.2 ppm Sn, 260 ppm S, which are all several orders of magnitude higher than that of Te (0.001 ppm) and (In) (0.05 ppm) [34]. The plenitude of these CZTS elements proposes a minimal cost of material and the potential for an expansive production scale of CZTS in contrast to CIGS and CdTe. Likewise, CZTS comprises of components that are non-lethal when contrasted with

Cadmium in CdTe. Given that CZTS is generally new material, published works report distinctive methodologies for synthesizing CZTS, including vacuum and non-vacuum techniques. The record efficiency for a CZT(S,Se) device, whose absorbing active layer was accomplished by a solution-based strategy, is 12.6% [35], though the most accomplished power conversion efficiency (PCE) of an sulfide CZTS device in view of a CZTS absorbing layer created utilizing thermal evaporation is 8.4% [36] although by thinning the CdS layer, a 9.4 % efficiency was achieved for CZTS PV cell [37]. In spite of the detectable advancement made toward accomplishing higher PCEs of CZTS-based solar cells, the performance of the best-announced device is still a long way from the hypothetically evaluated efficiency of around 30% [38]. Kesterite, Stannite and Wurtzite are the three principal structures of CZTS [39], with the kesterite and stannite sample having a tetragonal lattice structure and the Wurtzite has a hexagonal unit cell. The Wurtzite polymorph is a metastable type of CZTS that has a zinc mix crystal structure, while kesterite is a steadier polymorph with a tetragonal crystal framework like the chalcopyrite structure. In most synthetic techniques revealed, both auxiliary structures are present [40-42].

One of the principal challenges in synthesizing CZTS is controlling the film composition amid the film development process, controlling the phase stability of this compound is likewise troublesome and the issue of phase isolation is broadly reported. Phases, for example, $Cu_{2-x}S_4$ and $Cu_{2-x}Sn_xS_3$ are particularly inconvenient to the device in view of their metal conduct, which could prompt shunting of the cell. Thus, considering the effect of the different development parameters may give more understanding into how to keep away from their presence. A decent information of the material response pathway is additionally a critical segment to accomplishing top notch materials with extensive grain estimate, great crystallinity, and uniform organization. Distinctive reported works have

point by point routes for the formation pathway. Be that as it may, because of the distinctive growth approaches utilized, none of them is all round substantial in clarifying the compound reaction pathway.

1.2 RATIONALE, AIM AND OBJECTIVES

RATIONALE

Energy being an important component of modern life has become increasingly an interesting research area. The solar energy is a very suitable source to generate energy which can address most of the world's demand in that the incident energy from the sun on the earth in a day supersedes the current energy output of the world. Given the progress made in solar cell development and the consequence of the discovery of CZTS as a viable material for the absorber layer of solar cell, much improvement is needed to bring it to marketable stage. The incorporation of tellurium to this absorber layer would increase its absorption of light towards the redder zone of the light spectrum thereby improving its bandgap and as such improve its applicability to solar cell. This is due to the fact that tellurium is a better semiconductor than sulfur and selenium in group 13 of the periodic table.

AIM

The main aim of this study is to improve the absorption onset of the current kesterite CZTS(Se) nanoparticles by narrowing the bandgap below 1.7 eV. This will be achieved by incorporating tellurium into the structure of the ternary and quaternary kesterite to synthesize new kesterite nanoparticles containing tellurium; CZTSTe and CZTSSeTe. The aim of the study will be achieved by the following objectives (in sequence).

OBJECTIVES

- Synthesize Kesterite CZTS nanoparticle.
- Synthesize tellurium containing kesterite nanoparticles by incorporating tellurium anion during anion injection during synthesis to obtain kesterite nanoparticles with tellurium in their structure: CZTSSeTe and CZTSTe nanoparticles.
- Investigate the microscopic properties of the new kesterite nanoparticles using High-Resolution Transmission Electron Microscope (HRTEM) and High-Resolution Scanning Electron Microscope, determine the particle size using Small Angle X-ray Scattering (SAXS) and confirm the elemental composition by Energy Dispersive X-ray Spectroscopy (EDS).
- Obtain the crystal phase, structure and size of the synthesized nanoparticles using X-ray Diffraction Spectroscopy (XRD) and confirm the crystal phase through Raman Spectroscopy.
- Obtain the optical bandgaps of all synthesized kesterite nanoparticles by Ultraviolet-visible (UV-vis) spectroscopy.
- Determine the electrochemical behaviour of all kesterite nanomaterials by Cyclic Voltammetry (CV), Square Wave Voltammetry (SWV) and Electrochemical Impedance Spectroscopy (EIS).
- Obtain the power conversion efficiency (PCE) of all the synthesized nanoparticles through Current-Voltage (I-V) curve.

1.3 THESIS ORGANIZATION

This thesis is organized as follows:

Chapter 1, gives a brief introduction to the concept of photovoltaic cell, challenges that have been encountered, different solar cell materials that have been used and introduction to kesterite CZTS nanoparticles and its application to solar cell.

Chapter 2, is focused on literature review of previous works that have been reported on different energy sources, how it came down to solar energy, different solar cells that have been explored and how it came down to kesterite solar cells. This chapter goes deep into discussing various reports on the properties exhibited by kesterite solar cell material and ways to tackle some of the challenges that have been encountered

Chapter 3, explores the synthesis of CZTS, $CZTS_{0.5}Se_{0.25}Te_{0.25}$ (CZTSSeTe) and $CZTS_{0.75}Te_{0.25}$ (CZTSTe) and gives a background to various characterization techniques used to obtain the properties of the synthesized kesterite nanoparticles.

Chapter 4, delves into results from various characterization techniques used and discussion of these results in relation to the properties of the newly synthesized nanoparticles.

Chapter 5, talks about the procedure involved in the device fabrication and the efficiency obtained from the application.

Chapter 6, concludes the work and highlights recommendations for future work.

REFERENCES

[1] Energy Outlook, *International energy outlook* (EIA) (2017).

[2] S. Wang, G. Li and C. Fang, "Urbanization, economic growth, energy consumption, and CO_2 emissions: Empirical evidence from countries with different income levels," *Renewable and Sustainable Energy Reviews* 81 (2018) 2144-2159.

[3] R. Giridharan and R. Emmanuel, "The impact of urban compactness, comfort strategies and energy consumption on tropical urban heat island intensity: a review," *Sustainable cities and society* 40 (2018) 677-687.

[4] O. Akizu-Gardoki, G. Bueno, T. Wiedmann, J.M. Lopez-Guede, I. Arto, P. Hernandez and D. Moran, "Decoupling between human development and energy consumption within footprint accounts," *Journal of Cleaner Production* 202 (2018) 1145-1157.

[5] R. Muhumuza, A. Zacharopoulos, J.D. Mondol, M. Smyth and A. Pugsley, "Energy consumption levels and technical approaches for supporting development of alternative energy technologies for rural sectors of developing countries," *Renewable and Sustainable Energy Reviews* 97 (2018) 90-102.

[6] OECD/IEA, Key World Energy Statistics (2017). Retrieved from https://www.iea.org/publications/freepublications/publication/KeyWorld_Statistics_2017.pdf.

[7] OECD/IEA, CO_2 Emissions from Fuel Combustion (2018). Retrieved from http://wds.iea.org/wds/pdf/WorldCo2_Documentation.pdf

[8] T.P. Hughes, J.T. Kerry, A.H. Baird, S.R. Connolly, A. Dietzel, C.M. Eakin, S.F. Heron, A.S. Hoey, M.O. Hoogenboom, G. Liu, M. J. McWilliam, R.J. Pears, M.S.

Pratchett, W.J. Skirving, J.S. Stella and G. Torda, “Global warming transforms coral reef assemblages,” *Nature* 556 (2018) 492–496.

[9] T.A Tsalis, V.D. Botsaropoulou and I.E. Nikolaou, “A methodology to evaluate the disclosure practices of organizations related to climate change risks: a case study of international airports,” *International Journal of Global Warming* 15 (2018) 257-276.

[10] I.X. Tsiros, M. E. Hoffman, A. Tseliou, V. Christopoulou and S. Lykoudis, “An assessment to evaluate potential passive cooling patterns for climate change adaptation in a residential neighborhood of a Mediterranean coastal city (Athens, Greece),” *International Journal of Global Warming* 16 (2018) 181-208.

[11] S.G. Philander, “Is the temperature rising: the uncertain science of global warming,” *Princeton University Press* (2018).

[12] C. Mora, R.L. Rollins, K. Taladay, M.B. Kantar, M.K. Chock, M. Shimada and E.C. Franklin, “Bitcoin emissions alone could push global warming above 2 degrees C,” Nature Climate Change 9 (2019) 80.

[13] IEA, Electricity Information OECD Publishing, Paris (2010) https://doi.org/10.1787/electricity-2010-en

[14] IEA, Electricity Information OECD Publishing, Paris (2018) https://doi.org/10.1787/electricity-2018-en

[15] P. Lipscy, K. Kushida and T. Incerti, “The Fukushima Disaster and Japan’s Nuclear Plant Vulnerability in Comparative Perspective,” *Environmental Science and Technology* 47 (2013) 6082–6088.

[16] S. Suman, “Hybrid nuclear-renewable energy systems: A review,” *Journal of Cleaner Production* 181 (2018) 166-177.

[17] R. Prăvălie and G. Bandoc, “Nuclear energy: Between global electricity demand, worldwide decarbonization imperativeness, and planetary environmental implications,” *Journal of environmental management* 209 (2018) 81-92.

[18] K. Dong, R. Sun, H. Jiang and X. Zeng, “CO_2 emissions, economic growth and the environmental Kuznets curve in China: What roles can nuclear energy and renewable energy play,” *Journal of cleaner production* 196 (2018) 51-63.

[19] S.S. Ho, A.D. Leong, J. Looi, L. Chen, N. Pang and E. Tandoc Jr, “Science literacy or value predisposition? A meta-analysis of factors predicting public perceptions of benefits, risks, and acceptance of nuclear energy,” *Environmental Communication* (2018) 1-15.

[20] J-B. Chung, “Let democracy rule nuclear energy,” *Nature* 555 (2018) 415.

[21] X.G. Zhu, S.P. Long and D.R. Ort, “What is the maximum efficiency with which photosynthesis can convert solar energy into biomass?” *Current opinion in biotechnology* 19 (2008) 153-159.

[22] E. Kabir, P. Kumar, S. Kumar, A.A. Adelodun and K-H. Kim, “Solar energy: Potential and future prospects,” *Renewable and Sustainable Energy Reviews* 82 (2018) 894-900.

[23] S.K. Sansaniwal, V. Sharma and J. Mathur, “Energy and energy analyses of various typical solar energy applications: A comprehensive review,” *Renewable and Sustainable Energy Reviews* 82 (2018) 1576-1601.

[24] A.H. Elsheikh, S.W. Sharshir, M.E. Mostafa, F.A. Essa, M. Kamal and A. Ali, "Applications of nanofluids in solar energy: a review of recent advances," *Renewable and Sustainable Energy Reviews* 82 (2018) 3483-3502.

[25] R.L. Arantegui and A. Jäger-Waldau, "Photovoltaics and wind status in the European Union after the Paris Agreement," *Renewable and Sustainable Energy Reviews* 81(2018) 2460–2471.

[26] C. Brunet, O. Savadogo, P. Baptiste and M.A. Bouchard, "Shedding some light on photovoltaic solar energy in Africa–A literature review," *Renewable and Sustainable Energy Reviews* 96 (2018) 325-342.

[27] A. Ferreira, S.S. Kunh, K.C. Fagnani, T.A. De Souza, C. Tonezer, G.R. Dos Santos, and C.H. Coimbra-Araújo, "Economic overview of the use and production of photovoltaic solar energy in brazil," *Renewable and Sustainable Energy Reviews* 81 (2018) 181-191.

[28] N.A. Ludin, N.I. Mustafa, M.M. Hanafiah, M.A. Ibrahim, M.A.M. Terdi, S. Sepeai, A. Zaharim and K. Sopian, "Prospects of life cycle assessment of renewable energy from solar photovoltaic technologies: A review," *Renewable and Sustainable Energy Reviews* 96 (2018) 11-28.

[29] J. M. Woodcock, H. Schade, H. Maurus, B. Dimmler, J. Springer and A. Ricaud, "A study of the upscaling of thin film solar cell manufacture towards 500 MWp per annum," *Proceedings of the 14th European Photovoltaic Solar Energy Conference* 1 (1997) 857–860.

[30] M. Powalla, B. Dimmler, "20th European Photovoltaic Solar Energy Conference," (Eds.: Palz W, Ossenbrink HA, H. P), Barcelona, Spain, (2005) 1689.

[31] S. Niki, M. Contreras, I. Repins, M. Powalla, K. Kushiya, S. Ishizuka and K. Matsubara, "CIGS absorbers and processes," *Progress in Photovoltaics: Research and Applications* 18 (2010) 453-466.

[32] M.A. Green, K. Emery, Y. Hishikawa, W. Warta and E.D. Dunlop, "Solar cell efficiency tables," Progress *in Photovoltaics: Research and Applications* 21 (2013) 827-837.

[33] D.B Mitzi, O. Gunawan, T.K. Todorov, K. Wang and S. Guha, "The path towards a high-performance solution- kesterite solar cell," *Solar processed Energy Materials and Solar Cells* 95 (2011) 1421-1436.

[34] S.R. Taylor, S. M. McClennan, "The continental crust: its composition and evolution: an examination of the geochemical record preserved in sedimentary rocks," *Geological journa*l 21 (1986) 85-86

[35] W. Wang, M.T. Winkler, O. Gunawan, T. Gokmen, T.K. Todorov, Y. Zhu, and D.B. Mitzi, "Device characteristics of CZTSSe thin-film solar cells with 12.6% efficiency," *Advanced Energy Materials* 4 (2014) 1301465.

[36] B. Shin, O. Gunawan, Y. Zhu, N.A. Bojarczuk, S.J. Chey and S. Guha, "Thin film solar cell with 8.4% power conversion efficiency using an earth-abundant Cu_2ZnSnS_4 absorber," *Progress in Photovoltaics: Research and Applications* 21 (2013) 72-76.

[37] S. Tajima, M. Umehara, M. Hasegawa, T. Mise, and T. Itoh, "Cu_2ZnSnS_4 photovoltaic cell with improved efficiency fabricated by high-temperature annealing after CdS buffer-layer deposition," *Progress in Photovoltaics: Research and Applications* 25 (2016) 14–22.

[38] W. Shockley, and H.J. Queisser, “Detailed balance limit of efficiency of p-n junction solar cells,” *Journal of applied physics* 32 (1961) 510-519.

[39] X. Lu, Z. Zhuang, Q. Peng and Y. Li, “Wurtzite Cu_2ZnSnS_4 nanocrystals: a novel quaternary semiconductor,” *Chemical Communications* 47 (2011) 3141-3143.

[40] C.N. Bucherl, K.R. Oleson and H.W. Hillhouse, “Thin film solar cells from sintered nanocrystals,” *Current Opinion in Chemical Engineering* 2 (2013) 168-177.

[41] L. Shi, C. Pei, Y. Xu and Q. Li, “Template-directed synthesis of ordered single-crystalline nanowires arrays of Cu_2ZnSnS_4 and $Cu_2ZnSnSe_4$,” *Journal of the American Chemical Society* 133 (2011) 10328-10331.

[42] M.D. Regulacio, C. Ye, S.H. Lim, M. Bosman, E. Ye, S. Chen, Q.H. Xu and M.Y. Han, “Colloidal Nanocrystals of Wurtzite-Type Cu_2ZnSnS_4: Facile Non-Injection Synthesis and Formation Mechanism,” *Chemistry – A European Journal* 18 (2012) 3127-3131.

CHAPTER 2

LITERATURE REVIEW

2.1 BRIEF HISTORY OF SOLAR CELLS

In the year 1839 Edmond Becquerel found that two distinctive metal plates drenched in a fluid discharged a consistent current when shone with sunlight. It is an acknowledged idea, that he had really made a copper-cuprous oxide thin-film solar cell. In 1870s, Willoughby Smith, W. G. Adams, and R. E. Day found a PV impact in selenium [1]. A few years after the fact, an American named C. E. Frits put a sheet of amorphous selenium on a metal support and secured the selenium with a transparent gold leaf film [1]. He inferred that this selenium cluster delivered a current "that is ceaseless (continuous), steady, and of significant force when shone with sunlight. During this period, there was no quantum hypothesis and there was high distrust about his case of changing sunlight into electricity. In this way, he sent a sample to Werner Siemens in Germany, who was a standout amongst the most regarded specialists in electricity at the time. Siemens' investigations confirmed Fritts' claims. In any case, the conversion efficiencies of both the thin - film cuprous oxide and the nebulous selenium solar cells were under 1% [2]

Numerous years passed by before the discovery of quantum mechanics which was a great boost to the significance of single-crystal semiconductor being recognized, and p/n intersection (junction) behaviour was clarified. Chapin et al. [2,3] at Bell Labs had found, designed, and showed the silicon single-crystal solar cell with 6% efficiency in the year 1954. Few years following, analysts brought the silicon solar cell efficiency up to 15%. The timing was fortunate on the grounds that Sputnik was launched in 1957 and solar cells were the ideal lightweight low-support remote electric power source. Today, silicon solar cells are being utilized to power the space station. The world is progressively tilting its concentration from

ordinary (conventional) to sustainable power source attributable to nuclear fiasco, and to have simple access to remote territories. The nuclear energy shares 7% in world energy and 15% production of power. To administer the safety of nuclear power plants, the international energy agency patches up the safety controls and rules. France, Japan, EU, and the United States rely upon nuclear power plants for power in their energy assets of 75, 30, 28, and 19%, respectively. Up until this point, China, Russia, Korea, and Latin America have 28, 11, 5, and 8 nuclear power plants, respectively [4,5]. A ton of nations guaranteed that they will gradually desert the nuclear power plants keeping in mind the end goal to diminish hazard (risk) factor. Capacity of aggregate energy of the world is 4742 GW in which the contribution of solar energy is 37 GW. The solar energy produced by various nations like Germany, Italy, Czech Republic, Japan, and the United States is 7.5, 3.8, 1.2, 0.8, and 0.8 GW, respectively. In the current global sustainable energy projection, the creation of hydroelectricity is 0.5 TW, tides and sea streams (currents) of 2 TW, geothermal of 12 TW, wind power of 2-4 TW, and solar energy of 120,000 TW. Of all these, the contribution of solar energy is the most astounding [6]. In day by day life, the job of adaptable and convenient (portable) solar cell panels is conceivably helpful [7]. For instance, a cell phone is being charged utilizing a compact solar panel as seen in Figure 2.1.

Figure 2. 1: Application of flexible thin film solar panel for charging of mobile phones.

Of late, endeavors to develop low-cost thin-film solar cells as option in contrast to high cost silicon (Si) solar cells has expanded. The decrease in cost of production is less demanding in non-Si thin-film solar cells than in Si solar cells as alternations can be made to them in thin solar cells to enhance their performance while Si solar cells don't give much space to modify the parameters to improve the efficiency. The principal downside with the Si solar cells is because of its aberrant (indirect) band gap semiconductor and requires a thick layer around 180-300 µm to absorb photons [8]. The band gap of 1.1 eV for Si does not absorb over half of the visible range, i.e., blue and green regions. Henceforth, we have to focus to manufacture high-efficiency and low-cost thin-film solar cells. Every one of these components undermine endeavors to lessen the cost of Si solar cells. Environmentally friendly, savvy, efficient solutions are of incredible interest to take care of the clean energy supply issue, as energies, for example, coal and oil, are restricted and will run out [9]. Solar cells which convert sunlight into electricity are anticipated as suitable apparatus to create electricity from the sun. Solar

energy is clean, inexhaustible and cost-free. Solar cell innovations are generally partitioned into three primary classes known as generations. The first-generation solar cell innovation includes procedures which are cost and energy intensive [10]. They incorporate single-and multi-crystal silicon solar cells which are produced on a wafer bearing either just a single crystal or crystal grains. The ongoing power conversion efficiency (PCE) of a single crystal silicon solar cell is 25% while a multicrystalline silicon solar cell shows a PCE of 21% [11]. Second generation solar cells comprise of a-Si thin movies, mc-Si, CdTe, CIS and CIGS. The PCEs of CIGS (minimodule) is 18% while for CdTe (cell) PCE is recorded as 21% [11]. For a-Si and mc-Si thin-film solar cells, PCEs are 10% and 11% respectively [11]. In spite of the fact that the second-generation solar cells are less efficient than the first-generation solar cells, their expenses are lower; then again, they are more likely applicable to the building integration and are more perfect with adaptable substrates [10]. Third generation solar cells incorporate nanocrystal solar cells, organic, hybrid (organic-inorganic) solar cells, dye-sensitized solar cells, perovskite and kesterite solar cells. Third generation solar cells are novel advances which are cost and energy effective, suitable for adaptable substrates and can be effortlessly coordinated. In spite of numerous points of advantages, their lower efficiencies and stability issues has turned out to be real downsides towards their commercialization. Another group of photovoltaic compounds called "kesterite" have been the focal point of consideration and if the stability issues of this new sort of photovoltaics can be tended to and tackled it turns into a decent contender to rival the other PV advances which have officially had their spot in the PV market [11].

2.2 OPERATIONAL PRINCIPLE OF THIN-FILM SOLAR CELLS

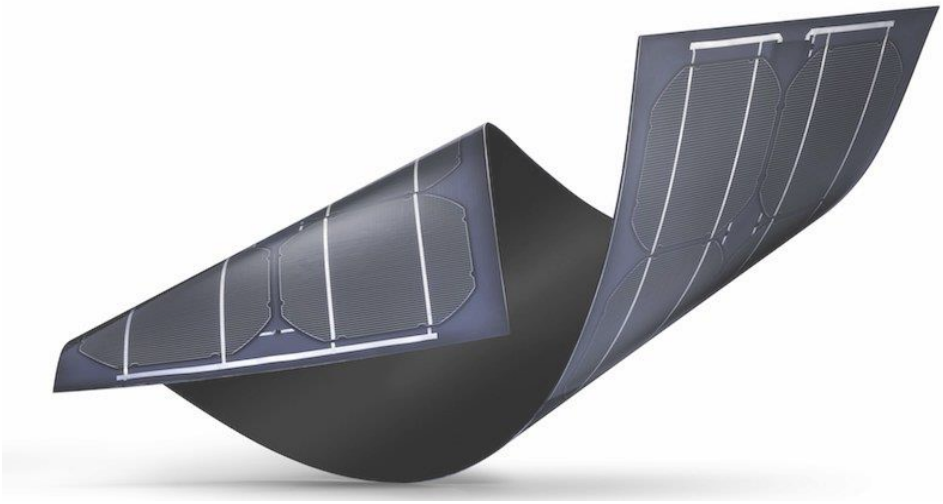

Figure 2. 2: Thin Film Solar Cell.

Thin film solar cells give better approaches to deliver electricity from sunlight than some other technique. These panels can be executed in forest regions, solar fields, traffic and road lights, and so on. The cost of this panel is considerably less in contrast with the more established silicon wafer cells [12].

The structure and schematics of thin film solar cell can be seen below (figures 2.3 and 2.4). The structure and working of thin film solar cells are relatively same as that of typical silicon wafer cells. The main contrast is in the thin adjustable arrangement of the different layers and the essential solar substance utilized. The thin adjustable arrangement of the layers delivers thin type of cells that is significantly more productive than the traditional silicon wafer cells [12].

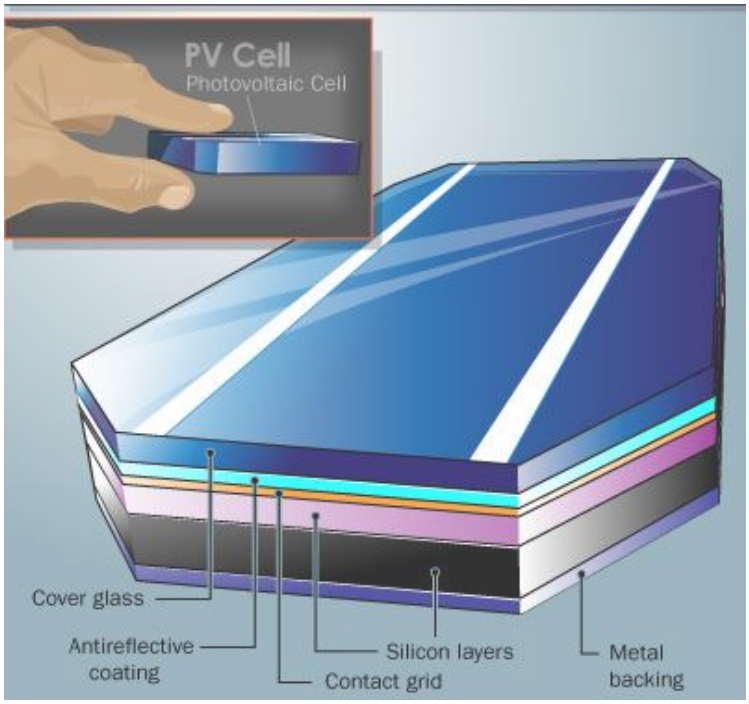

Figure 2. 3: Structure of thin film solar cells

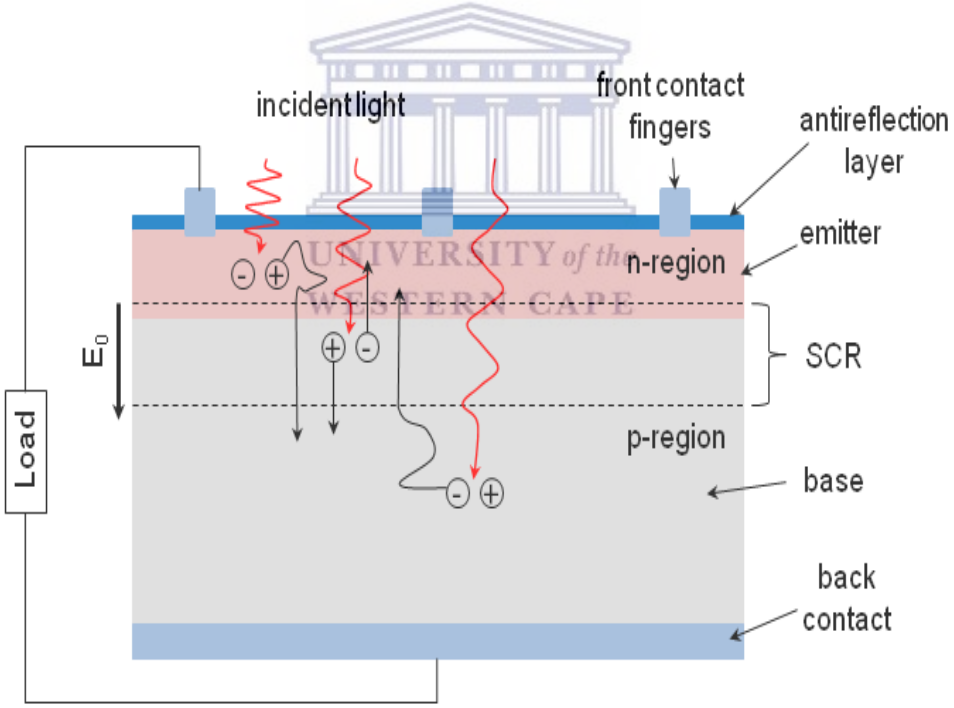

Figure 2. 4: Schematic cross-sectional illustration of a silicon solar cell. SCR = space-charge region.

The fundamental substance of a photovoltaic cell is semiconductors. The semiconductor doped with phosphorus builds up an abundance of free electrons (as a rule called n-type

material) and a semiconductor doped with boron, gallium or indium build up a vacancy (called holes) and this doped material known as p-type materials. These n-type and p-type materials consolidate (join) to shape a photovoltaic cell. While in absence of light, few atoms are energized and move over the intersection (junction). This causes a little voltage drop over the intersection. Within the presence of light, more molecules are energized and move through the intersection and cause a huge current at the output. This current can be stored in a rechargeable battery and utilized for several applications based on requirement [12].

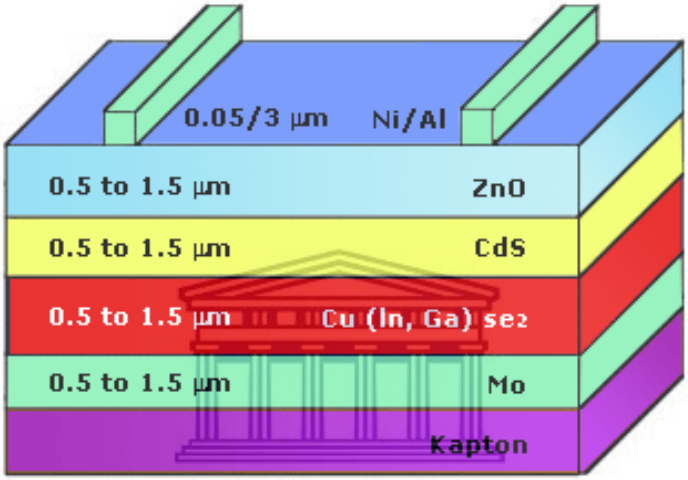

Figure 2. 5: Layer arrangement of thin film solar cell.

The old solar panel innovation utilizes silicon semiconductor for the generation of p-type and n-type layers and has a few inconveniences. Be that as it may, on account of Thin Film Layer innovation, the silicon semiconductor materials are supplanted by either cadmium telluride (CdTe) or copper indium gallium diselenide (CIGS) as found in figure 2.5.

2.3 INNOVATIONS OF THIN FILM SOLAR CELLS

The first set (generation) of solar cells were based on monocrystalline and multicrystalline silicon, which is a semiconductor with an aberrant energy bandgap of 1.12 eV. The material demonstrates various preferences and has a well built up innovation for producing and preparing silicon wafers with a high level of purity. The efficiency of the first reported solar cell (in the year 1941) in view of multicrystalline silicon (mc-Si) was around 1% [13]. Throughout the years, the effectiveness of Si solar cells rose rapidly, moving toward its hypothetically anticipated maximum of around 32%. In 2014, a record productivity of 25.6% was accomplished for a research produced single-crystalline Si cell [14]. For mc-Si cells, Trina Solar released another efficiency record of 21.25% in late 2015 [15,16]. Despite the fact that, Silicon-based PV is still the predominant innovation in the solar field, representing over 90% of aggregate production, the cost of electrical energy produced by the PV cell is still high in contrast with other sources. One of the elements adding to the high production cost of Si solar cells is the amount of material utilized. Around 90% of the solar cell cost is accounted by the Si wafer [17]. Because of the moderately little absorption coefficient of silicon (100 cm^{-1}), which is related with the circuitous bandgap of the material, the device must have a thickness of around 100-200 μm to absorb the greater part of the incident solar radiation and give sensible mechanical strength. Minimalized wafer thickness was one of the provisions reached to reduce the cost of PV-produced energy, and at present, 180 μm thick wafers are utilized. Additionally, cost decrease requires the utilization of more affordable materials and innovations. The second generation of solar cells in view of thin-film innovation has developed as an option in contrast to the regular Si cells. Thin-film PV gives an answer to reduce the measure of material utilized by using direct-bandgap semiconductors with higher absorption coefficients; along these lines, the aggregate thickness of the solar cell is in few microns. The device is manufactured on inexpensive substrates (e.g., glass, plastic, metal

foils) to give the fundamental mechanical quality, and the blend (synthesis) procedure does not require a high level of purity, unlike the case of Si cells. In this way, the synthesis procedure of thin-film PV devices utilizing various types of deposition methods is less difficult and more affordable. Thin-film solar cells depend for the most part on heterojunctions utilizing diversely doped, unique material where normally, a thin n-type semiconductor as a cradle layer is deposited over a p-type semiconductor, which represents the effective absorber layer to frame the p-n intersection (junction). A p-type material is favored for the effective absorbing layer, where the EHPs are generated, in light of the fact that the diffusion length of electrons in a p-type semiconductor is bigger than the diffusion length of holes in an n-type semiconductor. The n-type layer must be thin and made of a wide-band material to enable the incident light to go through to the absorber layer. For that, a CdS layer around 50 μm thick with energy bandgap of 2.4 eV is normally utilized. Two strong delegate materials for thin-film solar cells that show device efficiencies practically identical to those of mc-Si cells are cadmium telluride (CdTe) and copper indium-gallium diselenide, Cu(InGe)Se_2 (CIGS). These two materials have gotten to commercialization point for large scale manufacturing. Also, amorphous silicon (a-Si) solar cells are mass produced. Regardless of a-Si devices' low efficiency contrasted with CdTe and CIGS cells, they have application because of their minimal cost of production where low efficiencies are acceptable.

2.3.1 NEBULOUS (AMORPHOUS) SILICON

Nebulous silicon (a-Si) thin films are regularly deposited at low temperatures through plasma-enhanced chemical vapor statement (PECVD) with silane (SiH4) gas [18,19]. As such, a-Si can be produced on a variety of substrates including glass, plastic, or metal foils. The material shows non-crystalline structure (i.e., atoms are arbitrarily arrayed), which impacts the electronic properties of the semiconductor. For an enhanced quality of the material for PV

applications, hydrogen is fused to passivate the dangling bonds that emanate from the irregular array of the atoms. In contrast with crystalline Si, the hydrogenated nebulous silicon (α-Si:H) displays a direct bandgap of 1.7 eV and an optical absorption coefficient $\alpha > 105cm^{-1}$, allowing the absorption of most solar radiation within a couple of micrometers. The premier α-Si:H cell of a thickness of around 1 μm with an efficiency of 2.4% was made in 1976 using a p-I-n a-Si structure [20]. The device can be made into a single junction or multijunction (twofold or triple) with a superstrate (p-I-n) setup (i.e., light enters through the substrate) or substrate (n-I-p) arrangement (i.e., light infiltrates through the top n-layer). Figure 2.6. demonstrates the cross-sectional representations of single-and multi-junction (intersection) a-Si p-I-n cell structures in superstrate setup. The charge bearers are isolated by the electric field made over the absorber intrinsic layer by the p-and n-layers. Cells based on a-Si significantly experience the ill effects of performance degradation when shone with sunlight, a paradox known as the Staebler-Wronski impact (SWE) [21]. Through continued research, in recent years to stabilize the efficiency of a-Si:H cells, the record device for a single junction indicates stabilized efficiency of 10.2% [22]. Utilizing a multijunction structure, the record device shows stabilized efficiency of 13.6% [23].

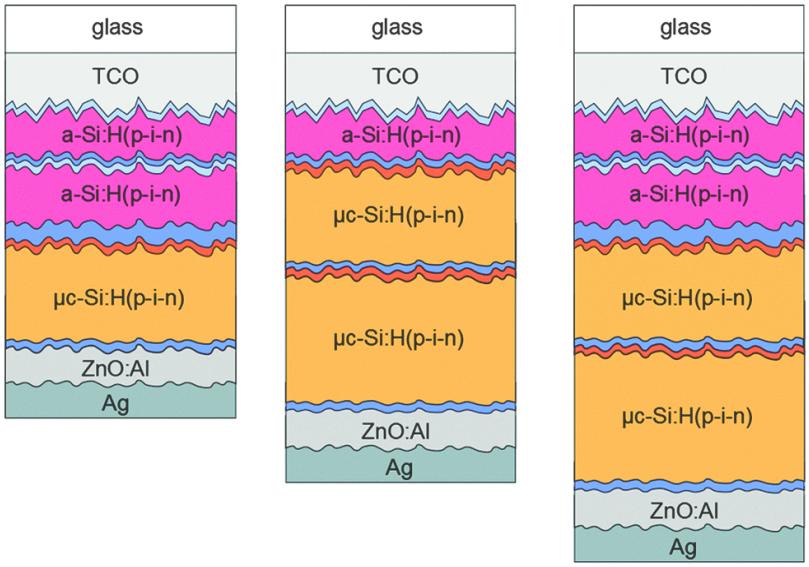

Figure 2. 6: Cross-sectional illustration of typical single- and multijunction a-Si:H solar cells in a superstrate configuration.

2.3.2 CADMIUM TELLURIDE

Cadmium telluride (CdTe) has for long been perceived as an ideal contender for thin-film PV applications [24] on the grounds that it is a chemically stable semiconductor compound with broad absorption coefficient that is >104 cm^{-1} and a direct bandgap of around 1.45 eV [25,26]. The material can be doped both as p-or n-type; be that as it may, the absorber layer of the CdTe solar cell is a p-type semiconductor. Ordinarily, CdTe devices are produced in superstrate design, where a pellucid (transparent) conducting oxide (TCO) as a front contact is first stored on a glass substrate, trailed by a n-type CdS window layer that structures the heterojunction with the p-type CdTe layer. The absorber CdTe layer is then deposited on the CdS layer at temperatures between 400 °C and 600 °C through distinctive deposition routes including close-spaced sublimation (CSS), which is a thermal evaporation technique [27, 28]; electrodeposition [29]; sputtering [30]; and screen printing [31]. Lastly, a metal film as the back contact is deposited on the CdTe layer. A schematic representation of a conventional CdTe/CdS solar cell is shown in figure 2.7.

The PCE of CdTe-based solar cells has expanded over the years to surpass 20%. In February 2016 press statement, First Solar announced another world record of 22.1% for a CdTe cell [32]. With the advancement made in the CdTe innovation by accomplishing financially savvy, high-efficiency devices that can without much of a stretch contend with mc-Si cells, a few issues associated with CdTe solar cells could influence their production in the future. The real issues are the poisonous nature (toxicity) of cadmium and the shortage of tellurium, which could adversely affect terawatt (TW)- scale generation in future, prompting increased cell and module costs.

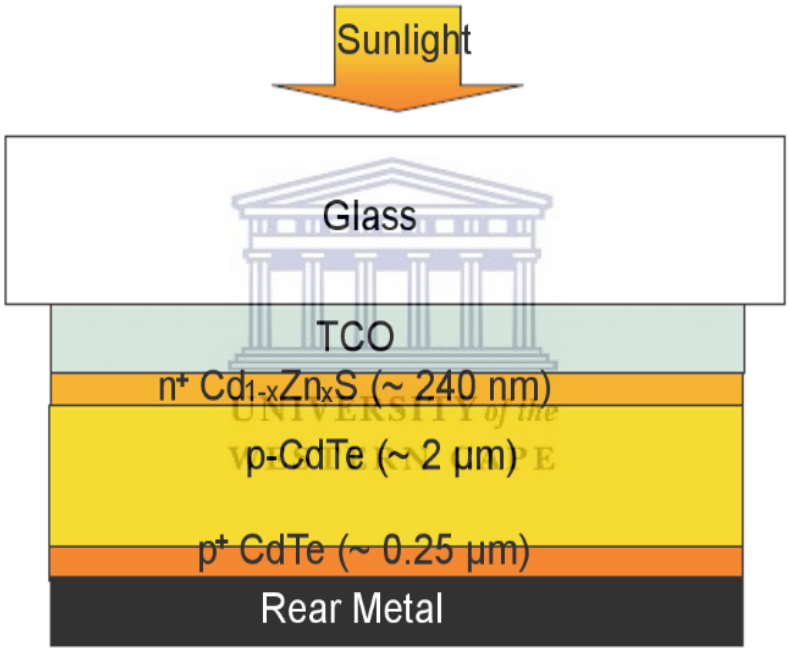

Figure 2. 7: Cross-sectional illustration of a CdTe solar cell in a superstrate configuration.

2.3.3 COPPER INDIUM GALIUM SULFIDE (CIGS)

Chalcopyrite semiconductor compounds, such as, copper indium diselenide ($CuInSe_2$), copper gallium indium diselenide ($CuGa_{1-x}In_xSe_2$), and copper indium disulfide ($CuInS_2$) display coordinate (direct) bandgaps and high optical absorption coefficients, making them convenient for PV application. The capability of the $CdS/CuInSe_2$ framework as a PV heterojunction was initially illustrated in 1974 [33]. The main thin-film CdS/CuInSe2heterojunction solar cell which was manufactured in 1976 by Kazmerski et al. demonstrated an efficiency of 4.5% [34]. Afterward, gallium (Ga) was fused in $CuInSe_2$ to create $Cu(InGa)Se_2$. The quaternary compound $Cu_2InGaSe_4$ (CIGS) is the best chalcopyrite absorber, with a record efficiency of 21.7% [35 ,36]. CIGS thin-films have been produced utilizing distinctive deposition techniques such as sputtering, electrodeposition, spray-deposition, and thermal evaporation [37-40]; notwithstanding, the greater part of the CIGS absorber layers of the devices that gave the best efficiencies were deposited by thermal evaporation. Figure 2.8 illustrates a cross-section of a conventional CIGS solar cell. Usually, CIGS devices are manufactured in substrate design, beginning with the deposition of a molybdenum layer as the back contact on a glass substrate, followed by the deposition of the absorber layer, trailed by a n-type CdS buffer layer that frames the heterojunction with the p-type CIGS. An intrinsic ZnO layer is deposited over the CdS, accompanied by an aluminum-doped ZnO layer that fills in as the top contact. Like the CdTe innovation, indium shortage creates an issue in CIGS PV applications, where the high cost of indium impacts cell and module costs and the material could encounter some shortage in near future.

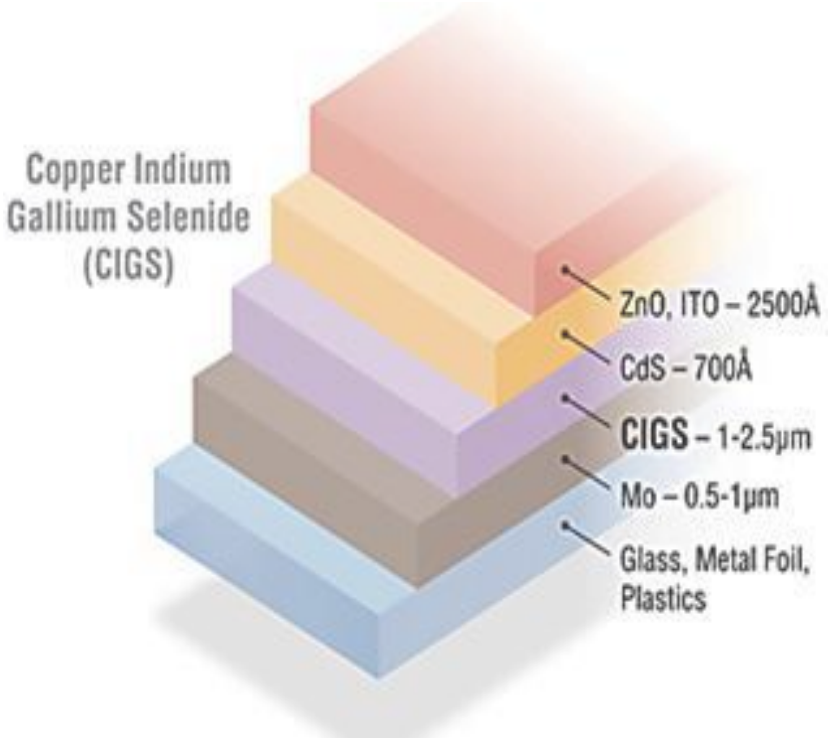

Figure 2. 8: Cross-sectional illustration of a typical CIGS cell in substrate configuration

2.4 KESTERITE SOLAR CELLS

Kesterite $Cu_2ZnSn(S(Se))_4$ or (CZTS(Se)), semiconductor has got huge consideration worldwide because of its great optical and electronic properties similar to that of Cu(InGa)Se2 (CIGSe) and CdTe materials, including its content of earth-abundant and low-harmful (non-toxic) constituents. Advancement has been made in CZTSSe solar cells in recent years and the highest efficiency (PCE) of 12.6% has been accomplished by a group at IBM [41] which revealed considerable commercial promise. Like CIGSe, CZTSSe thin-films can be manufactured by both vacuum and solution methods. Early work has been accounted for by Katagiri et al. on sulfide Cu_2ZnSnS_4 (CZTS) through vacuum-based evaporation technique with device conversion efficiency of 0.66% [42]. Besides, the systematic advancement in this procedure has brought about noteworthy change in the conversion efficiency of up to 8.4% for sulfide CZTS devices [43] and 11.6% for selenide $Cu_2ZnSnSe_4$ (CZTSe) devices [44]. Sputtering method has likewise been utilized and yielded 9.1% for CZTS devices [45], and

more than 10% for sulfoselenide CZTSSe devices [46,47]. In any case, these vacuum-based methods have a few downsides, such as high cost, low throughput, and, most prominently, extreme elemental losses during deposition. Accordingly, throughout the years, the quest for low-cost production has concentrated mostly on the non-vacuum deposition techniques. Solution-based procedures can be partitioned into two methodologies: electrodeposition and direct solution coating (including particulate-and molecular based solution coating). Note that a progression of record setting devices has been produced by the group at IBM through a hydrazine solution coating process [41, 48–50].

2.4.1 SYNTHESIS OF KESTERITE (CZTSSE) NANOPARTICLES

Kesterites CZTS(Se) are being investigated rigorously as substitute absorber material in thin film solar cells, which contains non-lethal and Earth sufficient components. Its structure is basically adapted from the related chalcopyrite CIGS solar cells [51–54] with a Mo back contact, a CdS cushion layer and a ZnO window. Kesterite solar cells have come to over 10% efficiency [51], while chalcopyrites are over 20% efficient [55].

2.4.1.1 HOT INJECTION METHOD

The synthesis of CZTS nanoparticles was initially reported by hot injection technique [56-59]. This involves the fast infusion of sulfur precursor into metal precursor at desired temperature. Basically, the metal precursor was set up by blending of Cu, Zn, Sn salts with the coordinating solvent (typically Oleylamine) and heated in a three-neck flask under inert gas condition. While incubating, the stable Cu-, Zn-, Sn-Oleylamine coordination complex will be formed [58]. The sulfur precursor was prepared independently in a 10 ml vial by dissolving elemental S into Oleylamine. Figure 2.9 presents the TEM and SEM micrographs of the average CZTS nanoparticles prepared by this method. As seen in Figure 2.9a and c, well crystalline CZTS nanoparticles with random shape and size in the scope of a few tens of nanometers were

obtained. The lattice spacing of 3.1 Å (Figure 2.9b) relates with the d-spacing of (112) planes for CZTS kesterite. Another group of researchers explored the hot injection method as a method of synthesis for a quaternary kesterite nanoparticles with chemical representation of CXTS (X: Co, Ni, Zn, and Mg) [59]. Later on, Kameyama et al. adjusted the synthesis with the elimination of injection process [60]. Contingently, the Cu, Zn, Sn salts, elemental S and oleylamine were combined and heated in one-pot to form CZTS nanoparticles. Moreover, the continuous production via a flow reactor makes production of CZTS nanoparticles in a large scale achievable [60].

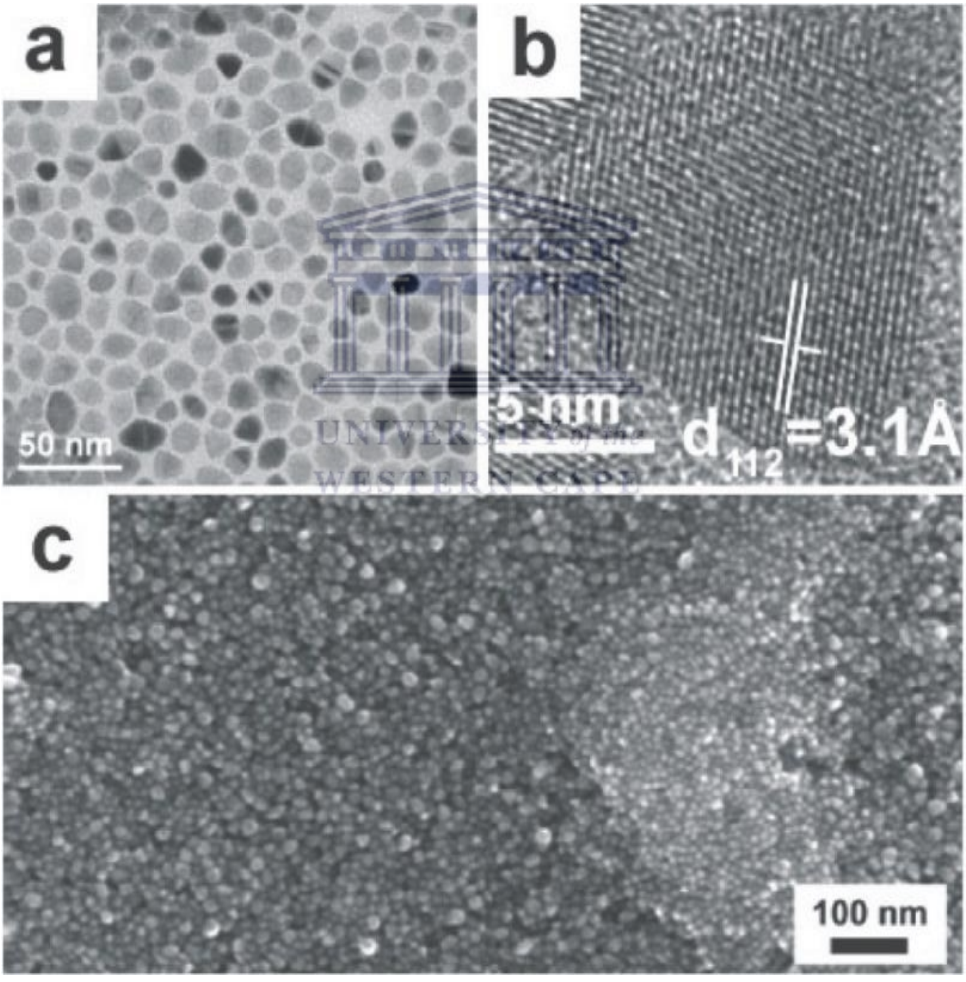

Figure 2. 9: (a) TEM, (b) HRTEM and (c) SEM images of the CZTS nanoparticles synthesized using hot injection method [57].

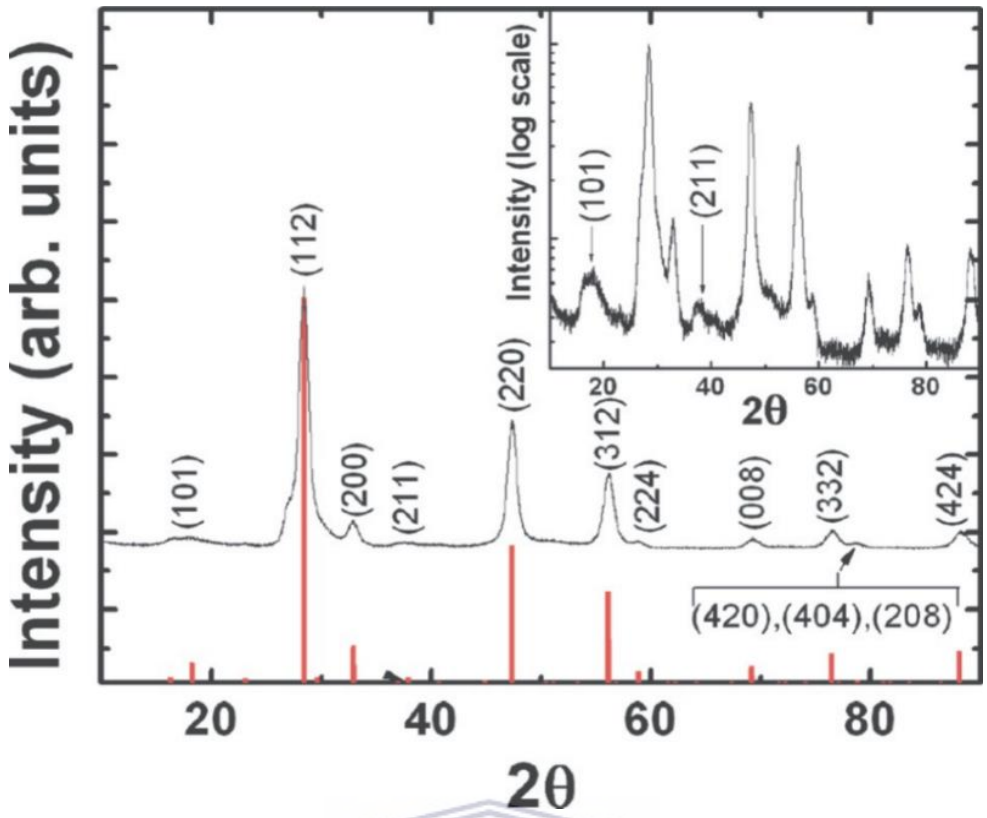

Figure 2. 10: The XRD pattern of CZTS nanoparticles prepared with hot injection method with red reference pattern as the standard XRD pattern for kesterite CZTS. [57].

2.4.1.2 SOLVOTHERMAL METHOD

This technique includes developing of single crystal from a non-aqueous solution in an autoclave (a thick-walled steel vessel) at high temperature (400 ˚C) and pressure. Zhou et al. disclosed the preparations of CZTS nanostructures in an autoclave using ethylene glycol as the solvent [61]. The synthesized CZTS nanocrystals self-assembled into a sphere like shape with the mean size of the sphere ranging from 100 to 150 nm. Using ethylenediamine, Cao et al. figured out how to get smaller particles (5 ~ 10nm) [62]. Wang et al. prepared CZTS nanoparticles utilizing two-phase technique with 1-octadecene and triethylene glycol [63]. A comparative setup to the hot coordinating solvent method was utilized.

2.4.1.3 HYDROTHERMAL METHOD

This method which offer a green synthesis method when compared with solvothermal method, is characterized as a strategy for synthesis of single crystals that relies upon the solubility of minerals in hot water under high pressure typically in an autoclave and is profoundly attractive in the preparations of CZTS nanoparticles. Wang et al. effectively exhibited CZTS nanostructures utilizing an autoclave with hydrothermal method [64]. The aqueous soluble thiourea was utilized as the sulfur precursor. Zhao et al. detailed hydrophilic CZTS nanocrystals by blending $(NH_4)_2S$ solution with copper, zinc, tin precursor solution at room temperature, which prevents the utilization of long chain ligands [65]. The hot injection technique has turned out to be a robust method to synthesize different semiconductor nanocrystals including CdSe, ZnS, PbS and Cu_2InSe_2 [66-69].

2.5 CHARACTERISTICS OF CZTS

2.5.1 CRYSTAL STRUCTURE

Kesterite is the phase that is most normally applied in CZTS-based solar cells. Its crystal structure can be gotten from the substitution of elements at the various lattice sites of two connecting unit cells of the zinc blende crystal structure. In the first place, Zn^{2+} ions in the zinc blende structure are supplanted by Cu^{+} and Fe^{3+} in a 1:1 proportion to frame a chalcopyrite crystal structure that is normal for CIGSe. On account of CIGSe, In^{3+} and Ga^{3+} are fused rather than Fe^{3+}. To shape a stannite CFTS, the Fe^{3+} ions are supplanted by Fe^{2+} and Sn^{4+}. On account of CZTS, Zn^{2+} ions are joined rather than $Fe^{2+.}$ Their relationship can be seen in figure 2.11. The auxiliary models of two common minerals are utilized to depict CZTS: kesterite and stannite crystal structures, as seen in figure 2.12. These crystal structures are close; in the two structures the cations are situated on tetrahedral sites yet their dispersions on planes opposite to the c-axis are not the same. Besides, the situation of the chalcogen particle

is somewhat extraordinary in these structures [70]. When looking at the accessible information on x-ray diffraction on CZTS and CZTSe from the International Council on Diffraction Data (ICDD), it gives the idea that the sulfide compound tends to appear in kesterite structure, while the selenide compound happens in stannite structure. Notwithstanding, in light of the fact that Cu^{+} and Zn^{2+} are isoelectronic, x-ray diffraction can't recognize kesterite and stannite structure since x-ray interfaces with the electron shell of the atoms. Then again, neutrons collaborate with the cores and can recognize Cu and Zn molecules [72]. In an exhaustive neutron diffraction investigation of different $Cu_2ZnSn(S_{1-x}Se_x)_4$ compounds, it was demonstrated that the sulfide and additionally the selenide occur in the kesterite structure, not in the stannite structure. Both demonstrate a certain issue in the middle of the Cu and Zn sites [72].

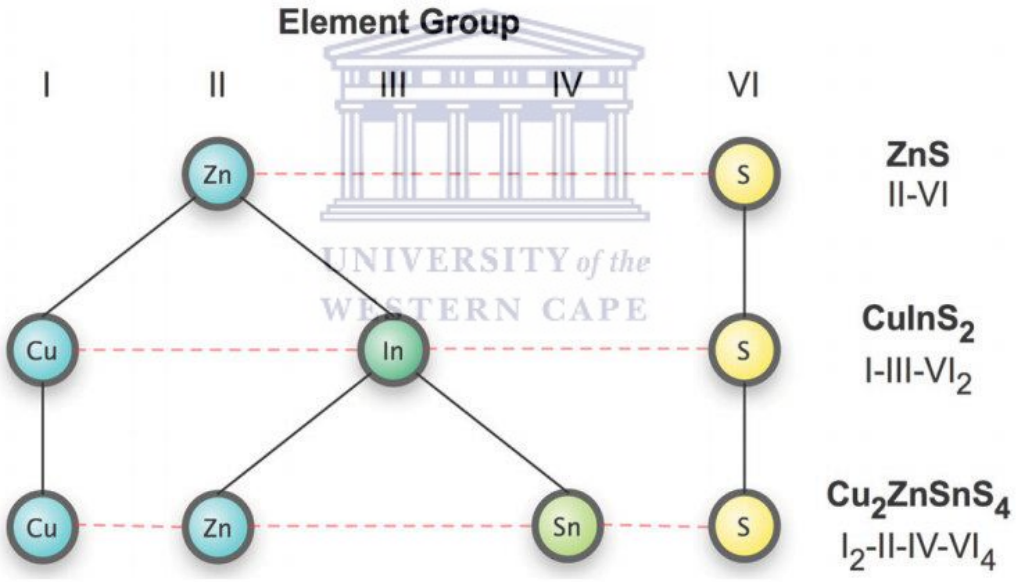

Figure 2. 11: Link between two, three, and four semiconductors to give CZTS.

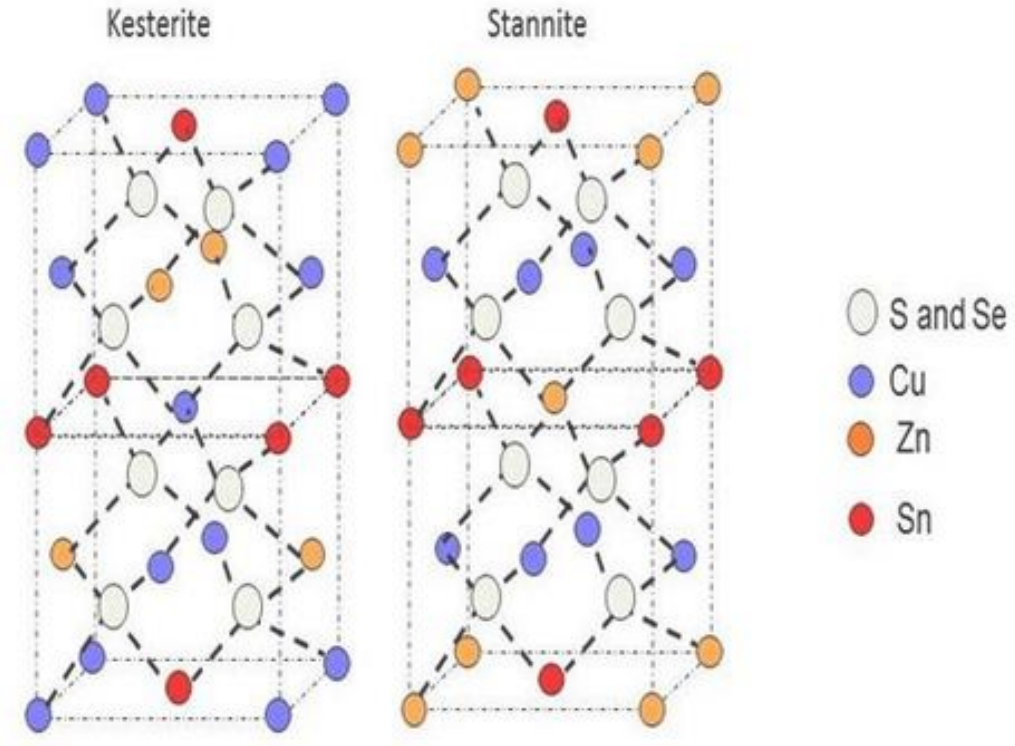

Figure 2. 12: Kesterite (left) and stannite (right) structure [72].

Thermodynamically, the kesterite structure has a lower energy and is steadier than the stannite structure, which was affirmed by the Madelung potentials [73]. Kesterite CZTS have XRD peaks fundamentally the same as those of auxiliary phases ZnS and Cu2SnS3 [74], and in order to separate them, Raman spectroscopy is vital [75]. In any case, when it is not possible to make a quantitative analysis of the secondary phases by Raman spectroscopy, for such a case, x-ray absorption near edge spectroscopy (XANES) can be utilized [76].

2.5.2 KESTERITE PHASE SPACE

Earlier experimental work has been done to ratify the calculated equilibrium phase space. Figure 2.13 (A) demonstrates the experimentally decided pseudo ternary Cu_2S– ZnS– SnS_2 framework, with single-phase CZTS occupying a small region in the middle [77], permitting a few mol % absolute deviations of any of the constituent binaries [78,79]. Subsequently, it is extremely challenging to prepare single-phase kesterite materials with copper-poor and zinc-rich chemical composition, which is required for high efficiency solar cells [80], while strategically avoiding the formation of auxiliary phases.

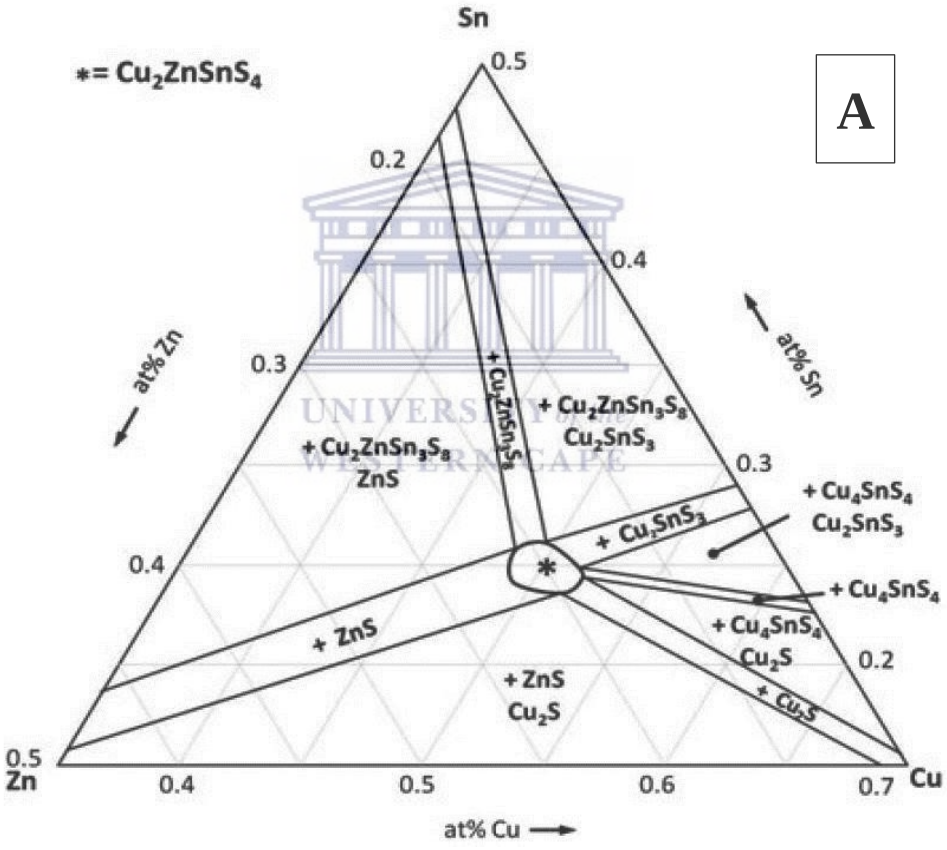

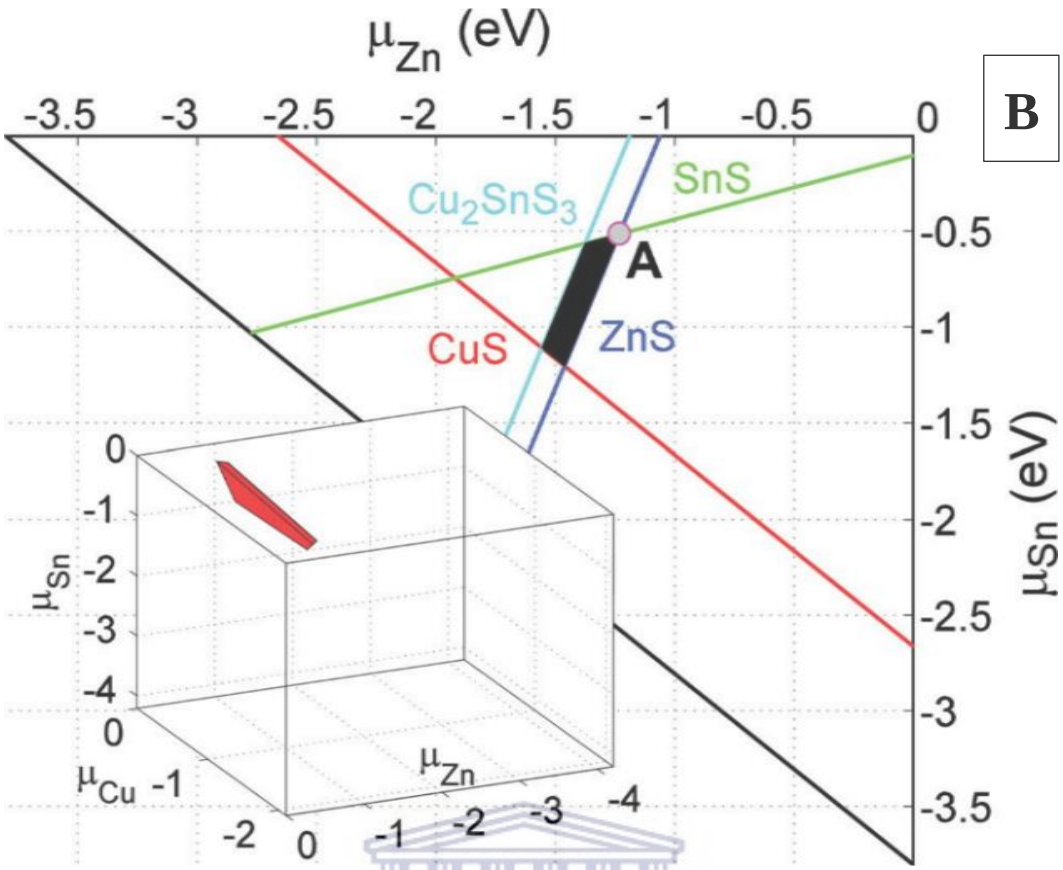

Figure 2. 13: (A) Phase diagram showing small central region where CZTS forms [77]. (B) The estimated chemical potential stability diagram of CZTS in a 2D copper-rich plane (inset is the stable 3D region) [81].

This is upheld by hypothetical estimation, as seen in Figure 2.13 (B), which demonstrates the chemical-potential diagram and the presence of other auxiliary (secondary) phases that can be obtained, as well as shows that the volume of the stable region for CZTS is small. In contrast with the stability region of $CuInSe_2$, with the chemical-potential window of In (μIn) around 1.0 eV wide, the CZTSe quaternary compound demonstrates a much smaller chemical-potential range of Zn (μZn) (under 0.2 eV wide) and Sn (μSn) (around 0.6 eV wide), which demonstrates that stricter chemical potential control of Zn and Sn is required in the synthesis process. A deviation outside this space will cause the formation of CuS, ZnS, SnS, or Cu_2SnS_3. The chemical potential space also illustrates that under harmonious conditions, a copper-rich

diffusion is required to create the single-phase kesterite, in spite of the essentially Cu-poor, Zn-rich conditions related with higher-efficiency devices [81]. In other words, under harmonious conditions the essentially Cu-poor, Zn-rich conditions utilized for high efficiency CZTSSe devices will probably create auxiliary phases, particularly ZnS(e). Experimentally, ZnS and Cu_2SnS_3 have regularly been seen which can be explained by the narrow accessible range of μZn, i.e., Zn-rich leads to ZnS, while Zn-poor leads to Cu_2SnS_3 [71]. Furthermore, this limited single-phase range is convoluted by Sn unpredictability during deposition. Subsequently, composition and phase control are a major challenge for kesterite CZTSSe fabrication.

2.5.2.1 SECONDARY (AUXILLARY) PHASES

Given its small area of composition, binary and ternary secondary phases can form in addition to CZTS throughout the growth period. These phases consist of ZnS, SnS, SnS_2, CuS, Cu_2S, and Cu_2SnS_3. Formation of secondary phases was suggested to be associated with the film composition [82]. As stated in the previous section, the best copper-poor and zinc-rich composition for the CZTS device results in ZnS or ZnSe phases present within the CZTS or CZTSe compound. Many published works stated the formation of this secondary phase in copper-poor and zinc-rich composition [83,84]. ZnS and ZnSe crystallize in the sphalerite and wurtzite structure composing of wide bandgap (around 3.6 eV for ZnS [83]), and they will build insulator areas in the absorber layer of the solar cell. Depending on its concentration, ZnS can limit the active area (where the electron-hole pairs are produced) and influence current accumulation. Because of the low conductivity of ZnS and ZnSe, they don't impact the V_{oc} of the device, yet could cause an expansion in the series obstruction [85]. The copper sulfide phases (CuS and Cu_2S) are expected in CZTS samples with Cu-rich composition. They have a chalcocite structure and show p-type nature with good metallic conduction, which is due to a high concentration of holes in the valence band [86–88]. Their presence is detrimental

to the solar cell because they can shunt the device. Tin sulfide phases can evolve in Sn-rich CZTS films as SnS or SnS_2. The SnS compound is a semiconductor with application in optoelectronic and PV fields. The material exhibits both p- and n-type conduction [89] with a bandgap of 1.2–1.7 eV [90–93]. Tin disulfide (SnS_2) is an n-type material with direct bandgap of 2.18–2.44 eV [89, 94, 95]. Although no harmful effects were reported of SnS phases on solar cell performance, a high concentration of the n-type semiconductor in the p-type active layer can build a second diode that hinders carrier collection and thus reduces fill factor. Cu_2SnS_3 (CTS) is a ternary secondary phase that forms in CZTS material with Zn-poor composition. The compound is a p-type semiconductor [96] with metallic character [97], crystallizing in different crystal structures including cubic, monoclinic, and hexagonal forms [98, 99]. However, the cubic form requires temperatures higher than 775 ˚C to crystallize [97]; therefore, it is unlikely to be detected in kesterite films, which are prepared in lower temperatures. Depending on the crystallographic structure, the optical bandgap is in the range of 0.93−1.35 eV [100]. As $Cu_{2-x}S$ phases, CTS is harmful to the solar cell because of its high conductivity, which could decrease the shunt resistance, and its low bandgap could reduce the V_{oc}. The x-ray diffraction (XRD) is viewed as the essential method for identifying elements and compounds. In any case, it has some constraint while distinguishing phases with comparable crystal structure in a compound. This case is available in the CZTS material since ZnS, CTS, and CZTS show diffraction peaks at similar positions (figure 2.14) because of the similitude in the crystal structure and lattice parameters [101, 102]. Other secondary phases, for example, CuS and SnS, can be identified effectively by XRD [102].

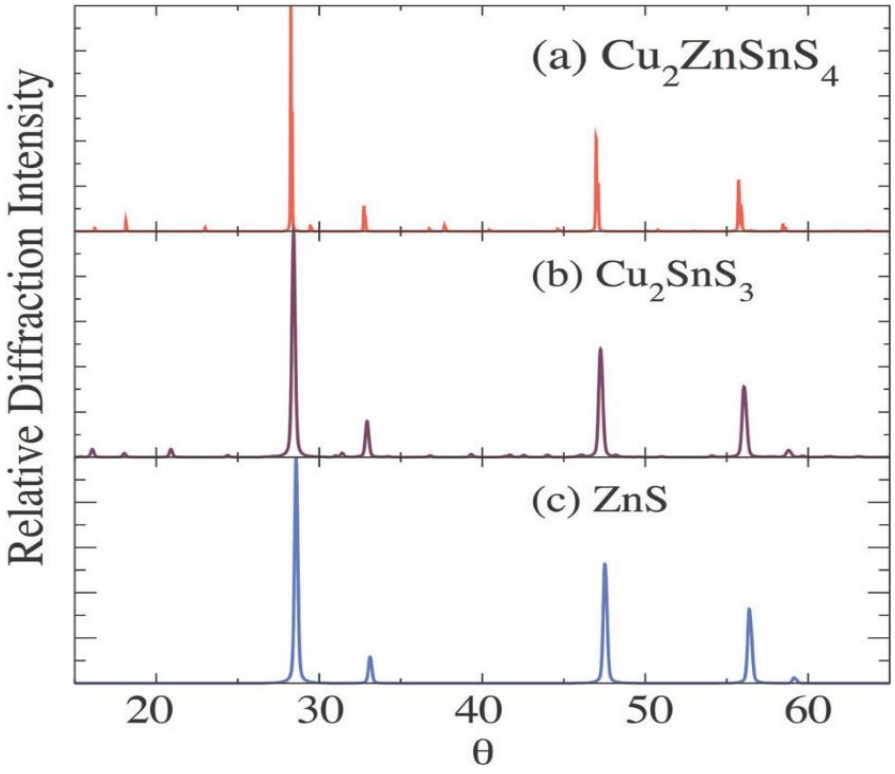

Figure 2. 14: Simulated X-ray diffraction spectra of kesterite CZTS, CTS, and ZnS showing overlap of the main peaks [81].

Raman spectroscopy is generally utilized as an integral method to identify auxiliary phases in CZTS. The kesterite CZTS displays two sharp peaks at 288– 289 cm^{-1} and 338– 239 cm^{-1}, a shoulder with a primary peak at 351 cm^{-1}, and a broad peak between 368– 373 cm^{-1} [103]. For the cubic zinc sulfide phase, one sharp peak shows up at 352 cm^{-1} and a weaker one at 271 cm^{-1} [104]. Raman shifts of monoclinic CTS show up at 290 cm^{-1} and 352 cm^{-1} [98], and of the cubic CTS at 267 cm^{-1}, 303 cm^{-1}, and 356 cm^{-1} [105,106]. The tetragonal CTS indicates two sharp peaks at 337 cm^{-1} and 352 cm^{-1}, and a broad peak between 280 cm^{-1} and 290 cm^{-1} with peak maximum at 297 cm^{-1} [105,106]. Table 2.1 records the places of Raman shift for CZTS and the generally observable auxiliary phases. Note that the greater part of previous attempts to obtain the properties of CZTS by Raman spectroscopy were performed via blue and green wavelength excitations of 488, 514.5, and 532 nm, which are normally used for Raman estimations. Latest investigations uncovered extra Raman modes by utilizing

nonstandard excitation wavelengths. Dimitrievska et al. [107] explored Raman scattering estimations of CZTS utilizing six distinctive excitation wavelengths from near infrared to ultraviolet and discovered 18 peaks attributed to CZTS which was credited to the 27 optical modes expected for CZTS. Considering that the ZnS stage has its fundamental Raman peak at 352 cm^{-1} and that CZTS displays one peak nearly at a similar position (351 cm^{-1}), it makes it hard to differentiate/recognize ZnS from CZTS. The trouble in separating ZnS from CZTS utilizing Raman scattering was explained to be as a result of utilizing excitation wavelengths in the visible region [108]. It has been shown tentatively that the ZnS auxiliary phase can be effectively recognized from CZTS by using an ultraviolet excitation wavelength of 325 nm [109].

Table 2 1: Raman shift positions of CZTS and of the common secondary phases.

Phase	Raman Shifts (cm^{-1})	Reference
CZTS	287, 338, 351, 368	[78, 103]
Monoclinic CTS	290, 352	[98]
Cubic CTS	267, 303, 356	[104, 105]
Tetragonal CTS	297, 337, 352	[105, 106]
Orthorhombic Cu_3SnS_4	318	[105, 106]
$Cu_{2-x}S$	264, 475	[103]
Cubic Zn	275, 352	[106]
SnS	163, 189, 220	[108]
SnS_2.	215, 315	[108]
Sn_2S_3	52, 60, 307	[108]
Hexagonal MoS_2	287, 383, 409	[109]

2.5.3 OPTICAL-ELECTRICAL PROPERTIES

The kesterite $Cu_2ZnSn(S_{1-x}Se_x)_4$ semiconductor offers with a high absorption coefficient and tunable band gap energy. The absorption coefficients α of the CZTS-based kesterite semiconductor are as high as 104–105 cm^{-1} [42]. Taking at least $\alpha = 104\ cm^{-1}$, 2.5 μm thick CZTS film can absorb in excess of 90 % of the incident light without reflection losses. The bandgap of kesterite can be tuned from 1.0 eV at x = 1 to 1.5 eV at x = 0 [42, 110]. It can be experimentally shown via optical transmission estimations [109] or quantum productivity estimations in solar cells [80]. Estimation of the electronic band structure of CZTS reveals an immediate bandgap at the gamma point of the Brillouin zone [71]. The bandgap has been hypothetically computed via density functional theory calculations in various approximations

[112–116], hybrid functionals [112, 115, 117] and GW computations [115]. Every single forecast for the kesterite structure concurs immensely with the hypothetically bandgaps, though the bandgaps in stannite structure are around 100 meV lower [118]. The extent of the bandgap of CZTS can be explained by the chemical behaviour of the valence and conduction band states, and specifically, the low binding energy of the filled Cu 3d valence band [71]. For all Cu-based chalcogenides, including the quaternary kesterite and ternary chalcopyrite compounds, the valence band maximum (V_{BM}) is an antibonding condition of the anion p and Cu d orbitals [119]. Since the valence p level of S has less value of energy than Se, the V_{BM} of the sulfide CZTS is lower than that of the selenide CZTSe. In any case, valence band offset (V_{BO}) between the sulfide CZTS and selenide CZTSe is very little (<0.2 eV), lower than that of ZnS and ZnSe (~0.52 eV [120]). This distinction is from p-d hybridization in Cu-based chalcogenides on the grounds that the hybridization is more grounded in the shorter Cu-S bond and pushes the antibonding V_{BM} level of the sulfide up in respect to that of the selenide. The conduction band maximum (C_{BM}) is comprised of a solitary band beginning from the Sn 5S and the S or Se p orbital [71]. The regular band arrangements, ascertained with reference to the energy contrast of deep atomic-like center states over the kesterite/CdS heterojunction [120], are plotted in figure 2.15. Contrary to silicon, where either particle of phosphorus or boron is deliberately doped to deliver n-type and p-type semiconductors, respectively, CZTS-based materials are self-doped through the formation of characteristic, interstitial and antisite deformity at the time of their growth [118]. The formation energies of most acceptor deformity are lower than those of the donors clarifying the experimentally observed p-type conductivity and indicates that n-type doping in these compounds will be problematic. In any case, the least energy defect is CuZn antisite, which is not quite the same as $CuInSe_2$ where the dominant deformity is the Cu vacancy (V_{Cu}) [122]. This CuZn antisite imperfection delivers a more profound contributor level than V_{Cu} in the bandgap of CZTS and causes huge bandgap energy

decrease, which is negative for CZTS solar cell efficiency. Hence, it is important to reduce the formation energy and improve the population of shallow V_{Cu} relative to CuZn via copper-poor and zinc-rich composition.

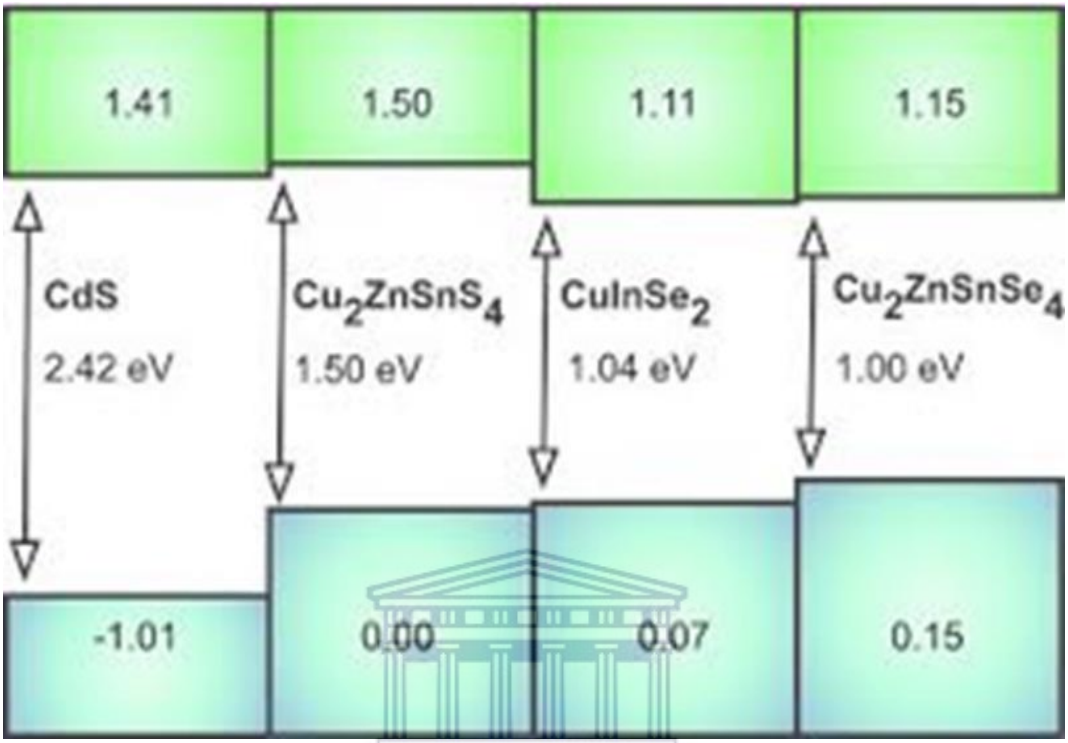

Figure 2. 15: The estimated band arrangements for CdS, CZTS, CZTSe and $CuInSe_2$. CdS acts as n-type window layer [121].

The hole density of typical kesterite materials is around 1016 cm^{-3} [111, 123–125], which is characteristic of CIGSe in high efficiency CIGSe solar cells. Hole density of 1018-1019 cm^{-3} also has been reported by some groups [126–128], due to the presence of $Cu_xS(e)$ secondary phases leading to the films being useless degenerate semiconductor.

2.5.4 MORPHOLOGY AND SIZE CONTROL

Size and shape are two vital parameters for nanoparticles because they give information in relation to the properties of the nanoparticles. An important example can be cited from CdSe nanocrystals where the absorption edge of CdSe nanocrystals blue shifts as the size increases from 17Å to 150Å, showing a decrease in the energy band gap [129]

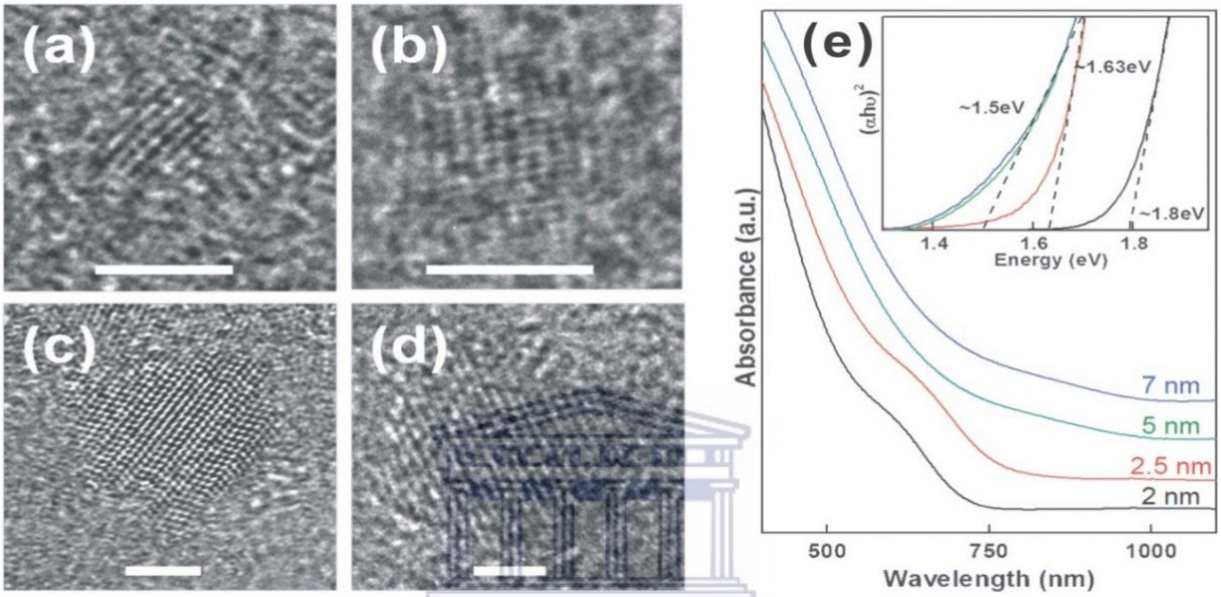

Figure 2. 16: HRTEM images (a, b, c, d) of synthesized CZTS nanocrystals in a scale of 2 nm (e) the UV-vis-NIR absorption measurement CZTS nanoparticles with different size. The inset displays the Tauc plot for the corresponding absorbance curves [130].

The size control of CZTS nanoparticles by tuning the amount of oleylamine and adjusting the reaction temperature was revealed by Khare et al [130]. In their work, the Cu, Zn, and Sn diethyl dithiocarbamate complexes were used as the metal precursors. The HRTEM micrographs show that the synthesized CZTS nanoparticles had sizes of 2 nm (figure 2.16a), 2.5 nm (figure 2.16b), 5 nm (figure 2.16c) and 7 nm (figure 2.16d). The optical absorption of the UV-vis-NIR absorption measurement of CZTS nanoparticles with crystal size corresponding to figure 2.16a-d is shown in figure 2.16e. The band gaps are estimated based

on the $(\alpha h\nu)^2$ vs. hν plot in figure 2.6e to be 1.8 eV (2 nm), 1.63 eV (2.5 nm), 1.5 eV (5 nm) and 1.5 eV (7 nm) respectively. The higher band gap energy than the usual 1.5 eV for particles size of 2 nm and 2.5 nm provides the evidence for quantum confinement. Beside kesterite structure, CZTS can also form wurtzite structure. Several research groups have disclosed the synthesis of wurtzite structures. Lu et al. prepared wurtzite CZTS nanoparticles in nanoprisms and nanoplates shape [131]. Singh et al. was able to form mono-dispersed wurtzite CZTS nanorods [132]. The size and shape control of CZTS wurtzite are easier than the kesterite phase, which is due to slow reaction dynamics for the formation of wurtzite structure.

2.6 FABRICATION OF CZTS SOLAR CELL.

2.6.1 DEVICE ARCHITECTURE

The semblance in structural and electrical properties allow the device architecture that is optimized for chalcopyrite CIGSe to work just the same for kesterite CZTSSe absorber. This conformity allows the knowledge gained from chalcopyrite research and development to enhance the understanding of kesterite materials and devices. Therefore, a review of kesterite CZTSSe and chalcopyrite CIGSe technologies is important to realize higher efficiencies for kesterite solar cells. Figure 2.17 (a) shows the typical architecture of kesterite CZTS(Se) solar cell, which is based on a heterojunction cell structure that is similar to a chalcopyrite CIGSe device architecture. In a typical kesterite solar cell, 500 nm to 1000 nm thick Mo layer is deposited as back contact on a suitable substrate such as soda lime glass, polyimide (PI) or steel foil followed by deposition of kesterite CZTSSe absorber with thickness of 700 nm to 2500 nm on the back contact by vacuum- or solution-based processes.

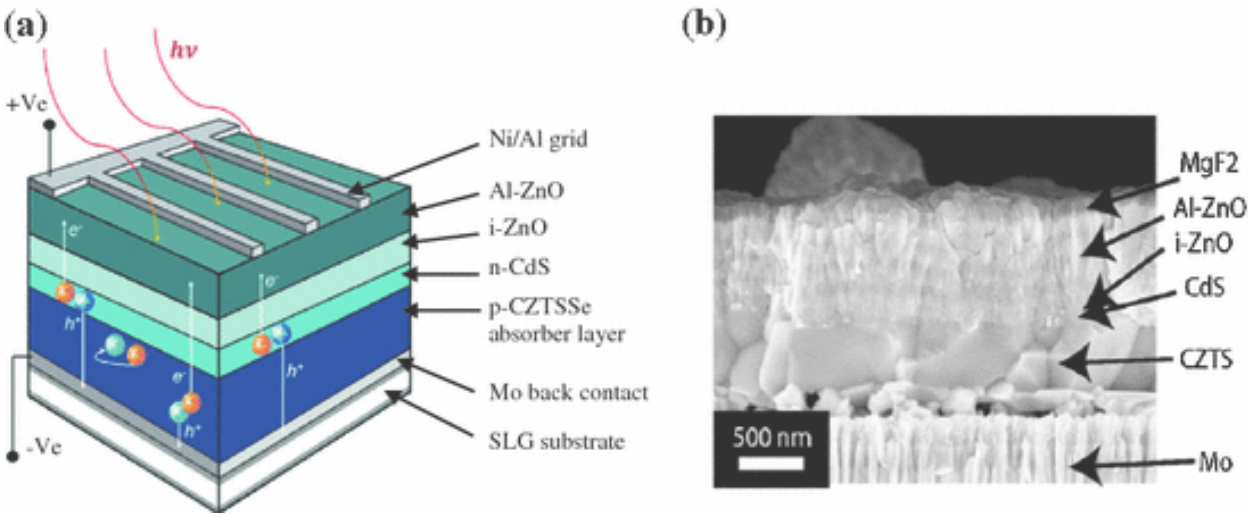

Figure 2. 17: (a) Typical architecture of kesterite CZTS(Se) solar cell device. (b) TEM micrograph of a typical CZTS solar cell device.

An n-type buffer layer is immediately grown to form a p-n junction with the p-type CZTS absorber. For most CZTS-based solar cells, a 50 nm thick CdS by chemical bath deposition is used. Next, a 50 nm to 100 nm thick window layer, such as intrinsic zinc oxide (i-ZnO), is deposited by RF sputtering. The reason for using the i-ZnO layer is to minimize shunting pathways and prevent intermixing between the absorber and the transparent conductive oxide (TCO) when the thin CdS layer does not provide complete coverage of the underlying CZTS layer. Subsequently, a TCO layer, such as indium tin oxide (ITO) or aluminum-doped zinc oxide (AZO), with a thickness of around 250 nm is sputtered. Finally, Ni/Al metal contacts, which serve as top electrode to collect the photogenerated electrons with minimal resistive losses, are deposited by evaporation on the TCO. A typical SEM micrograph of the CZTS device shown in figure 2.17 (b) [133]. The structure of a kesterite solar cell is quite complex because it contains several compounds as stacked films that may react with each other. Fortunately, no detrimental interface reactions occur at ambient temperatures. The formation of $MoS(e)_2$ at the back contact/CZTSSe interface during CZTSSe thin film growth is inevitable through reactions between Mo and chalcogen at high chalcogen partial pressure or

CZTSSe in the absence of chalcogen excess [134], which may facilitate an electrical quasi-ohmic contact and improve the adhesion of CZTSSe to Mo back contact, but leads to a high series resistance and accordingly reduces the device efficiency if not thin enough [135], similar to the case of CIGSe solar cells [136]. A mild diffusion of Cd into kesterite has been reported which is believed to be beneficial to the cell performance [137]. This could be interpreted as the occupation of Cd for vacant Cu sites in the Cu-poor and Zn-rich CZTS matrix (which favors the formation of Cu vacancies [138]) according to the first-principles calculations [139] and Sardashti's report [140]. In CIGSe solar cells, a similar behaviour at the CIGSe/CdS interface has been reported by many groups [141, 142] and is believed to be the key factor to the success of the CBD-CdS process [143]. Similar to the role of ordered vacancy compound $Cu(InGa)_3Se_5$ (OVC) in CIGSe, Cd on Cu sites would act as substitutional donors, and therefore give result in n-type absorber surface, facilitating a more effective buried homojunction [144].

2.6.2 TECHNIQUES FOR KESTERITE DEPOSITION.

The development of excellent CZTS thin film is beneficial for its application. The principal objectives were to obtain top-notch material (homogeneous single-phase films with large grains and no voids), a minimal cost fabrication process, and high deposition rate. Kesterite CZTS(Se) thin film can be combined using vacuum or non-vacuum deposition techniques in a few step manufacture processes. The one-step process deposits the four constituents (Cu, Zn, Sn, and S(Se)) at the same time on a substrate at high temperatures. High temperatures are important to facilitate the interdiffusion of the elements. In the two-step methodology, a precursor containing the metals or even the four elements will initially be deposited on a substrate and accordingly tempered at high temperatures in sulfur, selenium, or sulfur-selenium (for CZTSSe) atmosphere. Pure sulfide CZTS films is of special use in contrast with the selenide ones since sulfur is less lethal and more affordable than selenium, in spite of the

fact that the highest efficiencies were accomplished with devices where only selenium or sulfur/selenium was incorporated in the kesterite active layer of the solar cell. Precursors can be obtained by keeping all components at the same time (co-deposition) or as a heap of elemental layers. Growth techniques and synthesis process parameters, for example, temperature and time were observed to impact the film properties (e.g., grain estimate, synthetic synthesis, bandgap) [145-153].

2.6.2.1 VACUUM DEPOSITION TECHNIQUES

Deposition using these techniques occurs mainly at low pressure and requires high temperatures in some methods. Generally, vacuum-based deposition techniques, including thermal evaporation, sputtering, and pulsed laser deposition (PLD), provide good film reproducibility and easy control of film chemical composition [154]. Sputtering is one of the widely applied techniques for growing CZTS films. The CZTS thin-film fabrication process is usually a two-step process, where initially the precursor is deposited mostly on a glass substrate, and thereafter, is post-annealed in sulfur/selenium ambient (sulfurization/sulfurization). There are three main approaches for sputtering the precursors: sequential stacked precursors, simultaneously sputtered (co-sputtered) precursors, and precursors deposited from a quaternary target containing the four constituents. Both stacked and co-sputtered precursors can be deposited using single targets [155, 156] and/or alloy targets (binary or ternary) [157, 158]. Depositing a stacked precursor provides easier control of the film chemical composition by regulating the thickness of each element [101], whereas co-sputtering enables the deposition of a homogenous mixture of the elements and can minimize the diffusion of the metals during the annealing process. Only a few works reported on the synthesis of CZTS films deposited by sputtering from single quaternary targets [159–162]. This approach exhibited difficulties in controlling the film elemental composition due to the compositional deviation of the material source and the sputtered precursor [163]. Using

co-sputtering to deposit the precursor followed by sulfurization step in H_2S/N_2 ambient at 525 ˚C, Dhakal et al. [164] reported fabricating a CZTS thin-film solar cell with an efficiency of 6.2%. CZTSSe-based solar cells with up 8.03 % efficiency were obtained using sequential sputtering of Cu/SnS/ZnS layers followed by selenization at 570 ˚C [165].

Evaporation is basically based on heating a source material in a vacuum chamber so that the material evaporates and deposits on a substrate. The absorbing layer of some CIGS-based solar cells showing high conversion efficiencies were thermally evaporated [40, 166]. Using thermal evaporation, the CZTS film can be deposited in one step by evaporating all elements at high temperatures [167–169] or in two steps by first fabricating the precursor followed by annealing in sulfur atmosphere [170–172]. For pure sulfide CZTS, the highest achieved efficiency of 8.4 % was with a device having an active layer prepared with thermal evaporation [173]. Cells with efficiencies of 9.2% [174] and 11.6% [175] based on CZTSe compound were also synthesized with thermal evaporation.

Pulsed laser deposition (PLD) is another physical vapor deposition (PVD) method used to prepare CZTS thin films. In this deposition technique, a pulsed laser beam with high power is used in a vacuum chamber to strike a material target, causing material evaporation from the surface of the target. The evaporated material is then deposited as a thin film on a substrate. CZTS or CZTSe/CZTSSe pellets, which were prepared by the solid-state reaction method of Cu_2S, ZnS and SnS_2 (for CZTS) or $Cu_2S(Se)$, ZnS(Se), SnS_2, Sn, S, and Se powders (for CZTSSe) are used as a target to deposit the compound in one step [176, 177].

2.6.2.2 NON-VACUUM DEPOSITION TECHNIQUES

Although vacuum-based approaches can offer high quality and well controlled thin film, they are often less favored for mass production due to the high fabrication cost. Therefore, there is a trend to replace the vacuum deposition techniques with low-cost solution processable

fabrication methods including electrodeposition, spray pyrolysis and "ink"-based approach. Electrodeposition has been adopted in the synthesis of CZTS thin films. The early work of electrodeposition of CZTS was based on electroplating of Cu-, Zn- and Sn- stacked metal layers, which was then annealed in a H_2S gas environment [178]. Some examples of sequence of metal layers include Zn/Sn/Cu and Zn/Cu/Sn/Cu stacking. As for Zn/Cu/Sn/Cu stacking, an improve process employs aqueous KCN solution to etch away Cu-rich phase, yielding a device efficiency of 3.2% [179]. Later, the co-electrodeposition of Cu-, Zn- and Sn- metal precursors has been developed by precisely tuning of the concentration of each precursor [180]. The most recent achievement was a single-step deposition of the metal precursors and sulfur precursor [181].

Spray pyrolysis is also a low-cost solution-processable fabrication approach. Typically, the precursor solution contains Cu, Zn and Sn chlorides in stoichiometric ratio, and also an excess of thiourea to compensate sulfur loss and prevent oxidation. The proposed chemical reaction was described in equation 2.1 [182].

$$2CuCl + 2ZnCl_2 + SnCl_4 + 4SC(NH_2)_2 + 8H_2O \rightarrow Cu_2ZnSnS_4 + 8NH_4Cl + 4CO_2 \textbf{(2.1)}$$

The "ink"-based approach has been of particular interest in recent years. It allows the use of cost-effective, high-throughput deposition method including printing, spin-coating and spraying [183]. The "ink" can be solution, nanoparticles dispersion and mixed solution particle precursors. Sol-gel method has been demonstrated in the preparations of CZTS thin film [184]. The precursor contains Cu-, Zn-, Sn- salts, 2-methoxyethanol solvents and monoethanolamine stabilizer. Subsequently, the film is annealed in H_2S environment to form CZTS. In another contribution, pyridine was used as the solvent and thioacetamide was used as the sulfur source [185]. The as-prepared film then underwent thermal treatment to form CZTS film. Besides the pure solution base approaches, the quaternary CZTS nanocrystals ink

has also been investigated [56, 58]. Figure 2.18 illustrate the general overview of the nanocrystal ink approach which is reprinted from Bucherl et al [186]. In this method, the nanocrystals were first synthesized in solution, and purified through centrifuge processes. The as-prepared nanocrystals were then dissolved in proper solvent to form the nanocrystal ink. Subsequently, the ink could be deposited onto a substrate using various solution deposition techniques including blade coating, spin-coating and spraying. The nanoparticles thin film was then annealed or selenized to form dense absorber layer. Then the solar cells could be fabricated using the as-prepared absorber layer. As for CZTS, the CZTS nanocrystals dispersion is commonly used as the ink. However, the choices of ink are not limited to CZTS nanocrystals only. Recently, Cao et al. demonstrated high efficiency CZTSSe solar cells making use of well dispersed binary and ternary sulfides nanoparticles [187]. In addition to the above two ink approaches, a new type of inks containing both solution and nanoparticles has been developed. Todorov et al. prepared the CZTSSe absorber layer using ink comprised of CuSn-sulfide/selenide solution in hydrazine and readily dispersible particle-based Zn-sulfide/selenide precursor in hydrazine [188] Thin film solar cells using this approach have reached a very high PCE of 9.66%. Recently, the efficiency has been increased to more than 11% using such method [189]. The ink-based approaches are very promising considering their high device performance. However, the use of expensive, toxic solvents (e.g. oleylamine for CZTS nanocrystals ink, hydrazine for hybrid solution-particles ink) may hinder their large-scale production. In this regard, inks which are low-cost and environmentally friendly are highly desirable.

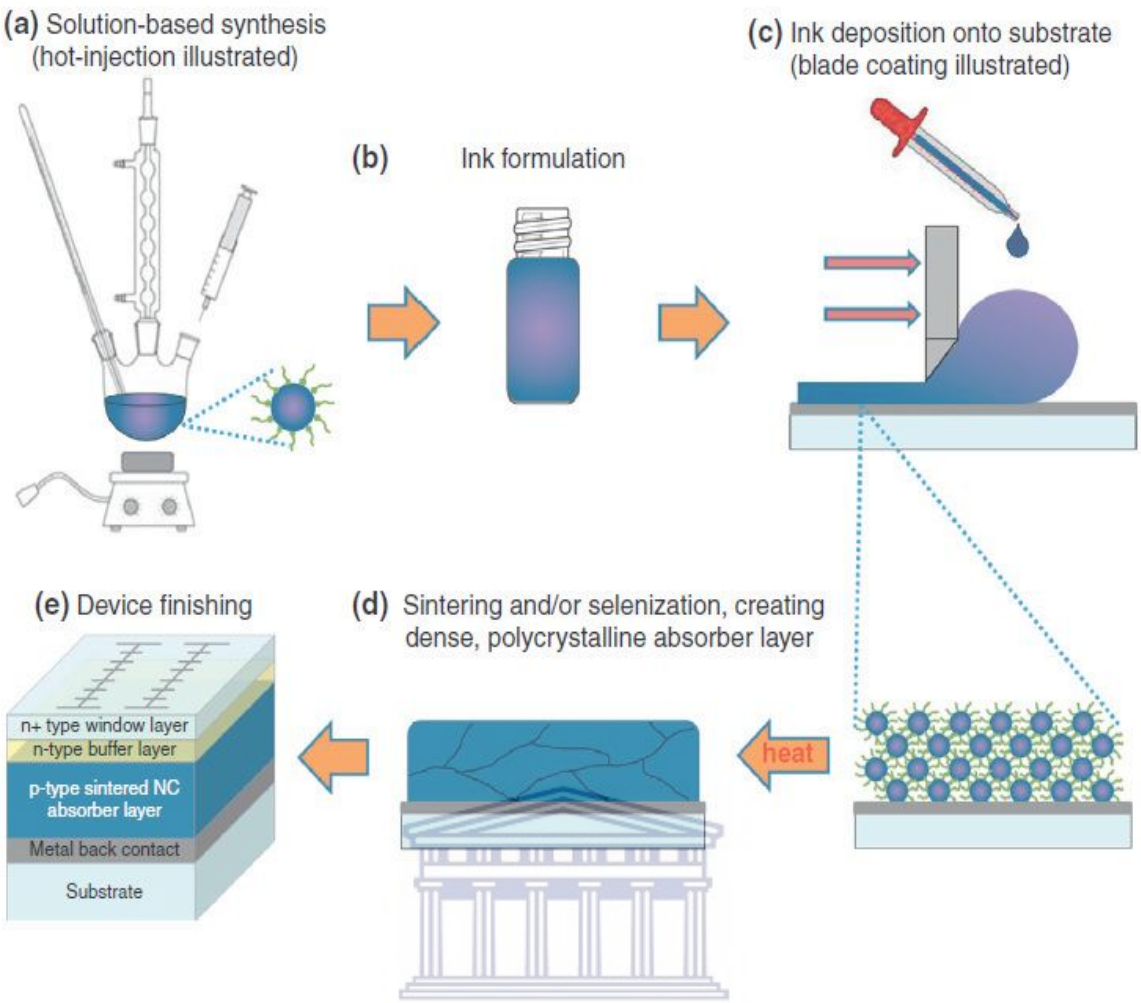

Figure 2. 18: Overview of solar cell fabrication using nanoparticles "ink" approach. (a) synthesis of nanoparticles, (b) nanoparticles ink formation, (c) film deposition, (d) heat treatment of as deposited film and (e) Device fabrication [186].

2.7 INNOVATIONS FOR IMPROVED KESTERITE DEVICE EFFICIENCY.

2.7.1 BACK CONTACT LAYER INTERFACE

Molybdenum (Mo) have been used as the back contact for CIGS solar cells due to its stability at high processing temperatures and resistance to alloying with Cu [190-193], excellent adhesion between the soda lime glass (SLG) substrates and CIGS absorbers, and low-resistance contact to the CIGS absorber. The importance of a $MoSe_2$ was demonstrated to reduce the contact recombination and contact resistance experienced at the interface of CIGS absorber layer and Mo back contact [194]. CZTS device structure replicates that of CIGS without the consideration of the material system difference of both materials [195]. Different from the case of CIGS, the Mo thin film back contact has been demonstrated to have some detrimental effects on CZTS device performance [196]. CZTSe is not stable at high processing temperature (500–600 °C) in the presence of Mo [197]. Equation 2.2 shows the decomposition of $Cu_2ZnSnS(e)_4$

$$2Cu_2ZnSnS(e)_4 \leftrightarrow 2Cu_2S(e) + 2ZnS(e) + 2SnS(e) + 2S(e)_{(g)} \quad \textbf{2.2}$$

Equation 2.3 describes the reaction that generates $MoS(e)_2$ at the CZTS(e)/Mo interface [198]:

$$Mo + 2S(e) \rightarrow MoS(e)_2 \quad \textbf{2.3}$$

The thermal instability of the CZTS(e)/Mo during thermal processing is given by the combination of equations 2.2 and 2.3 [199]:

$$2Cu_2ZnSnS(e)_4 + Mo \rightarrow 2Cu_2S(e) + 2ZnS(e) + 2SnS(e) + MoS(e)_2 \quad \textbf{2.4}$$

The free energy change of the reaction of equation 2.4 was calculated to be −100 kJ for CZTSe and −150 kJ for CZTS at 550 °C. Such negative free energy changes are indicative that the decomposition reaction is thermodynamically favorable and that the CZTS(e)/Mo interface may become unstable [198,199]. The instability of the Mo back contact can potentially cause

losses of V_{oc}, J_{sc} and FF in the CZTS device if not mitigated by film preparation conditions or device structure [197].

Alternative back contact metals have been explored to mitigate the problem encountered with the decomposition and contact resistance of the CZTS(e)/Mo interface. The metals that have been explored include: Au, W, Pd, Pt and Ni [196, 200]. Pd and Ni were observed to diffuse into the CZTSSe absorber extensively after annealing at 570 °C for 30 min, while Au did not react with the chalcogens, W reacted partially and Pt reacted completely. Therefore, Pd, Ni and Pt are not suitable as back contact materials under the conditions examined. W and Au are eligible contact materials because of their ability to enhance short circuit current (J_{sc}). In contrast to Mo, Au is a highly reflective back contact and increases the absorption of photons in the long wavelength range, therefore enhancing J_{sc} [201]. W may serve to passivate the CZTSSe absorber and improve the collection of carriers generated deep in the absorber [200]. However, Mo remains the best choice material for a back contact, so far (i.e. it is used for all record-performing devices), and achieved the highest conversion efficiency of 4.8% in this particular study. In contrast, cells with W and Au back contacts demonstrated deteriorated efficiencies of around 3.9%. The reduced efficiency was mainly attributed to decreases in fill factor (FF) [200]. In the case of a W back contact, a ~350-nm-thick $W(S,Se)_2$ layer was generated, which increased the series resistance and reduced FF. For the Au back contact, a high density of voids was observed in the CZTSSe absorber, resulting in a very low shunt resistance and deteriorated FF. Of course, with all of the above results, it is important to keep in mind that the suitability of a back-contact material will significantly depend not only on the choice of metal, but also on the specific processing approach used to deposit the CIGS or CZTSSe layer on top. For some of the above-mentioned back contact choices, it is possible that with optimization of the processing for the specific back contact material (which may not be the same best conditions as for deposition on Mo), high performance may be achieved [202].

An intermediate layer between the CZTS(e)/Mo interface have been explored as a solution to the problem described above [203-213]. An ultra-thin and intentionally introduced carbon layer has recently been developed to act as an intermediate layer between the kesterite absorber and the Mo back contact [213], in order to reduce the void-induced series resistance that is likely to arise in this region of the device. The evaporated carbon intermediate layer increases Jsc and conversion efficiency of CZTS devices with the absorbers fabricated by two-stage preparation, i.e. non-vacuum (sol–gel) or vacuum (sputtering) methods followed by high temperature sulfurization. Meanwhile, the carbon intermediate layer does not deteriorate V_{oc} and FF. The transmission electron microscopy (TEM) image and corresponding energy dispersive spectroscopy (EDS) mappings of the CZTS device with a carbon intermediate layer fabricated by the sol–gel method shows that carbon adheres on the inner walls of voids. By comparing EDS line scans on the CZTS devices with and without the carbon intermediate layer, it was confirmed that the carbon sticking on the inner walls of voids arose from the intentionally introduced carbon layer rather than the precursor solution used in the sol–gel method. The carbon aggregation better connects void-containing CZTS and the Mo back contact, which reduces the series resistance R_s and leads to increased J_{sc} and improved conversion efficiency [202, 213].

2.7.2 THE BUFFER LAYER INTERFACE

Alternative buffer layers other than the toxic CdS layer has been considered to be used for better band alignment in making kesterite solar cells [214-221]. The heterojunctions formed between $Cu_2ZnSn(S_xSe_{1-x})_4$ (CZTSSe) and three Cd-free n-type buffers, ZnS, ZnO, and In_2S_3, were studied using femtosecond ultraviolet photoemission and photovoltage spectroscopy [220-221]. A small positive spike conformation of 0.15 eV was produced between the hydrazine-processed CZTSSe absorber and an In_2S_3 buffer layer deposited by CBD, which reduces the interface recombination and does not form a barrier for the light-generated

electrons. Hence a large J_{sc} and reasonable V_{oc} and FF are obtained. A CZTSSe solar cell with such an In_2S_3 buffer layer achieved an efficiency of 7.19%, which was comparable to the efficiency of 7.75% made from the analogous CdS buffer layer [202, 220-221].

2.7.3 ABSORBER LAYER CATION SUBSTITUTION

Given the advantage of having an easily tunable band-gap, researchers have gone into replacing the cation components of the kesterite composition in order to find achieve a better efficiency [222-225]. The influence of partial substitution (up to 10%) of tin (Sn) by germanium (Ge) in $Cu_2ZnSn(S,Se)_4$ (CZTSSe) solid solution monograins was studied. The external quantum efficiency measurements of the CZTGSSe monograin layer solar cells showed an increase in the band gap energy of the Ge-substituted CZTGSSe. According to the current-voltage measurements, the higher band gap energy is accompanied with a larger open circuit voltage deficit showing the lowest value for the Ge-free sample of around 785 mV. The temperature dependent current-voltage measurements revealed strong recombination losses at the CdS/CZTGSSe interface contributing to the voltage deficit. The radiative recombination processes in CZGTSSe monograins were studied using low-temperature photoluminescence (PL) spectroscopy. The highest efficiency for the obtained for 10% Germanium substitution was 6.90%.

2.8 CHEMISTRY OF TELLURIUM

Tellurium (Te) with atomic number 52 belongs to the group of chalcogens (group 16) in the periodic table. As a chalcogen it has comparative qualities as Sulfur and Selenium. It is a fragile, somewhat harmful, rare, silver-white metalloid. It has a hexagonal crystal structure. Tellurium has two allotropes, crystalline and nebulous. Tellurium exist in eight oxidation states particularly; +6, +5, +4, +3, +2, +1, −1 and −2. Crystalline tellurium is a silvery white material having a metallic luster. It is a frangible and easily triturated metalloid. Nebulous

tellurium is dark brown, which is prepared via its precipitation from solution of telluric acid ($Te(OH)_6$) [226]. Tellurium is a semiconductor that indicates a more prominent electrical conductivity in specific ways relying upon atomic arrangement; the conductivity appreciates somewhat when light is shone on it (photoconductivity) [227]. As molten, tellurium is destructive to copper, iron, and tempered steel. It has melting and boiling points at 449.51 ˚C and 987.78 ˚C, respectively which is high when compared to other chalcogens [228]. Synthetically tellurium follows a polymeric structure comprising of crisscross chains of Te atoms known to be resistive to oxidation when exposed to air and is non-flammable.

2.9 APPLICATIONS OF TELLURIUM

Tellurium is a highly used material in iron, stainless steel, copper, and lead alloy metallurgy. The incorporation to steel and copper delivers a compound more machinable than anything else. It is alloyed into solid metal for advancing chill for spectroscopy, where the nearness of electrically conductive free graphite tends to meddle with spark emission testing results. In lead, tellurium enhances quality and toughness, and declines the destructive activity of sulfuric acid [229]. Tellurium is utilized in cadmium telluride (CdTe) solar panels with National Renewable Energy Laboratory trial of tellurium giving part of the best efficiencies for solar cell electric power generators and huge commercialized production of CdTe solar panels by First Solar has essentially expanded tellurium demand [230-231]. Replacing a portion of the cadmium in CdTe by zinc, creating (CdZn)Te, produces a strong state X-ray detector, giving a choice to single-use film badges [232]. Tellurium has likewise become useful in blend with different elements like bismuth and lead in phase change memory chips, and thermoelectric devices [233-234].

REFERENCES

[1] J. Perlin, "From Space to Earth, the Story of Solar Electricity" *AATEC Publications* (1999) 1-227

[2] L. Fraas and L. Partain, "Solar Cells and their Application," *John Wiley and Sons, Inc.* 2nd Edition (2010) 1-648.

[3] D.M. Chapin, C.S. Fuller and G.L. Pearson, "A new silicon p-n junction photocell for converting solar radiation into electrical power". *Journal of Applied Physics* 25 (1954) 676

[4] M. Olken, "Energy Metrics: Examining Traditional and Renewable Sources," *IEEE Power and Energy Magazine* 10 (2012) 4–6.

[5] H. Altomonte, "Japan's Nuclear Disaster: Its Impact on Electric Power Generation Worldwide," *IEEE Power and Energy Magazi*ne, 10 (2012) 96–94.

[6] M.I. Hoffert, K. Caldeira, G. Benford, D.R. Criswell, C. Green, H. Herzog, A.K. Jain, "Advanced Technology Paths to Global Climate Stability: Energy for a Greenhouse Planet," *Science* 298 (2002) 981-987.

[7] T.F. O'Connor, A.V. Zaretski, S. Savagatrup, A.D. Printz, C.D. Wilkes, M.I. Diaz, E.J. Sawyer and D.J. Lipomi, "Wearable organic solar cells with high cyclic bending stability: Materials selection criteria," *Solar Energy Materials and Solar Cells* 144 (2016) 438–444.

[8] A.M. Bagher, M.M.A. Vahid and M. Mohsen, "Types of Solar Cells and Application," *American Journal of Optics and Photonics* 3 (2015) 94-113.

[9] J. Weickert, R.B. Dunbar, H.C. Hesse, W. Wiedemann and L. Schmidt-Mende, "Nanostructured organic and hybrid solar cells," Advanced *Materials* 23 (2011) 1810-1828.

[10] S. Karazhanov and V. Kharton, “Novel materials for solar cells and related technologies,” *Materials Letters* 228 (2018) 450

[11] M.A. Green, K. Emery, Y. Hishikawa, W. Warta and E.D. Dunlop, “Solar cell efficiency tables version 47,” *Progress in Photovoltaics: Research and Applications* 24 (2016) 3-11.

[12] D. Abou-Ras, T. Kirchartz, and U. Rau, “Advanced Characterization Techniques for Thin Film Solar Cells,” *Wiley-VCH* 1 (2016) 1-712.

[13] M.A. Green, “The path to 25% silicon solar cell efficiency: History of silicon cell evolution,” *Progress in Photovoltaics: Research and Applications* 17 (2009) 183-189.

[14] K. Masuko, M. Shigematsu, T. Hashiguchi, D. Fujishima, M. Kai, N. Yoshimura, and T. Yamanishi, “Achievement of more than 25% conversion efficiency with crystalline silicon heterojunction solar cell. Photovoltaics,” *IEEE Journal of Photovoltaics* 4 (2014) 1433-1435.

[15] Trina Solar Announces New Efficiency Record of 21.25% Efficiency for Multicrystalline Silicon Solar Cell. (2015, November 9) Retrieved from http://www.trinasolar.com/us/about-us/newinfo_978.html

[16] M.A. Green, K. Emery, Y. Hishikawa, W. Warta and E.D. Dunlop, “Solar cell efficiency tables Version 47,” *Progress in photovoltaics: research and applications* 24 (2015) 3-11.

[17] C. Battaglia, A. Cuevas and S. De Wolf, “High-efficiency crystalline silicon solar cells: status and perspectives,” *Energy & Environmental Science* 9 (2016) 1552–1576.

[18] R.W. Miles, K.M. Hynes and I. Forbes, “Photovoltaic solar cells: An overview of state-of-the-art cell development and environmental issues,” *Progress in Crystal Growth and Characterization of Materials* 51 (2005) 1-42.

[19] F. Meillaud, M. Boccard, G. Bugnon, M. Despeisse, S. Hänni, F.J. Haug and C. Ballif, "Recent advances and remaining challenges in thin-film silicon photovoltaic technology," *Materials Today* 18 (2015) 378-384.

[20] D.E. Carlson and C.R. Wronski, "Amorphous silicon solar cell," *Applied Physics Letters* 28 (1976) 671-673.

[21] D.L. Staebler and C.R. Wronski, "Reversible conductivity changes in discharge-produced amorphous Si," *Applied Physics Letters* 31 (1977) 292-294.

[22] T. Matsui, H. Sai, T. Suezaki, M. Matsumoto, K. Saito, I. Yoshida and M. Kondo, "Development of highly stable and efficient amorphous silicon based solar cells," *European Photovoltaic Solar Energy Conference* 28 (2013) 2213-2217.

[23] H. Sai, T. Matsui, T. Koida, K. Matsubara, M. Kondo, S. Sugiyama and I. Yoshida, "Triple-junction thin-film silicon solar cell fabricated on periodically textured substrate with a stabilized efficiency of 13.6%," *Applied Physics Letters* 106 (2015) 213902.

[24] L. El Chaar and N. El Zein, "Review of photovoltaic technologies," *Renewable and Sustainable Energy Reviews* 15 (2011) 2165-2175.

[25] Z. Bai, J. Yang and D. Wang, "Thin film CdTe solar cells with an absorber layer thickness in micro-and sub-micrometer scale," *Applied Physics Letters* 99 (2011) 143502

[26] N. Romeo, A. Bosio and A. Romeo, "An innovative process suitable to produce high-efficiency CdTe/CdS thin-film modules," *Solar Energy Materials and Solar Cells* 94 (2010) 2-7.

[27] N. Romeo, A. Bosio, D. Menossi, A. Romeo and M. Aramini, "Last Progress in CdTe/CdS Thin Film Solar Cell Fabrication Process," *Energy Procedia* 57 (2014) 65-72.

[28] J. Britt and C. Ferekides, “Thin-film CdS/CdTe solar cell with 15.8 % efficiency,” *Applied Physics Letters* 62 (1993) 2851-2852.

[29] P.V. Meyers, “Design of a thin film CdTe solar cell,” *Solar Cells* 23 (1988) 59-67

[30] A. Gupta, V. Parikh and A.D. Compaan, “High efficiency ultra-thin sputtered CdTe solar cells,” *Solar Energy Materials and Solar Cells* 90 (2006) 2263-2271.

[31] H. Matsumoto, K. Kuribayashi, H. Uda, Y. Komatsu, A. Nakano and S. Ikegami, “Screen-printed CdS/CdTe solar cell of 12.8% efficiency for an active area of 0.78 cm^2,” *Solar Cells* 11 (1984) 367-373.

[32] First Solar press release. (2016). Retrieved from http://investor.firstsolar.com/releasedetail.cfm?ReleaseID=956479.

[33] P. Jackson, D. Hariskos, R. Wuerz, O. Kiowski, A. Bauer, T.M. Friedlmeier and M. Powalla, “Properties of Cu(In,Ga)Se_2 solar cells with new record efficiencies up to 21.7%,” *Physica status solidi (RRL)-Rapid Research Letters* 9 (2015) 28-31

[34] S. Wagner, J.L. Shay, P. Migliorato and H.M. Kasper, “$CuInSe_2$/CdS heterojunction photovoltaic detectors,” *Applied Physics Letters* 25 (1974) 434-435.

[35] L.L. Kazmerski, F.R. White and G.K. Morgan, G. K. “Thin-film $CuInSe_2$/CdS heterojunction solar cells,” *Applied Physics Letters* 29 (1976) 268-270.

[36] K. Ramanathan, M.A. Contreras, C.L. Perkins, S. Asher, F.S. Hasoon, J. Keane, D. Young, M. Romero, W. Metzger, R. Noufi and J. Ward, “Properties of 19.2% efficiency ZnO/CdS/$CuInGaSe_2$ thin-film solar cells,” *Progress in Photovoltaics: Research and Applications* 11 (2003) 225-230.

[37] J.H. Shi, Z.Q. Li, D.W. Zhang, Q.Q. Liu, Z. Sun and S.M. Huang, "Fabrication of Cu(In,Ga)Se_2 thin films by sputtering from a single quaternary chalcogenide target," *Progress in Photovoltaics: Research and Applications* 19 (2011) 160-164.

[38] P.J. Sebastian, M.E. Calixto, R.N. Bhattacharya and R. Noufi, "CIS and CIGS based photovoltaic structures developed from electrodeposited precursors," *Solar energy materials and solar cells* 59 (1999) 125 -135.

[39] S. Ahn, K.H. Kim, J.H. Yun and K.H. Yoon, "Effects of selenization conditions on densification of Cu(In,Ga)Se_2 (CIGS) thin films prepared by spray deposition of CIGS nanoparticles," *Journal of Applied Physics* 105 (2009) 113533.

[40] I. Repins, M.A. Contreras, B. Egaas, C. DeHart, J. Scharf, C.L. Perkins and R. Noufi, "19.9%-efficient ZnO/CdS/$CuInGaSe_2$ solar cell with 81.2% fill factor," *Progress in Photovoltaics: Research and applications* 16 (2008) 235-239.

[41] W. Wang, M.T. Winkler, O. Gunawan, T. Gokmen, T.K. Todorov, Y. Zhu and D.B Mitzi, "Device characteristics of CZTSSe thin-film solar cells with 12.6% efficiency," *Advanced Energy Materials* 4 (2014) 1301465.

[42] H. Katagiri, N. Sasaguchi, S. Hando, S. Hoshino, J. Ohashi and T. Yokota, "Preparation and evaluation of Cu_2ZnSnS_4 thin films by sulfurization of e- evaporated precursors," *Solar Energy Materials and Solar Cells* 49 (1997) 407–414.

[43] B. Shin, O. Gunawan, Y. Zhu, N.A. Bojarczuk, S.J. Chey and S. Guha, "Thin film solar cell with 8.4% power conversion efficiency using an earth- abundant Cu_2ZnSnS_4 absorber," *Progress in Photovoltaics: Research and Applications* 21 (2013) 72–76.

[44] Y.S. Lee, T. Gershon, O. Gunawan, T.K. Todorov, T. Gokmen, Y. Virgus and S. Guha, "$Cu_2ZnSnSe_4$ thin-film solar cells by thermal co-evaporation with 11.6% efficiency and improved minority carrier diffusion length," *Advanced Energy Materials* 5 (2015) 1401372.

[45] M.A. Green, K. Emery, Y. Hishikawa, W. Warta and E.D. Dunlop, "Solar cell efficiency tables Version 47," *Progress in Photovoltaics: Research and Applications* 24 (2016) 905–913.

[46] J. Li, H. Wang, M. Luo, J. Tang, C. Chen, W. Liu, F. Liu, Y. Sun, J. Han and Y. Zhang, "10% Efficiency $Cu_2ZnSn(S,Se)_4$ thin film solar cells fabricated by magnetron sputtering with enlarged depletion region width," *Solar energy materials and solar cells* 149 (2016) 242–249.

[47] H. Sugimoto, C. Liao, H. Hiroi, N. Sakai and T. Kato, "Lifetime Improvement for High Efficiency Cu_2ZnSnS_4 Submodules," *IEEE Photovoltaic Specialists Conference* (PVSC) 39 (2013) 3208–3211.

[48] T.K. Todorov, K.B. Reuter and D.B. Mitzi, "High-efficiency solar cell with earth-abundant liquid-processed absorber," *Advanced Materials* 22 (2010) E156-E159.

[49] D.A.R. Barkhouse, O. Gunawan, T. Gokmen, T.K. Todorov and D.B. Mitzi, "Device characteristics of a 10.1% hydrazine-processed $Cu_2ZnSn(S,Se)_4$ solar cell," *Progress in Photovoltaics: Research and Applications* 20 (2012) 6–11.

[50] T.K. Todorov, J. Tang, S. Bag, O. Gunawan, T. Gokmen, Y. Zhu and D.B. Mitzi, "Beyond 11 % efficiency: Characteristics of state-of-the-art $Cu_2ZnSn(S,Se)_4$ solar cells," *Advanced Energy Materials* 3 (2013) 34–38.

[51] D.A.R. Barkhouse, O. Gunawan, T. Gokmen, T.K. Todorov, D.B. Mitzi, "Device characteristics of a 10.1% hydrazine-processed $Cu_2ZnSn(Se,S)_4$ solar cell," *Progress in Photovoltaics: Research and Applications* 20 (2012) 6-11.

[52] I. Repins, C. Beall, N. Vora, C.D. Hart, D. Kuciauskas, P. Dippo, B. To, J. Mann, W.C. Hsu, A. Goodrich, R. Noufi, "Co-evaporated $Cu_2ZnSnSe_4$ films and devices," *Solar Energy Materials and Solar Cells* 101 (2012) 154-159.

[53] B. Shin, O. Gunawan, Y. Zhu, N.A. Bojarczuk, S.J. Chey, S. Guha, "Thin film solar cell with 8.4% power conversion efficiency using an earth-abundant Cu2ZnSnS4 absorber," *Progress in Photovoltaics: Research and Applications* 21 (2013) 72-76.

[54] A. Redinger, D.M. Berg, P.J. Dale, R. Djemour, L. Gütay, T. Eisenbarth, N. Valle, S. Siebentritt, "Route Toward High-Efficiency Single-Phase $Cu_2ZnSn(S,Se)_4$ Thin-Film Solar Cells: Model Experiments and Literature Review," *IEEE Journal of Photovoltaics* 1 (2011) 200-206.

[55] P. Jackson, D. Hariskos, E. Lotter, S. Paetel, R. Wuerz, R. Menner, W. Wischmann, M. Powalla, "New World Record Efficiency for Cu(In,Ga)Se_2 Thin-Film Solar Cells beyond 20%," *Progress in Photovoltaics: Research and Applications* 19 (2011) 894-897.

[56] S. Jain, D. Singh, N. Vijayan and S.N. Sharma, "Time-controlled synthesis mechanism analysis of kesterite-phased Cu_2ZnSnS_4 nanorods via colloidal route," *Applied Nanoscience* 8 (2018) 435–446.

[57] C. Steinhagen, M.G. Panthani, V. Akhavan, B. Goodfellow, B. Koo and B.A. Korgel, "Synthesis of Cu_2ZnSnS_4 nanocrystals for use in low-cost photovoltaics," *Journal of the American Chemical Society* 131 (2009) 12554-12555.

[58] S.C. Riha, B.A. Parkinson and A.L. Prieto. "Solution-Based Synthesis and Characterization of Cu_2ZnSnS_4 Nanocrystals," *Journal of the American Chemical Society* 131 (2009) 12054- 12055.

[59] A. Sarilmaz and F. Ozel, “Synthesis of band-gap tunable earth-abundant CXTS (X= Mn^{+2}, Co^{+2}, Ni^{+2} and Zn^{+2}) nanorods: Toward a generalized synthesis strategy of quaternary chalcogenides,” *Journal of Alloys and Compounds* 780 (2019) 518–522.

[60] T. Kameyama, T. Osaki, K. Okazaki, T. Shibayama, A. Kudo, S. Kuwabata and T. Torimoto, “Preparation and photoelectrochemical properties of densely immobilized Cu_2ZnSnS_4 nanoparticle films,” *Journal of Materials Chemistry* 20 (2010) 5319-5324.

[61] A. Shavel, D. Cadavid, M. Ibanez, A. Carrete and A. Cabot, “Continuous production of Cu_2ZnSnS_4 nanocrystals in a flow reactor,” *Journal of the American Chemical Society* 134 (2012) 1438-1441.

[62] Y.L. Zhou, W.H. Zhou, Y.F. Du, M. Li and S.X. Wu, “Sphere-like kesterite Cu_2ZnSnS_4 nanoparticles synthesized by a facile solvothermal method,” *Materials Letters* 65 (2011) 1535-1537.

[63] M. Cao and Y. Shen, “A mild solvothermal route to kesterite quaternary Cu_2ZnSnS_4 nanoparticles,” *Journal of Crystal Growth* 318 (2011) 1117-1120.

[64] X. Wang, Z. Sun, C. Shao, D.M. Boye and J. Zhao, “A facile and general approach to polynary semiconductor nanocrystals via a modified two-phase method,” *Nanotechnology* 22 (2011) 245605.

[65] C. Wang, C. Chen, Y. Cao, W. Fang, L. Zhao and X. Xu, “Synthesis of Cu_2ZnSnS_4 nanocrystalline by a hydrothermal route,” *Japanese Journal of Applied Physics* 50 (2011) 065003.

[66] Y. Zhao, W.H. Zhou, J. Jiao, Z.J. Zhou and S.X. Wu, “Aqueous synthesis and characterization of hydrophilic Cu_2ZnSnS_4 nanocrystals,” *Materials Letters* 96 (2013) 174-176.

[67] C.B. Murray, D.J. Norris and M.G. Bawendi, “Synthesis and characterization of nearly monodisperse CdE (E=sulfur, selenium, tellurium) semiconductor nanocrystallites,” *Journal of the American Chemical Society* 115 (1993) 8706-8715.

[68] J.H. Yu, J. Joo, H.M. Park, S.I. Baik, Y.W. Kim, S.C. Kim and T. Hyeon, Synthesis of quantum-sized cubic ZnS nanorods by the oriented attachment mechanism,” *Journal of the American Chemical Society* 127 (2005) 5662-5670.

[69] M.A. Hines and G.D. Scholes, “Colloidal PbS nanocrystals with size-tunable near-infrared emission: observation of post-synthesis self-narrowing of the particle size distribution,” *Advanced Materials* 15 (2003) 1844-1849.

[70] J. Tang, S. Hinds, S.O. Kelley and E.H. Sargent, “Synthesis of colloidal $CuGaSe_2$, $CuInSe_2$, and $Cu(InGa)Se_2$ nanoparticles,” *Chemistry of Materials* 20 (2008) 6906-6910.

[71] P. Bonazzi, L. Bindi, G.P. Bernardini and S. Menchetti, “A model for the mechanism of incorporation of Cu, Fe and Zn in the stannite–kesterite series Cu_2FeSnS_4– Cu_2ZnSnS_4,” *Canadian Mineralogist* 41 (2003) 639–647.

[72] A. Walsh, S.Y. Chen, S.H. Wei and X.G. Gong, “Kesterite Thin-Film Solar Cells: Advances in Materials Modelling of Cu_2ZnSnS_4,” *Advanced Energy Materials* 2 (2012) 400–409.

[73] S. Schorr, “The crystal structure of kesterite type compounds: A neutron and X-ray diffraction study,” *Solar Energy Materials and Solar Cells* 95 (2011) 1482–1488.

[74] C.R.A. Catlow, Z.X. Guo, M. Miskufova, S.A. Shevlin, A.G.H. Smith, A.A. Sokol, A. Walsh, D.J. Wilson and S.M. Woodley, “Advances in computational studies of energy materials,” *Philosophical Transactions of the Royal Society A* 36 (2010) 3379–3456.

[75] S. Schorr, H.J. Hoebler and M. Tovar, “A neutron diffraction study of the stannite-kesterite solid solution series,” *European Journal of Mineralogy* 19 (2007) 65–73.

[76] P.A. Fernandes, P.M.P. Salome and A.F. da Cunha, “Growth and Raman scattering Cu_2ZnSnS_4 thin films,” *Thin Solid Films* 517 (2009) 2519–2523.

[77] J. Just, D. Luzenkirchen-Hecht, R. Frahm, S. Schorr, and T. Unold, “Determination of secondary phases in kesterite Cu_2ZnSnS_4 thin films by x-ray absorption near edge structure analysis,” *Applied Physics Letter* 99 (2011) 262105.

[78] I.D. Olekseyuk, I.V. Dudchak and L.V. Piskach, “Phase equilibria in the Cu_2S–ZnS–SnS_2 system,” *Journal of Alloy Compounds* 368 (2004) 135–143.

[79] I.V. Dudchak and L.V. Piskach, “Phase equilibria in the Cu_2SnSe_3 -$SnSe_2$ -ZnSe system,” *Journal of Alloy Compounds* 351 (2003) 145–150.

[80] A. Nagaoka, K. Yoshino, H. Taniguchi, T. Taniyama and H. Miyake, “Growth of $Cu_2ZnSnSe_4$ single crystals from Sn solutions,” *Journal of Crystal Growth* 354 (2012)147–151

[81] D.B. Mitzi, O. Gunawan, T.K. Todorov, K. Wang and S. Guha, “The path towards a high-performance solution-processed kesterite solar cell,” *Solar Energy Materials and Solar Cells* 95 (2011) 1421–1436.

[82] S.Y. Chen, X.G. Gong, A. Walsh and S.H. Wei, “Defect physics of the kesterite thin-film solar cell absorber Cu_2ZnSnS_4,” *Applied Physics Letter* 96 (2010) 021902

[83] O. Vigil-Galán, M. Espíndola-Rodríguez, M. Courel, X. Fontané, D. Sylla, V. Izquierdo-Roca and A. Pérez-Rodríguez, “Secondary phases dependence on composition ratio in sprayed

Cu_2ZnSnS_4 thin films and its impact on the high-power conversion efficiency," *Solar Energy Materials and Solar Cells* 117 (2013) 246-250.

[84] A. Redinger, K. Hönes, X. Fontané, V. Izquierdo-Roca, E. Saucedo, N. Valle, and S. Siebentritt, "Detection of a ZnSe secondary phase in co-evaporated $Cu_2ZnSnSe_4$ thin films," *Applied Physics Letters* 98 (2011) 101907.

[85] K. Wang, B. Shin, K.B. Reuter, T. Todorov, D.B. Mitzi and S. Guha, "Structural and elemental characterization of high efficiency Cu_2ZnSnS_4 solar cells," *Applied Physics Letters* 98 (2011) 1912.

[86] Z. Li, B. Liu, S. Yu, J. Wang, Q. Li, B. Zou and J. Liu, "The study of structural transition of ZnS nanorods under high pressure," *The Journal of Physical Chemistry C* 115 (2010) 357-361.

[87] S. Siebentritt and S. Schorr, "Kesterites-a challenging material for solar cells," *Progress in Photovoltaics: Research and Applications* 20 (2012) 512-519.

[88] H. Nozaki, K. Shibata and N. Ohhashi, "Metallic hole conduction in CuS," *Journal of Solid-State Chemistry* 91 (1991) 306-311.

[89] W. Liang and M.H. Whangbo, "Conductivity anisotropy and structural phase transition in covellite CuS," *Solid State Communications* 85 (1993) 405-408.

[90] R. Wagner and H.D. Wiemhöfer, "Hall effect and conductivity in thin films of low temperature chalcocite Cu_2S at 20° C as a function of stoichiometry," *Journal of Physics and Chemistry of Solids* 44 (1983) 801-805.

[91] B. Thangaraju and P. Kaliannan, "Spray pyrolytic deposition and characterization of SnS and SnS_2 thin films," *Journal of Physics D: Applied Physics* 33 (2000) 1054.

[92] O.E. Ogah, G. Zoppi, I. Forbes and R.W. Miles, “Thin films of tin sulphide for use in thin film solar cell devices,” *Thin Solid Films* 517 (2009) 2485-2488.

[93] R.W. Miles, O.E. Ogah, G. Zoppi and I. Forbes, “Thermally evaporated thin films of SnS for application in solar cell devices,” *Thin Solid Films* 517 (2009) 4702-4705.

[94] M. Calixto-Rodriguez, H. Martinez, A. Sanchez-Juarez, J. Campos-Alvarez, A. Tiburcio-Silver and M.E. Calixto, “Structural, optical, and electrical properties of tin sulfide thin films grown by spray pyrolysis,” *Thin Solid Films* 517 (2009) 2497-2499.

[95] D. Avellaneda, M.T.S. Nair and P.K. Nair, “Photovoltaic structures using chemically deposited tin sulfide thin films,” *Thin Solid Film* 517 (2009) 2500-2502.

[96] N.G. Deshpande, A.A. Sagade, Y.G. Gudage, C.D. Lokhande and R. Sharma, “Growth and characterization of tin disulfide (SnS_2) thin film deposited by successive ionic layer adsorption and reaction (SILAR) technique,” *Journal of alloys and compound* 436 (2007) 421-426.

[97] X. Hu, G. Song, W. Li, Y. Peng, L. Jiang, Y. Xue and J. Hu, “Phase controlled synthesis and photocatalytic properties of SnS, SnS_2 and SnS/SnS_2 heterostructure nanocrystals,” *Materials Research Bulletin* 48 (2013) 2325-2332.

[98] D. Tiwari, T.K. Chaudhuri, T. Shripathi, U. Deshpande and R. Rawat, “Non-toxic, earth-abundant 2% efficient Cu_2SnS_3 solar cell based on tetragonal films direct-coated from single metal-organic precursor solution,” *Solar Energy Materials and Solar Cells* 113 (2013) 165-170.

[99] C. Wu, Z. Hu, C. Wang, H. Sheng, J. Yang and Y. Xie, “Hexagonal Cu_2SnS_3 with metallic character: Another category of conducting sulfides,” *Applied physics letters* 91 (2007) 143104.

[100] D.M. Berg, R. Djemour, L. Gütay, S. Siebentritt, P.J. Dale, X. Fontane and A. Pérez-Rodriguez, "Raman analysis of monoclinic Cu_2SnS_3 thin films," *Applied Physics Letters* 100 (2012) 192103.

[101] K. Chino, J. Koike, S. Eguchi, H. Araki, R. Nakamura, K. Jimbo and H. Katagiri, "Preparation of Cu_2SnS_3 thin films by sulfurization of Cu/Sn stacked precursors," *Japanese Journal of Applied Physics* 51 (2012) 10NC35.

[102] L.L. Baranowski, P. Zawadzki, S. Christensen, D. Nordlund, S. Lany, A.C. Tamboli and A. Zakutayev, "Control of doping in Cu_2SnS_3 through defects and alloying," *Chemistry of Materials* 26 (2014) 4951-4959.

[103] S.W. Shin, S.M. Pawar, C.Y. Park, J.H. Yun, J.H. Moon, J.H. Kim and J.Y. Lee, "Studies on Cu_2ZnSnS_4 (CZTS) absorber layer using different stacking orders in precursor thin films," *Solar Energy Materials and Solar Cells* 95 (2011) 3202-3206.

[104] P.A. Fernandes, P.M.P. Salomé and A.F. Da Cunha, "Study of polycrystalline Cu_2ZnSnS_4 films by Raman scattering," *Journal of alloys and compounds* 509 (2011) 7600-7606.

[105] P.A. Fernandes, P.M.P. Salomé and A.F. Da Cunha, "Growth and Raman scattering characterization of Cu_2ZnSnS_4 thin films," *Thin solid films* 517 (2009) 2519-2523.

[106] W.G. Nilsen, "Raman spectrum of cubic ZnS," *Physical Review* 182 (1969) 838.

[107] P.A. Fernandes and A.F. Da Cunha, "A study of ternary Cu_2SnS_3 and Cu_3SnS_4 thin films prepared by sulfurizing stacked metal precursors," *Journal of Physics D: Applied Physics* 43 (2010) 215403.

[108] P.A. Fernandes, P.M.P. Salomé and A.F. Da Cunha, "Cu_xSnS_{x+1}(x= 2.3) thin films grown by sulfurization of metallic precursors deposited by dc magnetron sputtering," *Physica status solidi (c)* 7 (2010) 901-904.

[109] M. Dimitrievska, A. Fairbrother, X. Fontané, T. Jawhari, V. Izquierdo-Roca, E. Saucedo and A. Pérez-Rodríguez, "Multiwavelength excitation Raman scattering study of polycrystalline kesterite Cu_2ZnSnS_4 thin films," *Applied Physics Letters* 104 (2014) 021901.

[110] D.M. Berg, M. Arasimowicz, R. Djemour, L. Gütay, S. Siebentritt, S. Schorr and P.J. Dale, "Discrimination and detection limits of secondary phases in Cu_2ZnSnS_4 using X-ray diffraction and Raman spectroscopy," *Thin Solid Films* 569 (2014) 113-123.

[111] X. Fontané, L. Calvo-Barrio, V. Izquierdo-Roca, E. Saucedo, A. Pérez-Rodriguez, J.R. Morante and S. Siebentritt, "In-depth resolved Raman scattering analysis for the identification of secondary phases: characterization of Cu_2ZnSnS_4 layers for solar cell applications," *Applied Physics Letters* 98 (2011) 181905.

[112] K. Ito, and T. Nakazawa, "Electrical and optical properties of stannite-type quaternary semiconductor thin films," *Japanese Journal of Applied Physics* 27 (1988) 2094.

[113] F. Liu, Y. Li, K. Zhang, B. Wang, C. Yan, Y. Lai, Z. Zhang, J. Li and Y. Liu, "In situ growth of Cu_2ZnSnS_4 thin films by reactive magnetron co-sputtering," *Solar Energy Materials and Solar Cells* 94 (2010) 2431–2434.

[114] S.Y. Chen, X.G. Gong, A. Walsh and S.H. Wei, "Crystal and electronic band structure of Cu_2ZnSnX_4 (X= S and Se) photovoltaic absorbers: First- principles insights," *Applied Physics Letter* 94 (2009) 041903.

[115] J. Paier, R. Asahi, A. Nagoya and G. Kresse, "Cu_2ZnSnS_4 as a potential photovoltaic material: A hybrid Hartree-Fock density functional theory study," *Physics Review B* 79 (2009) 115126.

[116] C. Persson, Electronic and optical properties of Cu_2ZnSnS_4 and $Cu_2ZnSnSe_4$," *Journal of Applied Physics* 107 (2010) 053710.

[117] S. Botti, D. Kammerlander and M.A.L. Marques, "Band structures of Cu_2ZnSnS_4 and $Cu_2ZnSnSe_4$ from many-body methods," *Applied Physics Letter* 98 (2011) 241915.

[118] N.B. Mortazavi Amiri and A. Postnikov, "Electronic structure and lattice dynamics in kesterite-type $Cu_2ZnSnSe_4$ from first-principles calculations," *Physics Review B* 82 (2010) 205204.

[119] J. Paier, R. Asahi, A. Nagoya and G. Kresse, "Cu_2ZnSnS_4 as a potential photovoltaic material: A hybrid Hartree-Fock density functional theory study," *Physics Review B* 79 (2009) 115126.

[120] S. Siebentritt and S. Schorr, "Kesterites a challenging material for solar cells," *Progress in Photovoltaics: Research and Applications* 20 (2012) 512–519.

[121] J.E. Jaffe and A. Zunger, "Theory of the band-gap anomaly in ABC 2 chalcopyrite semiconductors," *Physics Review B* 29 (1984) 1882–1906.

[122] Y.H. Li, A. Walsh, S. Chen, W.J. Yin, J.H. Yang, J. Li, J.L.F. Da Silva, X.G. Gong, and S.H. Wei, "Revised ab initio natural band offsets of all group IV, II-VI, and III-V semiconductors," *Applied Physics Letter* 94 (2009) 212109.

[123] S.Y. Chen, A. Walsh, J.H. Yang, X.G. Gong, L. Sun, P.X. Yang, J.H. Chu and S.H. Wei, "Compositional dependence of structural and electronic properties of $Cu_2ZnSn(S,Se)_4$ alloys for thin film solar cells," *Physics Review B* 83 (2011) 125201.

[124] S.B. Zhang, S.H. Wei, A. Zunger and H. Katayama-Yoshida, "Defect physics of the $CuInSe_2$ chalcopyrite semiconductor," *Physics Review B* 57 (1998) 9642–9656.

[125] J.J. Scragg, P.J. Dale and L.M. Peter, "Towards sustainable materials for solar energy conversion: Preparation and photoelectrochemical characterization of Cu_2ZnSnS_4," *Electrochemical Communication* 10 (2008) 639–642.

[126] H. Katagiri, "Cu_2ZnSnS_4 thin film solar cells," *Thin Solid Films* 480 (2005) 426–432.

[127] X. Wu, W. Liu, S. Cheng, Y. Lai and H. Jia, "Photoelectric properties of Cu_2ZnSnS_4 thin films deposited by thermal evaporation," *Journal of Semiconductors* 33 (2012) 022002.

[128] K. Ito and T. Nakazawa, "Electrical and optical properties of stannite-type quaternary semiconductor thin films," *Japanese Journal of Applied Physics* 27 (1988) 2094–2097.

[129] J.S. Seol, S.Y. Lee, J.C. Lee, H.D. Nam and K.H. Kim, "Electrical and optical properties of Cu_2ZnSnS_4 thin films prepared by rf magnetron sputtering process," *Solar Energy Materials and Solar Cells* 75 (2003) 155–162.

[130] J. Zhang and L.X. Shao, "Cu_2ZnSnS_4 thin films prepared by sulfurizing different multilayer metal precursors," *Science in China Series E* 52 (2009) 269–272.

[131] A. Khare, A.W. Wills, L.M. Ammerman, D.J. Norris and E.S. Aydil, "Size control and quantum confinement in Cu_2ZnSnS_4 nanocrystals," *Chemical Communications* 47 (2011) 11721-11723.

[132] L. Shi, C. Pei, Y. Xu and Q. Li, “Template-directed synthesis of ordered single-crystalline nanowires arrays of Cu_2ZnSnS_4 and $Cu_2ZnSnSe_4$,” *Journal of the American Chemical Society* 133 (2011) 10328-10331.

[133] X. Lu, Z. Zhuang, Q. Peng and Y. Li, “Wurtzite Cu_2ZnSnS_4 nanocrystals: a novel quaternary semiconductor,” *Chemical Communications* 47 (2011) 3141-3143.

[134] A. Singh, H. Geaney, F. Laffir and K.M. Ryan, “Colloidal synthesis of wurtzite Cu_2ZnSnS_4 nanorods and their perpendicular assembly,” *Journal of the American Chemical Society* 134 (2012) 2910-2913.

[135] F. Liu, K. Sun, W. Li, C. Yan, H. Cui, L. Jiang, X. Hao and M.A. Green, “Enhancing the Cu_2ZnSnS_4 solar cell efficiency by back contact modification: Inserting a thin TiB_2 intermediate layer at Cu_2ZnSnS_4/Mo interface,” *Applied Physics Letter* 104 (2014) 051105.

[136] J.J. Scragg, T. Ericson, T. Kubart, M. Edoff and C. Platzer-Bjorkman, “Chemical Insights into the instability of Cu_2ZnSnS_4 films during annealing,” *Chemical Materials* 23 (2011) 4625–4633.

[137] B. Shin, N.A. Bojarczuk and S. Guha, “On the kinetics of MoSe2 interfacial layer formation in chalcogen-based thin film solar cells with a molybdenum back contact,” *Applied Physics Letter* 102 (2013) 091907.

[138] X. Zhu, Z. Zhou, Y. Wang, L. Zhang, A. Li and F. Huang, “Determining factor of MoSe2 formation in Cu(In,Ga)Se_2 solar cells,” *Solar Energy Materials and Solar Cells* 101 (2012) 57–61.

[139] F. Liu, C. Yan, J. Huang, K. Sun, F. Zhou, J.A. Stride, M.A. Green and X. Hao, “Nanoscale microstructure and chemistry of Cu_2ZnSnS_4 /CdS interface in kesterite Cu_2ZnSnS_4 solar cells,” *Advanced Energy Materials* 6 (2016) 1600706.

[140] S. Chen, A. Walsh, X.G. Gong and S.H. Wei, “Classification of lattice defects in the kesterite Cu_2ZnSnS_4 and $Cu_2ZnSnSe_4$ earth-abundant solar cell absorbers,” *Advanced Materials* 25 (2013) 1522–1539.

[141] M. Tsuyoshi, N. Satoshi and W. Takahiro, “First-principles study on Cd doping in Cu_2ZnSnS_4 and $Cu_2ZnSnSe_4$,” *Japanese Journal of Applied Physics* 51 (2012) 10NC11.

[142] K. Sardashti, R. Haight, T. Gokmen, W. Wang, L.Y. Chang, D.B. Mitzi and A.C. Kummel, “Impact of nanoscale elemental distribution in high-performance kesterite solar cells,” *Advanced Energy Materials* 5 (2015) 1402180

[143] D. Abou-Ras, G. Kostorz, A. Romeo, D. Rudmann and A.N. Tiwari, “Structural and chemical investigations of CBD- and PVD-CdS buffer layers and interfaces in $Cu(In,Ga)Se_2$ -based thin film solar cells,” *Thin Solid Films* 480–481 (2005) 118–123.

[144] T. Nakada, “Nano-structural investigations on Cd-doping into $Cu(In,Ga)Se_2$ thin films by chemical bath deposition process,” *Thin Solid Films* 361–362 (2000) 346–352.

[145] K. Ramanathan, R. Noufi, J. Granata, J. Webb and J. Keane, “Prospects for in situ junction formation in $CuInSe_2$ based solar cells,” *Solar Energy Materials and Solar Cells* 55 (1998) 15–22.

[146] K. Ramanathan, H. Wiesner, S. Asher, D. Niles, R. Bhattacharya, J. Keane, M.A. Contreras and R. Noufi, “High-efficiency $Cu(In,Ga)Se_2$ thin film solar cells without intermediate buffer layers,” *Proceedings of the 2nd World Conference and Exhibition on Photovoltaic Solar Energy Conversion, Vienna, Austria* (1998) 477–481,

[147] J. Márquez, M. Neuschitzer, M. Dimitrievska, R. Gunder, S. Haass, M. Werner and I. Forbes, “Systematic compositional changes and their influence on lattice and optoelectronic

properties of $Cu_2ZnSnSe_4$ kesterite solar cells," *Solar Energy Materials and Solar Cells* 144 (2016) 579-585.

[148] S.M. Pawar, A.I. Inamdar, K.V. Gurav, S.W. Shin, Y. Jo, J. Kim and J.H. Kim, "Growth of void free Cu_2ZnSnS_4 (CZTS) thin films by sulfurization of stacked metallic precursor films," *Vacuum* 104 (2014) 57-60.

[149] M.P. Suryawanshi, S.W. Shin, U.V. Ghorpade, K.V. Gurav, G.L. Agawane, C.W. Hong and A.V.A Moholkar, "chemical approach for synthesis of photoelectrochemically active Cu_2ZnSnS_4 (CZTS) thin films," *Solar Energy* 110 (2014) 221-230.

[150] P.M.P. Salomé, J. Malaquias, P.A. Fernandes, M.S. Ferreira, J.P. Leitão, A.F. Da Cunha and E.R. Viana, "The influence of hydrogen in the incorporation of Zn during the growth of Cu_2ZnSnS_4 thin films," *Solar Energy Materials and Solar Cells* 95 (2011) 3482-3489.

[151] K. Maeda, K. Tanaka, Y. Fukui and H. Uchiki, "Dependence on Annealing Temperature of Properties of Cu_2ZnSnS_4 Thin Films Prepared by Sol–Gel Sulfurization Method," *Japanese Journal of Applied Physics* 50 (2011) 01BE10.

[152] K.V. Gurav, S.M. Pawar, S.W. Shin, G.L. Agawane, P.S. Patil, J.H. Moon and J.H. Kim, "Electrosynthesis of CZTS films by sulfurization of CZT precursor: Effect of soft annealing treatment," *Applied Surface Science* 283 (2013) 74-80.

[153] E.M. Mkawi, K. Ibrahim, M.K.M. Ali and A.S. Mohamed, "Dependence of copper concentration on the properties of Cu_2ZnSnS_4 thin films prepared by electrochemical method," *International Journal of Electrochemical Science* 8 (2013) 359-368.

[154] S. Thiruvenkadam, D. Jovina, and A.L. Rajesh, "The influence of deposition temperature in the photovoltaic properties of spray deposited CZTS thin films," *Solar Energy* 106 (2014) 166-170.

[155] V.G. Rajeshmon, C.S. Kartha, K.P. Vijayakumar, C. Sanjeeviraja, T. Abe and Y. Kashiwaba, "Role of precursor solution in controlling the opto- electronic properties of spray pyrolysed Cu_2ZnSnS_4thin films," *Solar Energy* 85 (2011) 249-255.

[156] H. Wang, "Progress in thin film solar cells based on," *International journal of Photoenergy* (2011) 801292

[157] M. Abusnina, H. Moutinho, M. Al-Jassim, C. DeHart and M. Matin, "Fabrication and Characterization of CZTS Thin Films Prepared by the Sulfurization of RF-Sputtered Stacked Metal Precursors," *Journal of Electronic Materials* 43 (2014) 3145-3154.

[158] H. Yoo and J. Kim, "Growth of Cu_2ZnSnS_4 thin films using sulfurization of stacked metallic films," *Thin Solid Films* 518 (2010) 6567-6572.

[159] J. Han, S.W. Shin, M.G. Gang, J.H. Kim and J.Y. Lee, "Crystallization behaviour of co-sputtered Cu_2ZnSnS_4 precursor prepared by sequential sulfurization processes," *Nanotechnology* 24 (2013) 095706.

[160] J. Ge, W. Yu, H. Cao, J. Jiang, J. Ma, L. Yang and J. Chu, "Fabrication of Cu_2ZnSnS_4 absorbers by sulfurization of Sn-rich precursors," *physica status solidi a* 209 (2012) 1493-1497.

[161] J. He, L. Sun, Y. Chen, J. Jiang, P. Yang and J. Chu, "Cu_2ZnSnS_4 thin film solar cell utilizing rapid thermal process of precursors sputtered from a quaternary target: a promising application in industrial processes," *RSC Advances* 4 (2014) 43080-43086.

[162] J. He, L. Sun, K. Zhang, W. Wang, J. Jiang, Y. Chen and J. Chu, "Effect of post-sulfurization on the composition, structure and optical properties of Cu_2ZnSnS_4 thin films deposited by sputtering from a single quaternary target," *Applied Surface Science* 264 (2013) 133-138.

[163] P. Fan, J. Zhao, G.X. Liang, D. Gu, Z.H. Zheng, D.P. Zhang and F. Ye, "Effects of annealing treatment on the properties of CZTSe thin films deposited by RF-magnetron sputtering," *Journal of Alloys and Compounds* 625 (2015) 171-174.

[164] R. Sun, M. Zhao, D. Zhuang, Q. Gong, M. Xie, L. Ouyang and L. Zhang, "Effects of selenization on phase transition and S/(S+ Se) ratios of as- deposited Cu_2ZnSnS_4 absorbers sputtered by a quaternary target," *Materials Letters* 164 (2016) 140-143.

[165] L. Sun, J. He, Y. Chen, F. Yue, P. Yang and J. Chu, "Comparative study on Cu_2ZnSnS_4 thin films deposited by sputtering and pulsed laser deposition from a single quaternary sulfide target," *Journal of Crystal Growth* 361 (2012) 147-151.

[166] T.P. Dhakal, C.Y. Peng, R.R. Tobias, R. Dasharathy and C.R. Westgate, "Characterization of a CZTS thin film solar cell grown by sputtering method," *Solar Energy* 100 (2014) 23-30.

[167] D.H. Son, D.H. Kim, S.N. Park, K.J. Yang, D. Nam, H. Cheong and J.K. Kang, "Growth and Device Characteristics of CZTSSe Thin-Film Solar Cells with 8.03% Efficiency," *Chemistry of Materials* 27 (2015) 5180-5188.

[168] J.S. Ward, K. Ramanathan, F.S. Hasoon, T.J. Coutts, J. Keane, M.A. Contreras and R.A. Noufi, "21.5% efficient Cu(In,Ga)Se_2 thin-film concentrator solar cell," *Progress in Photovoltaics: Research and Applications* 10 (2002) 41-46.

[169] B.A. Schubert, B. Marsen, S. Cinque, T. Unold, R. Klenk, S. Schorr and H.W. Schock, "Cu_2ZnSnS_4 thin film solar cells by fast coevaporation," *Progress in Photovoltaics: Research and Applications* 19 (2011) 93-96.

[170] K. Oishi, G. Saito, K. Ebina, M. Nagahashi, K. Jimbo, W.S. Maw, and A. Takeuchi, "Growth of Cu_2ZnSnS_4 thin films on Si (100) substrates by multisource evaporation," *Thin Solid Films* 517 (2008) 1449-1452.

[171] T. Tanaka, D. Kawasaki, M. Nishio, Q. Guo and H. Ogawa, "Fabrication of Cu_2ZnSnS_4 thin films by co-evaporation," *physica status solidi c* 3 (2006) 2844- 2847.

[172] H. Katagiri, N. Ishigaki, T. Ishida and K. Saito, "Characterization of Cu_2ZnSnS_4 thin films prepared by vapor phase sulfurization," *Japanese Journal of Applied Physics* 40 (2001) 500.

[173] W. Xinkun, L. Wei, C. Shuying, L. Yunfeng and J. Hongjie, "Photoelectric properties of Cu_2ZnSnS_4 thin films deposited by thermal evaporation," *Journal of Semiconductors* 33 (2012) 022002.

[174] F. Biccari, R. Chierchia, M. Valentini, P. Mangiapane, E. Salza, C. Malerba and A. Mittiga, "Fabrication of Cu_2ZnSnS_4 solar cells by sulfurization of evaporated precursors," *Energy Procedia* 10 (2011) 187-191.

[175] W.C. Hsu, I. Repins, C. Beall, C. DeHart, B. To, W. Yang and R. Noufi, "Growth mechanisms of co-evaporated kesterite: a comparison of Cu-rich and Zn-rich composition paths," *Progress in Photovoltaics: Research and Applications* 22 (2014) 35-43.

[176] Y.S. Lee, T. Gershon, O. Gunawan, T.K. Todorov, T. Gokmen, Y. Virgus and S. Guha, "$Cu_2ZnSnSe_4$ Thin-Film Solar Cells by Thermal Co-evaporation with 11.6% Efficiency and Improved Minority Carrier Diffusion Length," *Advanced Energy Materials* 5 (2015) 1401372.

[177] A.V Moholkar, S.S. Shinde, A.R. Babar, K.U. Sim, H.K. Lee, K.Y. Rajpure and J.H. Kim, "Synthesis and characterization of Cu_2ZnSnS_4 thin films grown by PLD: solar cells," *Journal of Alloys and Compounds* 509 (2011) 7439-7446.

[178] L. Sun, J. He, Y. Chen, F. Yue, P. Yang and J. Chu "Composition dependence of structure and optical properties of $Cu_2ZnSn(S,Se)_4$ solid solutions: an experimental study," *Journal of Alloys and Compounds* 511 (2012) 129-132.

[179] G. Larramona, S. Bourdais, A. Jacob, C. Chon, T. Muto, Y. Cuccaro and G. Dennler, "8.6% efficient CZTSSe solar cells sprayed from water–ethanol CZTS colloidal solutions," *The journal of physical chemistry letters* 5 (2014) 3763-3767

[180] J.J. Scragg, P.J. Dale, L.M. Peter, G. Zoppi and I. Forbes, "New routes to sustainable photovoltaics: evaluation of Cu_2ZnSnS_4 as an alternative absorber material," *physica status solidi b* 245 (2008) 1772-1778.

[181] J.J. Scragg, D.M. Berg and P.J. Dale, "A 3.2% efficient Kesterite device from electrodeposited stacked elemental layers," *Journal of Electroanalytical Chemistry* 646 (2010) 52-59.

[182] H. Araki, Y. Kubo, K. Jimbo, W.S. Maw, H. Katagiri, M. Yamazaki, K. Oishi and A. Takeuchi, "Preparation of Cu_2ZnSnS_4 thin films by sulfurization of co-electroplated Cu-Zn-Sn precursors," *physica status solidi c* 6 (2009) 1266-1268.

[183] S.M. Pawar, B.S. Pawar, A.V. Moholkar, D.S. Choi, J.H. Yun, J.H. Moon, S.S. Kolekar, J.H. Kim, "Single step electrosynthesis of Cu_2ZnSnS_4 (CZTS) thin films for solar cell application," *Electrochimica Acta* 55 (2010) 4057-4061.

[184] N. Kamoun, H. Bouzouita and B. Rezig, "Fabrication and characterization of Cu_2ZnSnS_4 thin films deposited by spray pyrolysis technique," *Thin Solid Films* 515 (2007) 5949-5952.

[185] T. Todorov and D.B. Mitzi, "Direct liquid coating of chalcopyrite light-absorbing layers for photovoltaic devices," *European Journal of Inorganic Chemistry* 1 (2009, 2010) 17-28.

[186] K. Tanaka, N. Moritake and H. Uchiki, “Preparation of thin films by sulfurizing sol-gel deposited precursors,” *Solar Energy Materials and Solar Cells* 91 (2007) 1199-1201.

[187] A. Fischereder, T. Rath, W. Haas, H. Amenitsch, J. Albering, D. Meischler, S. Larissegger, M. Edler, R. Saf, F. Hofer and G. Trimmel, “Investigation of Cu_2ZnSnS_4 formation from metal salts and thioacetamide,” *Chemistry of Materials* 22 (2010) 3399-3406.

[188] T.K. Todorov, K.B. Reuter and D.B. Mitzi, “High-efficiency solar cell with earth-abundant liquid-processed absorber,” *Advanced Materials* 22 (2010) E156-E159.

[189] T.K. Todorov, J. Tang, S. Bag, O. Gunawan, T. Gokmen, Y. Zhu and D.B. Mitzi, “Beyond 11 % efficiency: characteristics of state-of-the-art $Cu_2ZnSn(S,Se)_4$ solar cells,” *Advanced Energy Materials* 3 (2012) 34-38.

[190] X. Dai, A. Zhou, L. Feng, Y. Wang, J. Xu and J. Li, “Molybdenum thin films with low resistivity and superior adhesion deposited by radio-frequency magnetron sputtering at elevated temperature,” *Thin Solid Films* 567 (2014) 64–7.

[191] S.-F. Wang, H.-C. Yang, C.-F. Liu and H.-Y.Y. Bor, “Characteristics of bilayer molybdenum films deposited using RF sputtering for back contact of thin film solar cells,” *Advances in Materials Science and Engineering* 2014 (2014) 1–6.

[192] C.-Y. Su, K.-H. Liao, C.-T. Pan and P.-W. Peng “The effect of deposition parameters and post treatment on the electrical properties of Mo thin films,” *Thin Solid Films* 520 (2012) 5936–5939.

[193] Z.-H. Li, E.-S. Cho and S.J. Kwon, “Molybdenum thin film deposited by in-line DC magnetron sputtering as a back contact for $Cu(In,Ga)Se_2$ solar cells,” *Applied Surface Science* 257 (2011) 9682-9688.

[194] J. Malmström, S. Schleussner and L. Stolt, “Enhanced back reflectance and quantum efficiency in Cu(In,Ga)Se_2 thin film solar cells with a ZrN back reflector,” *Applied Physics Letters* 85 (2004) 2634-2636.

[195] H. Cui, X. Liu, F. Liu, X. Hao, N. Song and C. Yan, “Boosting Cu_2ZnSnS_4 solar cells efficiency by a thin Ag intermediate layer between absorber and back contact,” *Applied Physics Letters* 104 (2014) 041115.

[196] T.J. Huang, X. Yin, G. Qi and H. Gong, “CZTS-based materials and interfaces and their effects on the performance of thin film solar cells,” *Physica status solidi (RRL)-Rapid Research Letters* 08 (2014) 735-762.

[197] J.J. Scragg, T. Kubart, J.T. Wätjen, T. Ericson, M.K. Linnarsson and C. Platzer-Björkman, “Effects of back contact instability on Cu_2ZnSnS_4 devices and processes,” *Chemistry of Materials* 25 (2013) 3162–3171.

[198] J.J. Scragg, P.J. Dale, D. Colombara and L.M. Peter, “Thermodynamic aspects of the synthesis of thin-film materials for solar cells,” *Chemphyschem* 13 (2012) 3035-3046.

[199] J.J. Scragg, J.T. Watjen, M. Edoff, T. Ericson, T. Kubart and C. Platzer-Bjorkman, “A detrimental reaction at the molybdenum back contact in $Cu_2ZnSn(S,Se)_4$ thin-film solar cells,” *Journal of the American Chemical Society* 134 (2012) 19330–19333.

[200] G. Altamura, L. Grenet, C. Roger, F. Roux, V. Reita, R. Fillon, H. Fournier, S. Perraud and H. Mariette, “Alternative back contacts in kesterite $Cu_2ZnSn(S_{1-x}Se_x)_4$ thin film solar cells,” *Journal of Renewable and Sustainable Energy* 6 (2014) 011401.

[201] Z.J. Li-Kao, N. Naghavi, F. Erfurth, J.F. Guillemoles, I. Gérard, A. Etcheberry, J.L. Pelouard, S. Collin, G. Voorwinden and D. Lincot, “Towards ultrathin copper indium gallium

diselenide solar cells: proof of concept study by chemical etching and gold back contact engineering," *Progress in Photovoltaics: Research and Applications* 20 (2012) 582–587.

[202] X. Liu, Y. Feng, H. Cui, F. Liu, X. Hao, G. Conibeer, D.B. Mitzi and M. Green, "The current status and future prospects of kesterite solar cells: a brief review," *Progress in Photovoltaics: Research and Applications* 24 (2016) 879–898.

[203] S. Englund, V. Paneta, D. Primetzhofer, Y. Ren, O. Donzel-Gargand, J. Larsen, J. Scragg and C.P. Björkman, "Characterization of TiN back contact interlayers with varied thickness for $Cu_2ZnSn(S,Se)_4$ thin film solar cells," *Thin Solid Films* 639 (2017) 91–97.

[204] F. Liu, J. Huang, K. Sun, C. Yan, Y. Shen, J. Park, A. Pu, F. Zhou, X. Liu, J.A. Stride, M.A. Green and X. Hao, "Beyond 8% ultrathin kesterite Cu2ZnSnS4 solar cells by interface reaction route controlling and self-organized nanopattern at the back contact," *NPG Asia Materials* 9 (2017) e401.

[205] O.K. Simya, A. Mahaboobbatcha and K. Balachander, "A comparative study on the performance of Kesterite based thin film solar cells using SCAPS simulation program," *Superlattices and Microstructures* 82 (2015) 248–261.

[206] F.Z. Boutebakh, M.L. Zeggar, N. Attaf, and M.S. Aida, "Electrical properties and back contact study of CZTS/ZnS heterojunction," *Optik* 144 (2017) 180–190.

[207] S. Englund, S. Grini, O. Donzel-Gargand, V. Paneta, V. Kosyak, D. Primetzhofer, J.J.S. Scragg and C. Platzer-Björkman, "TiN Interlayers with Varied Thickness in $Cu_2ZnSnS(e)_4$ Thin Film Solar Cells: Effect on Na Diffusion, Back Contact Stability, and Performance," *Physica Status Solidi (a)* 215 (2018) 1800491.

[208] C. Platzer-Björkman, "Kesterite compound semiconductors for thin film solar cells," *Current Opinion in Green and Sustainable Chemistry* 4 (2017) 84-90.

[209] Z. Tong, K. Zhang, K. Sun, C. Yan, F. Liu, L. Jiang and J. Li, “Modification of absorber quality and Mo-back contact by a thin Bi intermediate layer for kesterite Cu_2ZnSnS_4 solar cells,” *Solar Energy Materials and Solar Cells* 144 (2016) 537–543.

[210] H. Cui, C.-Y. Lee, W. Li, X. Liu, X. Wen and X. Hao, “Improving Efficiency of Evaporated Cu_2ZnSnS_4Thin Film Solar Cells by a Thin Ag Intermediate Layer between Absorber and Back Contact,” *International Journal of Photoenergy* 2015 (2015) 1–9.

[211] J. Park, J. Huang, K. Sun, Z. Ouyang, F. Liu, C. Yan and Hao, X. (2018). The effect of thermal evaporated MoO_3 intermediate layer as primary back contact for kesterite Cu_2ZnSnS_4 solar cells,” *Thin Solid Films* 648 (2018) 39–45.

[212] S. Lopez-Marino, M. Placidi, A. Perez-Tomas, J. Llobet, V. Izquierdo-Roca, X. Fontane, A. Fairbrother, M. Espindola-Rodriguez, D. Sylla, A. Perez-Rodriguez and E. Saucedo, “Inhibiting the absorber/Mo-back contact decomposition reaction in $Cu_2ZnSnSe_4$ solar cells: the role of a ZnO intermediate nanolayer,” *Journal of Materials Chemistry A* 1 (2013) 8338–8343.

[213] F. Zhou, F. Zeng, X. Liu, F. Liu, N. Song, C. Yan, A. Pu, J. Park, K. Sun and X. Hao, “Improvement of Jsc in a Cu2ZnSnS4 solar cell by using a thin carbon intermediate layer at the Cu_2ZnSnS_4/Mo interface,” *ACS Applied Materials & Interfaces* 7 (2015) 22868–22873.

[214] E. Garcia-Llamas, J.M. Merino, R. Gunder, K. Neldner, D. Greiner, A. Steigert, S. Giraldo, V. Izquierdo-Roca, E. Saucedo, M. León, S. Schorr and R. Caballero, “Cu_2ZnSnS_4 thin film solar cells grown by fast thermal evaporation and thermal treatment,” *Solar Energy* 141 (2017) 236-241.

[215] K. Sun, C. Yan, J. Huang, F. Liu, H. Sun, A. Pu, M. Green and X. Hao, "Boosting the efficiency of kesterite Cu_2ZnSnS_4 solar cells by optimizing the heterojunction interface quality," *IEEE 7th World Conference on Photovoltaic Energy Conversion* 7 (2018) 18288176.

[216] C. Platzer-Björkman, C. Frisk, J.K. Larsen, T. Ericson, S.-Y. Li, J.J.S. Scragg, J. Keller, F. Larsson, and T. Törndahl, "Reduced interface recombination in Cu_2ZnSnS_4 solar cells with atomic layer deposition Zn1−xSnxOy buffer layers," *Applied Physics Letters* 107 (2015) 243904.

[217] M. Nguyen, K. Ernits, K.F. Tai, C.F. Ng, S.S. Pramana, W.A. Sasangka, S.K. Batabyal, T. Holopainen, D. Meissner, A. Neisser and L.H. Wong, "ZnS buffer layer for $Cu_2ZnSn(S,Se)_4$ monograin layer solar cell," *Solar Energy* 111 (2015) 344–349.

[218] H. Sun, K. Sun, J. Huang, C. Yan, F. Liu, J. Park, A. Pu, J.A. Stride, M.A. Green and X. Hao, "Efficiency Enhancement of Kesterite Cu_2ZnSnS_4 Solar Cells via Solution-Processed Ultrathin Tin Oxide Intermediate Layer at Absorber/Buffer Interface," *ACS Applied Energy Materials* 1 (2018) 154-160.

[219] N. Khemiri, F. Aousgi and M. Kanzari, "Tunable optical and structural properties of Zn(S,O) thin films as Cd-free buffer layer in solar cells," Materials Letters 199 (2017) 1-4.

[220] R. Haight, A. Barkhouse, W. Wang, Y. Luo, X. Shao, D.B. Mitzi, H. Hiroi and Hiroki Sugimoto, "CdS and Cd-Free Buffer Layers on Solution Phase Grown $Cu_2ZnSn(S_xSe_{1-x})_4$:Band Alignments and Electronic Structure Determined with Femtosecond Ultraviolet Photoelectron Spectroscopy," *MRS Proceedings* 1638 (2014).

[221] R. Haight, A. Barkhouse, W. Wang, Y. Luo, X. Shao, D.B. Mitzi, H. Hiroi and Hiroki Sugimoto, "Cd-free buffer layer materials on $Cu_2ZnSn(S_xSe_{1-x})_4$: Band alignments with ZnO, ZnS, and In_2S_3," Applied Physics Letters 100 (2012) 193904.

[222] A. Lafond, C. Guillot-Deudon, J. Vidal, M. Paris, C. La, and S. Jobic, “Substitution of Li for Cu in Cu_2ZnSnS_4: Toward Wide Band Gap Absorbers with Low Cation Disorder for Thin Film Solar Cells,” *Inorganic Chemistry* 56 (2017) 2712–2721.

[223] Z. Su, W. Li, G. Asim, T.Y. Fan and L.H. Wong, “Cation Substitution of CZTS Solar Cell with >10% Efficiency,” *IEEE 43rd Photovoltaic Specialists Conference* (2016) 16484060.

[224] J. Li, D. Wang, X. Li, Y. Zeng and Y. Zhang, “Cation Substitution in Earth-Abundant Kesterite Photovoltaic Materials,” *Advance Science* 5 (2018) 1700744.

[225] S. Oueslati, M. Grossberg, M. Kauk-Kuusik, V. Mikli, K. Ernits, D. Meissner and J. Krustok, “Effect of germanium incorporation on the properties of kesterite $Cu_2ZnSn(S,Se)_4$ monograins,” *Thin Solid Films* 669 (2019) 315-320.

[226] G.W. Leddicotte, “The radiochemistry of tellurium,” Nuclear science series. Subcommittee on Radiochemistry, National Academy of Sciences-National Research Council 5 (1961)

[227] Berger, L. Isaakovich, “Tellurium,” *Semiconductor materials CRC Press*. (1997) 89-91.

[228] Periodic Table. ptable.com

[229] W.X. Guo, D. Shu, H.Y. Chen, A.J. Li, H. Wang, G.M. Xiao, C.L. Dou, S.G. Peng, W.W. Wei, W. Zhang, H.W. Zhou and S. Chen, “Study on the structure and property of lead tellurium alloy as the positive grid of lead-acid batteries,” *Journal of Alloys and Compounds* 475 (2009) 102–109

[230] V.M. Fthenakis, K.H. Chul and A. Erik, “Emissions from Photovoltaic Life Cycles,” *Environmental Science & Technology* 42 (2008) 2168–2174.

[231] P. Sinha, C.J. Kriegner, W.A. Schew, S.W. Kaczmar, M. Traister and D.J. Wilson, “Regulatory policy governing cadmium-telluride photovoltaics: A case study contrasting life cycle management with the precautionary principle,” *Energy Policy* 36 (2008) 381–387

[232] G.B. Saha, “Cadmium zinc telluride detector,” *Physics and radiobiology of nuclear medicine New York: Springer*. (2001) 87–88.

[233] S. Hudgens and B. Johnson, “Overview of Phase-Change Chalcogenide Nonvolatile Memory Technology,” *Material Research Society Bulletin* 29 (2004) 1–4.

[234] L. Geppert, “The New Indelible Memories,” *IEEE Spectrum* 40 (2003) 48–54

CHAPTER 3

SYNTHESIS AND CHARACTERIZATION TECHNIQUES.

3.1 MATERIALS

All the reagents were of analytical grade and no further purification was performed. The reagents used were: copper (II) chloride (Sigma-Aldrich), zinc chloride (Sigma-Aldrich), tin (II) chloride (Sigma-Aldrich), isopropanol (Sigma-Aldrich), diethylene glycol (Sigma-Aldrich), sodium borohydride (Sigma-Aldrich). Deionized water was prepared with Millipore filtration system (Millipore-Sigma), tellurium powder (Sigma-Aldrich), selenium powder (Sigma-Aldrich), sulfur powder (Sigma-Aldrich).

3.2 SYNTHESIS AND EXPERIMENTAL PROCEDURE.

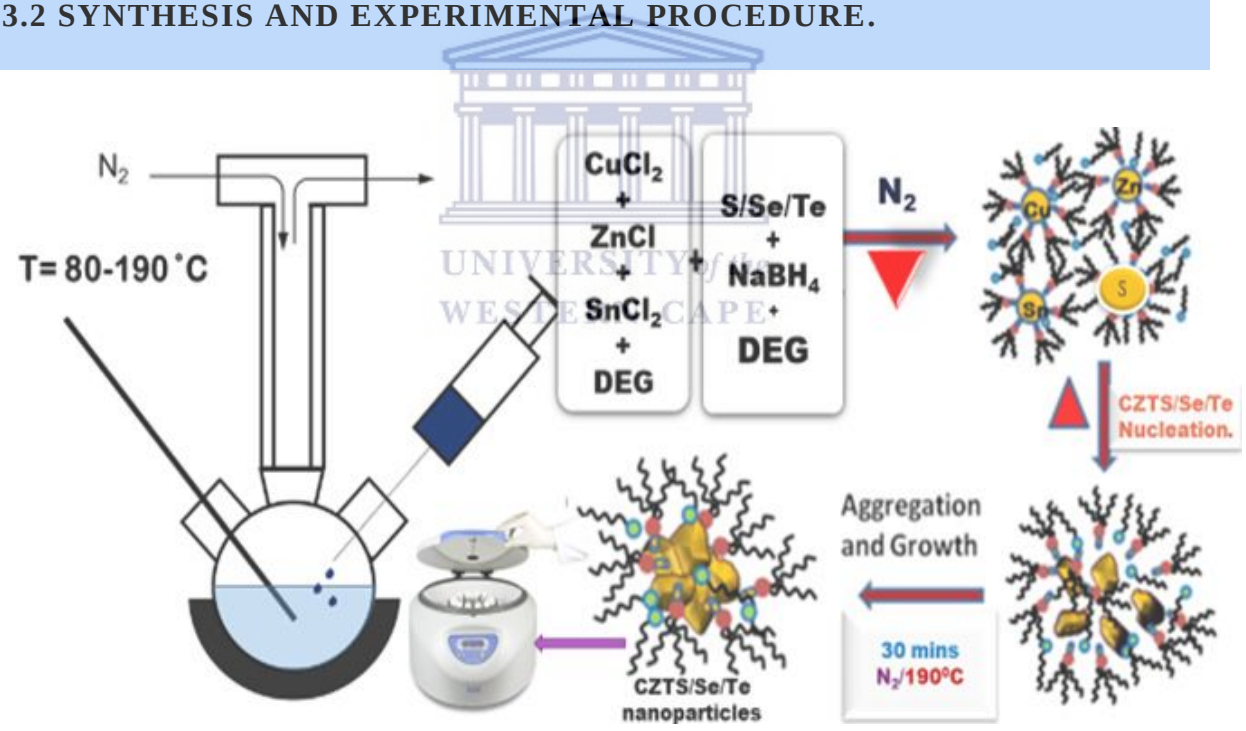

Figure 3. 1: A schematic of the synthesis route of the kesterite nanoparticles.

The synthesis involved two precursor preparations before the final mixture. All experimental procedure was done under inert condition. The synthesis method used was a modified method used by H. Dong et al [1].

1. The cation Precursor: 1.68 mmol of copper chloride, 1.1 mmol of zinc chloride and 1.0 mmol Tin chloride was added to 120ml of diethylene glycol in a two-necked flask and was refluxed at one of the necks which performed two roles: (a) inlet for the inert gas and (b) inlet and outlet for water throughout the experiment. The mixture was allowed to reach a temperature of 80 ˚C. Before the anion precursor was injected
2. The anion Precursor: Elemental Sulfur, Selenium and Tellurium powder with a total of 3.78 mmol was added to 10mls of diethylene glycol and 7.36 mmol of Sodium Borohydride. The working molar ratio for the non-metal's compositions will be $(S_xTe_{1-x})_4$ and $(S_xSe_{1-x}Te_{1-x})_4$. The values of x used were (1, 0.75 and 0.25). The mixture was done under nitrogen inert system as described in (1) above and was allowed to heat slowly above 30 ˚C to facilitate the reduction process which was confirmed by color change. The resulting solution was injected to the cation precursor.
3. The Final mixture: When the temperature of the cation precursor had reached 80 ˚C, the solution of the anion precursor was slowly injected into reaction vessel containing the cation precursor under magnetic stirring leading to a color change from yellowish brown to deep black indicating nucleation and subsequent growth of the kesterite nanocrystals has occurred. The new mixture was then allowed to heat up to 190 ˚C and kept for 30 minutes after which it was cooled to room temperature naturally.
4. Collection: After 30 min, the mixture was cooled to room temperature and the nanocrystals were precipitated by diluting with Isopropanol followed by 10 min of centrifugation at 4500 rpm. This process of washing and centrifuging was repeated twice and the precipitate was then air dried.

At the end three nanoparticle samples was prepared which had chemical composition of CZTS, $CZTS_{0.5}Se_{0.25}Te_{0.25}$ and $CZTS_{0.75}Te_{0.25}$. These three samples were then characterized with the following characterization techniques below.

3.3 CHARACTERIZATION TECHNIQUES.

3.3.1 MICROSCOPIC CHARACTERIZATION

Microscopy is the specialized field of utilizing microscope to see items and regions of objects that can't be seen with the naked eye (objects that are not inside the resolution range of the normal eye) [2]. There are three parts of microscopy: optical, electron, and scanning probe microscopy. Electron microscopy include the diffraction, reflection, or refraction of electromagnetic radiation/electron beams associating with the sample, and the gathering of the scattered radiation or another signal to make a micrograph. Electron microscope produce micrographs of material microstructures with considerably higher amplification and resolution than light microscopes. The high resolution of electron microscope results from short wavelengths of the electrons utilized for microscope illumination. The wavelength of electrons in electron microscopes is around ten thousand times shorter than visible light. The resolution of electron microscope reaches the order of 0.1 nm if focal point distortions can be limited. Such high resolution makes electron microscopes greatly helpful for uncovering ultrafine subtle elements of material microstructure. There are two principal sorts of electron microscope: transmission electron microscope (TEM) and scanning electron microscope (SEM). The optics of the TEM is like the conventional transmission light microscope, while that of SEM is more similar to that of scanning confocal laser microscope [3].

3.3.1.1 SCANNING ELECTRON MICROSCOPY (SEM).

The scanning electron microscope (SEM) is the most universally used type of electron microscope. It explores microscopic structure by scanning the surface of materials, similar to scanning confocal microscopes but with much higher resolution and much greater depth of field. A SEM micrograph is framed by a focused electron beam that scans over the surface area of a specimen. Perhaps the vital feature of SEM is the three-dimensional appearance of

its images because of its large depth of field. In addition, SEM system allows us to gather the chemical information from a specimen by using various techniques, such as being equipped with energy dispersive x-ray spectrometer (EDS). EDS is alternatively introduced as a technique for chemical analysis [4]. SEM can achieve resolution better than one nanometer. Specimens are observable in high vacuum through conventional SEM, or in low vacuum through environmental SEM, and at a wide range of cryogenic or high temperatures with improved specialized instruments.

Figure 3. 2: Image of Scanning Electron Microscope.

The most crucial SEM mode is the detection of secondary electrons that are emitted by atoms which were excited by the electron beam. The detection of a number of secondary electrons depends, among other things, on specimen topography. A micrograph detailing the topography of the surface of the sample is created when the sample is scanned and secondary

electrons that are emitted are collected using a special detector. The signals that produces the micrograph by a scanning electron microscope is as a result of interactions between the electron beam with atoms at various parts of the sample [4].

3.3.1.2 TRANSMISSION ELECTRON MICROSCOPY (TEM)

A transmission electron microscope, similar to a transmission light microscope, has the following components along its optical path: light source, condenser lens, specimen stage, objective lens and projector lens. The main differences are that, in a TEM, the visible light ray is replaced by an electron ray and glass lenses for visible light are replaced by electromagnetic lens for the electron beam. TEM has more lenses (the intermediate lens) and more apertures (including the selected area aperture). It contains further features arising from using electrons as illumination. For example, a vacuum environment is required in TEM because collisions between high energy electrons and air molecules significantly absorb electron energy [5]. Transmission electron microscopy is a microscopy technique where a beam of electrons produces a micrograph when transmitted through a specimen. The sample is regularly a ultrathin area below one hundred nm thick or a suspension on a grid. A micrograph is made from the association of the electrons with the sample as the beam is transmitted through the sample. The image is then amplified and centered onto an imaging device; a fluorescent screen, a layer of photographic film, or a sensor such as a charge-coupled device.

Figure 3. 3: Image of Transmission Electron Microscope (TEM)

Transmission electron microscope are ideal for imaging at a higher resolution than light microscope, inferable from the littler de-Broglie wavelength of electrons. This empowers the instrument to detect fine detail-even as little as a single section of atoms, littler than a resolvable object found in a light microscope. Transmission electron microscopy is a crucial analysis strategy in the physical, chemical and natural sciences. TEMs are applied in growth research and materials science in addition to research in virology, contamination, nanotechnology and semiconductor. At lower amplifications TEM micrograph contrast is because of differential absorption of electrons by the material because of contrasts in arrangement or thickness of the material. At higher amplifications, complex wave synergy tweaks the intensity of the picture, requiring experienced examination of the micrographs. Other interchangeable modes enable TEM to detect tweaks in chemical property, crystal

arrangement, electronic structure and sample induced electron stage shift in addition to the standard absorption-based imaging. [5].

3.3.2 SPECTROSCOPIC CHARACTERIZATION

Spectroscopy is the investigation of the synergy between matter and electromagnetic radiation. Previously, spectroscopy began through the investigation of visible light scattered by its wavelength, by a prism. Later the idea was extended extraordinarily to incorporate any synergy with radiative energy as a relation to its wavelength or frequency. Spectroscopic information is frequently detailed by an emission spectrum, a plot of the response of interest in regards to wavelength or frequency.

3.3.2.1 ENERGY-DISPERSIVE X-RAY SPECTROSCOPY (EDS OR EDX)

A microanalyzer is an EDS type of X-ray spectrometer that is usually affixed in a scanning or a transmission electron microscope. The EDS microanalyzer is an electron microscope that utilizes a primary electron beam to excite the emission of characteristic x-rays from the sample atoms. Since the electron beam can be readily focused on a microscopic area on a sample, the EDS microanalyzer can determine chemical compositions in a microscopic area.

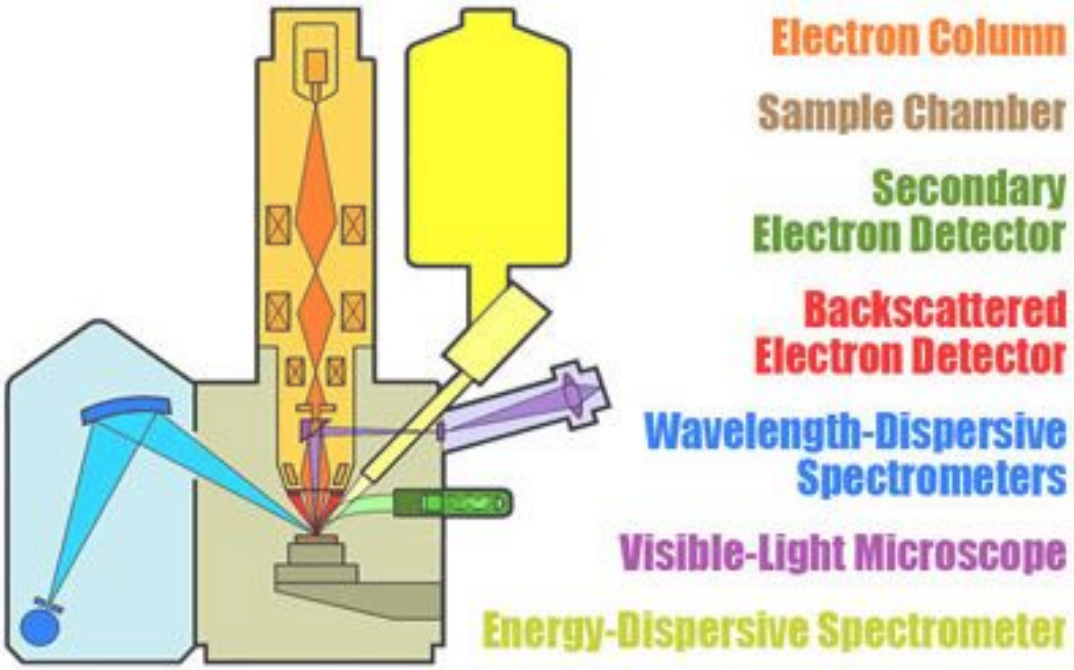

Figure 3. 4: Schematic cut away diagram of an Electron probe micro-analyzer.

Energy-dispersive x-ray spectroscopy (EDS), is an expository procedure utilized for the elemental investigation or chemical properties of a sample. It depends on synergy between source of x-ray excitation and a sample. The ability to reveal the properties of a sample is based on the fundamental rule that each element has a distinct atomic structure thereby having a unique set of peaks on its electromagnetic emission spectrum. [4].

3.3.2.2 ULTRAVIOLET-VISIBLE SPECTROSCOPY (UV-VIS)

In spite of the fact that we see sunlight (or white light) as uniform or homogeneous in shading, it is really made out of an expansive scope of radiation wavelengths in the ultraviolet (UV), visible and infrared (IR) bits of the spectrum. Electromagnetic radiation, for example, visible light is regularly regarded as a wave paradox, portrayed by a wavelength or frequency. Wavelength is defined as the separation between adjacent peaks (or troughs), and might be designated in meters, centimeters or nanometers (10-9 meters). Frequency is the amount of wave cycles that transit past a fixed point for each unit of time, and is normally given in cycles

per second, or hertz (Hz). Visible wavelengths cover a range from around 400 to 800 nm. The longest visible wavelength has a characteristic color of red and the shortest violet. Other basic colors of the spectrum, arranged by decreasing wavelength, can be recollected by the memory aide: ROY G BIV. The wavelengths of what we see as specific colors in the visible region of the spectrum are shown and recorded below.

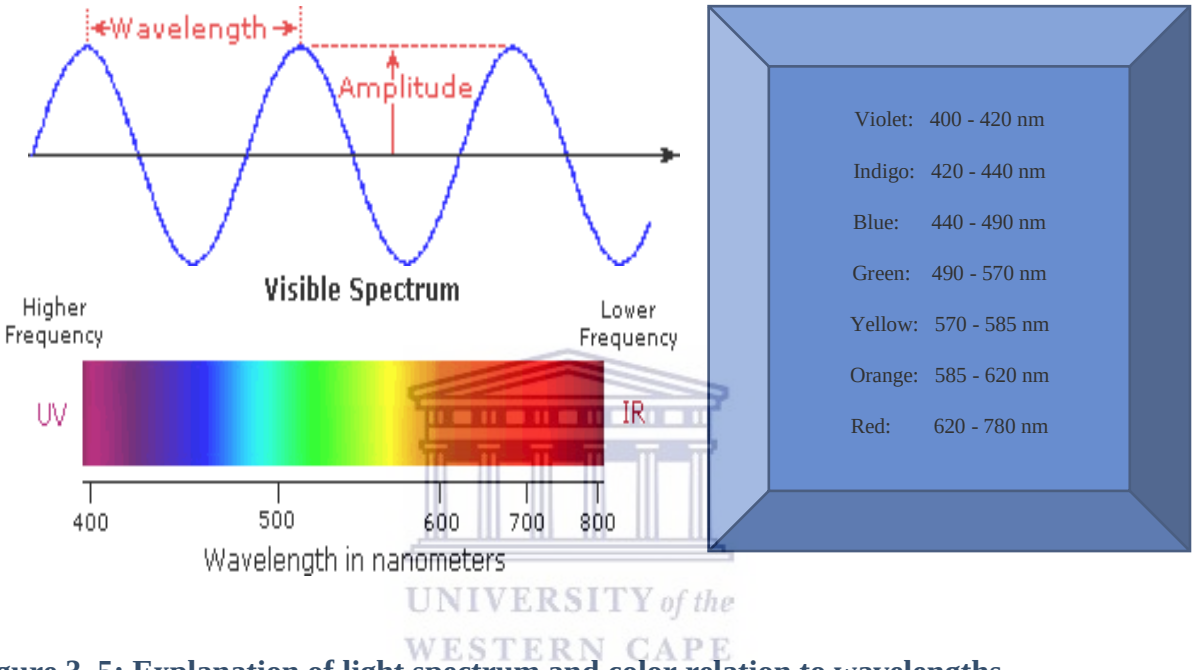

Figure 3. 5: Explanation of light spectrum and color relation to wavelengths

Ultraviolet–visible spectroscopy alludes to absorption spectroscopy or reflectance spectroscopy in the ultraviolet-visible spectral region. This implies it utilizes light in the visible and adjacent ranges. The absorption or reflectance in the visible range directly impacts the apparent color of the chemicals involved. In this region of the electromagnetic range, molecules and atoms experience electronic changes [6].

Figure 3. 6: UV-vis Spectrophotometer.

In UV-vis spectroscopy, the force of light that is going through the sample is estimated. Nanoparticles have optical properties that are exceptionally sensitive to size, shape, agglomeration, and concentration changes. The distinct optical properties of metal nanoparticles are a result of the aggregate motions of conduction electrons, which when energized by electromagnetic radiation are called surface plasmon polariton resonances [7]. Those progressions have an impact on the refractive index alongside the nanoparticle's surface; hence, it is conceivable to explain the properties of nanomaterials using UV-Vis spectroscopy. UV-Vis spectroscopy is a quick and easy to-use method to obtain the properties of nanoparticle, particularly for colloidal suspensions [8]. There are a handful of advantages of UV-Vis methods which are but not limited to, simplicity, sensitivity, and selectivity to nanoparticles and brief time of estimation, and what is more, calibration is not needed. Therefore, the method is progressively utilized for nanoparticle characterization in numerous fields of science and industry.

3.3.2.3 RAMAN SPECTROSCOPY

Raman Spectroscopy is a spectroscopic method used to explore vibrational, rotational, and other low-frequency modes in a system. Raman spectroscopy is generally utilized in science to give a basic structural fingerprint by which molecules can be classified. It depends on inelastic scattering, or Raman scattering, of monochromatic light, normally from a laser in the visible, near infrared, or near visible spectrum. The laser light connects with molecular vibrations, phonons or other excitations in the framework, bringing about the energy of the laser photons being moved up or down. The shift in energy provides data about the vibrational modes in the framework. [9].

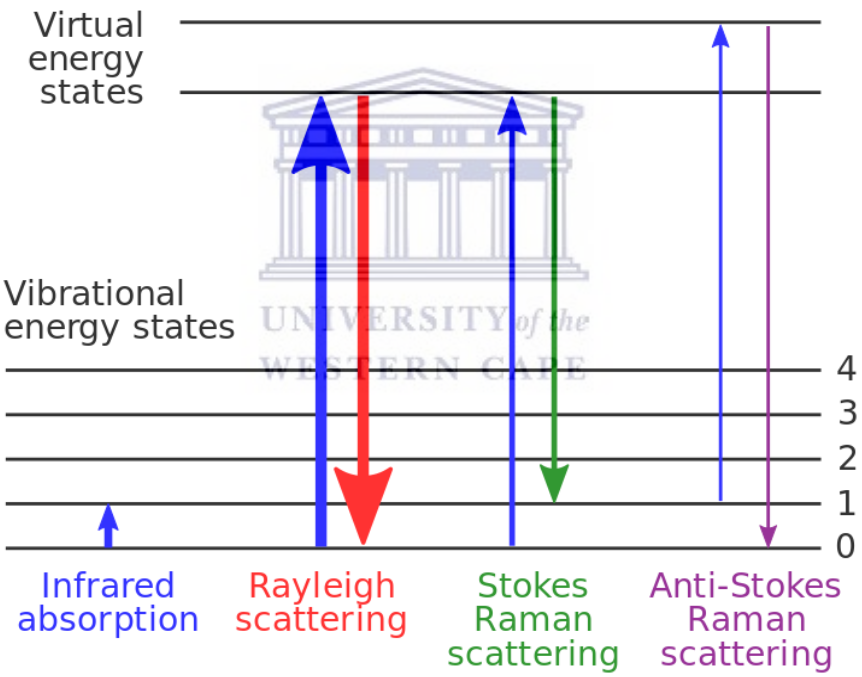

Figure 3. 7: Energy-level diagram showing the states involved in Raman spectra.

A sample is illuminated with a laser beam. Electromagnetic radiation from the illuminated spot is retrieved with a lens and sent through a monochromator. Flexible scattered radiation at the wavelength relating to the laser line (Rayleigh scattering) is sifted through by either a notch channel, edge pass channel, or a band pass channel, while whatever remains of the

collected light is dispatched onto a detector. Spontaneous Raman scattering is usually frail, and therefore the major problem of Raman spectroscopy is isolating the feeble inelastically scattered light from the intense Rayleigh scattered laser light. Verifiably, Raman spectrometers utilized holographic gratings and numerous dispersion stages to accomplish a high level of laser rejection. Before, photomultipliers were the most used detectors for dispersive Raman setups, which brought about long acquisition times.

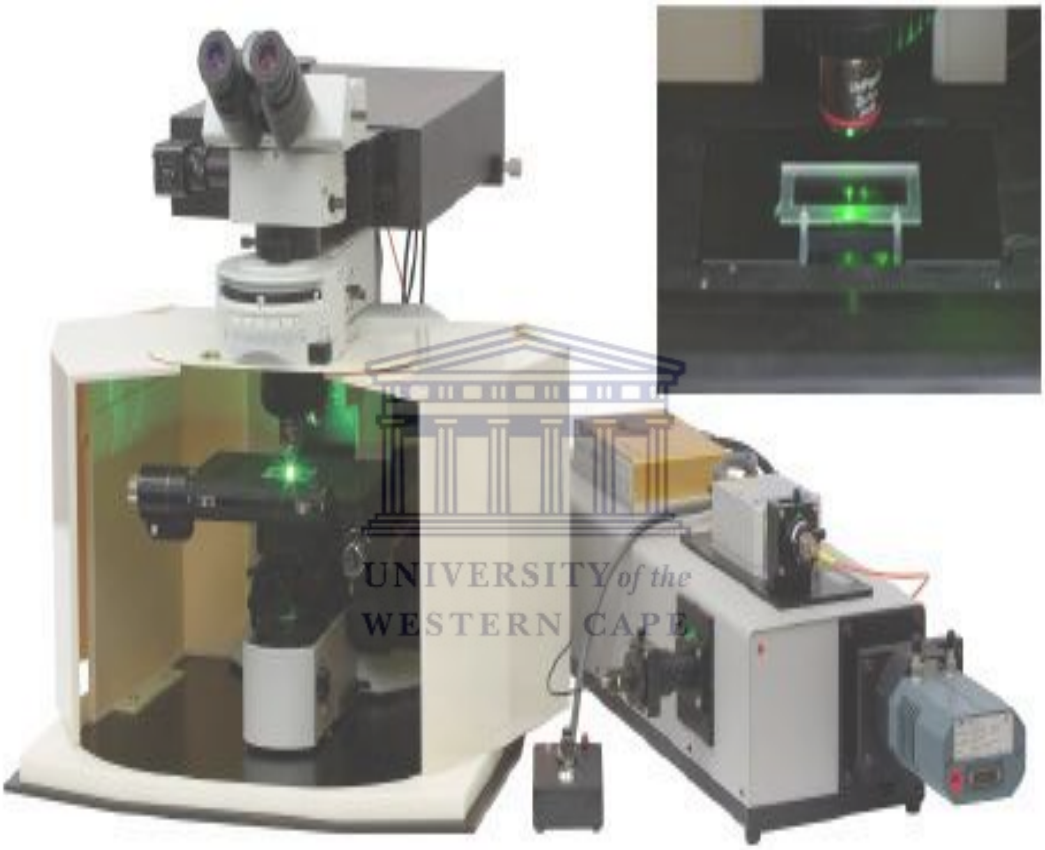

Figure 3. 8: Raman Spectrophotometer.

Raman spectroscopy is utilized in science to distinguish molecules and investigate chemical bonding. Since vibrational frequencies are peculiar to a molecule's chemical bonds and symmetry (the fingerprint region of organic particles is in the wavenumber range of 500-1500 cm^{-1}). Raman gives a unique fingerprint to differentiate molecules. For example, Raman and IR spectra were utilized to decide the vibrational frequencies of SiO, Si_2O_2, and Si_3O_3 based

on ordinary coordinate analyses. In strong state material science, Raman spectroscopy is utilized to describe materials, measure temperature, and discover the crystallographic orientation of a sample. [10].

3.3.3 ELECTROCHEMICAL CHARACTERIZATION

Electrochemical characterization is the most powerful technique used to evaluate the performance of nanomaterials in energy generation and storage applications as well as sensors to understand the relevant reaction mechanisms involved in charge transfer, mass transport, electrolyte transport, electron transport, etc. The electrochemical workstation/electrochemical analyzer is a unit that helps to carry out all the electrochemical characterization techniques/methods, like cyclic voltammetry (CV), square wave voltammetry (SW), chronoamperometry (CA), chronopotentiometry (CP), galvanostatic charge discharge (GCD), electrochemical impedance spectroscopy (EIS), etc. This can be used for various applications like sensor studies, batteries, capacitors, solar cells etc.

In electrochemical characterization, the measurement of potential, charge, or current is used to determine an analyte's concentration or to characterize an analyte's chemical reactivity. The potential, charge, and current are the basic electrochemical signals that act as analytical signals. Hence these signals form the core experimental designs for all the electrochemical characterization techniques.

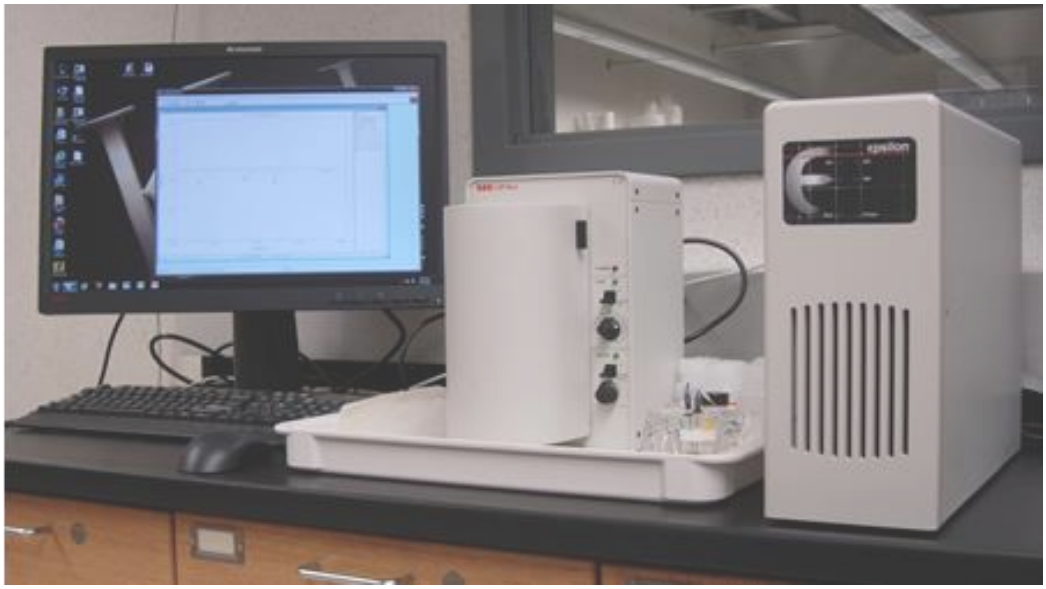

Figure 3. 9: An Electrochemical Workstation

Electrochemical characterization is performed to study the electrochemical behaviour of the materials under various electrochemical conditions. In an electrochemical cell, there are three kinds of electrode systems available, the two-electrode system, three-electrode system, and four electrode systems. Electrochemical characterizations can be performed using any of these electrode systems. The electrochemical cell consists of a working electrode and a counter electrode. The potential of the working electrode is sensitive to the analyte's concentration. The counter electrode closes the circuit. The potential of the working electrode should be calculated with respect to the counter electrode, as it acts as a reference potential. Hence, the potential of the counter electrode should remain constant. If the potential of the counter electrode is not constant, then two electrodes replace the counter electrode, a reference electrode whose potential remains constant and an auxiliary electrode to complete the electrical circuit. The area of the auxiliary electrode should be sufficient to support the current available in the circuit. On the other hand, in the three-electrode system, the voltage is measured between the reference and the working electrode. In both of the two and three electrode systems, the current flows through the counter and the working electrodes. In

addition, the reference electrode is chosen so as to exhibit an ideal nonpolarizable (depolarized) behaviour (it is a type of an electrode that restricts the change in its potential on passage of current through it). Hence its voltage remains over a large range of current densities so that it should act as a reference and the measurement from the working electrode voltage can be accurately done [11]. Electrochemical characterization of an electrochemical cell depends on various factors such as the condition of the working electrode and the counter electrode, the ions of the analyte in the electrolyte, and the current, charge, and voltage. All these things will be directly or indirectly connected to the redox reactions and will be responsible for the changes in the electrochemical properties of the materials.

3.3.3.1 CYCLIC VOLTAMMETRY (CV)

Cyclic Voltammetry (CV) is the basic electrochemical test for materials. In this, the current is recorded by sweeping the potential back and forth (from positive to negative and negative to positive) between the chosen limits. The information obtained from CV can be used to learn about the electrochemical behaviour of the material. The graphical analysis of a cyclic voltammogram gives the redox peaks (refer to CV in Figure 3.10), which are reduction and oxidation peaks of the material, predicting the capacitive behaviour of the electrode. Hence, the potential at which the material is oxidized and reduced can be found.

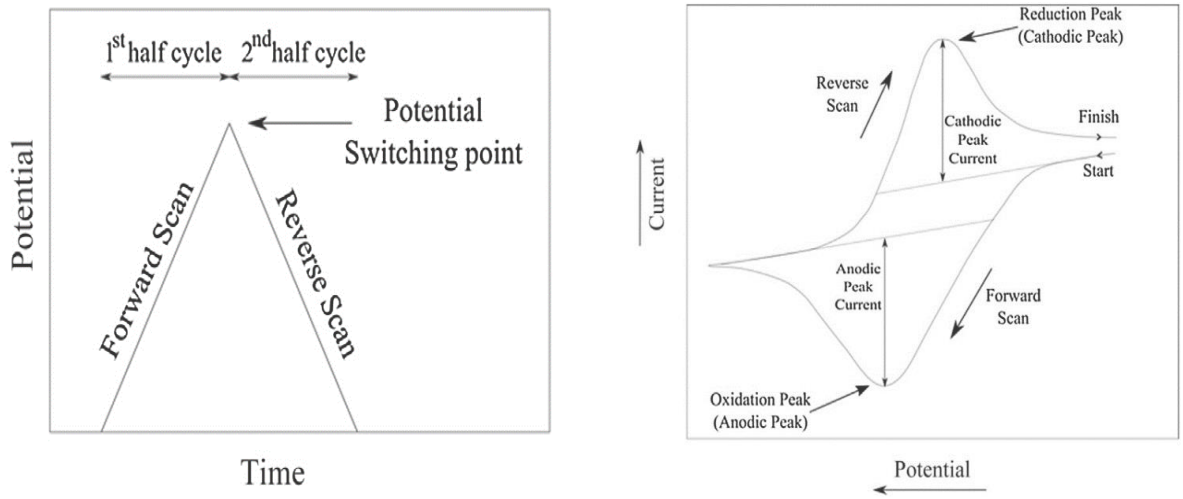

Figure 3. 10: Schematic of Cyclic Voltammetry.

A ramp signal is provided as an input to CV. For the forward scan, a positive ramp (having positive slope) signal is provided, while the voltage is switched after the first half-cycle, followed by a negative ramp, which inverts the nature of the cyclic voltammogram for the second (next) half cycle. As the system tries to achieve the equilibrium state with the help of redox reactions, it strives to reach the same position where it started. It follows a cyclic pattern, wherein the pattern gives information about the changes that the system has gone through. By properly analyzing the CV curve, one can make many important conclusions regarding the material and its properties (like capacitive nature, etc.) along with the system behaviour (reversible, irreversible, or quasi-reversible). The CV experiment can be carried out with one cycle or multiple potential cycles. The slope of the ramp signal expressed in volts per unit time is termed as the scan rate. The range of this scan rate can be from a few fractions of millivolts per second to several hundreds of volts per second. The scan rate of the system can be varied to get a clear idea of the electrochemistry of the cell. Hence, the scan rate plays a crucial role in the voltammetric behaviour of the sample to be tested. Based on the scan rate, one can expect some changes in the oxidation and reduction peak currents along with peak potentials. Also, if the peak current (faradaic current) is increasing with the increasing scan

rate, then it represents a good rate capability along with better pseudocapacitive behaviour of the electrode material. Higher scan rate results in a higher number of redox reactions due to the presence of the electroactive species at the electrode's (working electrode) surface. For a slower scan rate, however, there is the possibility of missing the peak (either forward or reverse scan peak) owing to the sufficient time available for the products from the reduction or oxidation to participate in a chemical reaction whose products may not be electroactive [12]. This peak current in the CV can be calculated using the Randles Sevcik equation:

$$i_{\mathrm{p}} = 2.69 \times 10^{5} n^{3/2} AC\sqrt{vD} \qquad \textbf{(3.1)}$$

Where 2.69 x 10^5 is a constant at a temperature of 25 ˚C, i_{p} is the peak current in amperes, n represents the number of electrons in the redox reaction, A represents the area of the working electrode in cm^2, *C* represents the concentration of the electroactive species at the electrode in mol/cm^3, *v* is the scan rate in V/s, and *D* represents the diffusion coefficient in cm^2/s of the electroactive species.

All these parameters play a crucial role in determining the peak current in CV and data obtained from CV helps to find the electron transfer coefficient (number of electrons transferred), rate-limiting factor (the factor that limits the rate of the reaction), and rate constant of the reaction. The difference in the two peak potentials of the CV gives an idea of the effects of the diffusion rates of the analytes. Also, the reversible, irreversible, and quasi-reversible nature of the system can be found using the ratio of the anodic and the cathodic peak currents. If the ratio is equal to one (1), it means both the anodic and the cathodic peak currents are the same, and it tells about the reversible nature of the system. If the ratio is not equal to 1, then it tells about the quasi-reversible nature of the system, whereas the system can be said to be irreversible when its oxidized or reduced product is not reversible. The current peaks are basically obtained, since the CV is taken in a situation in which the solution is kept

unstirred; otherwise the peak current may be replaced by the limiting current. Even the pH of the medium plays a crucial role in affecting the electrode reaction. In the case of polymers, by using the band gaps, electron affinities, and work functions of the materials, CV can easily predict the electrochemical behaviour of the polymer [13]. Hence, CV is used for studying the chemical and electrochemical behaviour of the compound. Along with all the aforementioned advantages, CV can also help in the functionalization of materials by performing various redox reactions using multiple scans.

3.3.3.2 SQUARE-WAVE VOLTAMMETRY (SWV)

This is a type of electrochemical technique wherein a linearly increasing input signal is provided in the form of a square wave for a voltammetric application. By using square-wave voltammetry (SWV) the current passing through the working electrode can be found and the potential across the working and the reference electrode will be sweeping in time linearly.

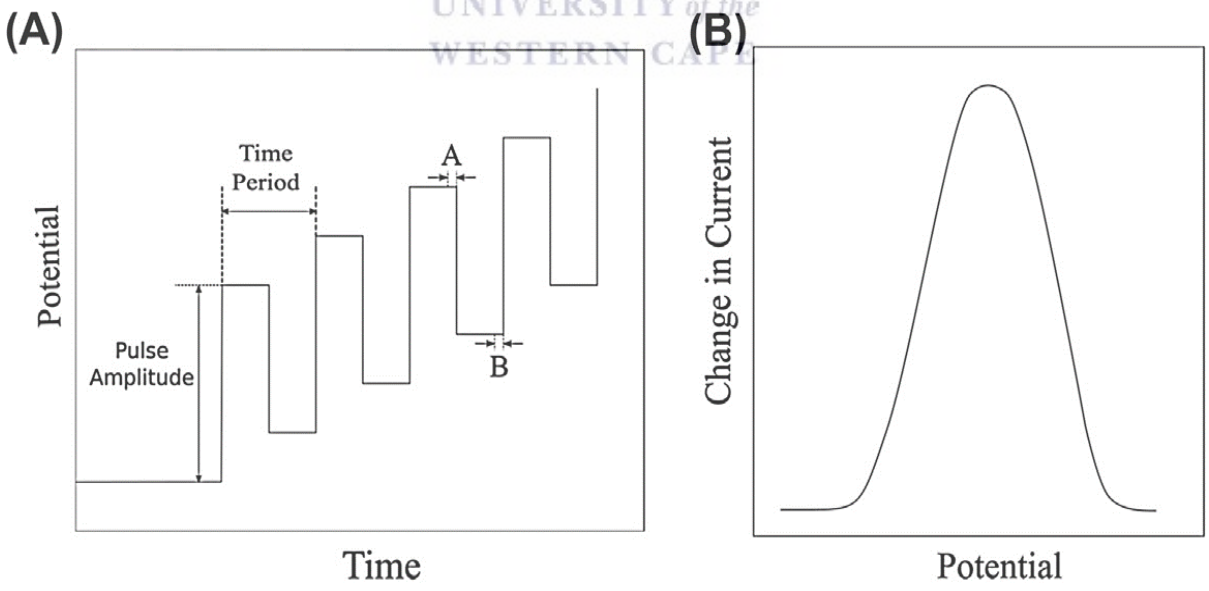

Figure 3. 11: (A) General input nature of the linear sweep square-wave voltammogram. (B) Output of a linear sweep square-wave voltammograms.

The amplitude of this linearly sweeping square wave is always constant. The obtained current is measured by sampling the linearly sweeping input square waveform at the end of each half-cycle. This current is measured in the forward half-cycle as well as in the reverse half-cycle and the difference between the two gives the output current waveform as the function of applied potential. For example, as shown in Fig. 3.11A, the forward current is measured by sampling the potential at "A" and the reverse current is measured by sampling the potential at "B". As "A" and "B" represent certain amounts of time at the end of each pulse, the potential is sampled during that amount of time and the difference between those two sampled potential values generates the output waveform of Fig. 3.11B as shown. The adsorbed electroactive organic molecules on the electrode surface can be determined perfectly using adsorptive stripping SWV [14]. SWV is a very sensitive technique. It can easily identify the adsorption of any specific reactant by showing a significant enhancement in its peak current [15].

3.3.3.3 ELECTROCHEMICAL IMPEDANCE SPECTROSCOPY (EIS)

Electrochemical Impedance Spectroscopy is used to measure the opposition that a circuit presents to a current when a voltage is applied (impedance) to electrochemical cell. Impedance can be calculated by applying a sinusoidal (AC) voltage of small amplitude to the electrode under study, which results in generating the current whose amplitude and phase angle are measured with respect to the applied sinusoidal voltage. Following this, using Ohm's law, the impedance is determined. Because the impedance is a function of frequency, to obtain an impedance spectrum, the different ranges of frequencies have to be examined. EIS tests are carried out in a specific frequency domain with proper signal parameters like the signal amplitude perturbation in millivolts and data acquisition rates [16]. (For the analysis of the EIS, the AC voltage signal should be given in the specific frequency range.) The measurements are usually performed at room temperature. The data collected from the EIS experiment can be compared with a modified Randles circuit and the impedance spectra can

be interpreted. The Randles circuit gives an equivalent circuit of the cell as shown in Fig. 3.12.

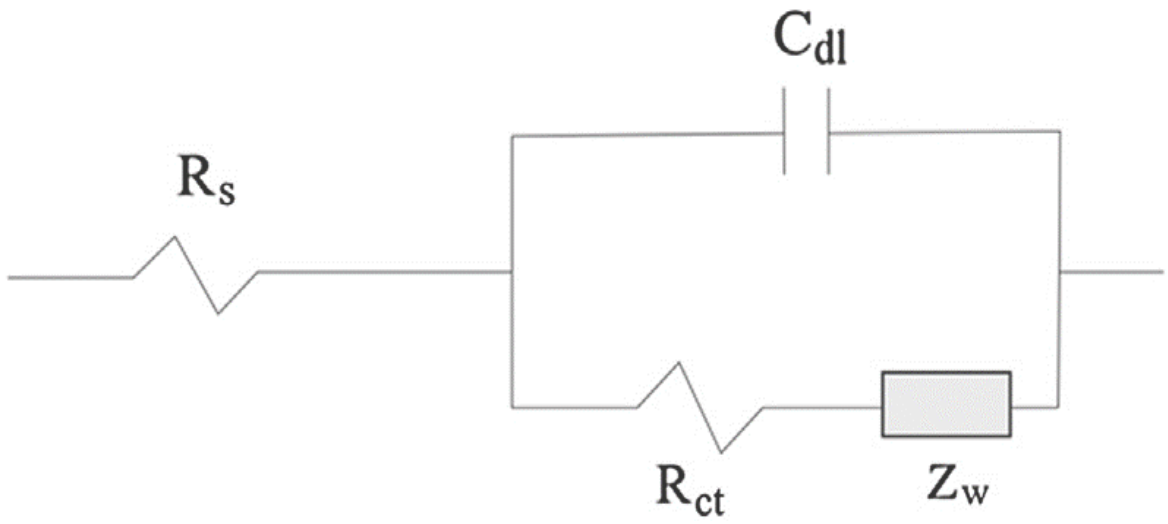

Figure 3. 12: Randles Circuit

In Fig. 3.12, R_s is the solution (electrolyte) resistance, C_{dl} is the double-layer capacitance, R_{ct} is the charge transfer resistance, and Z_w is the Warburg impedance. The Warburg impedance helps in evaluating the Warburg diffusion coefficient value. Warburg is basically a constant phase element with a constant phase shift of 45 degrees and its impedance is defined by resolving Fick's law, which in turn helps to extract the diffusion coefficient from the following equation [16]:

$$Z_w = \frac{RT}{(nF)^2 C\sqrt{jwD}} = Z_o\left(w^{-1/2} - jw^{-1/2}\right) \quad \textbf{(3.2)}$$

where Z_w is the Warburg impedance, R is the ideal gas constant, T is the thermodynamic temperature, n is the valency (number of electrons), F is the Faraday constant, C is the concentration of the electrolyte, w is the pulse frequency, D is diffusion coefficient, and Z_0 is the Warburg coefficient. The properties of conducting polymers can be analyzed very well using EIS. It can also be used for corrosion studies [15] and for the determination of the flat-band potential using the Motte-Schottky equation [17]. The Motte-Schottky equation relates

the semiconductor electrolyte interfacial capacitance to voltage. For studying the corrosion properties of coatings, a specific scan rate and the potential window from below the open circuit potential to above the open circuit potential are usually considered. Nyquist plots are nothing but the graphical output of the EIS. The Nyquist plots consist of two regions, one is high frequency and the other is low frequency. The Charge Transfer Resistance (R_{ct}) occurs at the electrode/electrolyte interface, and it is responsible for the semicircular nature of the graph in the high frequency region. However, the diffusion of ions from the electrolyte into the interior of the electrode material, which is termed as Warburg impedance (Z_w), is responsible for the straight-line (constant slope) behaviour of the graph in the low-frequency region of the EIS spectra [18]. Both R_{ct} and Z_w together are termed as polarization resistance. Because the Nyquist plot is plotted between the real and the imaginary part of the impedance, the high-frequency intercept of the Nyquist plot with the real axis gives the bulk resistance (as the imaginary part of the impedance becomes zero on the real axis).

EIS can be used for water electrolyte uptake. It needs a sufficiently conductive electrolyte for carrying out the measurements through EIS. For the same, different types of salts are used, which helps in increasing the conductivity of the electrolyte. NaCl and KCl are the most commonly used salts for this purpose. Mixing of NaCl in the electrolyte causes the environment to be corrosive, although it helps in increasing the conductivity of the electrolyte. Several methods exist to analyze an EIS spectrum; one of the most popular includes fitting the spectrum to an equivalent circuit [19]. The conventional method for the analysis of water uptake was by simulating EIS data with the Randles equivalent circuit and performing the water uptake calculation using the Brashere Kingsbury equation [20]. EIS can also be used for the characterization of liquid electrolyte-based batteries. In the case of micro-batteries, their design and small dimensions make their inner characterizations difficult. EIS is a good

compromise for the characterization of such microcell batteries [16]. The basic equivalent circuit model and the corresponding impedance plot is shown in Fig. 3.13.

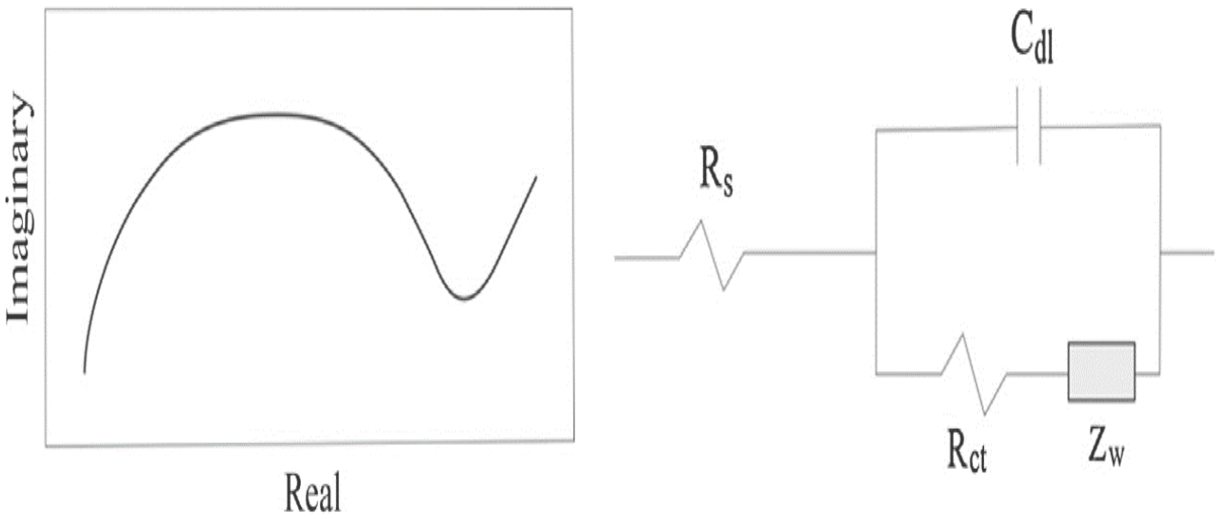

Figure 3. 13: EIS circuit model describing the electrode processes when both kinetics and diffusion are important

3.3.3.4 CURRENT-VOLTAGE CURVE (I-V CURVE)

The I-V Curves, which is short for Current-Voltage Characteristic Curves or basically I-V curves of an electrical device, are an arrangement of graphical curves which are utilized to characterize its activity inside an electrical circuit. As its name shows, I-V curves demonstrate the connection between the current flowing through an electronic device and the applied potential over its terminals. I-V curves are commonly utilized as a technique to determine and comprehend the basic parameters of a component or device and which can likewise be utilized to mathematically show its behavior within an electronic circuit. When there is no light present to generate any current, the PV cell behaves like a diode. As the intensity of incident light increases, current is generated by the PV cell. Although the illuminated current shifts the I-V curve in the negative direction, conventionally the I-V curve of the solar cells is mirrored along the horizontal axis and shown as in figure 3.14.

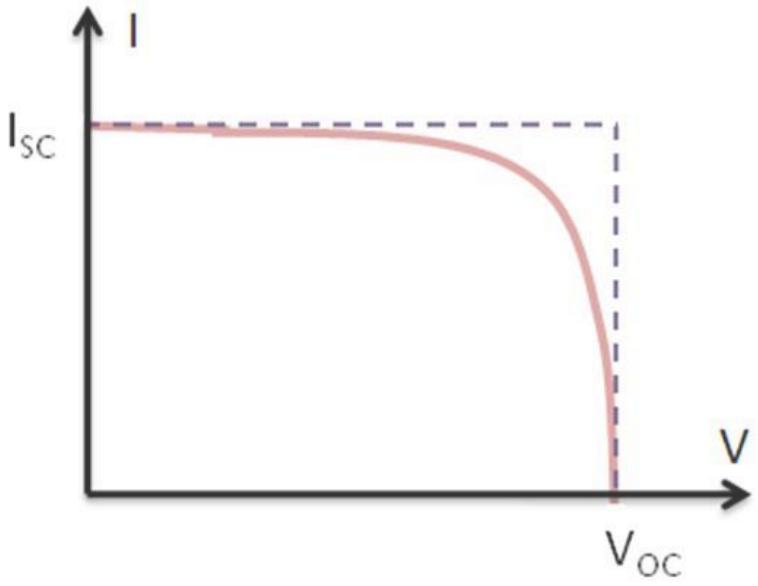

Figure 3. 14 I-V curve of a Solar Cell.

The short circuit current I_{sc} correspond to the short circuit condition when the impedance is low and is calculated when the voltage equals 0 and the open circuit voltage V_{oc} occurs when there is no current passing through the cell [21].

The Efficiency of a PV cell can be obtained from I-V curve. Efficiency is defined as a ratio of the power output of the PV cell to the power input of the PV cell [22]. At determined conditions, the power incident on a solar cell is about 1000 W/m^2 which is called power input (P_{in}). Other notable values used in calculating efficiency are Fill-Factor (*FF*) in %, P_{max} is the maximum power output of the PV cell with unit of W/m^2, V_{max} is the voltage at P_{max} and current at P_{max} is defined as I_{max} shown in figure 3.15.

Therefore, the efficiency can be defined as:

$$\eta = \frac{FF \times V_{oc} \times J_{sc}}{P_{In}} \times 100\% \qquad \textbf{(3.3)}$$

Where Fill-Factor (FF) is given as

$$FF = \frac{J_{max} \times V_{max}}{J_{sc} \times V_{oc}} \quad \textbf{(3.4)}$$

But maximum power P_{max} is given as

$$P_{max} = J_{max} \times V_{max} \quad \textbf{(3.5)}$$

Therefore, efficiency (η) is given as

$$\eta = \frac{P_{max}}{P_{in}} \times 100\% \quad \textbf{(3.6)}$$

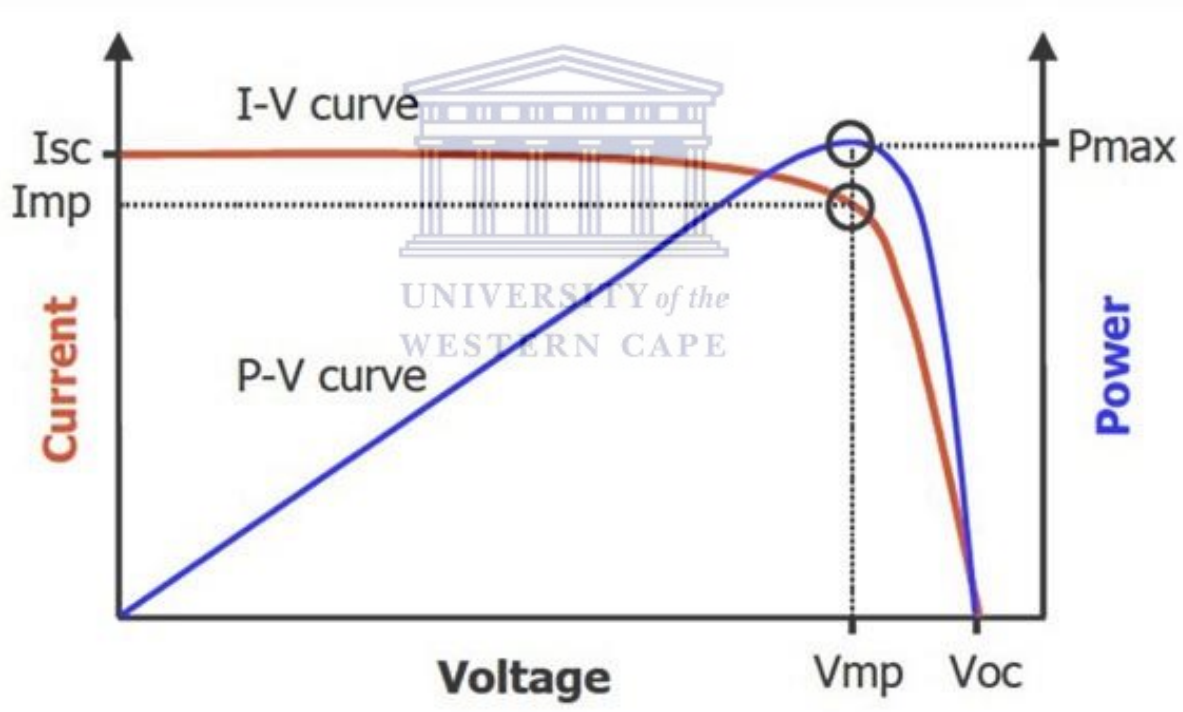

Figure 3. 15 I-V and Power curve of a solar cell.

For an ideal solar cell, the V_{max} will be equal to V_{oc} and I_{max} will be equal to I_{sc} therefore the I-V curve will have a perfect rectangular shape [21].

3.3.4 OTHER CHARACTERIZATIONS

3.3.4.1 THERMOGRAVIMETRY ANALYSIS (TGA)

TGA is useful in the investigation of the thermal stability of materials. It provides details into how the weight of samples decreases as temperature is increased and offers the point where the weight loss of the material become less (at this point the material is stable).

3.3.4.2 FOURIER TRANSFORM INFRARED SPECTROSCOPY (FTIR)

FTIR is an infrared spectroscopic method used to explore and analyze molecules and atoms within the structure of materials. Vibration bands characteristic of the functional groups are produced when infrared radiation reacts with sample molecules. These infrared radiations can be absorbed or transmitted producing absorption or transmission spectrum as the case may be which are molecular fingerprint of the sample. These absorption peaks relate to the frequencies of vibrations between the bonds of the atoms and molecules that make up the material. Given that molecules are different from each other in their chemical composition and structure, it is possible to derive clear identification of materials [23].

3.3.4.3 X-RAY DIFFRACTOMETRY (XRD)

X-ray diffraction is a typical strategy for the investigation of crystal structures and atomic spacing, reliant on constructive interference of monochromatic X-rays and a crystalline sample. The X-rays are made from cathode ray tube, sifted to deliver monochromatic radiation, modified to focus, and coordinated toward the sample. Useful interferences are created by the interaction of the incident rays and the sample when conditions fulfill Bragg's law: $n\lambda = 2d \sin\theta$, where n is an integer, λ is the wavelength of the X-rays, d is the interplanar spacing producing the diffraction, and θ is the diffraction angle. The wavelength of electromagnetic radiation is identified with the diffraction angle and the lattice spacing in a crystalline example by this law. These diffracted X-beams are then recognized, prepared and tallied. The sample is

looked over a scope of 2θ angles so all conceivable diffraction directions of the lattice ought to be accomplished because of the arbitrary orientation of the powdered material. The transformation of the diffraction peaks to d-spacings permits recognizable proof of the compound on the grounds that each compound has an arrangement of remarkable d-spacings [24].

3.3.4.4 SMALL AREA X-RAY SCATTERING (SAXS)

SAXS Small-angle X-ray scattering (SAXS) is a small-angle scattering technique by which nanoscale density differences in a sample can be quantified. This implies it can determine nanoparticle size distributions, resolve the size and shape of (monodisperse) macromolecules, determine pore sizes, characteristic distances of partially ordered materials, and much more [25]. SAXS as a technique was used to provide informing on the particle size distribution as well as the shape of the nanomaterials.

REFERENCES

[1] H. Dong, T. Schnabel, E. Ahlswede and C. Feldman, "Poly mediated synthesis of $Cu_2ZnSn(S,Se)_4$ kesterite nanoparticles and their use in thin-film solar cells," *Solid State Sciences* 29 (2014) 52-57

[2] The University of Edinburgh. "What is Microscopy?" (2018) Retrieved April 9, 2018.

[3] M. von Heimandahl, "Electron Microscopy of Materials: an introduction," Academic Press, New York. (1980) 1-228.

[4] P.J. Goodhew and F.J. Humphreys, "Electron Microscopy and Analysis," 2nd edition, Taylor & Francis Ltd, London. (2000) 1-254.

[5] D.B. Williams and C.B. Carter, "Transmission electron microscopy: A textbook for material science," 2nd Edition, Springer, London (2009) 3-22.

[6] D.A. Skoog, F.J. Holler and S.R. Crouch, "Principles of Instrumental Analysis," Belmont, CA: Thomson Brooks/Cole 6 (2007) 169–173.

[7] D.D. Evanoff Jr. and G. Chumanov, "Synthesis and optical properties of silver nanoparticles and arrays," *ChemPhysChem* 6 (2005) 1221-31.

[8] X. Huang, P.K. Jain, I.H. El-Sayed and M.A. El-Sayed, "Gold nanoparticles: interesting optical properties and recent applications in cancer diagnostics and therapy," *Nanomedicine* 2 (2007) 681-693.

[9] G.S. Bumbrah and R.M. Sharma, "Raman spectroscopy and basic principle, instrumentation and selected applications for the characterization of drugs of abuse," *Egyptian Journal of Forensic Science* 6 (2016) 209-215.

[10] "FDA approves Gilead cystic fibrosis drug Cayston". *BusinessWeek* (2010). Retrieved 11-09-2018

[11] S. Thomas, R. Thomas, A. Zachariah and R. Mishra, "Spectroscopic Methods for Nanomaterials Characterization" 1st Edition, Elsevier (2017) 19-50

[12] T. Kim, A. Ramadoss, B. Saravanakumar, G.K. Veerasubramani and S.J. Kim, "Synthesis and characterization of $NiCo_2O_4$ nanoplates as efficient electrode materials for electrochemical supercapacitors," *Applied Surface Science* 370 (2016) 452-458.

[13] A. Kamath, S. Raghu and H. Devendrappa, "Methyl blue dyed polyethylene oxide films: optical and electrochemical characterization and application as a single layer organic device," *Optical Materials* 51 (2016) 213-222.

[14] M. Lovric, "Square-wave voltammetry, Electroanalytical Methods: Guide to Experiments and Applications," Springer Berlin Heidelberg, Berlin, Heidelberg (2002) 111-136.

[15] G.C. Barker, J.A. Bolzan, "Effects in polarography attributable to specific adsorption of depolarizers," *Analytical and Bioanalytical Chemistry* 216 (1966) 215-238.

[16] J.M. Ferreira, K.P. Souza, F.M. Queiroz, I. Costa and C.R. Tomachuk, "Electrochemical and chemical characterization of electrodeposited zinc surface exposed to new surface treatments," *Surface Coating Technology* 294 (2016) 36-46.

[17] S. Larfaillou, D. Guy-Bouyssou, F. Le Cras and S. Franger, "Comprehensive characterization of all-solid-state thin films commercial microbatteries by electrochemical impedance spectroscopy," *Journal of Power Sources* 319 (2016) 139-146.

[18] K.L. Gelderman and S.W. Donne, "Flat-band potential of a semiconductor: using the Motte Schottky equation," *Journal of Chemical Education* 84 (2007) 685.

[19] H. Li, S. Wu, C. Liao, Z. Zhou, X. Liu, A. Djurisic and M. Xie, “Facile synthesis, characterization, and electrochemical performance of multi-scale AgVO3 particles,” *Journal Alloyed Compound* 674 (2016) 56-62.

[20] M. Dornbusch, S. Kirsch, C. Henzel, C. Deschamps and S. Overmeyer, “Characterization of the water uptake and electrolyte uptake of organic coatings and the consequences by means of electrochemical impedance spectroscopy and UV-vis spectroscopy,” *Progress in Organic Coatings* 89 (2015) 332-343.

[21] P. Würfel and U. Würfel, “Physics of Solar Cells: From Basic Principles to Advanced Concepts,” 3rd Edition, Wiley-VCH, Sommerset, New Jersey (2016) 1-289.

[22] A.M. Green, “Solar Cells Operating Principles Technology and System Applications,” 1st Edition, Prentice Hall, United States (1982) 1-139

[23] Y. Chen, C. Zou, M. Mastalerz, S. Hu, C. Gasaway and X. Tao, “Application of micro-Fourrier transform infrared spectroscopy (FTIR) in the geological sciences-A Review,” *Molecular Sciences* (2015) 30223-30250.

[24] A. A. Bunaciu, E.G. Udristioiu and H.Y. Aboul-Enien, “X-Ray Diffraction: Instrumentation and Applications,” *Critical Reviews in Analytical Chemistry* 45 (2015) 289–299

[25] O. Glatter and O. Kratky, “Small angle x-ray scattering,” Academic Press, London (1982) 1-523.

CHAPTER 4

RESULTS AND DISCUSSIONS

This chapter will focus on analyzing the results obtained from various characterization techniques performed on the as-synthesized nanoparticles of copper zinc tin sulfide (CZTS), copper zinc tin sulfide selenide telluride (CZTSSeTe) and copper zinc tin sulfide telluride (CZTSTe). The various characterizations help determine the various properties exhibited by these synthesized nanoparticles.

4.1 SURFACE CONDITIONING

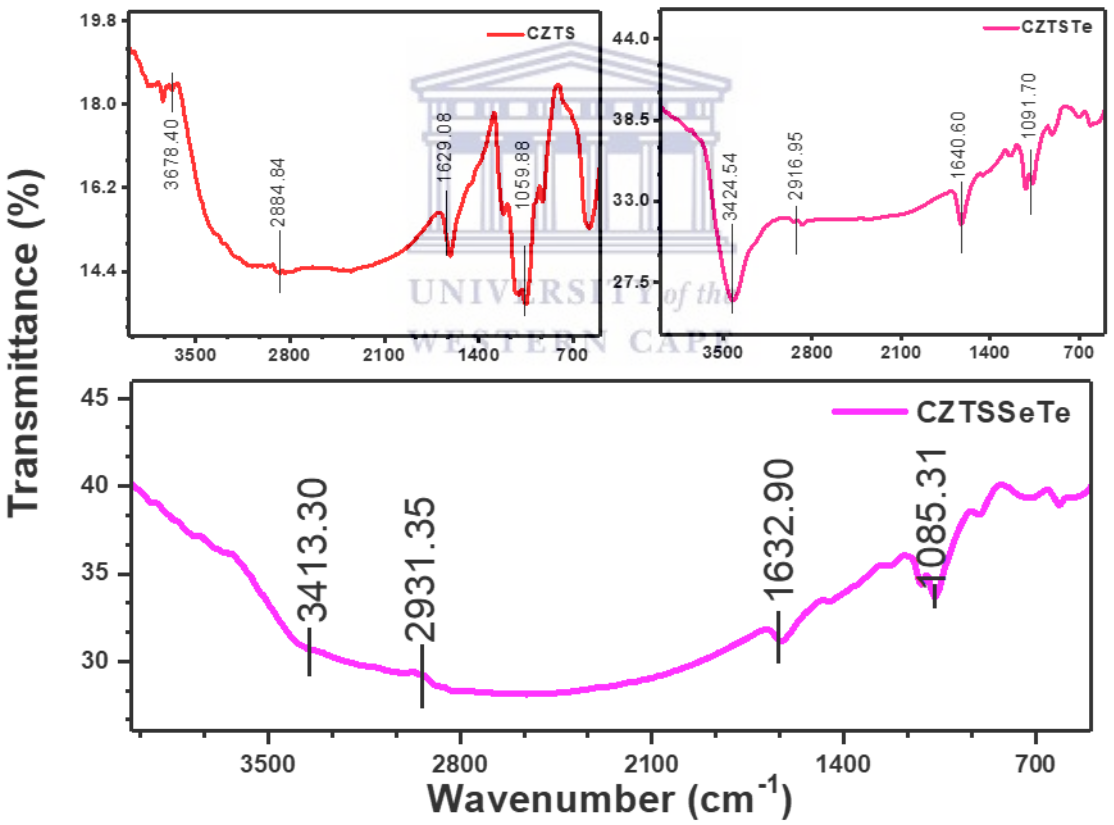

Figure 4. 1: FT-IR spectrum of the synthesized nanoparticles of CZTS, CZTSTe and CZTSSeTe with various vibrations bands.

The surface condition of the synthesized nanoparticles was analyzed through Fourier transform infra-red spectroscopy **(**FTIR**).** The instrument used for the analysis was Perkin Elmer spectrum Two FTIR spectrometer. The vibration bands obtained from the spectra of the synthesized nanoparticles showed similar vibrational bands characteristic of diethylene glycol (DEG). The bands found in the spectrum include ν (O-H) (3750-3250 cm^{-1}), ν (C-H) (3000-2750 cm^{-1}), ν (C-C) (1700-1550 cm^{-1}) and ν (C-O) (1350-900 cm^{-1}) [1]. These vibrations are in good agreement with the spectrum of pure DEG as a reference (figure 4.2). The formation of new compounds can be seen from the observable differences and shifts from the spectrum of the nanoparticles and that of the solvent as shown in figures 4.1 and 4.2. CZTS and CZTSSeTe show some shifts and reduced bands at the (3750-3250 cm^{-1}) and (3000-2750 cm^{-1}). This behaviour can be ascribed to the surface bonding of DEG on surface of these nanoparticles and attributed to the presence of sulfur in these nanoparticles. Also reduced bands can be seen in CZTSSeTe and CZTSTe at the ν (C-O) stretching which is also indicative of the surface bonding of DEG with the nanoparticles and behaviour can be attributed to the presence of tellurium. Small amounts of DEG as a surface capping agent in previous studies doesn't restrict the manufacturing and performance of thin-film solar cell since DEG can easily be removed during annealing process [2].

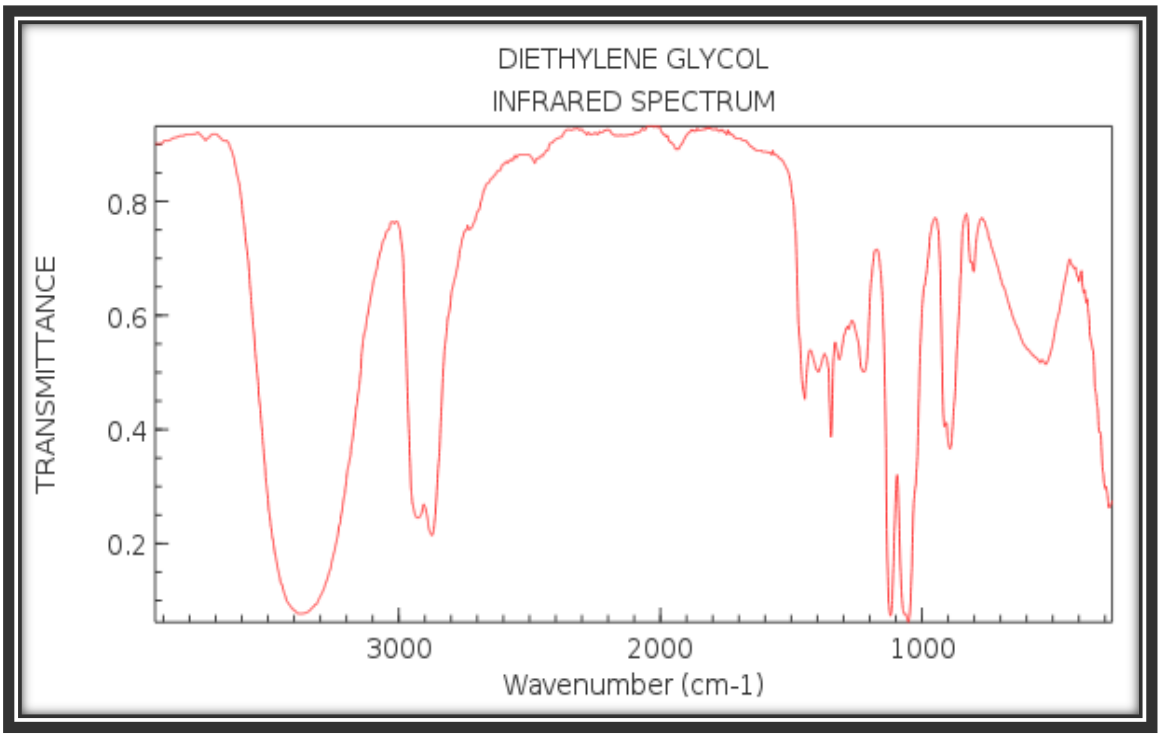

Figure 4. 2: FT-IR spectrum of DEG with its various vibrational bands.

4.2 SURFACE MORPHOLOGY

The surface appearance of the synthesized nanoparticles was investigated using Scanning electron microscope. The instrument used for this analysis is ZEISS ULTRA scanning electron microscope with acceleration voltage of 5.0 kV. The micrograph obtained showed that the nanoparticles were agglomerated forming large nanoparticle clusters. Comparison of the three nanoparticles shows a denser morphology for CZTSSeTe followed by CZTSTe and then CZTS. The trend is attributed to the number of constituent elements that make up the nanoparticles. The dark portions of the micrograph can be ascribed to the surface bonding of the DEG molecules to the particle surface of the synthesized nanoparticles. It also reveals the small particle size of the nanoparticles. CZTSSeTe is seen to have rod-like and spherical shape while still maintaining the general flower-like morphology seen in both CZTS and CZTSTe as shown in figure 4.3 below

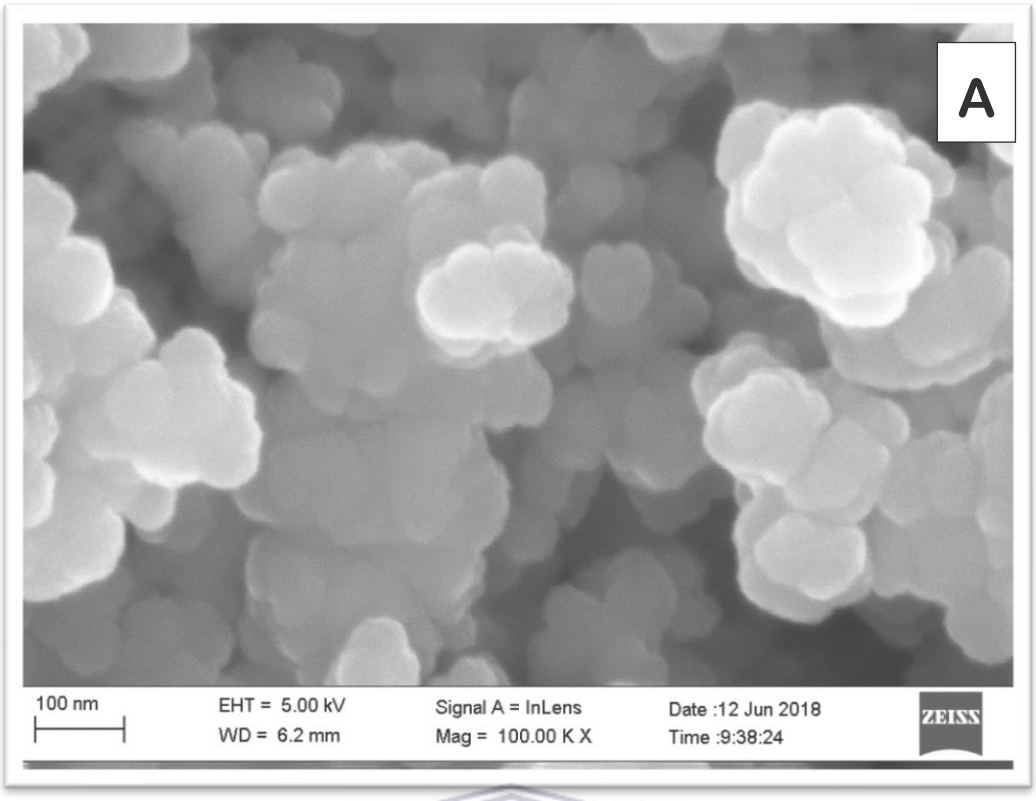

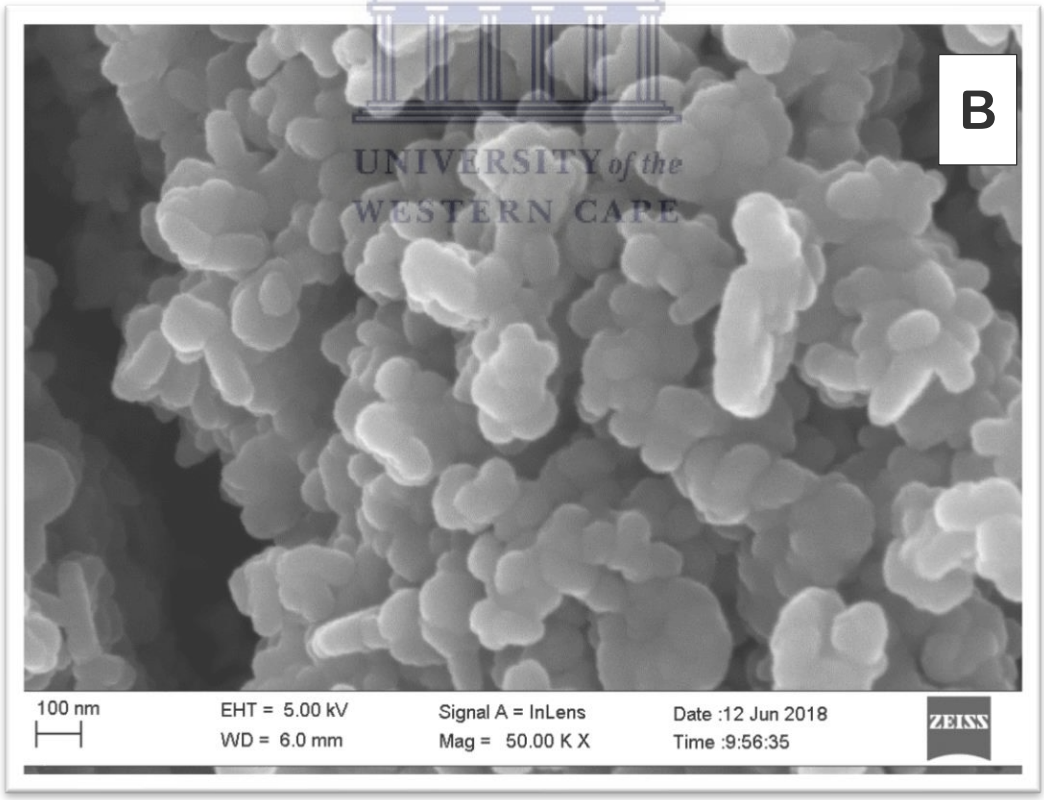

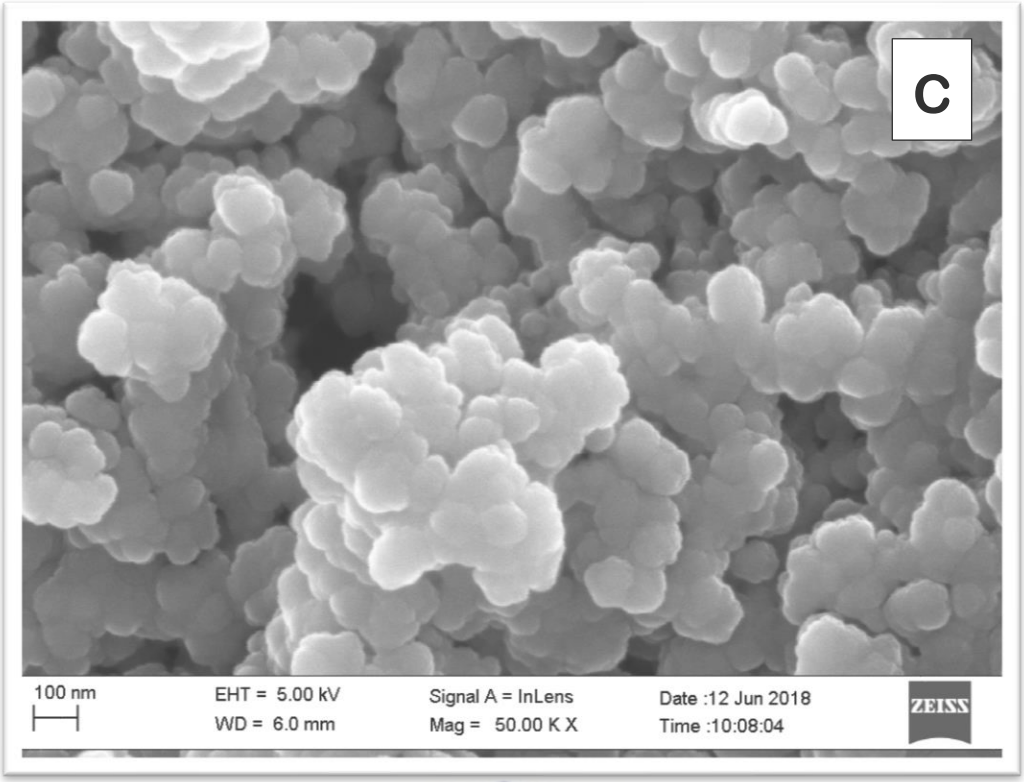

Figure 4. 3:HR-SEM micrograph of the synthesized nanoparticles of (A) CZTS, (B) CZTSSeTe and (C) CZTSTe showing flower-like morphology due to agglomeration.

The flower-like morphology has been widely reported as the morphological appearance of the kesterite nanoparticles [3-10]. This morphology has been reported to exhibit good photocatalytic behaviour as it regards to kesterite nanoparticles [3].

4.3 INTERNAL STRUCTURE

The internal structure of the synthesized nanoparticles was evaluated by transmission electron microscope (TEM). The TEM used for this analysis is the TECNAI G2 F2O X-TWIN MAT 200 kV field emission, where nickel grid was used to coat the material for better conductivity. The micrograph obtained through TEM didn't reveal much of the internal structure of the synthesized nanoparticles. This is because of the solvents which are still covering the surface of the nanoparticles as seen in FTIR result above (see Figure 4.1). The micrograph obtained for the nanoparticles shows the polydisperse nature of the nanoparticles. The micrograph

shows some rod-like structure for CZTS and CZTSSeTe as can be seen in figure 4.4 below, the internal structure of the synthesized nanoparticles also reveal agglomeration as well as presence of small particle size. The flower-like morphology can be seen in the micrograph obtained from TEM analysis. Although, the micrograph obtained did not provide a distinct image for the internal structure of the nanoparticles and as such was not used to determine the particle size of the nanoparticles, this situation is not new as earlier publications have been reported with such issues [3].

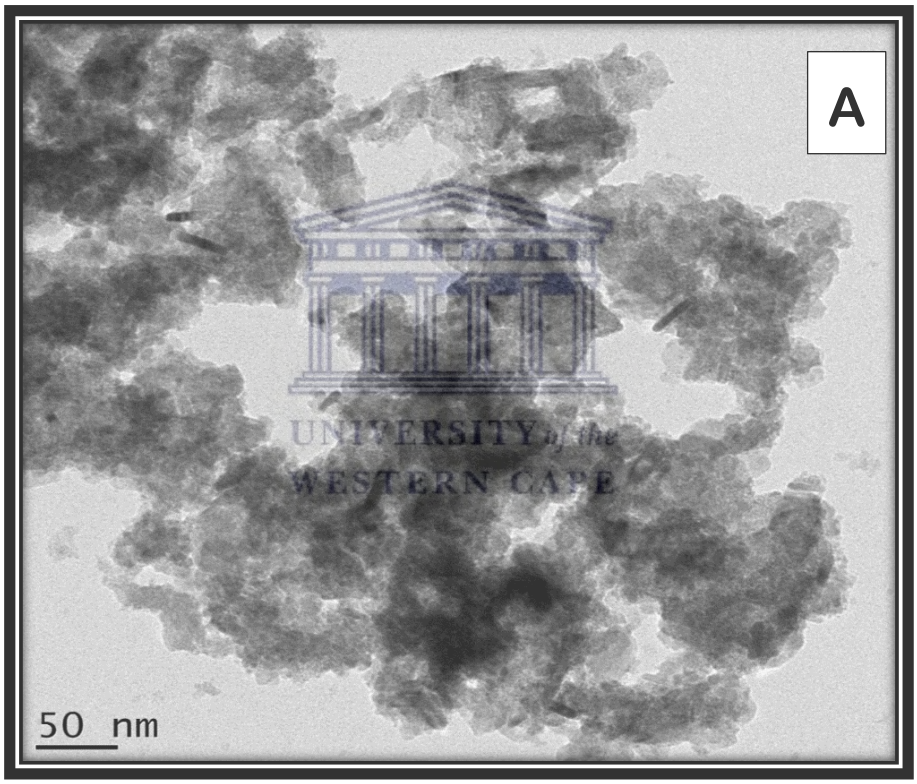

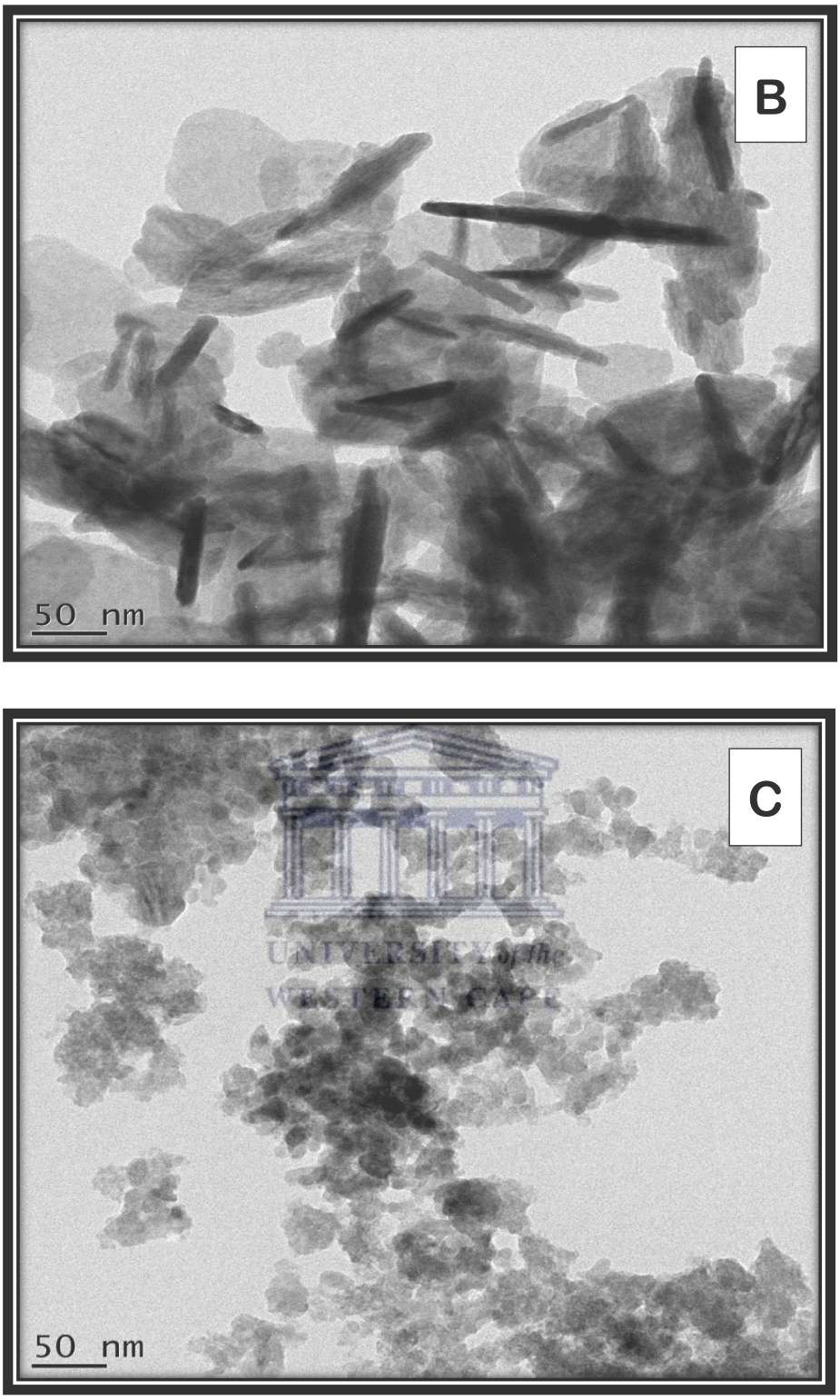

Figure 4. 4: TEM micrograph of the synthesized nanoparticles of (A) CZTS, (B) CZTSSeTe and (C) CZTSTe showing their internal structure and agglomeration.

As TEM could not be used to determine the internal structure of the nanoparticles, another technique was used to determine the internal structure of the synthesized nanoparticles which is Small Angle X-ray Scattering (SAXS). The SAXS analysis was performed using SAXS Space by **Anton Paar**. The shape analysis plot reveals that the nanoparticles were agglomerated and that CZTS and CZTSSeTe had a core and a shell. The shell is attributed to the solvent DEG as earlier seen in FTIR result above [1]. The core is the nanoparticles themselves. The shape obtained for the nanoparticles is summarized in the table 4.1 below and plots can be seen in figure 4.5 below.

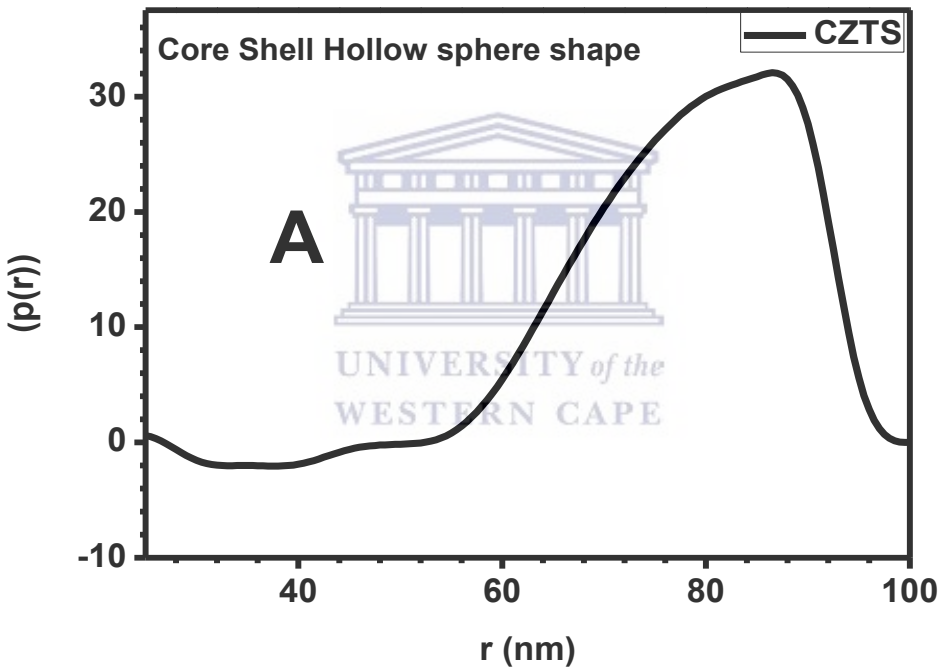

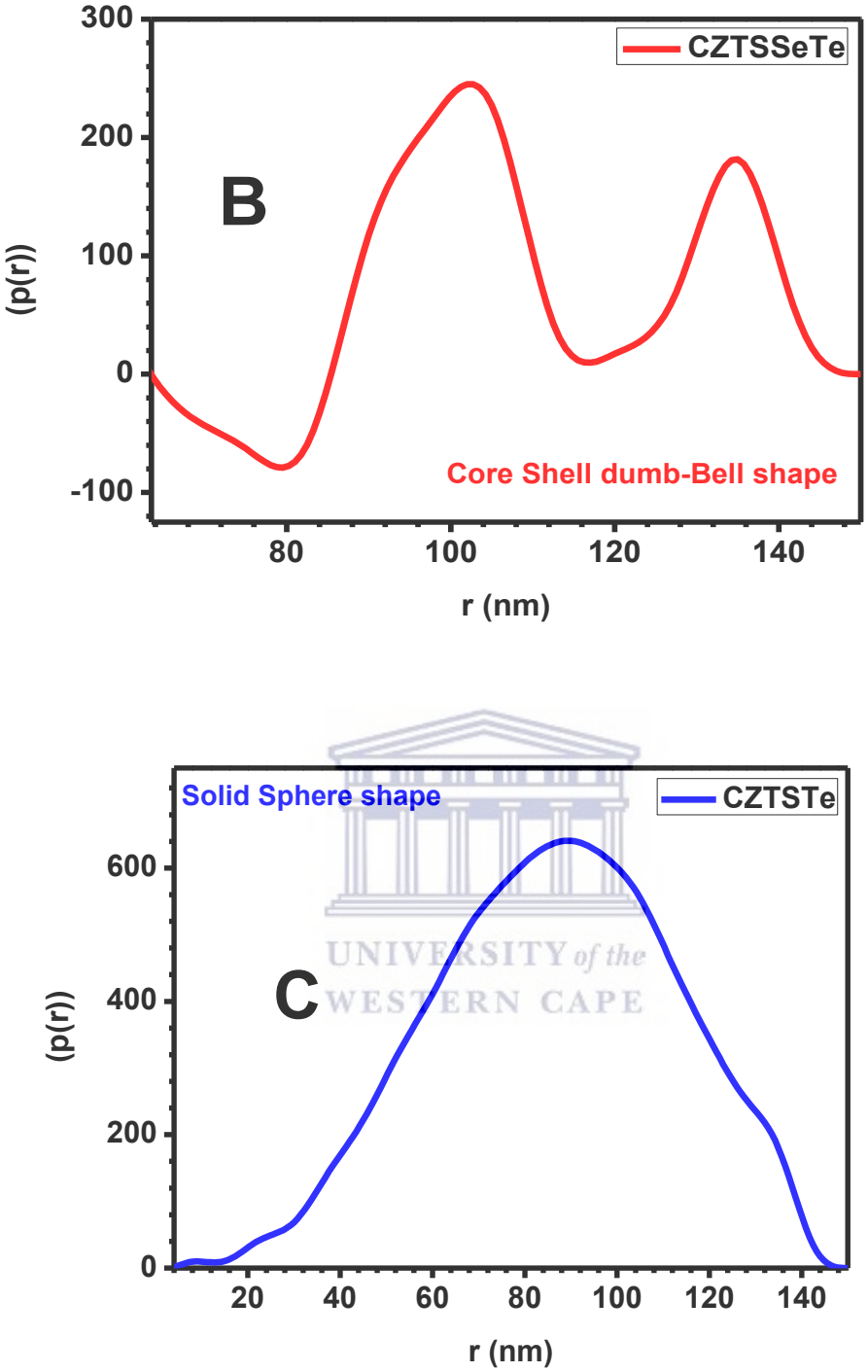

Figure 4. 5: SAXS plot of the internal structure/shape of the synthesized nanoparticles of (A) CZTS, (B) CZTSSeTe and (C) CZTSTe.

Table 4 1: Shapes obtained for the synthesized nanoparticles.

SAMPLES	SHAPES
CZTS	CORE SHELL HOLLOW SPHERE
CZTSSeTe	CORE SHEL DUMB-BELL
CZTSTe	SOLID SPHERE

The shoulders seen in the SAXS plots above indicate agglomeration or aggregation [11] of the nanoparticles as evidenced in HR-SEM and TEM images in figures 4.3 and 4.4 respectively. The spherical shape obtained for the nanoparticles agrees with the morphology earlier reported from the SEM and TEM result as the flower-like morphology stems from the spherical shape of the nanoparticles.

4.4 PHASE COMPOSITION (CRYSTALLINITY)

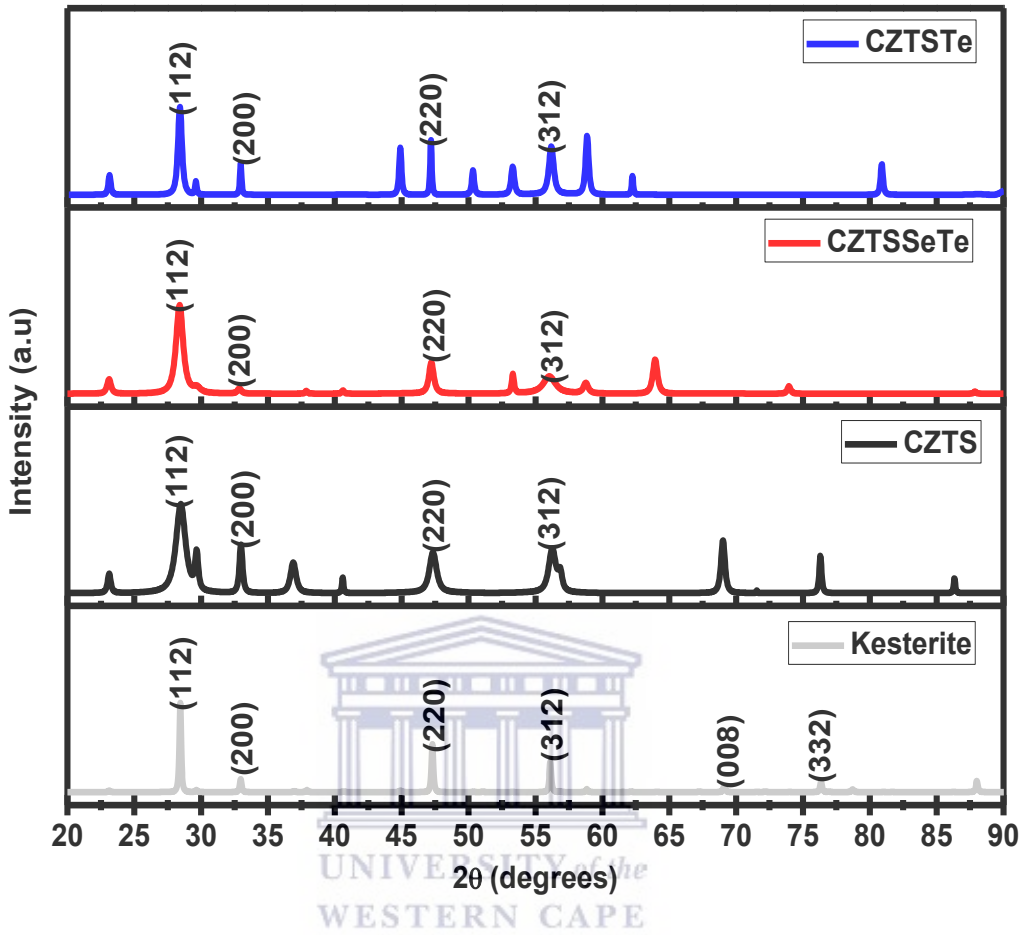

Figure 4. 6: XRD plot of the synthesized nanoparticles of CZTS, CZTSSeTe and CZTSTe with kesterite phase plot (data obtained from MATCH software)

The phase composition and crystalline structure of the synthesized nanoparticles were investigated through powder X-ray diffraction (XRD). The XRD data was collected with a BRUKER AXS DS Advance diffractometer with 2θ values ranging from 20-90 º, with a step size of 0.028 º operating at 45 kV and 40mA at Ithemba Labs Cape Town. The XRD results obtained were refined with crystal-impact software known as MATCH to remove the noise and obtain only the available peaks of the diffraction. As expected, the XRD pattern of the synthesized nanoparticles showed broad Bragg peaks indicative of small particle size as seen

in figure 4.6 [12]. The presence of tetragonal kesterite phase was observed for all samples (JCPDS 00-026-0575). After more baseline corrections and use of calculated peaks obtained from MATCH software indicated above, the Bragg peaks became much sharper and are in accordance with the reference tetragonal CZTS/kesterite (JCPDS 00-026-0575). This is welcomed because the tetragonal modification was frequently reported for its high-power conversion efficiency as compared to the hexagonal modifications [13-15]. The intense peaks observed in the spectrum also indicate the degree of crystallinity of the nanoparticles [16]. The observed peaks with the standard kesterite reference peak indicate that the kesterite phase was formed in the nanoparticles (JCPDS 00-026-0575). There was presence of secondary phases in the spectrum observed especially for CZTS and CZTSTe [17-20]. These secondary phases can be removed by chemical etching during fabrication and other impurities can be removed during annealing at high temperature [2]. The kesterite peaks observed for the nanoparticles are:

CZTS- (112, 200, 220 and 312), CZTSSeTe-(112, 200, 220 and 312) and CZTSTe-(112, 200, 220 and 312) (JCPDS 00-026-0575). These peaks were also confirmed by the diffraction obtained from selected area electron diffraction (SAED). The crystallinity of the nanoparticles can also be seen from the spectrum which shows the nanoparticles to be polycrystalline [21]. This is also an observable trend seen in SAED micrograph obtained from TEM analysis. The trend for the crystallinity of the nanoparticles was CZTSSeTe > CZTS > CZTSTe meaning that CZTSSeTe had the highest degree of crystallinity. The crystal size of the nanoparticles was evaluated from the XRD data obtained and this was also used to simulate the crystal structure of the nanoparticles as will be shown below. Each miller index plane has a characteristic d-spacing value, the lattice fringe micrograph obtained from TEM for the nanoparticles was evaluated and used to determine the plane at which the fringe was obtained.

Below is a run-down of the d-spacing value obtained from the XRD data analyzed using crystal impact software (MATCH)

2theta [deg]	d [A]	I/I0	Counts	FWHM total	FWHM instr.	FWHM sample	Correlated phase(s)	
23.184	3.8335	136.3	23	0.2744	0.0900	0.1844	Kesterite	
28.451	3.1346	386.2	194	0.8232	0.0900	0.7332	Kesterite	
29.640	3.0115	293.7	37	0.2058	0.0900	0.1158	Kesterite	
33.039	2.7091	333.3	56	0.2744	0.0858	0.1886	Kesterite	
37.032	2.4256	185.2	54	0.4802	0.0805	0.3997	Kesterite	
44.933	2.0157	624.3	52	0.1372	0.0972	0.0400	Kesterite	
47.227	1.9230	362.4	136	0.6174	0.0930	0.5244	Kesterite	CZTS
50.285	1.8130	365.1	137	0.6174	0.0900	0.5274	Kesterite	
51.050	1.7876	84.0	7	0.1372	0.0900	0.0472	Kesterite	
69.061	1.3589	339.2	71	0.3430	0.0936	0.2494	Kesterite	

2theta [deg]	d [A]	I/I0	Counts	FWHM total	FWHM instr.	FWHM sample	Correlated phase(s)	
16.395	5.4023	34.6	50	0.1372	0.0900	0.0472	Kesterite	
23.134	3.8416	107.7	386	0.3430	0.0900	0.2530	Kesterite	
28.508	3.1285	354.6	2288	0.6174	0.0900	0.5274	Kesterite	
29.601	3.0154	201.1	1009	0.4802	0.0900	0.3902	Kesterite	
32.879	2.7219	38.1	136	0.3430	0.0860	0.2570	Kesterite	
37.888	2.3727	25.3	55	0.2058	0.0815	0.1243	Kesterite	
40.620	2.2192	30.3	65	0.2058	0.0911	0.1147	Kesterite	CZTSSeTe
44.810	2.0210	181.6	391	0.2058	0.0975	0.1083	Kesterite	
47.360	1.9179	672.9	2895	0.4116	0.0928	0.3188	Kesterite	
56.103	1.6380	272.4	2930	1.0290	0.0900	0.9390	Kesterite	

2theta [deg]	d [A]	I/I0	Counts	FWHM total	FWHM instr.	FWHM sample	Correlated phase(s)	
23.077	3.8511	301.6	44	0.2058	0.0900	0.1158	Kesterite	
28.466	3.1330	147.1	36	0.3430	0.0900	0.2530	Kesterite	
29.596	3.0159	283.1	28	0.1372	0.0900	0.0472	Kesterite	
32.899	2.7202	261.2	26	0.1372	0.0860	0.0512	Kesterite	
40.635	2.2185	327.6	48	0.2058	0.0911	0.1147	Kesterite	CZTSTe
47.241	1.9225	327.0	32	0.1372	0.0930	0.0442	Kesterite	
50.978	1.7900	171.8	25	0.2058	0.0900	0.1158	Kesterite	
53.238	1.7192	179.6	35	0.2744	0.0900	0.1844	Kesterite	

Selected Area Electron Diffraction (SAED) was obtained from HRTEM which revealed and confirmed that the nanoparticles were crystalline. The planes found in XRD plot above was also observed in the SAED image obtained, which confirms the kesterite phase composition of the synthesized nanoparticles [22-30]. The images obtained from SAED analysis, shows

that CZTSSeTe was more crystalline than CZTS and CZTSTe in that order. The high crystallinity displayed by CZTSSeTe did not translate into a high electroactivity which was the expected outcome although it gave a improved photocatalytic property [31] as seen from the discussions of electrochemistry of the nanoparticles and their optical properties which leads to a possible correlation between high crystallinity and electroactivity as the least crystalline of the nanoparticles (CZTSTe) displayed a better electroactivity when compared to CZTSSeTe and CZTS which were more crystalline.

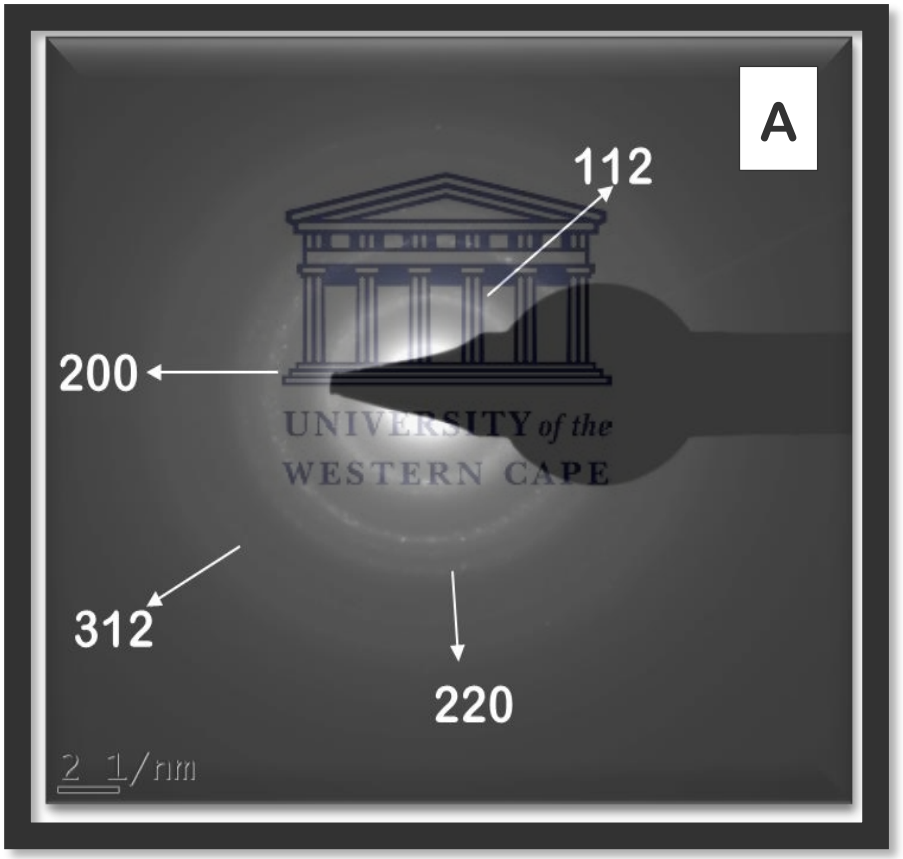

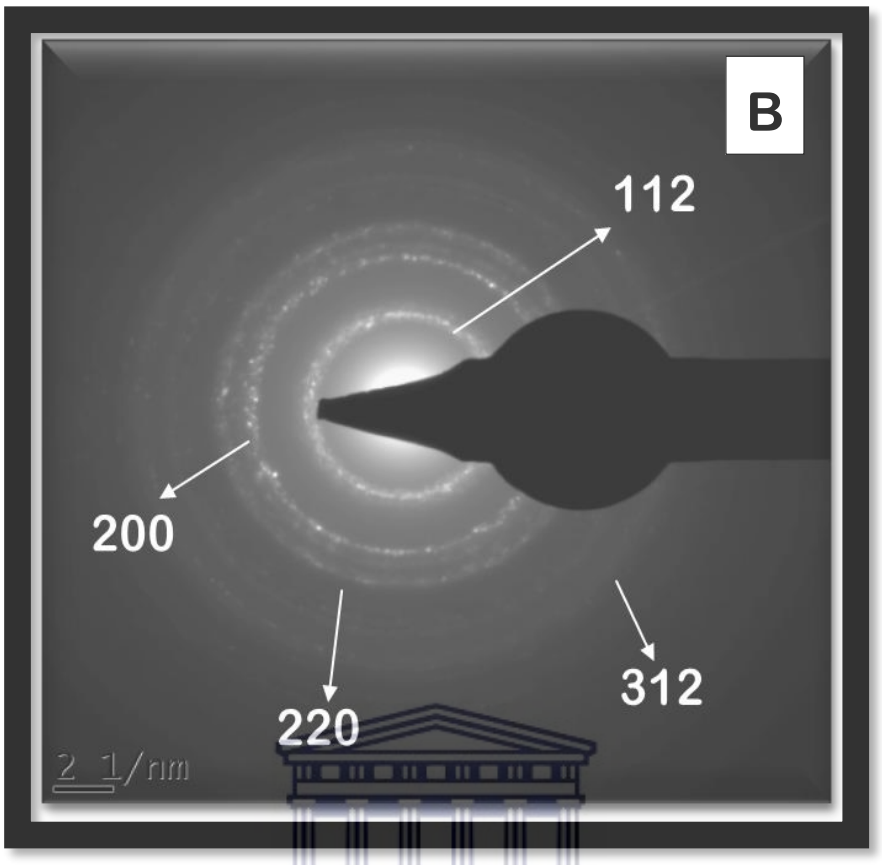

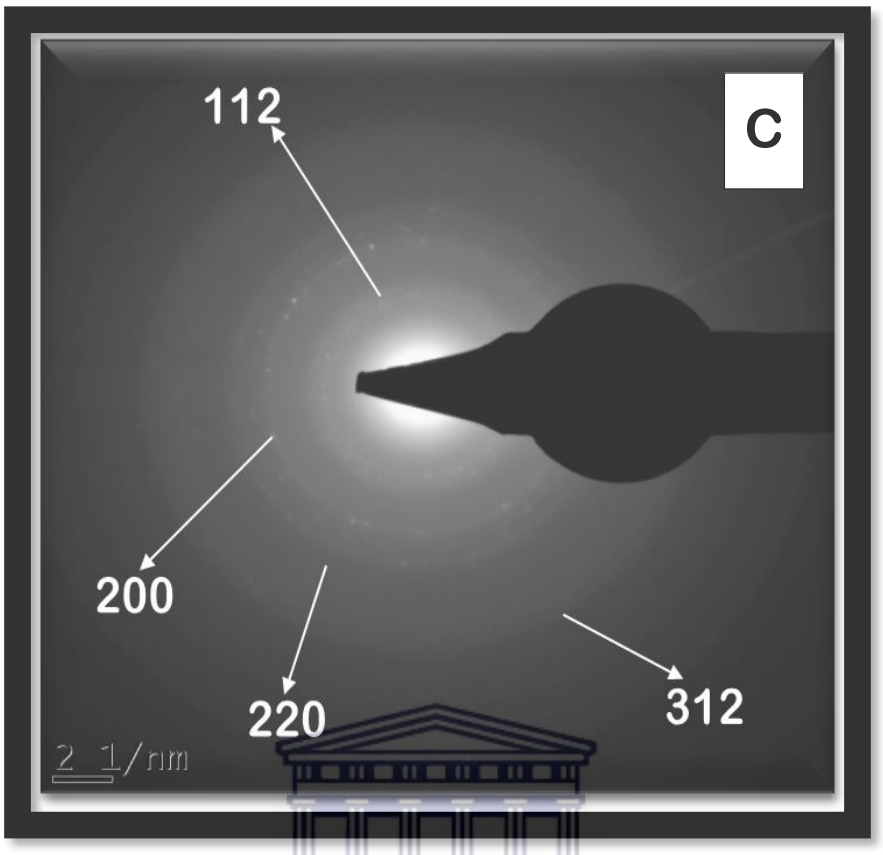

Figure 4. 7: SAED micrograph of the synthesized nanoparticles of (A) CZTS (B) CZTSSeTe and (C) CZTSTe confirming the hkl miller index (planes) found in XRD.

The lattice fringe images obtained for the synthesized nanoparticles further confirms that the nanoparticles were crystalline and the d-spacing value of the lattice fringes was evaluated and assigned with the corresponding plane (miller index) as can be seen in figure 4.8 below

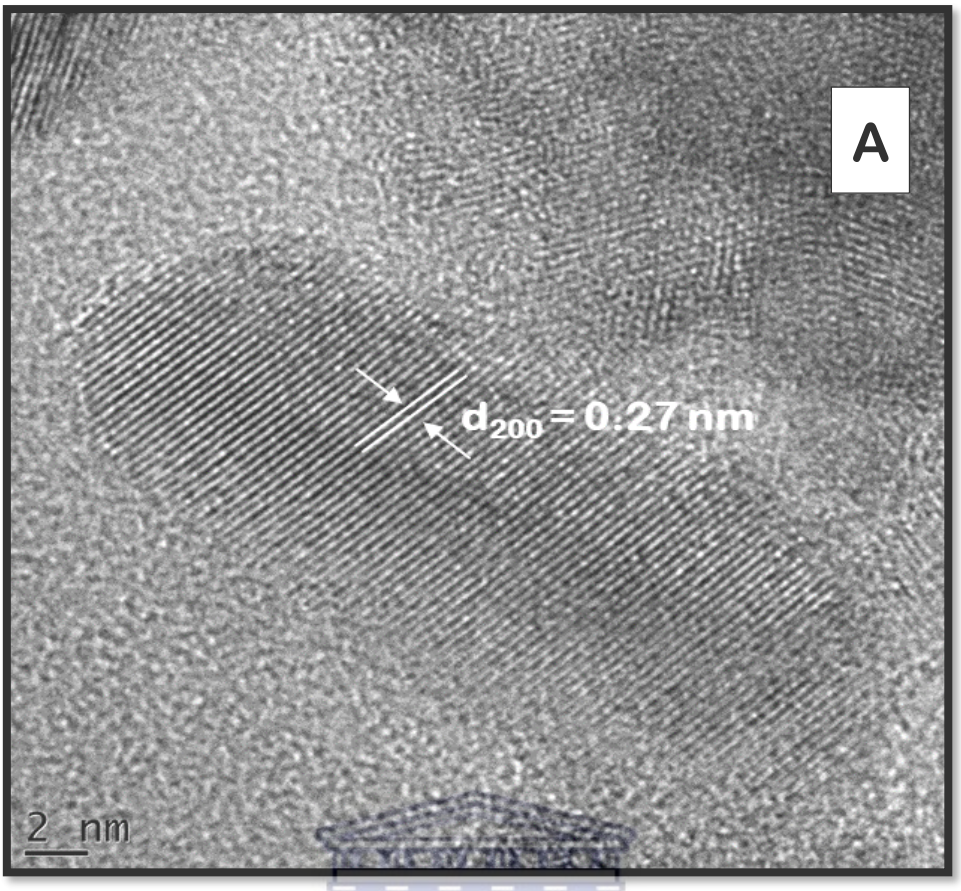

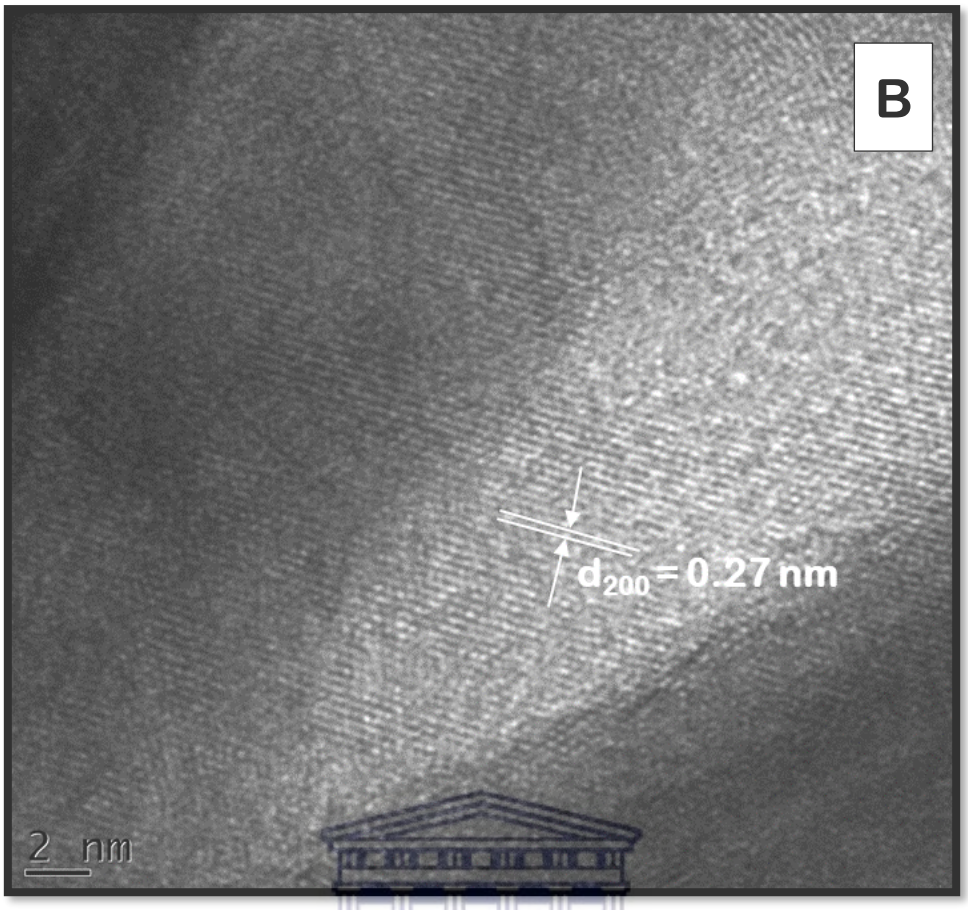

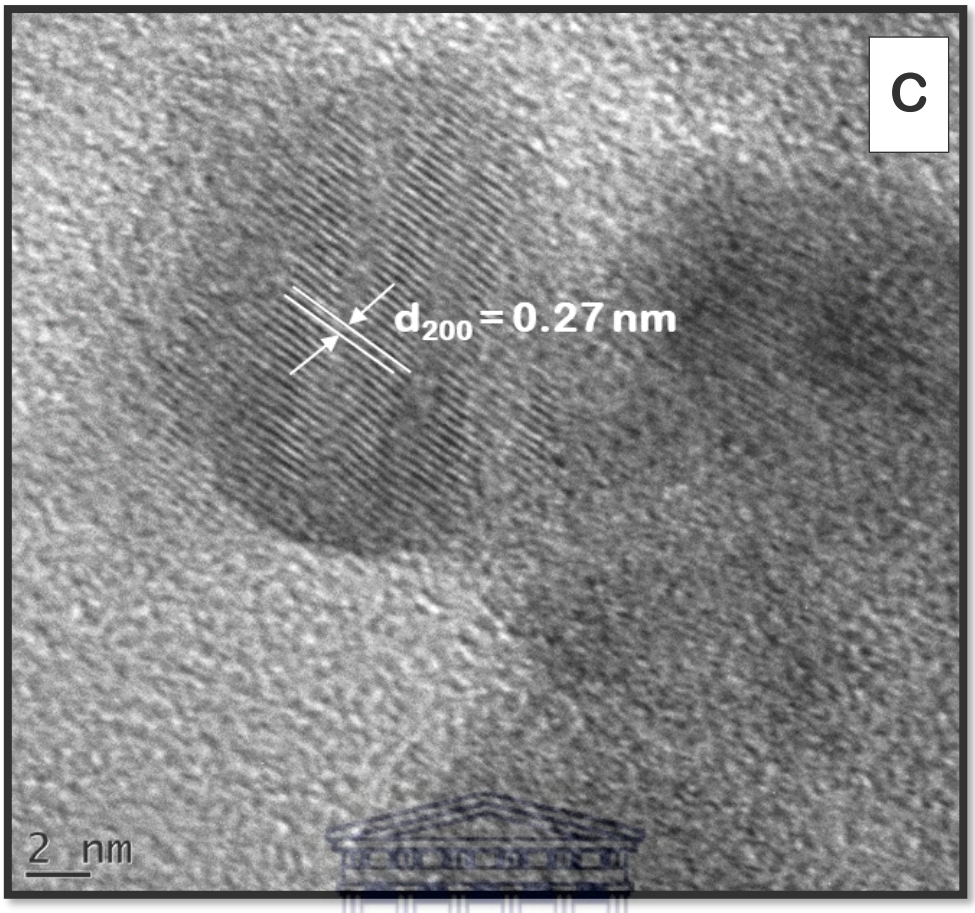

Figure 4. 8: HR-TEM image showing the lattice fringe and d-spacing value of the lattice fringe indicating the plane with the d-space value for the synthesized nanoparticles of (A) CZTS, (B) CZTSSeTe and (C) CZTSTe.

The d-spacing obtained for the three samples from the analyzed image gave a value of 0.27 nm which corresponds to the calculated d-spacing value for the 200 planes.

ENDEAVOR, a software by crystal-impact was used to simulate the crystal structure of the synthesized nanoparticles from XRD data. The parameter used in simulating the crystal structure for each of the synthesized nanoparticles is summarized below as determined from the crystal impact software:

#not indexed	FoM	#peaks	V/V1	a	b	c	alpha	beta	gamma	V	Progr.	
1	17	13	1	5.43682	5.43682	10.8388	90	90	90	320.38	Treor90	CZTS

#not indexed	FoM	#peaks	V/V1	a	b	c	alpha	beta	gamma	V	Progr.	
1	18	14	1	5.4354	5.4354	10.8391	90	90	90	320.22	Treor90	CZTSSeTe

#not indexed	FoM	#peaks	V/V1	a	b	c	alpha	beta	gamma	V	Progr.	
1	19	13	1	5.44221	5.44221	10.8578	90	90	90	321.58	Treor90	CZTSTe

The simulation obtained agreed with the conventional tetragonal structure of the kesterite phase (see figure 2.12). The simulations obtained for the synthesized nanoparticles are shown in figure 4.9 below:

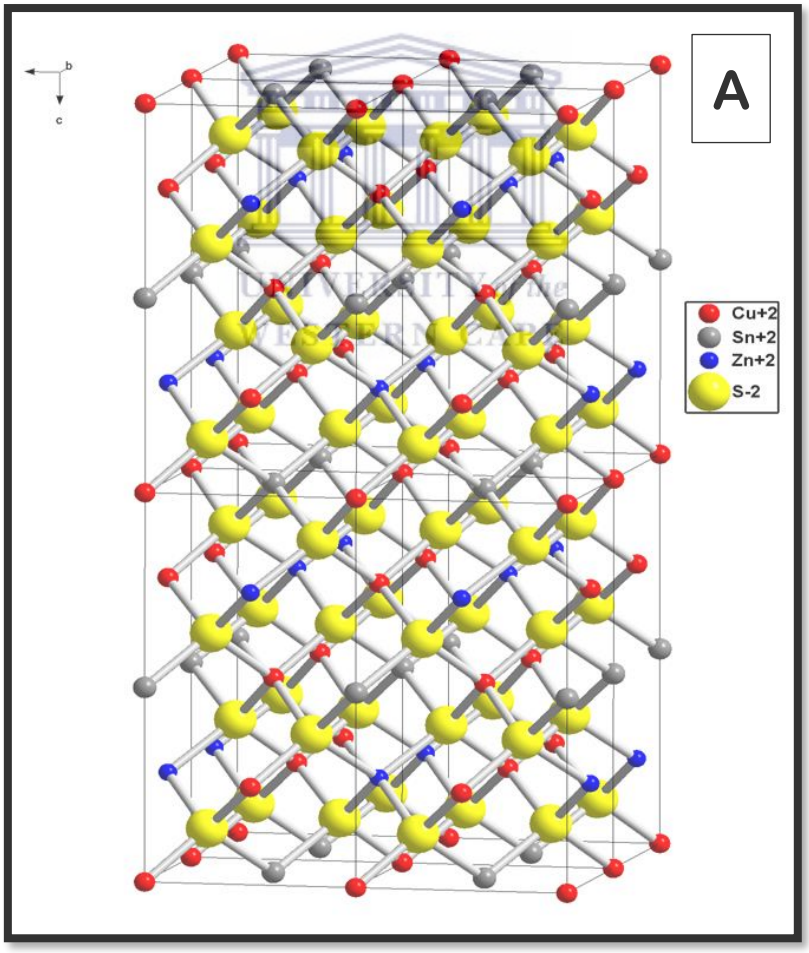

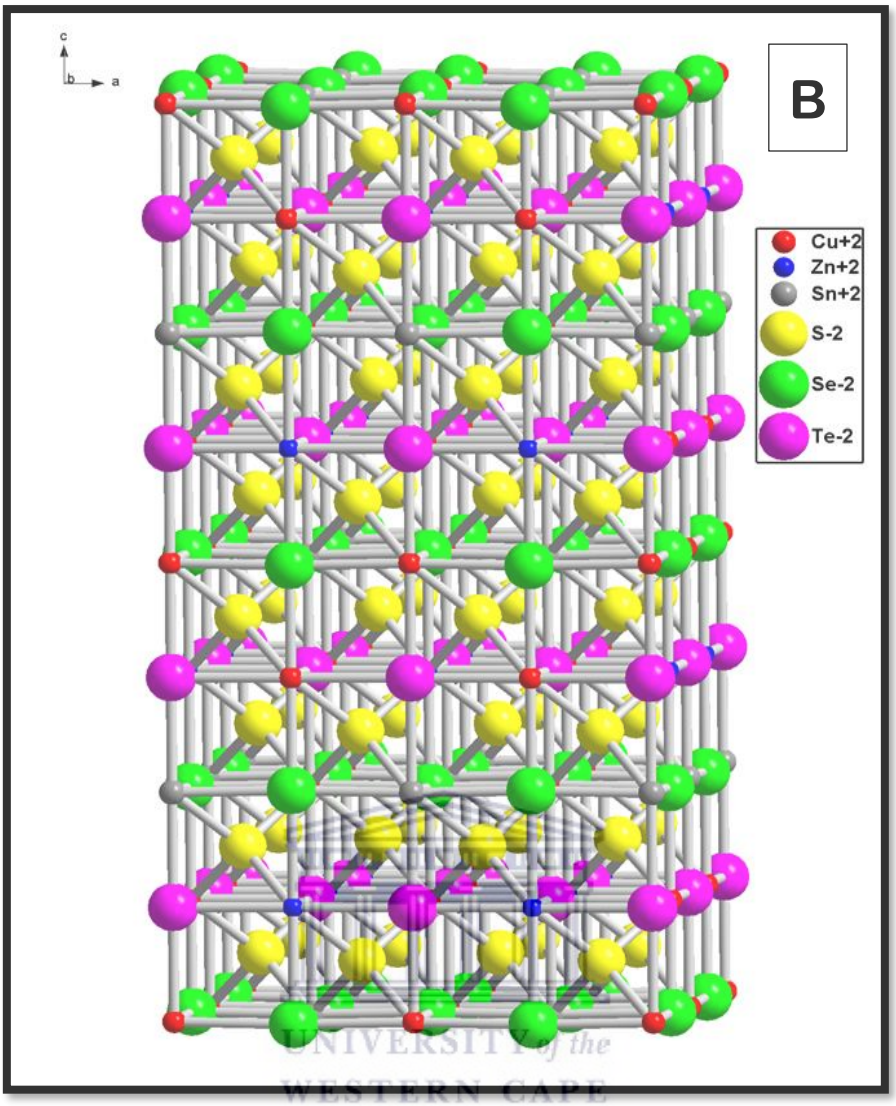

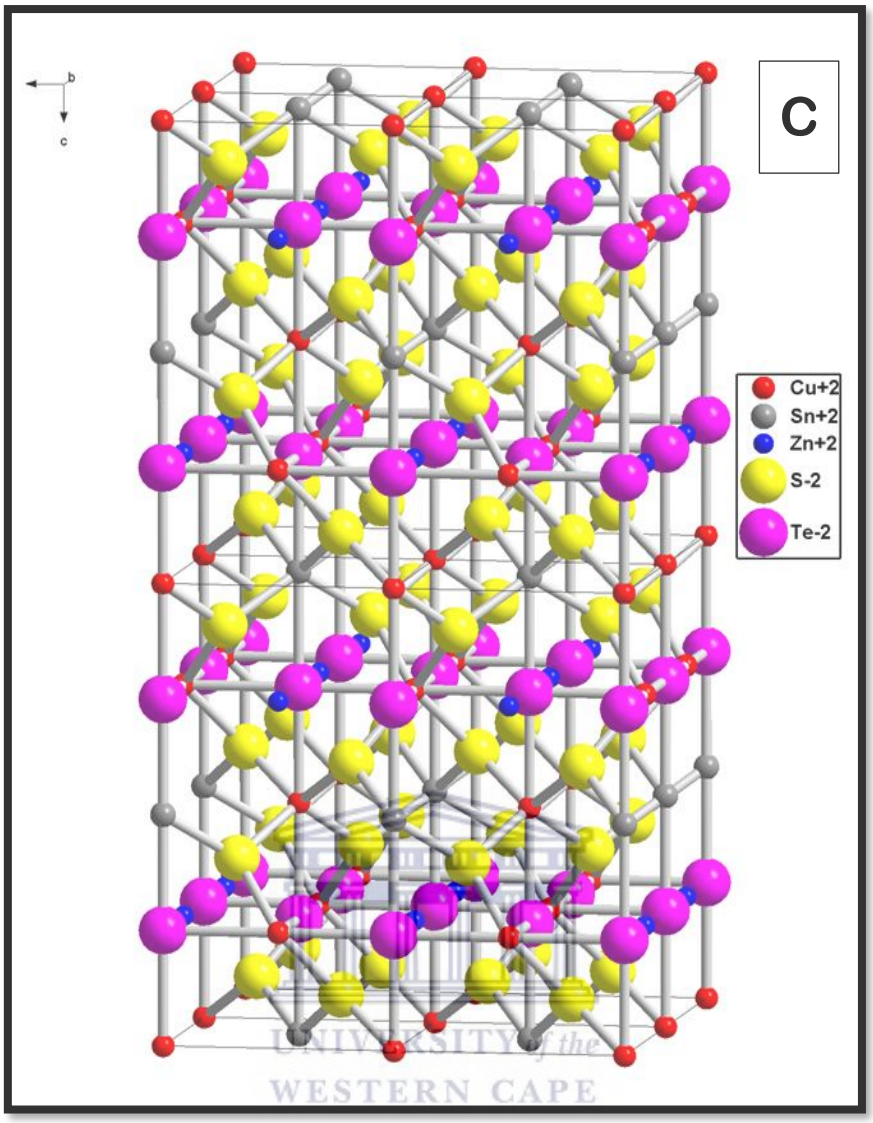

Figure 4. 9: ENDEAVOR software simulation of the XRD data of the synthesized nanoparticles of (A) CZTS (B) CZTSSeTe and (C) CZTSTe showing the tetragonal kesterite crystal structure.

In order to confirm that the kesterite phase was present in the synthesized nanoparticles, Raman Spectroscopy was carried out. The instrument used for the analysis is Horiba Jobin Yvon LabRam Xplora system equipped with an excitation wavelength of 633 nm. The Raman spectra of the as-synthesized nanoparticles showed the presence of the kesterite phase. In CZTS there was presence of some secondary phases (SnS) and (ZnS) as seen in figure 4.10 below, but the peak of CZTS phase although shifted to the right of its dominant wavenumber

of 338 cm^{-1} [32, 33] and it was more pronounced than the secondary phases. The wavenumber to which this peak was shifted to does not correspond to any of the secondary phases found in CZTS nanoparticles and so could only be CZTS peak. This shift can be attributed to the surface bonding of DEG to the particle surface of CZTS. The peaks observed for CZTSSeTe corresponds to the peaks expected of CZTS, CZTSe and CZTTe from literature investigations [22,34]. These peaks confirm the presence of the kesterite phase in CZTSSeTe nanoparticle. The peaks of CZTSTe also validate the presence of kesterite phase in the synthesized nanoparticle. The presence of the secondary phases (ZnS and SnS) doesn't pose any much troubles as earlier stated can be easily removed by annealing during device fabrication [2].

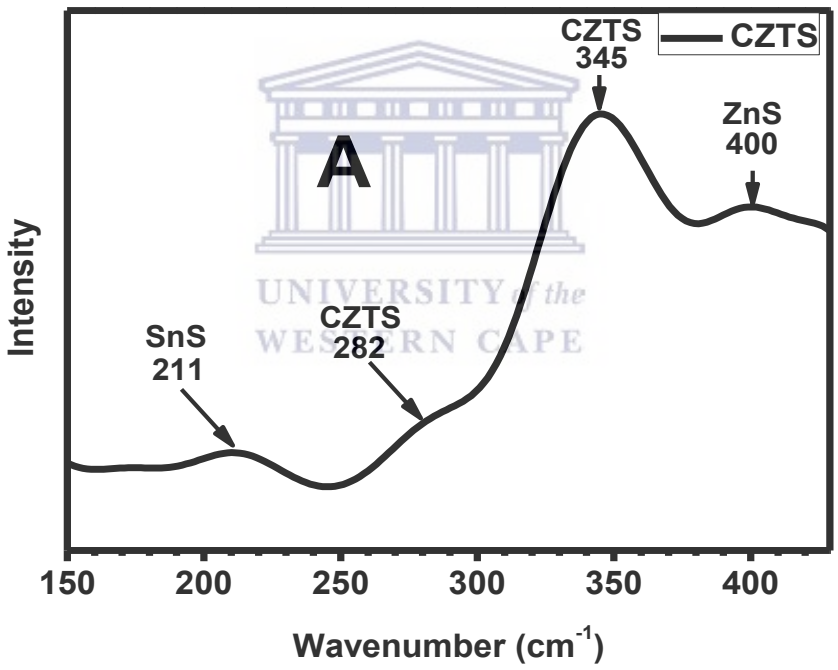

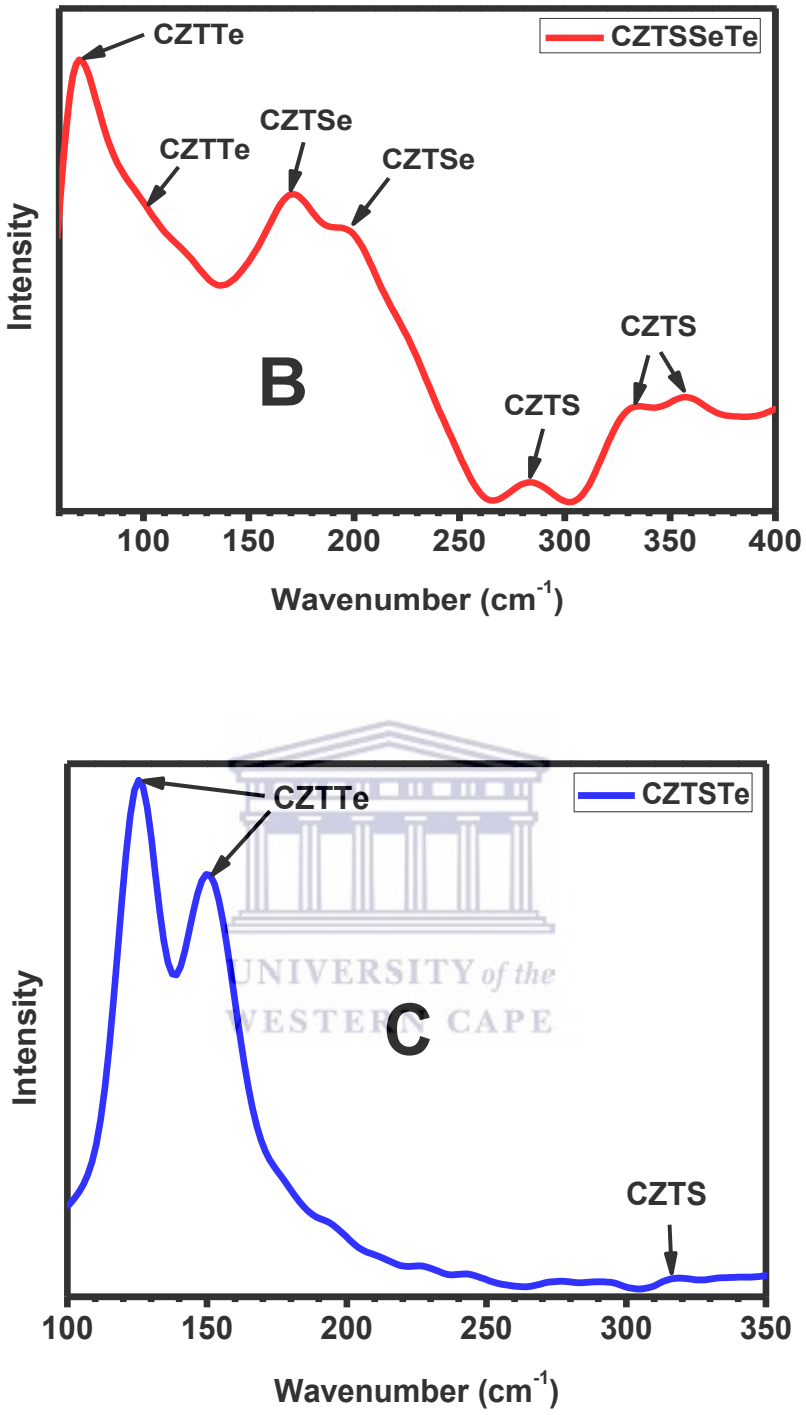

Figure 4. 10: Raman Spectra of synthesized nanoparticles of (A) CZTS, (B) CZTSSeTe and (C) CZTSTe showing the presence of the kesterite phase in the crystal structure of the nanomaterials.

4.5 ELEMENTAL COMPOSITION

The elemental composition of the as-synthesized nanoparticles was evaluated using Energy Dispersive X-ray spectroscopy (EDX) as shown in figure 4.11. The instrument used is the EDS analyzer coupled into the High-Resolution Transmission Electron Microscope used for TEM analysis.

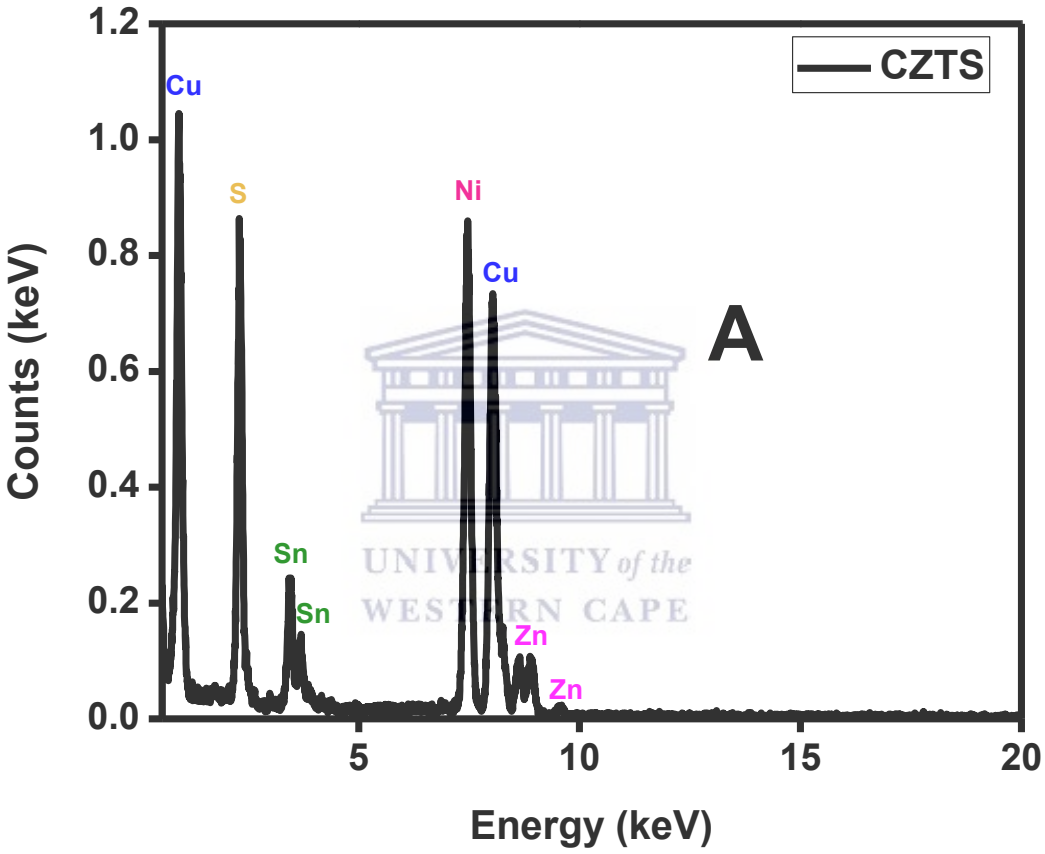

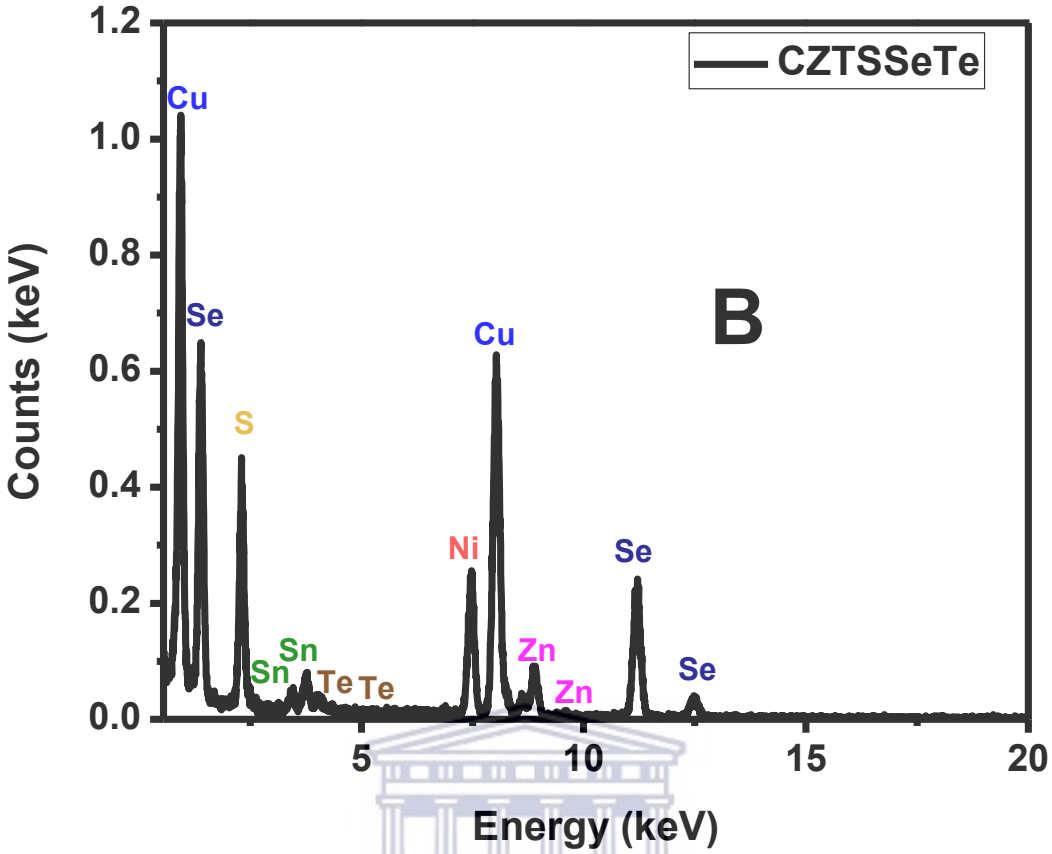

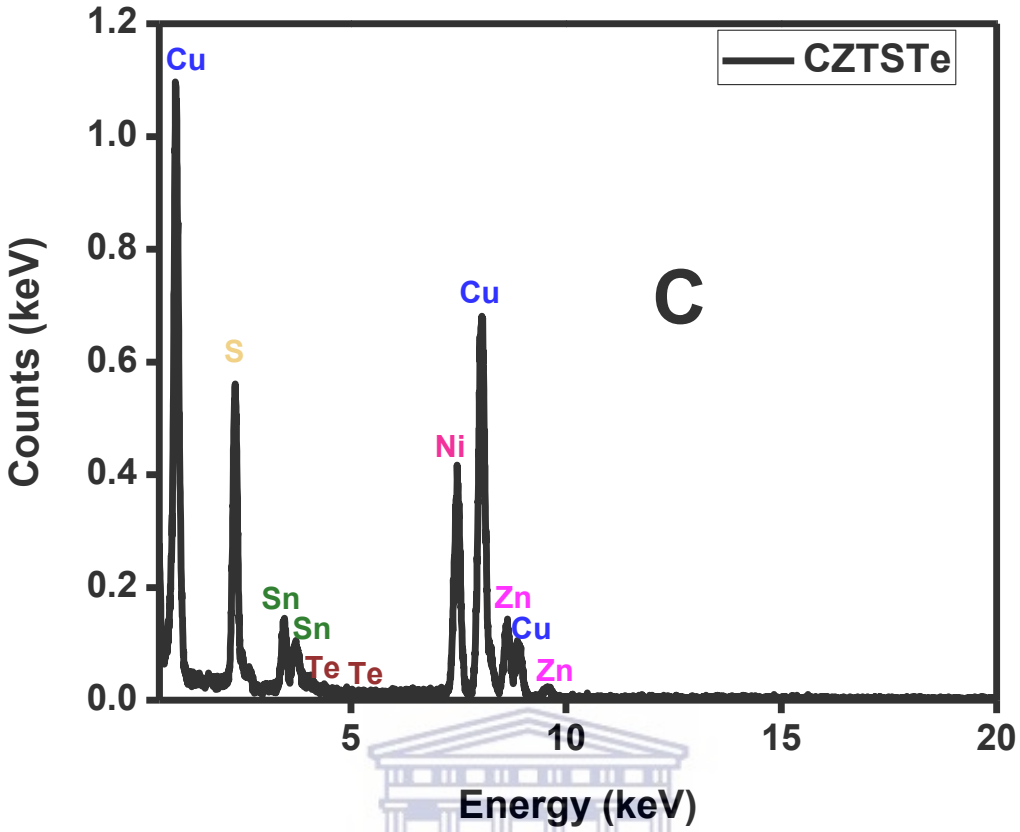

Figure 4. 11: EDS showing the chemical composition of the synthesized nanoparticles of (A) CZTS, (B) CZTSSeTe and (C) CZTSTe.

The EDS spectra of the synthesized showed all the elements expected for the nanoparticles. CZTS spectra shows the presence of copper, zinc, tin and sulfur. CZTSSeTe spectra shows the presence of copper, zinc, tin, sulfur, selenium and tellurium. CZTSTe spectra also showed the presence of copper, zinc, tin, sulfur and tellurium [4-8]. Nickel grid was used for TEM analysis and is depicted by the peak assigned with Ni.

4.6 SIZE DISTRIBUTION

The size distribution of the synthesized nanoparticles was studied and evaluated. The particle size was evaluated using SAXS and the crystal size was evaluated from XRD data of the synthesized nanoparticles. Given the fact that the TEM images obtained were not clear enough and as such was not used to calculate the size of the nanoparticles, SAXS size distribution comes in handy [11]. The summary of the size distribution for the synthesized nanoparticles is given by the SAXS plot of the size distribution in figure 4.12.

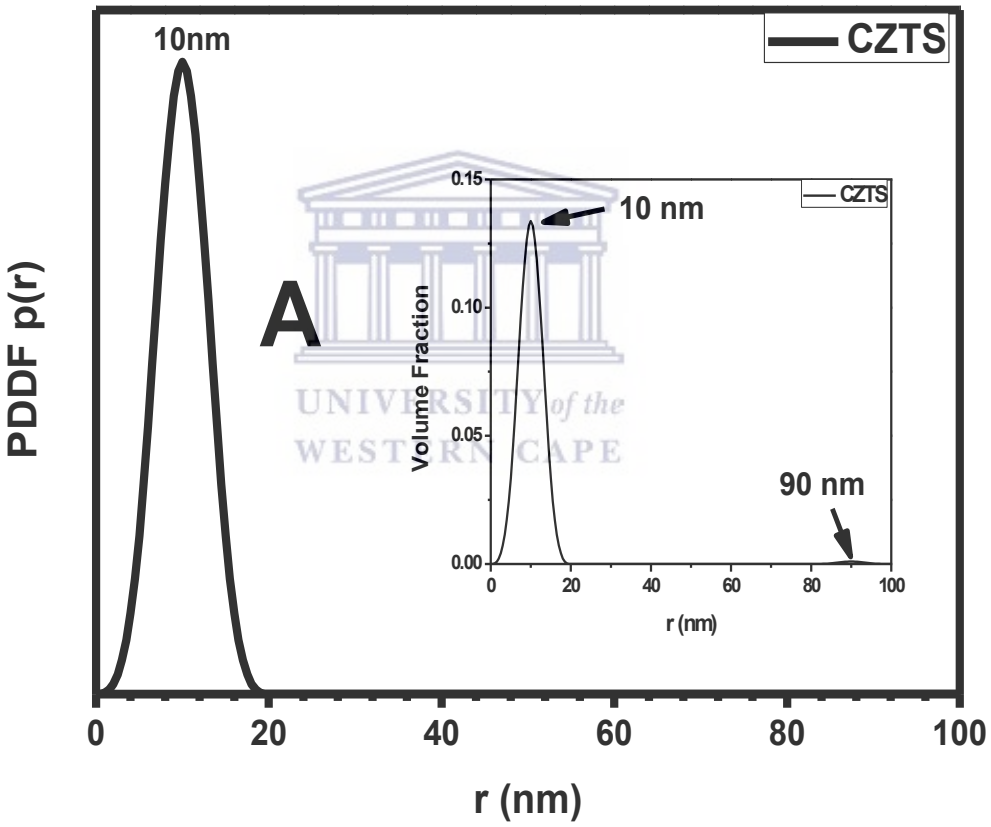

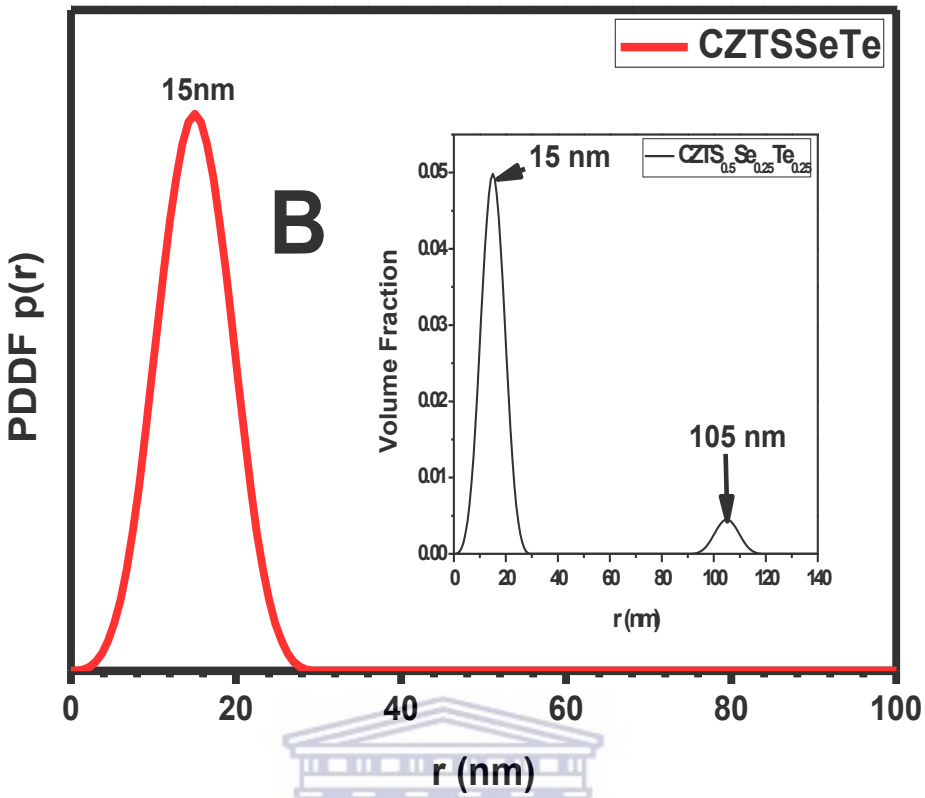

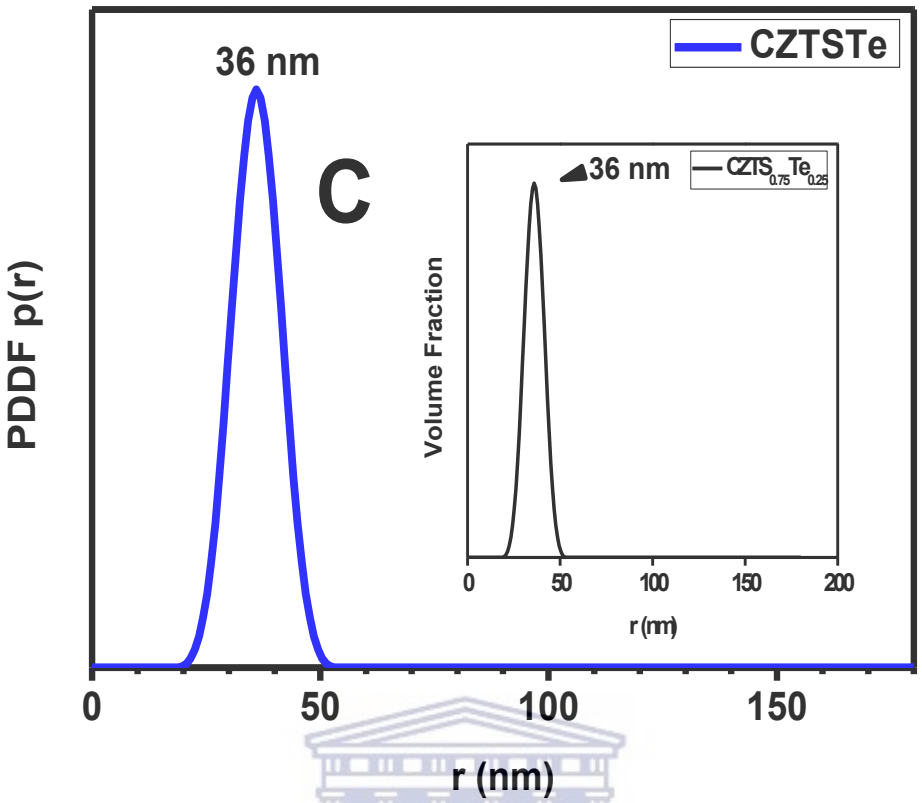

Figure 4. 12: SAXS plot of the particle size distribution of the synthesized nanoparticles of (A) CZTS, (B) CZTSSeTe and (C) CZTSTe.

The particle size distribution obtained from SAXS plot shows that CZTS has a mean particle size of 10 nm with a big particle size of 90 nm which is attributed to the agglomeration which can be seen in the SAXS shape plot and TEM micrograph earlier shown in figures 4.5 and 4.4 respectively. The CZTSSeTe plot shows a narrow mean particle size distribution of 15 nm with a wide particle size distribution of 105 nm also attributed to agglomeration of the nanoparticles evidenced in the SAXS shape plot and TEM micrograph. The plot of CZTSTe showed a mean size distribution of 36 nm with no additional size distribution although, the SAXS shape plot and TEM micrograph revealed presence of agglomeration of the nanoparticles.

XRD can also be useful in size determination [35]. This is achieved by calculating the crystal size of the synthesized nanoparticles and compare the size obtained with that of the SAXS size distribution. The crystal size obtained for the synthesized nanoparticles is summarized in table 4.2 below and the plot of the phase used is shown in figure 4.13.

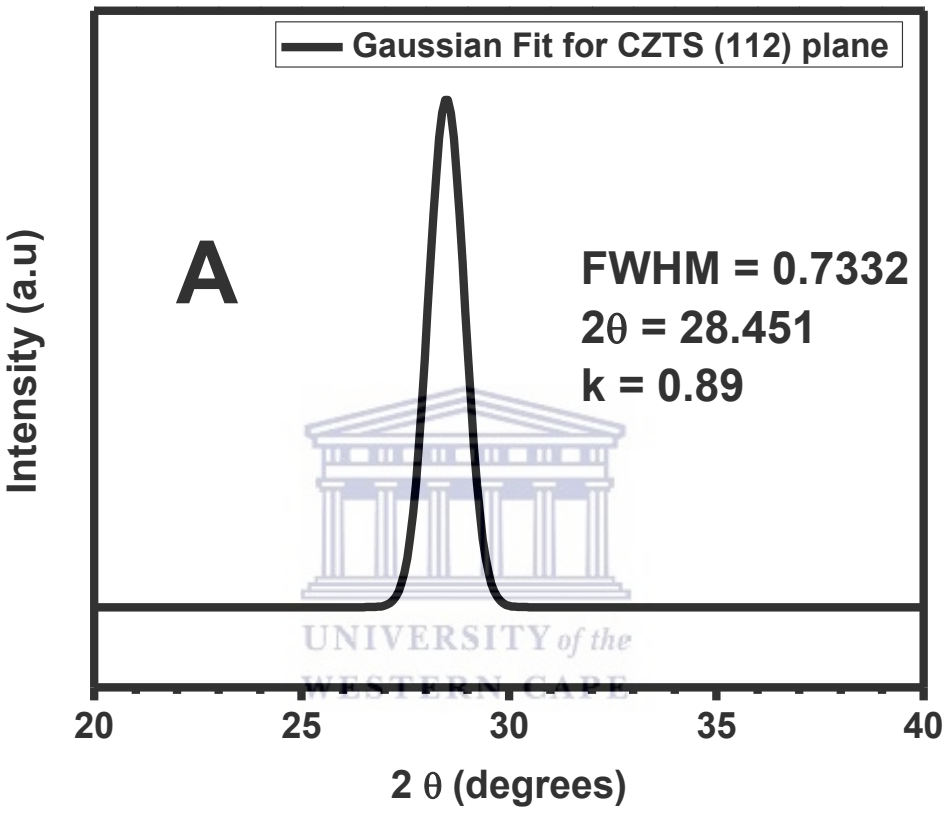

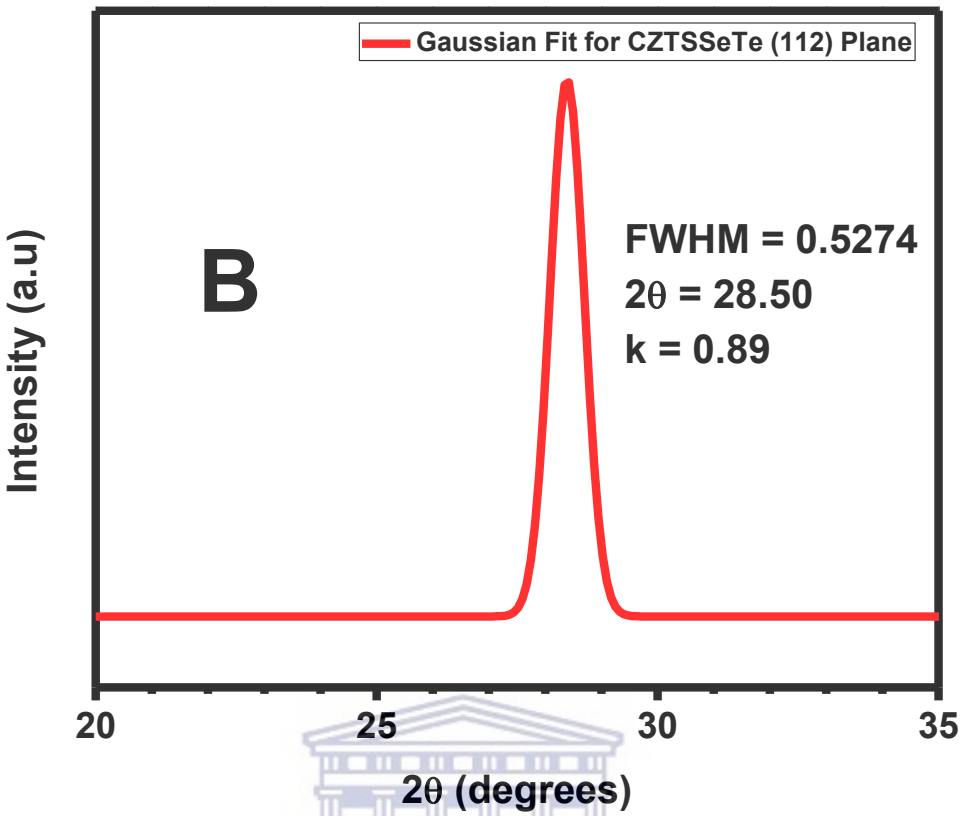

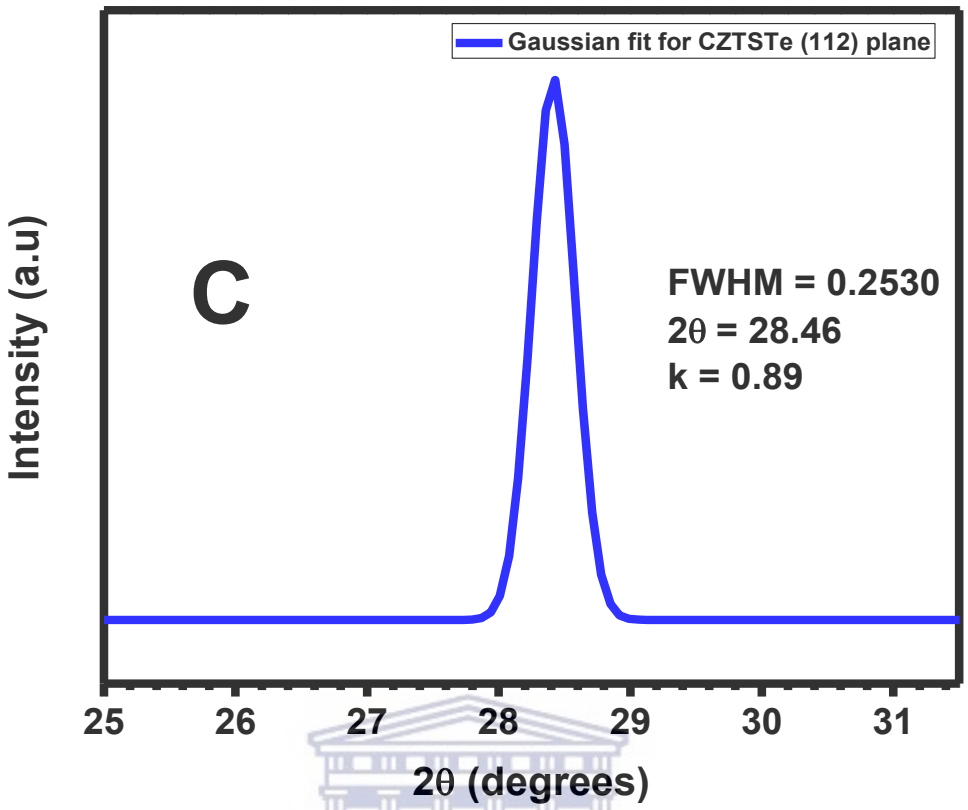

Figure 4. 13: Gaussian Fit plot of XRD peak of (112) plane used to extrapolate the FWHM for the synthesized nanoparticles of (A) CZTS, (B) CZTSSeTe and (C) CZTSTe which is used to calculate the crystal size of the nanoparticles.

In order to calculate the crystal size of the as-synthesized nanoparticles, the Debye-Scherrer equation was used which is given as:

$$B(2\theta) = \frac{k\lambda}{l\cos\theta} \qquad \textbf{(4.1)}$$

where $B(2\theta)$ is full width at half maximum, k is Scherrer constant which can take values from 0.89 to 1, for this calculation I chose to use 0.89, λ is the wavelength of the x-ray which has a value of 1.54058, and θ is the angle in radians and l is the crystallite size usually in Angstroms but can be converted to nm. Also, the FWHM value is converted to radians. The plane calculated was the (112) which had the most intense peak. Table 4.2 below gives the various

values used for the calculation of the crystallite size of the as-synthesized nanoparticles and subsequently the crystal size gotten for each of the nanoparticles.

Table 4 2: Various parameters used for the calculation of the crystal size of the synthesized nanoparticles.

SAMPLE	2-θ	θ (Rad)	FWHM	FWHM (Rad)	k-value	Wavelength	Crystal size (nm)
CZTS	28.45	0.2483	0.7332	0.0130	0.89	1.54058	11
CZTSSeTe	28.50	0.2487	0.5274	0.00920	0.89	1.54058	15
CZTSTe	28.47	0.2484	0.2530	0.00442	0.89	1.54058	31

From the table above, the crystal size for CZTS is 11 nm, CZTSSeTe is 15 nm and CZTSTe is 31 nm. These values agree with the values obtained from SAXS plot of the particle size distribution of the synthesized nanoparticles which had value for CZTS as 10 nm, CZTSSeTe as 15 nm and CZTSTe as 36 nm.

4.7 THERMOSTABILITY

The thermal stability of the synthesized nanoparticles was investigated by Thermogravimetry analysis. The instrument used for the analysis PerkinElmer Pyriss simultaneous TGA/DTA Analyzer (TG-4000). The temperature range used for the analysis is from 30 ˚C to 600 ˚C under nitrogen gas atmosphere at a heating rate of 10 ˚C min^{-1}. Results are shown in figure 4.14.

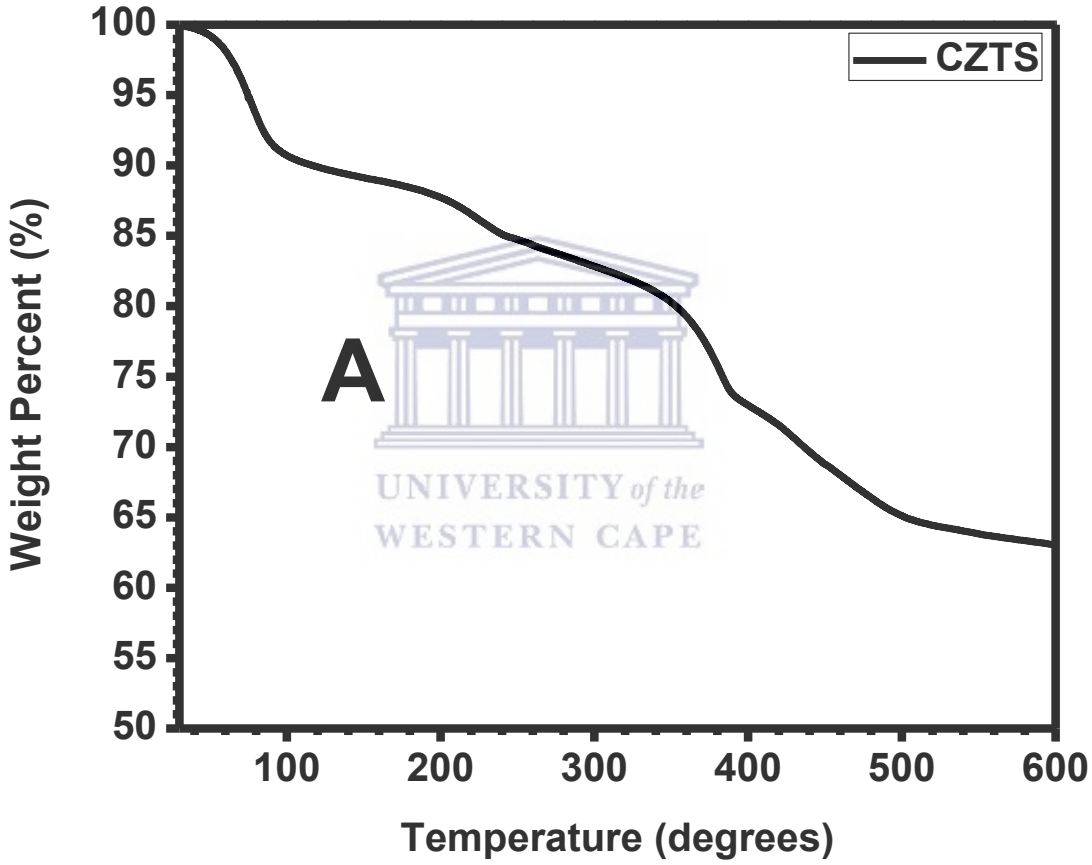

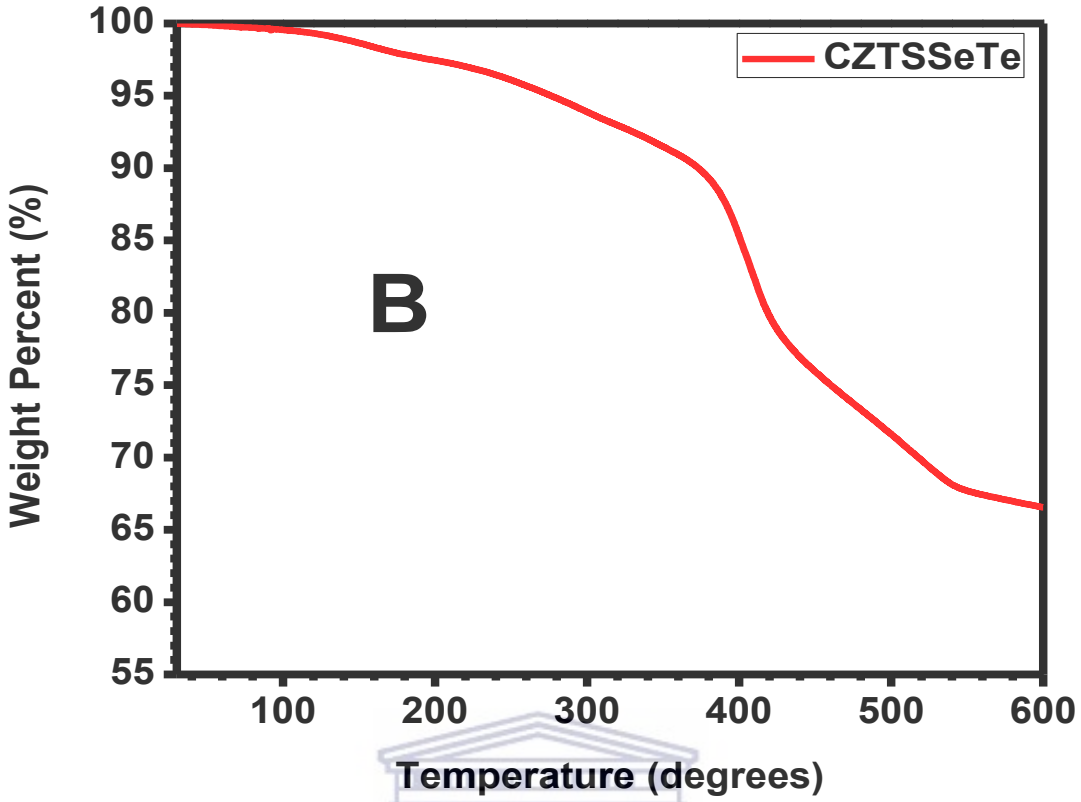

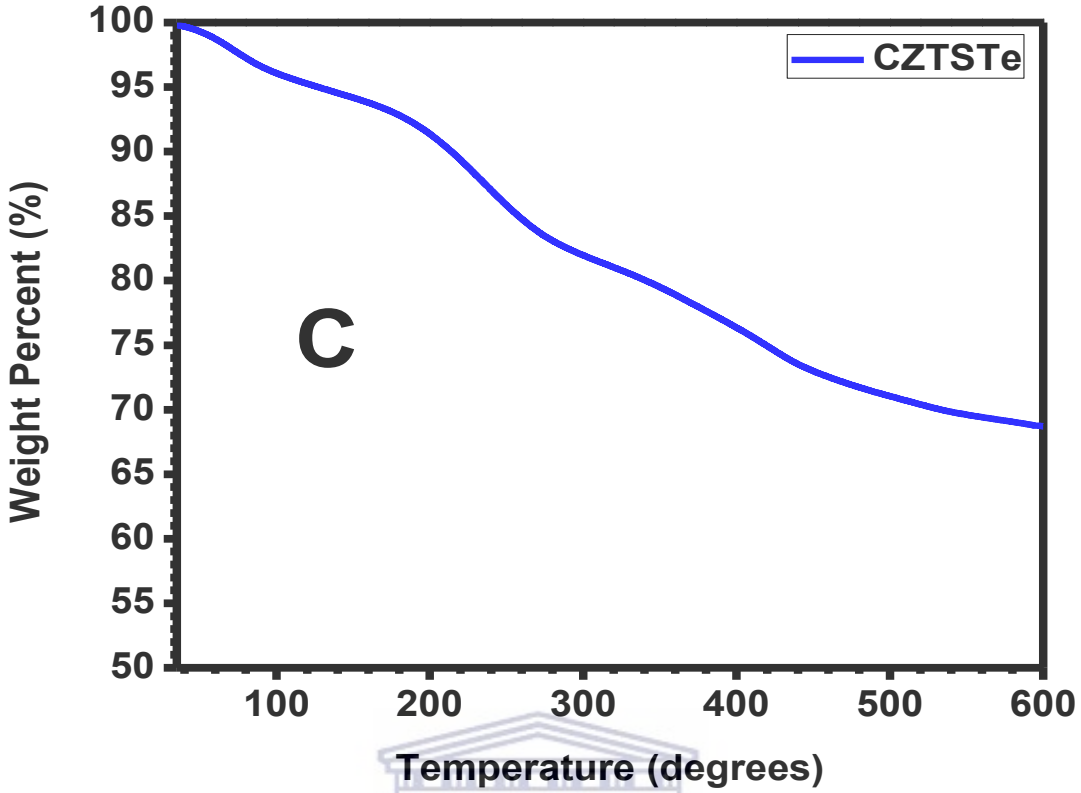

Figure 4. 14: Thermogram of the synthesized nanoparticles of (A) CZTS, (B) CZTSSeTe and (C) CZTSTe observed from temperature range of 30 ºC to 600 ºC

The initial weight loss of about 9% for CZTS, 1% for CZTSSeTe and 4% for CZTSTe at about 100 ˚C can be attributed to an evaporation of water. Further weight loss of 4% for CZTS, 2% for CZTSSeTe and 5% for CZTSTe at about 200 ˚C can be ascribed to the loss of Isopropanol or DEG from the nanoparticles. Further heating to temperature up to 400 ˚C with weight loss of 14% in CZTS, 7% in CZTSSeTe and 13% in CZTSTe can be ascribed to the loss of chalcogens that do not actually incorporate into the lattice of the synthesized nanoparticles [36-38]. The weight loss of about 9% in CZTS, 22% in CZTSSeTe and 8% in CZTSTe at temperatures above 400 ˚C results in the loss of Sn through the sublimation of SnS [39, 40].

4.8 OPTICAL ABSORPTION

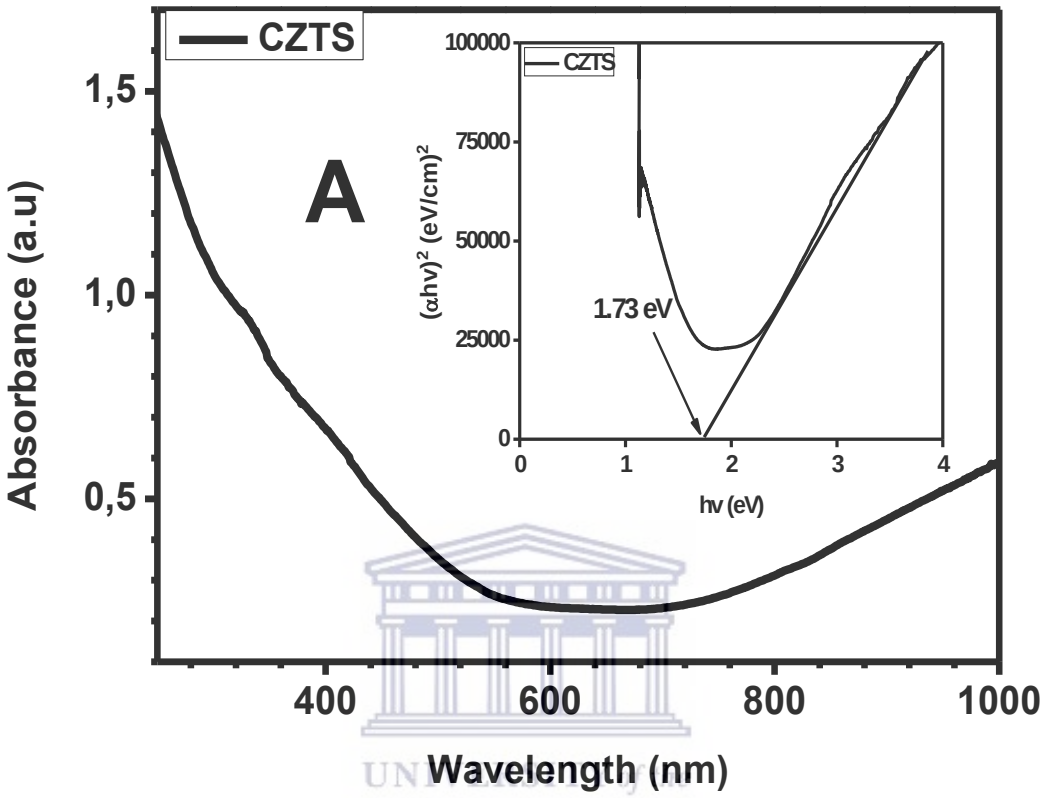

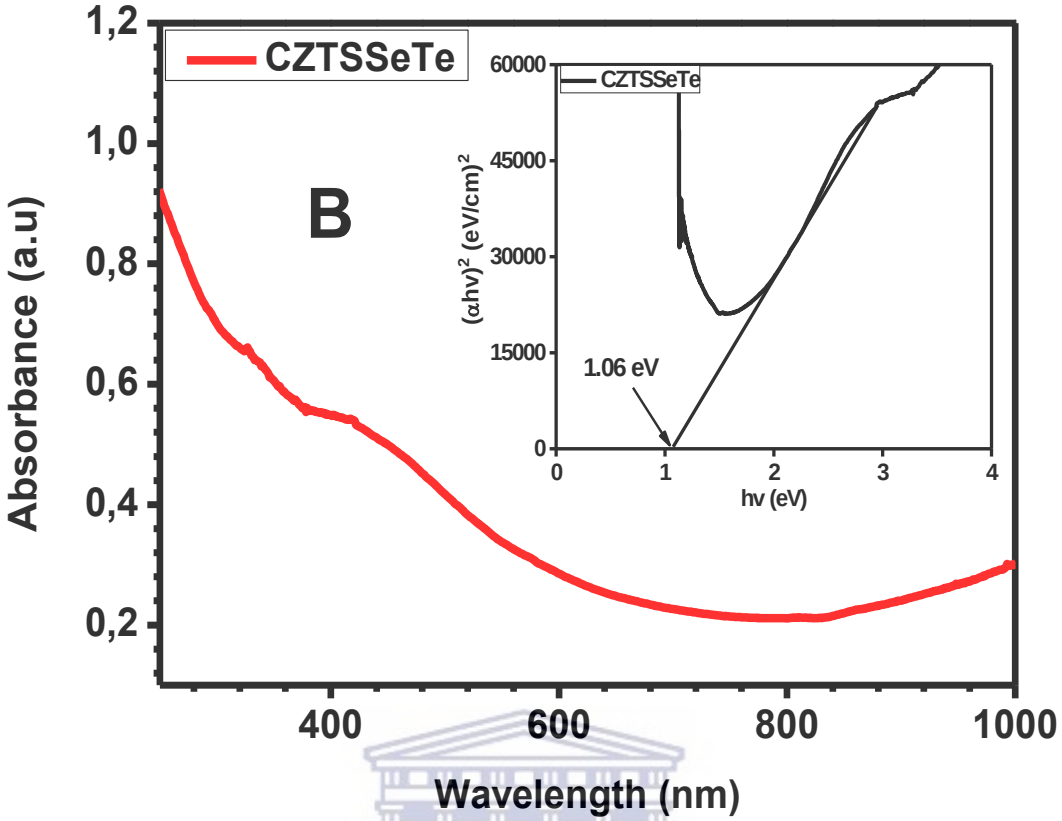

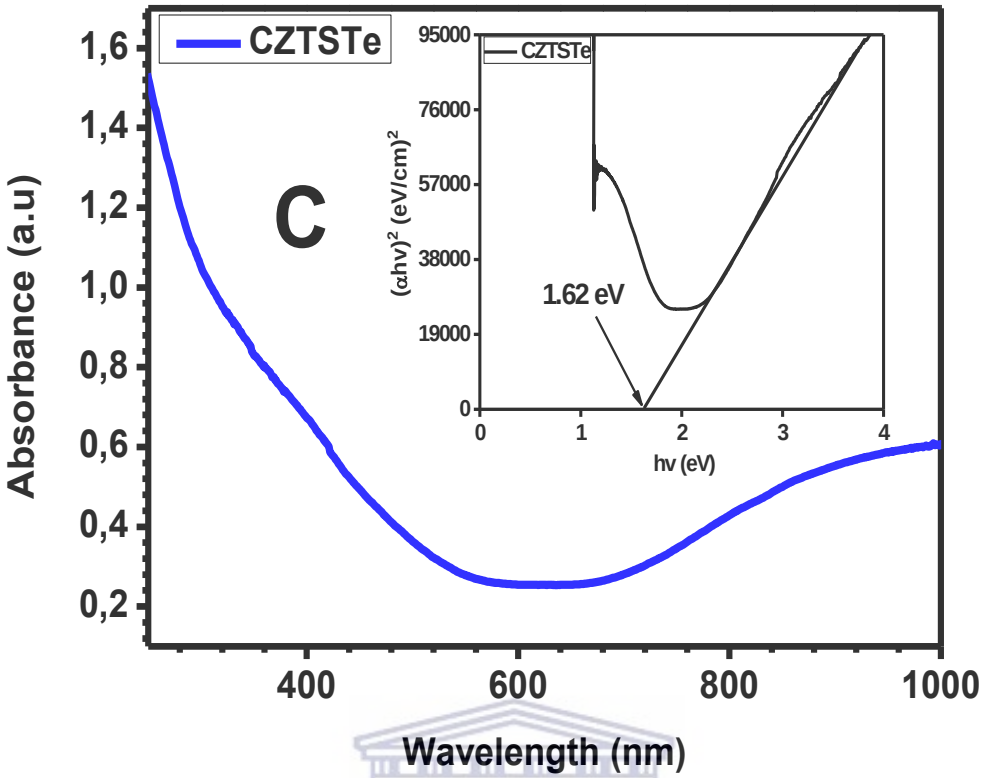

Figure 4. 15: UV-Vis spectra of the synthesized nanoparticles of (A) CZTS, (B) CZTSSeTe and (C) CZTSTe showing the absorptions of the nanoparticles and inlet of the Tauc plot of the band-gap of the nanoparticles.

The optical absorption spectra of the synthesized nanoparticles of CZTS, CZTSSeTe and CZTSTe were measured and found that the nanoparticles show high absorbance of light in the visible region. Kesterite is considered as direct band gap semiconductor and the band gap was calculated from classical relation [41-42]. For direct band gap compounds, the band gap may be calculated by plotting the product of photon energy and absorbance squared versus photon energy from the absorbance spectrum, or $(\alpha hv)^2$ versus hv, and finding the intercept of the abscissa. The inset plots in the spectra of the synthesized nanoparticles in figure 4.15 shows the $(\alpha hv)^2$ versus hv plot. The band gap which was extrapolation of the straight line to zero absorption for the synthesized nanoparticles is summarized in the table 4.3 below. The band

gap obtained showed that the incorporation of tellurium to kesterite nanomaterial narrowed the band gap which has been investigated to give a better power conversion efficiency of the solar cell. It has also been found that a high amount of Sulphur content in kesterite increases the band-gap value which can affect the PCE of the solar cell [43]. The values of the band-gap obtained from the Tauc plot are quite close to the optimum value of semiconductor band gap required for highly efficient solar cell [44]. The narrower band gap obtained by the addition of tellurium to the nanoparticles is expected as tellurium is a better semiconductor element when compared to sulfur and selenium in chalcogen family [45,46]. A much narrower band gap seen in CZTSSeTe can be attributed to the combination of selenium and tellurium which are better semiconductors than sulfur. As earlier reported [43], addition of selenium reduces the bandgap of the kesterite nanoparticles. This trend was observed in the case of CZTSSeTe since selenium is a constituent of the nanoparticle. This trend was also reported for CZTSTe which showed a reduced bandgap. These reduced bandgaps seen with addition of tellurium in the kesterite nanoparticles is a welcomed outcome. These direct band-gaps obtained for the synthesized nanoparticles makes them suitable for photovoltaic cell application.

Table 4 3: The values of the band-gap of the synthesized nanoparticles extrapolated from Tauc-plot.

SAMPLE	BAND-GAP (eV)
CZTS	1.73
CZTSSeTe	1.06
CZTSTe	1.62

4.9 ELECTROCHEMISTRY OF THE NANOPARTICLES

The electrochemical properties of the synthesized nanoparticles were investigated by the following electrochemical techniques:

- Cyclic voltammetry (CV)
- Square Wave voltammetry (SWV)
- Electrochemical Impedance spectroscopy (EIS) and
- Current-voltage (I-V) curve

4.9.1 VOLTAMMETRY: CYCLIC AND SQUARE WAVE

The electroactivity of the precursor materials for the synthesis of the nanoparticles was investigated through cyclic voltammetry using 0.1M Lithium perchlorate as electrolyte prepared in Acetonitrile which referred to as **blank** in the cyclic voltammogram. The potential window used for the investigation is 0.0 V to +1.5 V. The precursor materials that were investigated were Copper (II) chloride, Zinc chloride, Tin (II) chloride, Sulphur powder, selenium powder and tellurium powder. Scan rates of 10 mV/s, 50 mV/s and 100 mV/s were studied for each of the precursor material. A three-electrode system comprising of working electrode, counter electrode and reference electrode was used. The working electrode used was glassy-carbon electrode while the counter electrode was platinum electrode and the reference electrode used was Ag/AgCl reference electrode. As scan rate was initiated, potential was applied to the material within the potential window, at a characteristic potential value the materials responded with a current peak assuming they exhibit electrochemical behaviour within that window. The voltammograms of the precursor materials that showed cathodic and anodic peaks are summarized in figure 4.16.

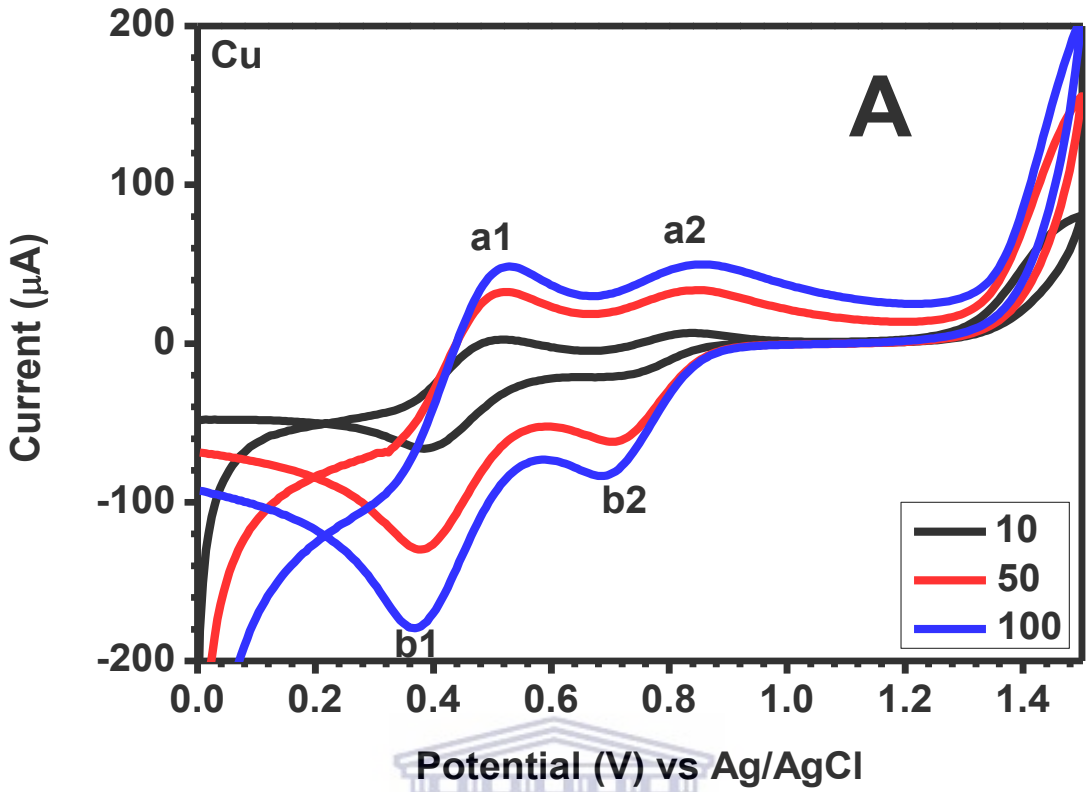

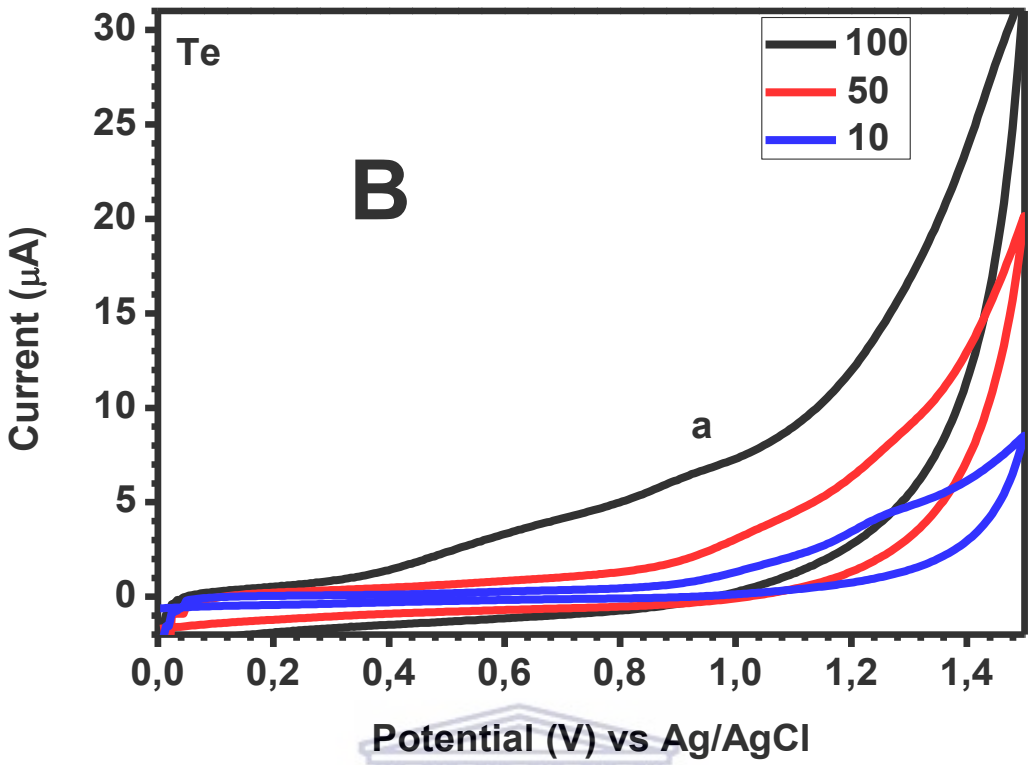

Figure 4. 16: Cyclic voltammograms of the precursor materials used for the synthesis of the synthesized nanoparticles. The precursors are (A) Cu and (B) Te.

The cyclic voltammogram of the precursor materials reveals their behaviour in the electrolyte within the potential window used. At all three scan rates (10, 50 and 100 mV/s), Two oxidation (anodic) peaks and two reduction (cathodic) peaks were observed for copper (Cu) precursor which has redox reaction as follows [47]:

Oxidation Reaction for Cu

$(a1)\ Cu_{(s)} \rightarrow Cu^{+}_{(aq)} + e^{-}$

$(a2)\ Cu^{+}_{(aq)} \rightarrow Cu^{2+}_{(aq)} + e^{-}$

Reduction Reaction for Cu

$(b2)\ Cu^{2+}_{(aq)} + e^{-} \rightarrow Cu^{+}_{(aq)}$

$(b1)\ Cu^{+}_{(aq)} + e^{-} \rightarrow Cu_{(s)}$

The potentials and corresponding value of the currents at the maximum of the observed peaks for copper are given as:

(a1) 0.53 V, 0.047 mA corresponding to oxidation of $Cu^{(0)}$ to $Cu^{(+1)}$;

(a2) 0.85 V, 0.053 mA corresponding to oxidation of $Cu^{(+1)}$ to $Cu^{(+2)}$;

(b2) 0.70 V, -0.086 mA corresponding to reduction of $Cu^{(+2)}$ to $Cu^{(+1)}$ and

(b1) 0.37 V, -0.183mA corresponding to reduction of $Cu^{(+1)}$ to $Cu^{(0)}$.

There was no electrochemical activity in Zinc, Tin, Sulphur and Selenium precursors within the potential window used since no peak was observed. Tellurium showed electrochemical activity at all three scan rates. One oxidation peak was observed for the three scan rates which is attributed to oxidation of tellurium from oxidation state of -2 to oxidation state of 0. It can be observed that the peak shifted to a more positive as the scan rates decreased from 100 mV/s to 10 mV/s. The value of the peak potentials observed for the various scan rates is summarized as follows;

1.26 V (0.04 mA) for 10 mV/s,

1.07 V (0.041 mA) for 50 mV/s and

0.93 V (0.064 mA) for 100 mV/s.

The cyclic voltammetry is a very important electrochemical test for synthesized nanoparticles as it reveals the electrochemical behaviour of the materials. This is achieved by sweeping

potential back and forth (from positive to negative and negative to positive), which records currents at these potentials. The graphical analysis of the cyclic voltammogram gives the redox (reduction and oxidation) peaks of the nanoparticles. The current peaks obtained sheds light to the potential at which the nanomaterials are oxidized and reduced.

The cyclic voltammetry of the synthesized nanoparticles was observed in the same potential window (0.0 V to +1.5 V) as that of the precursor materials at different scan rates of 10, 50 and 100 mV/s. 0.1M Lithium perchlorate in acetonitrile (**Blank**) was used as the supporting electrolyte for the analysis. The observed voltammogram is given in figure 4.18 below.

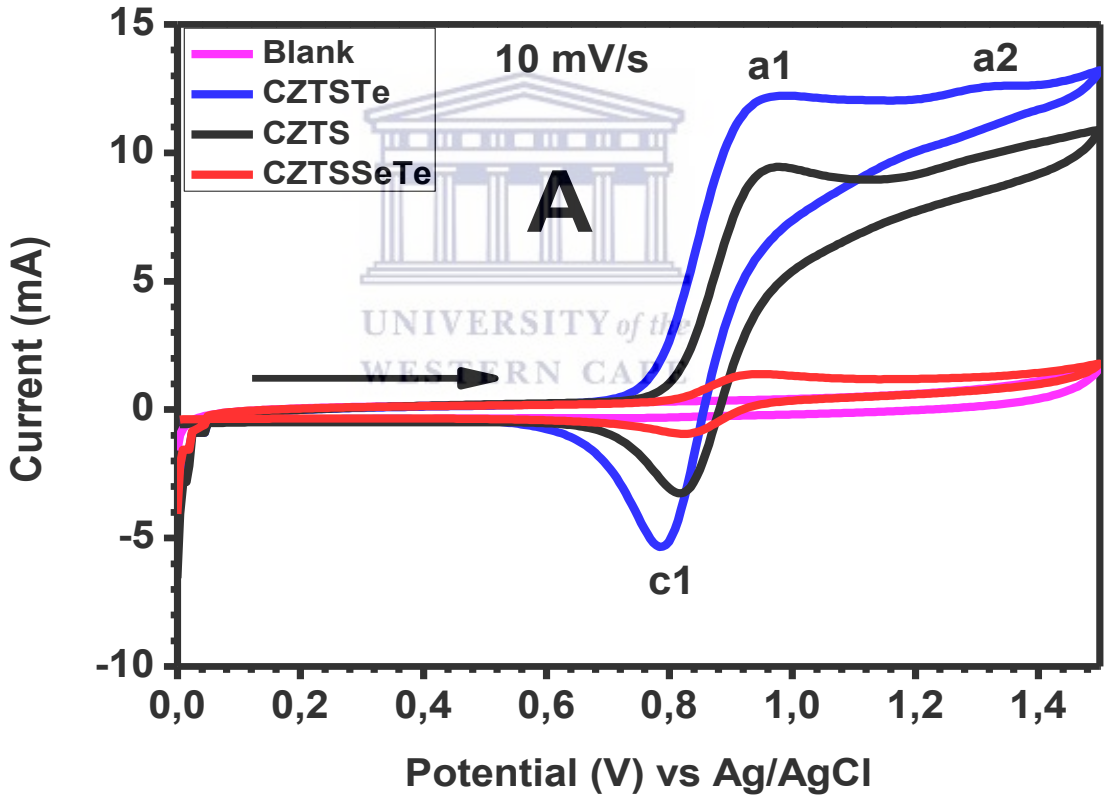

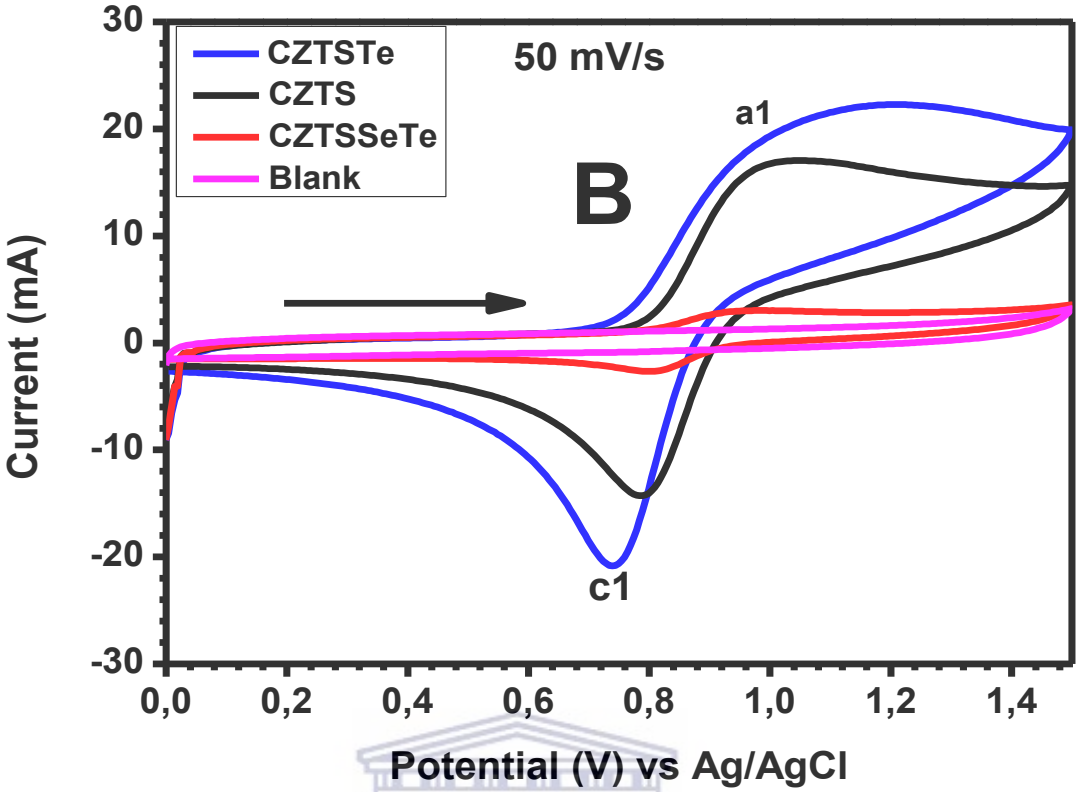

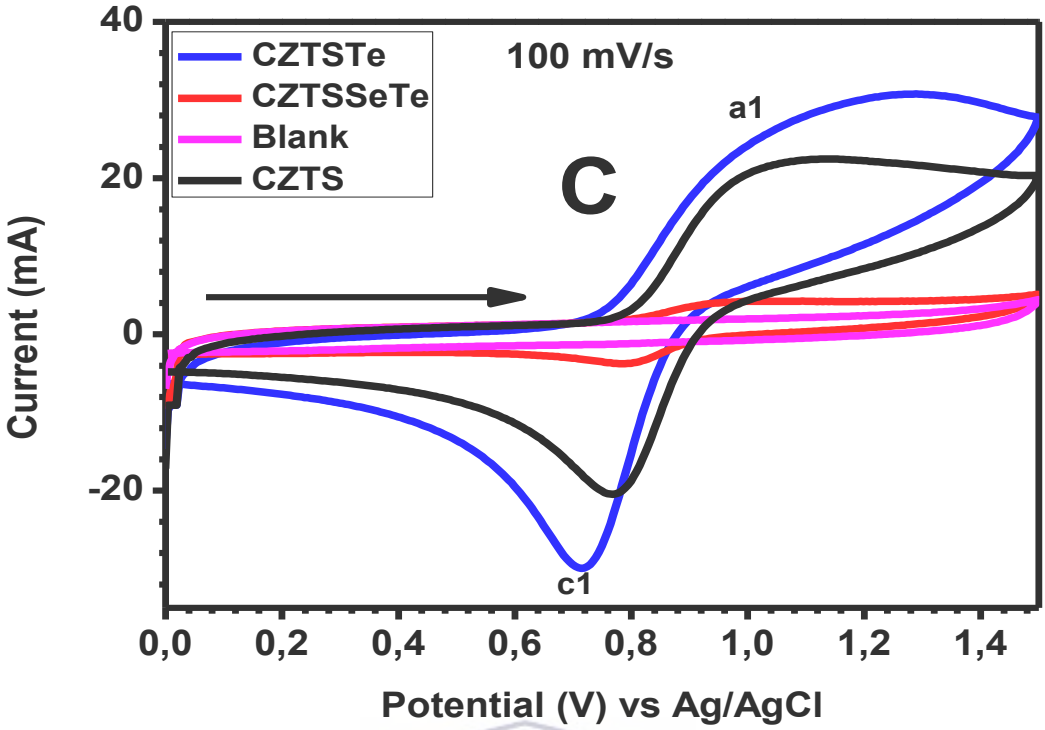

Figure 4. 17: Cyclic Voltammogram of the synthesized nanoparticles of CZTS, CZTSSeTe and CZTSTe showing the oxidation and reduction peaks observed for the nanoparticles at scan rates of (A) 10, (B) 50 and (C) 100 mV/s in reference to Ag/AgCl reference electrode and supporting electrolyte of 0.1M $LiClO_4$ in Acetonitrile.

All the synthesized nanoparticles showed one oxidation peak and one reduction peak at all scan rate used which has been reported [48-49] except CZTSTe which had a second oxidation peak (assigned as a_2) at scan rate of 10 mV/s. No peak was observed for the electrolyte on glassy carbon electrode at the potential window used. The peaks observed in the cyclic voltammogram were attributed to the presence of copper in the nanoparticles as observed in the precursor material and can be summarized as follows:

Oxidation of copper from oxidation state of +1 to +2

$$a1: 2Cu^{+}_{(aq)} \rightarrow 2Cu^{2+}_{(aq)} + 2e^{-}$$

Reduction of copper from oxidation state of +2 to +1

$$c1: 2Cu^{2+}_{(aq)} + 2e^{-} \rightarrow 2Cu^{+}_{(aq)}$$

Oxidation reaction of Te from oxidation state of -2 to 0

$$a2: Te^{2-}_{(aq)} + Te^{(0)}_{(s)} \rightarrow 2e^{-}$$

From the cyclic voltammogram obtained for the synthesized nanoparticles, CZTSTe had a more cathodic and anodic peak current value than CZTS and CZTSSeTe in that order as shown in table 4.4 below.

Table 4 4a: The peak values for CZTS at scan rates of 10, 50, and 100 mv/s

Scan Rate (mV/s)	I_{pa1} (mA)	I_{pc1} (mA)	E_{pa1} (V)	E_{pc1} (V)
10	0.009	0.003	0.96	0.81
50	0.017	0.014	1.00	0.78
100	0.021	0.021	1.04	0.76

Table 4.4b: The peak values for CZTSSeTe at scan rates of 10, 50 and 100 mV/s.

Scan Rate (mV/s)	I_{pa1} (mA)	I_{pc1} (mA)	E_{pa1} (V)	E_{pc1} (V)
10	0.001	0.001	0.93	0.83
50	0.003	0.003	0.92	0.81
100	0.004	0.004	0.91	0.79

Table 4.4c: The peak values of CZTSTe at scan rates of 10, 50 and 100 mV/s.

Scan Rate (mV/s)	I_{pa1} (mA) and I_{pa2} (mA)	I_{pc1} (mA)	E_{pa1} (V) and E_{pa2} (V)	E_{pc1} (V)
10	0.011, 0.012	0.006	0.94, 1,31	0.79
50	0.021	0.014	1.11	0.73
100	0.029	0.030	1.13	0.71

From the tables above, CZTSTe nanoparticles are more conductive than those of CZTS and CZTSSeTe as its anodic and cathodic peak current values show higher current values and it also shifted to more positive potential value at oxidation and shifted to more negative potential value at reduction. It can be observed that the potential values of the cathodic peaks of the nanoparticles decreased with increasing scan rate while the potential at the anodic peak increased with increasing scan rate. Also, the current values for both anodic and cathodic peaks increased with increasing scan rate for all nanoparticles indicating a reversible electron transfer system, which will be confirmed by the linearity obtained from the plot of peak current value against square root of scan rate.

At high scan rates of 50 and 100 mV/s, the oxidation peaks of the nanoparticles of CZTS, CZTSTe and CZTSSeTe were observed to be broadened with the tellurium peak observed at 10mV/s for CZTSTe disappearing. This is due to the high scan rate used, the potential was high to the extent that the peak of the tellurium became overshadowed by the copper oxidation peak. This shows that the high scan rates are not a sufficient or good parameter at which the

electrochemical behaviour of the materials can be sufficiently studied. The best electrochemical study can be achieved at very low scan rate for the synthesized nanoparticles to obtain the best possible electrochemical behaviour.

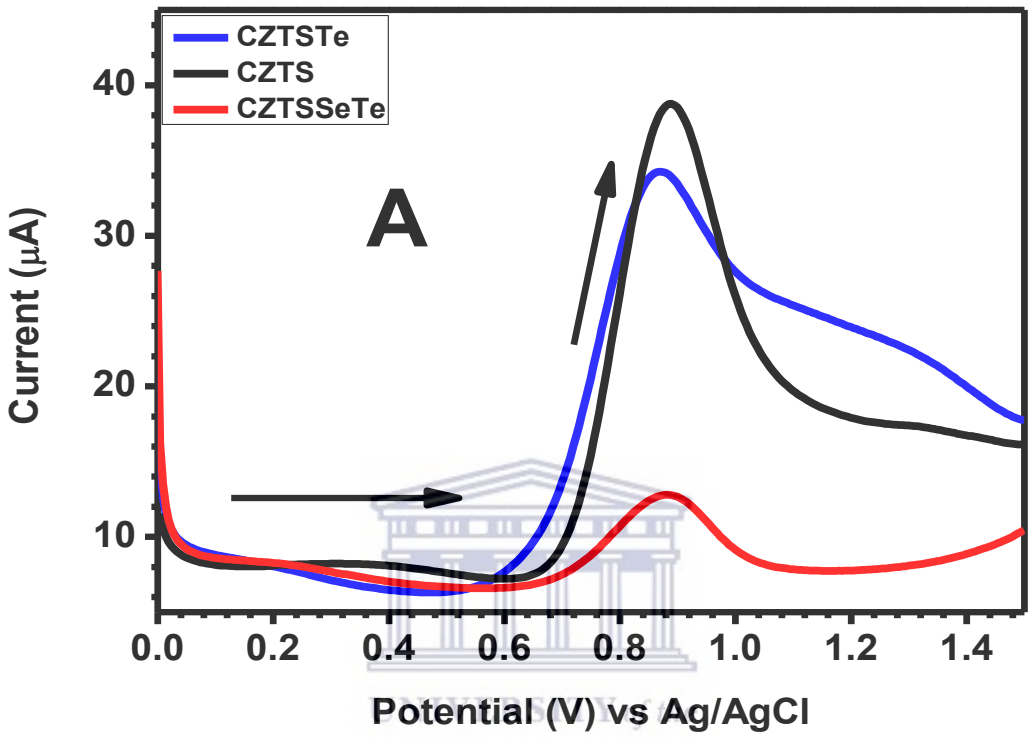

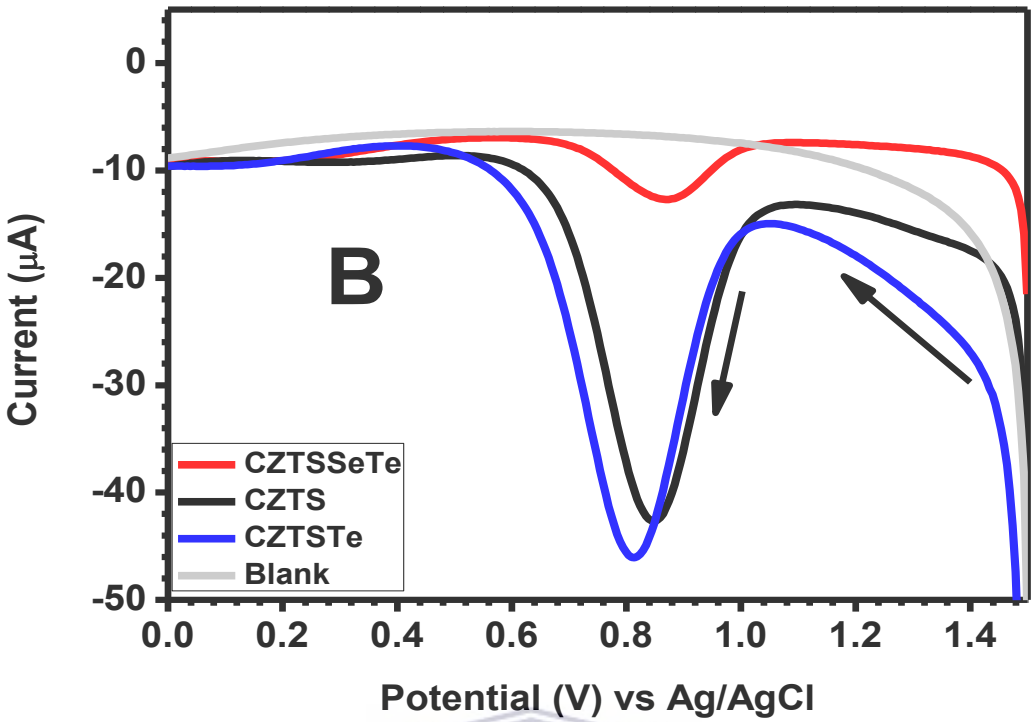

Figure 4. 18: Square-wave voltammogram (SWV) of the synthesized nanoparticles of CZTS, CZTSSeTe and CZTSTe (A) forward reaction (oxidation) (B) backward reaction (reduction).

In order to validate the peaks that were seen in the cyclic voltammogram, the square wave voltammetry was carried out to rule out the presence of other peaks that were not picked up during CV analysis. This is because square-wave is a more sensitive voltammetry technique than CV and can easily detect any electroactivity faster and make it become more pronounced. From the voltammogram obtained the current peaks that were seen in the CV voltammograms were the same peaks obtained from the square-wave voltammogram thereby ruling out availability of other peaks that were not detected by CV as seen in figure 4.18.

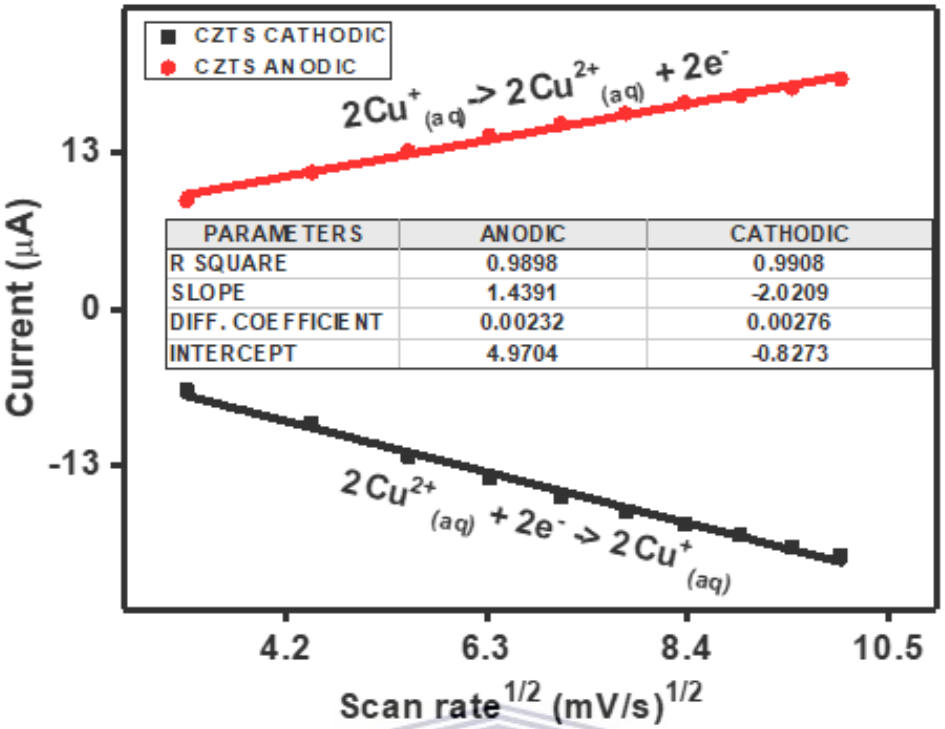

PARAMETERS	ANODIC	CATHODIC
R SQUARE	0.9898	0.9908
SLOPE	1.4391	-2.0209
DIFF. COEFFICIENT	0.00232	0.00276
INTERCEPT	4.9704	-0.8273

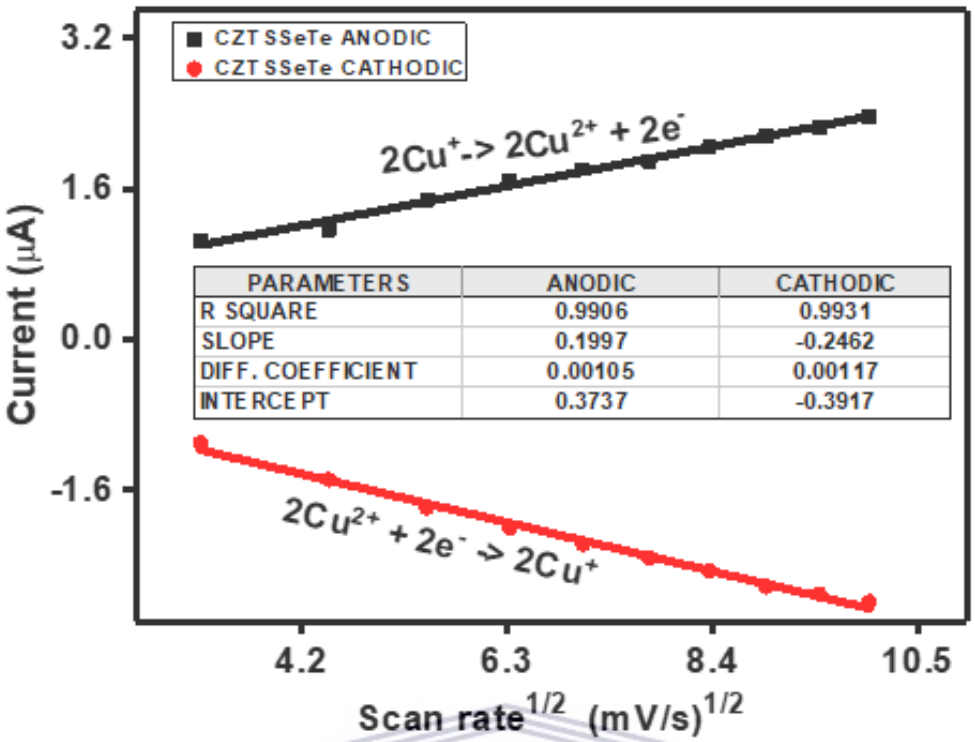

PARAMETERS	ANODIC	CATHODIC
R SQUARE	0.9906	0.9931
SLOPE	0.1997	-0.2462
DIFF. COEFFICIENT	0.00105	0.00117
INTERCEPT	0.3737	-0.3917

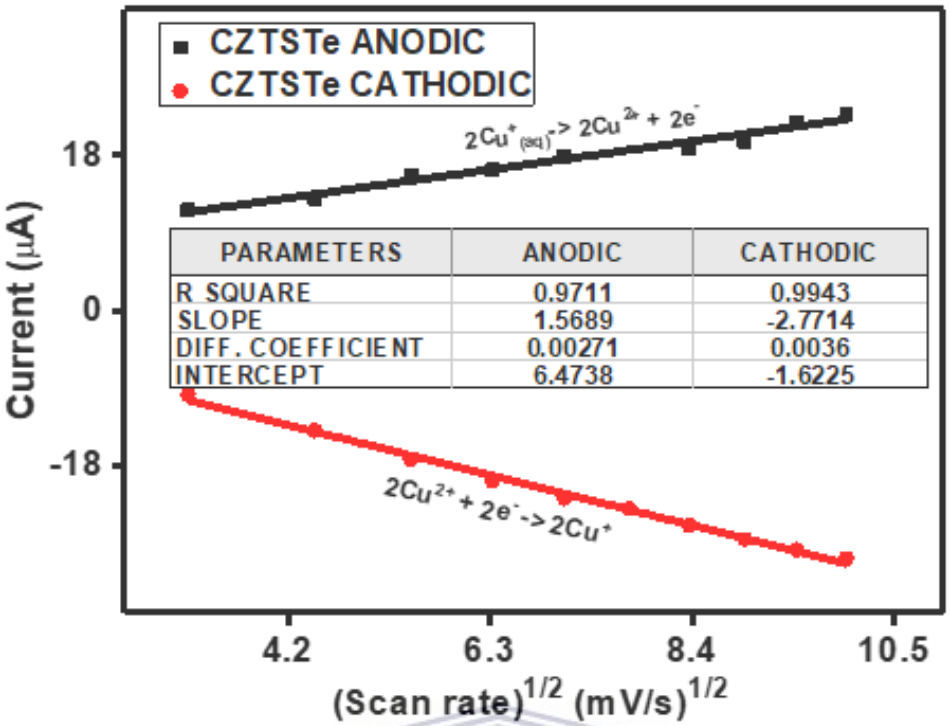

Figure 4. 19: Cathodic and Anodic peak currents of the synthesized nanoparticles of (A) CZTS, (B) CZTSSeTe and (C) CZTSTe showing a table with values for the slope used for calculation of diffusion coefficient.

The diffusion coefficient of the nanoparticles was calculated by plotting the anodic peak current value and cathodic peak current value at different scan rates against the square root of the scan rates (10 mV/s to 100 mV/s) as seen in figure 4.19 above. A condensed Randle-Sevcik equation for a temperature condition of 25 ˚C was used to evaluate the diffusion coefficient of the nanoparticles. The equation is given as

$$i_p = 2.69 \times 10^5 n^{\frac{3}{2}} AC\sqrt{vD} \quad \textbf{(4.2)}$$

and rewritten as

$$D = \sqrt{\frac{slope}{2.69\ x\ 10^5 n^{3/2} AC}} \quad \textbf{(4.3)}$$

where slope = i_p *divided by square root of scan rate, n* is the number of electrons during redox reaction which has the value of 2 from calculation, *A* is the surface area of the electrode (in this case glassy-carbon electrode which has a surface area of 0.017 cm^2) and *C* is the concentration of the nanoparticles used for analysis.

In order to calculate the number of electrons (n) the following equation was used:

$$\left|E_p - E_{p/2}\right| = \frac{2.303\,RT}{nF} \qquad \textbf{at 25 ˚C} \qquad \textbf{(4.4)}$$

where *n* is the number of electrons, E_p is the formal potential, $E_{p/2}$ is half-peak potential, *R* is gas constant, *T* is temperature in Kelvin and *F* is faraday constant. By making *n* the subject of the formula and 2.303 *RT* divided by *F* having a value of 59.19 mV at 25 ˚C, where 2.303 *RT* has a value of 0.593 kcal/mol at 25 ˚C and *F* is 23.06 kcal/mol V, the equation is rearranged to;

$$n = \frac{59.19\,mV}{E_p - E_{p/2}} \qquad \textbf{(4.5)}$$

The value of *n* obtained from the equation above for the synthesized nanoparticles of CZTS, CZTSSeTe and CZTSTe is two (2). The concentration of the synthesized nanoparticles is 4 mM. The diffusion coefficient of the nanoparticles explains the rate at which the electrons move towards the electrode. The rate of diffusion of the nanoparticles shows how fast the material releases electrons towards the electrode. CZTSTe nanoparticles diffused faster than the other nanoparticles which agrees with the high peak current value seen in the cyclic voltammograms. The value of the diffusion coefficient is summarized in table 4.5.

Table 4 5: Diffusion coefficient values of the synthesized nanoparticles

SAMPLE	DIFFUSION COEFFICIENT ANODIC PEAK (cm^2/s)	DIFFUSION COEFFICIENT CATHODIC PEAK (cm^2/s)
CZTS	0.00232	0.00276
CZTSSeTe	0.00105	0.00107
CZTSTe	0.00271	0.0036

4.9.2 ELECTROCHEMICAL IMPEDANCE (EIS)

EIS is used for evaluating the impedance of the electrochemical cell. It can be calculated by applying a sinusoidal (AC) voltage of small amplitude to electrode connected to material under study, resulting in generation of current whose amplitude and phase angle are measured with respect to the applied sinusoidal voltage. Since impedance is a function of frequency, to obtain an impedance spectrum, the different ranges of frequencies have to be examined.

EIS is an important electrochemical technique in that its spectra can be analyzed to determine the resistance of the solution R_s, double layer capacitance C_{dl}, charge transfer resistance R_{ct}

which is usually the resistance value of the material under study and Warburg impedance which helps in evaluating the Warburg diffusion coefficient value. Warburg is basically a constant phase element with a constant phase shift of 45 º and its impedance can be defined by resolving Fick's law. The resistance values, Warburg diffusion coefficient and double layer capacitance values can be obtained by fitting the data of the EIS experiment in ZView software. By this fitting the equivalent circuit of the EIS spectra can be obtained.

The spectra can be plotted in two ways Bode plot and Nyquist plot. Nyquist plot shows the relation between the imaginary impedance and real impedance and Bode plot is the plot of total Impedance (sometimes called magnitude) against frequency both as logarithm values and also phase angle against frequency where frequency is in logarithm form. The Nyquist plot of the nanoparticles is shown in figure 4.20.

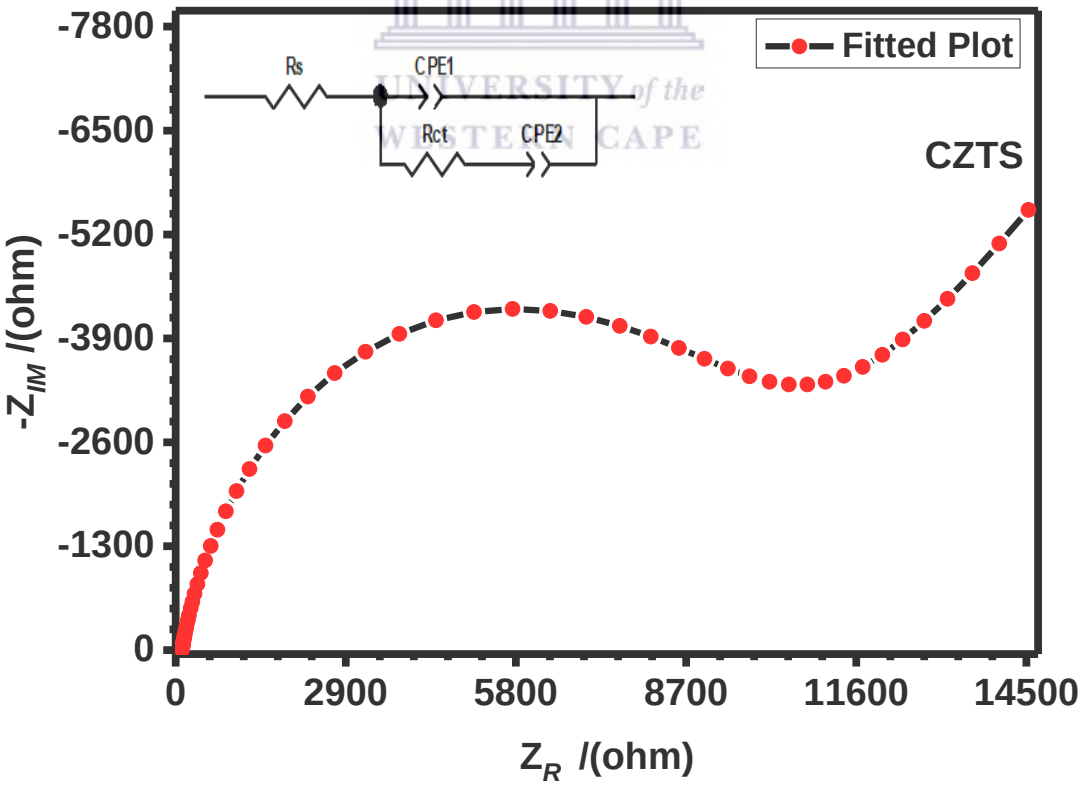

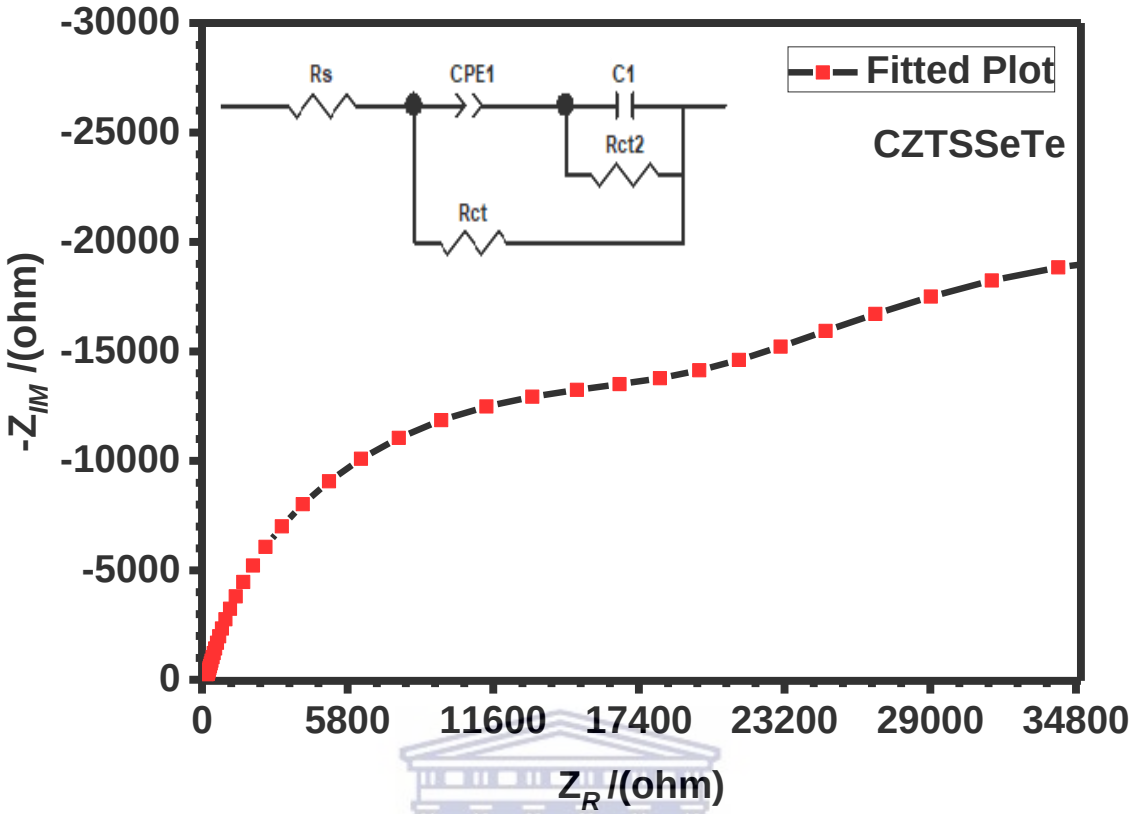

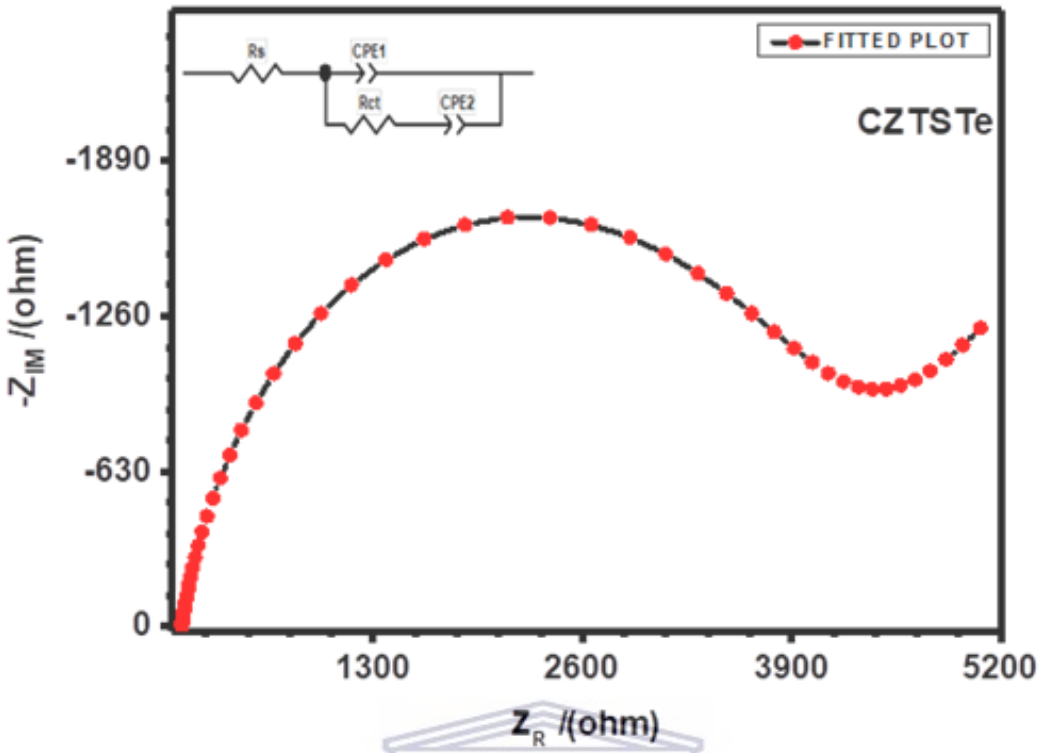

Figure 4. 20: Fitted plot (obtained from ZView) Nyquist plot of the synthesized nanoparticles of (A) CZTS, (B) CZTSSeTe and (C) CZTSTe with inset of the equivalent circuit simulated using ZView.

The fitted equivalent circuit for CZTS

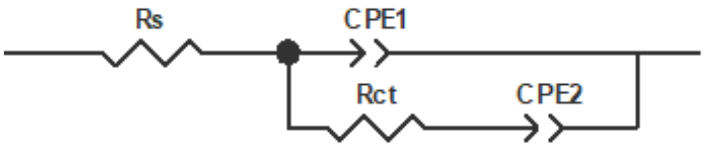

, CZTSSeTe

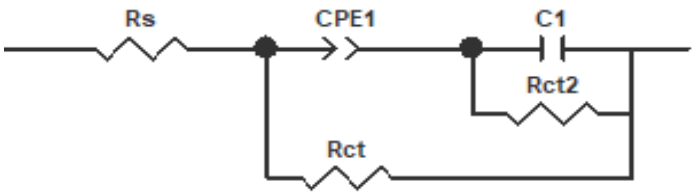

and CZTSTe

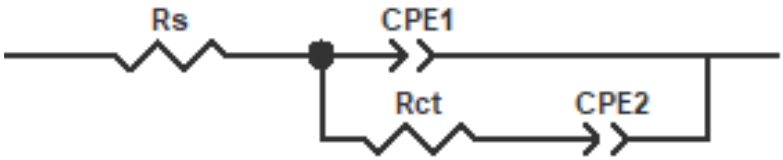

didn’t fit a Warburg as the phase angle didn’t start or end at 45 º which is constant parameter for a Warburg diffusion [51] as seen in bode plot figure 4.22. To compare the spectra of the three nanoparticles, fitted and unfitted plots were obtained as shown in figure 4.21.

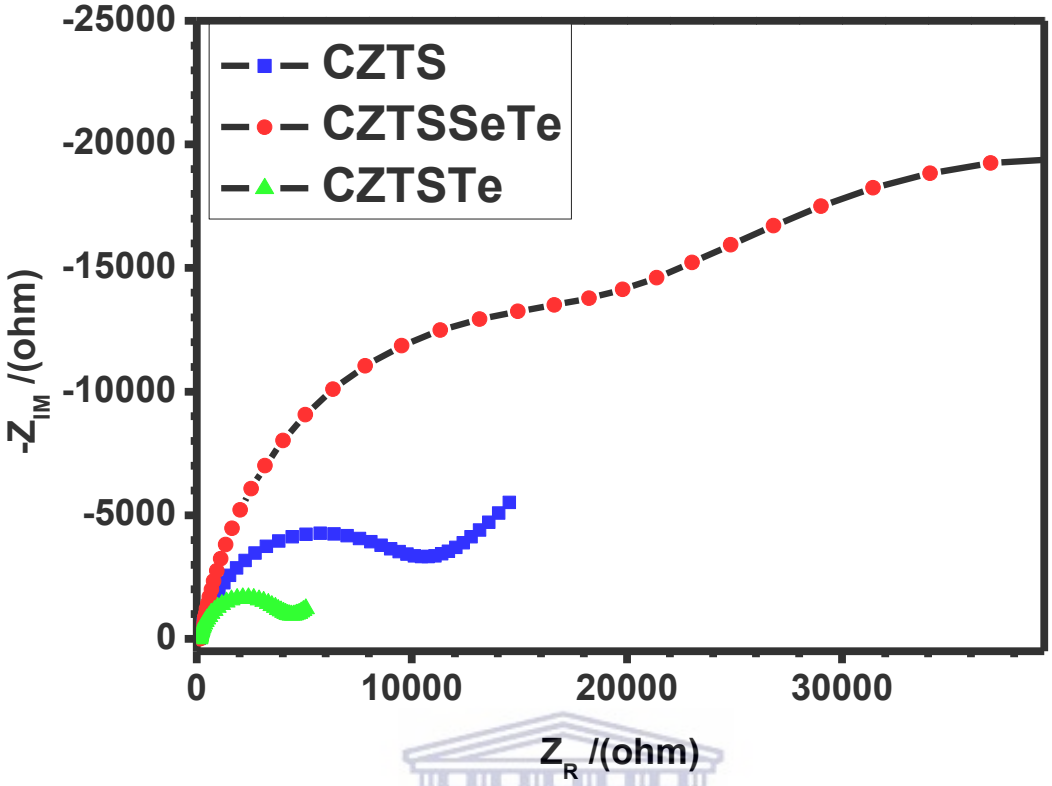

Figure 4. 21: Nyquist plot showing comparison between the synthesized nanoparticles.

Table 4 6: Fitted equivalent circuit values for the synthesized nanoparticles.

SAMPLE	R_s (ohm)	R_{ct} (ohm)	R_{ct2} (ohm)	CPE_1 (degrees)	CPE_2 (degrees)
CZTS	106.5	9855		0.8556	0.5048
CZTSSeTe	165.6	67938	15932	0.7776	
CZTSTe	107.2	3945		0.8585	0.4738

From the values in table 4.6 above, we can compare the resistance of the synthesized nanoparticles. The lowest R_{ct} value was obtained for CZTSTe and the highest R_{ct} value was obtained for CZTSSeTe. The R_{ct} value represents the resistance of the nanoparticles under review. The low R_{ct} obtained for CZTSTe shows that the nanoparticle is the most conductive of the three nanoparticles [50-52]. The high R_{ct} value obtained for CZTSSeTe shows that it is the least conductive of the three. This corresponds to the CV peaks current observed for the nanoparticles where CZTSTe had high cathodic and anodic peaks current when compared to the other samples and CZTSSeTe had the least peak current for the oxidation and reduction. The Nyquist plot of the three nanoparticles also shows the high resistance of CZTSSeTe and a low resistance for CZTSTe. The second R_{ct} value obtained for CZTSSeTe as shown at the equivalent circuit is due to another reaction taking place. All fitted equivalent circuit of the nanoparticles didn't fit with a Warburg and this can be proven from the Bode plot where the

phase angles of the nanoparticles did not start or end at 45 º which is a constant phase parameter for a Warburg diffusion [50].

Bode plot of the nanoparticles was also used to compare the conductivity of the synthesized nanoparticles figure 4.22.

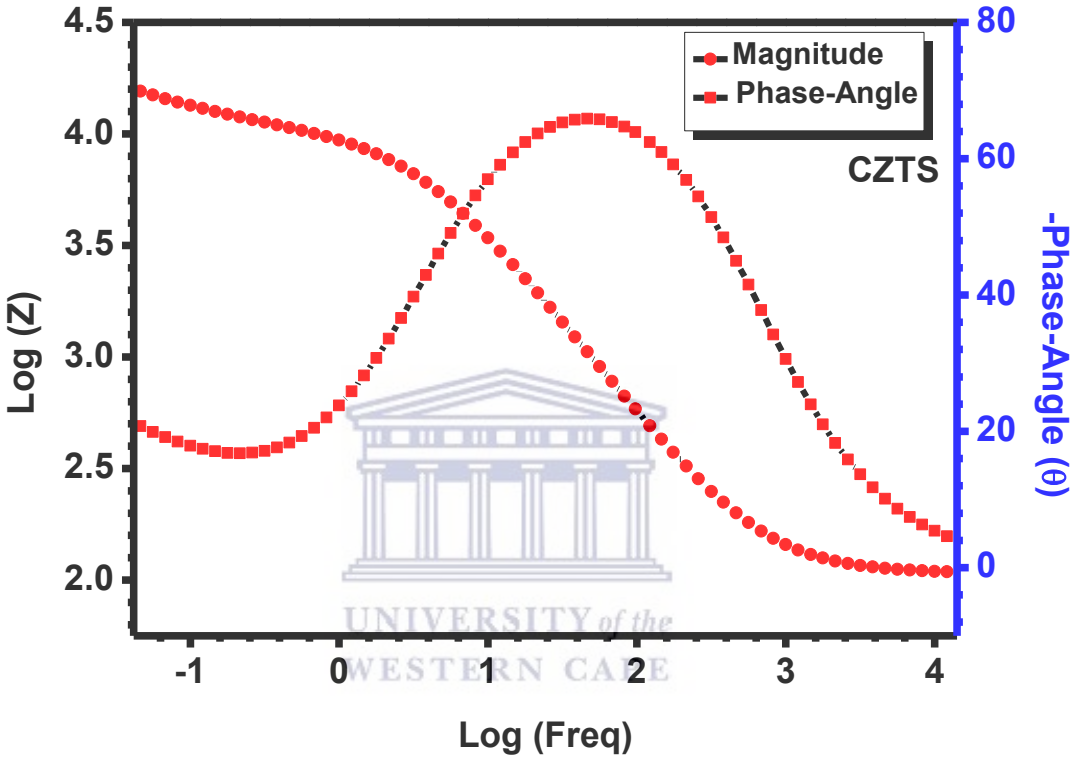

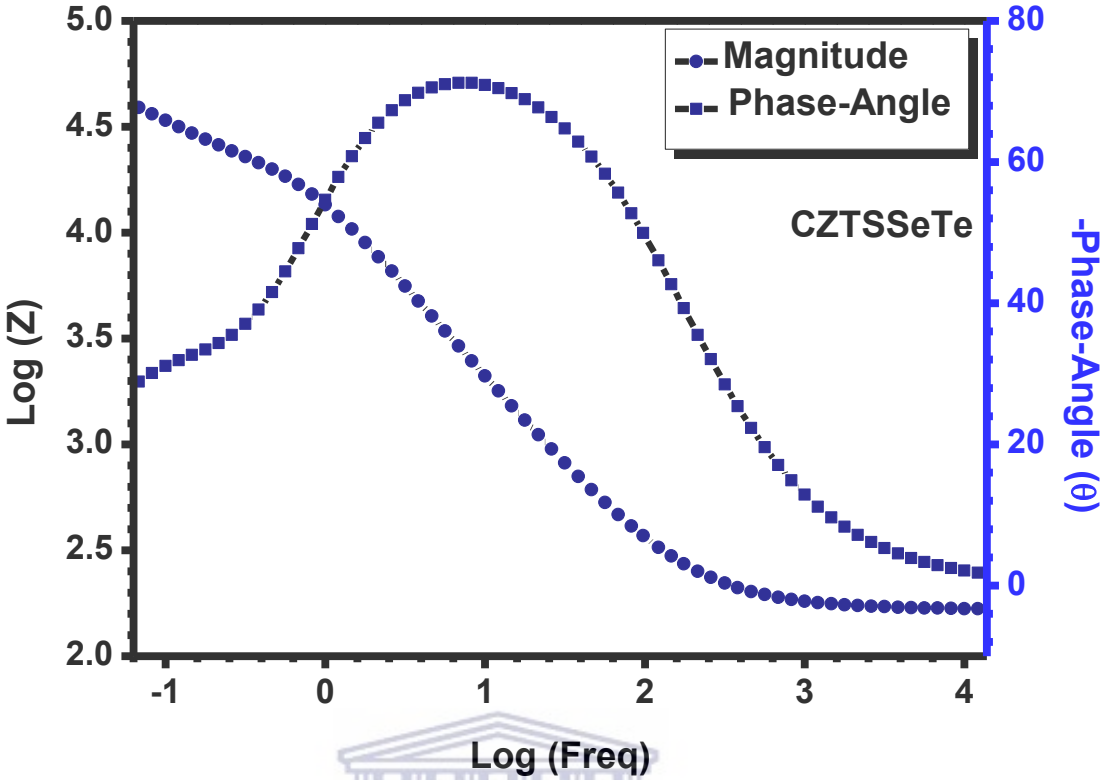

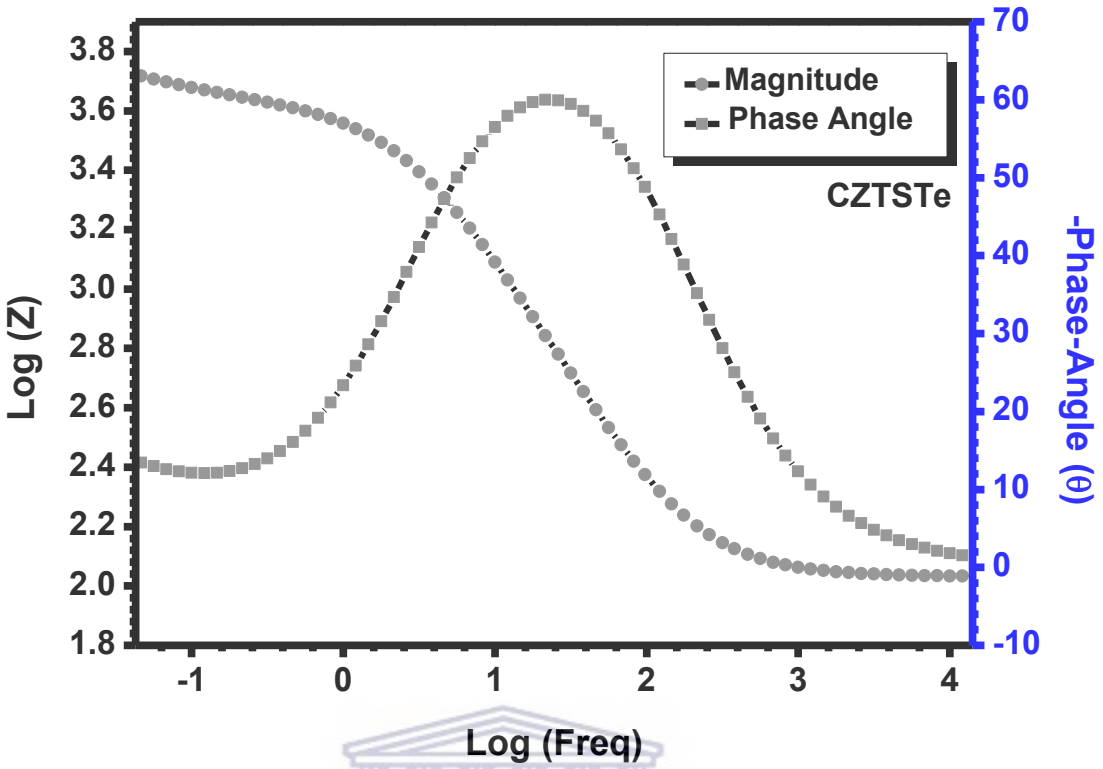

Figure 4. 22: Fitted plot of the synthesized nanoparticles of (A) CZTS, (B) CZTSSeTe and (C) CZTSTe showing the total impedance (magnitude) and Phase angle.

It can be seen from the phase angle plot of the synthesized nanoparticles that none of them ended or started from the 45 º value and so cannot fit into a Warburg diffusion. The total impedance plot of CZTS starts from a low frequency value -1.33 Hz with a corresponding magnitude of 4.22 Ω. At frequency value of zero Hz, the magnitude became 3.97 Ω and run down to a high frequency of 4.08 Hz with magnitude value of 2.02 Ω. Similarly, CZTSSeTe started from a low frequency value of -1.25 Hz with a magnitude value of 4.64 Ω, and has a magnitude value of 4.13 Ω at zero Hz frequency and runs down to a high frequency value of 4.08 Hz at magnitude of 2.21 Ω. CZTSTe started at a low frequency value of -1.33 Hz with a magnitude of 3.74 Ω and has a magnitude value of 3.55 Ω at zero Hz frequency. It ends with a high frequency of 4.08 Hz having a magnitude value of 2.02 Ω. The magnitude values

obtained at the low frequencies are the total impedance for each of the synthesized nanoparticles. The total impedance values obtained shows that CZTSSeTe had the highest value while CZTSTe had the lowest value, which follows the trend obtained from the Nyquist plot as well as the CV plot, which establishes the fact that CZTSSeTe was the most resistive of the three synthesized nanoparticles and as such is the least conductive of the synthesized nanoparticles.

Figure 4.23 and figure 4.24 show the Bode plot of the total impedance of the three nanoparticles and the phase angle respectively for the fitted (data obtained after ZView fit of equivalent circuit) and unfitted. The phase angle plot obtained for CZTS shows a start from a low frequency of -1.33 Hz having a phase angle value of -12.8 º, it continues to a maximum phase angle value of -66 º with a frequency which is more shifted towards the high frequency region of value 1.67 Hz, it finally comes to an end with a phase angle of -9.6 º at a high frequency value of 4.08 Hz. CZTSSeTe started from a low frequency of -1.25 Hz with a phase angle value of -27.5 º and continued to a maximum phase angle value of -71 º at a frequency value of 0.91 Hz which is more to the low frequency region. It then finally ends with a high frequency value of 4.08 Hz with a phase angle of -6.8 º. Although CZTSSeTe can be seen here having the highest phase angle value (-71 º), it is worthy to note that the value is more to the low frequency region and as such still maintains the trend of being the least conductive. Taking into consideration the fact that its spectrum for the phase angle started at a higher phase angle value of -27.5 º, that bump in value gives it that edge of having the highest phase angle value. But logically if all samples were to start at the same phase angle value or if the bump advantage that CZTSSeTe and CZTS had were removed and all materials were assessed at the same starting point to the same ending point it will be seen that CZTSTe will have the highest phase angle value thereby, following the trend of being the most conductive of all three materials.

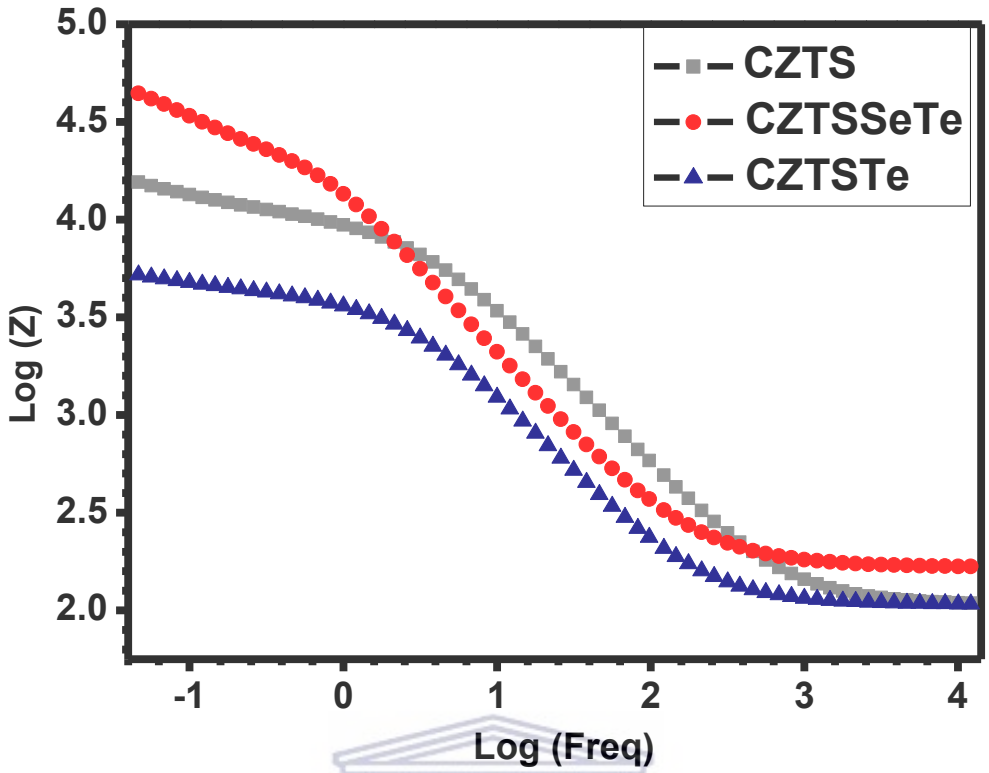

Figure 4. 23: Bode plot of total impedance of the nanoparticles.

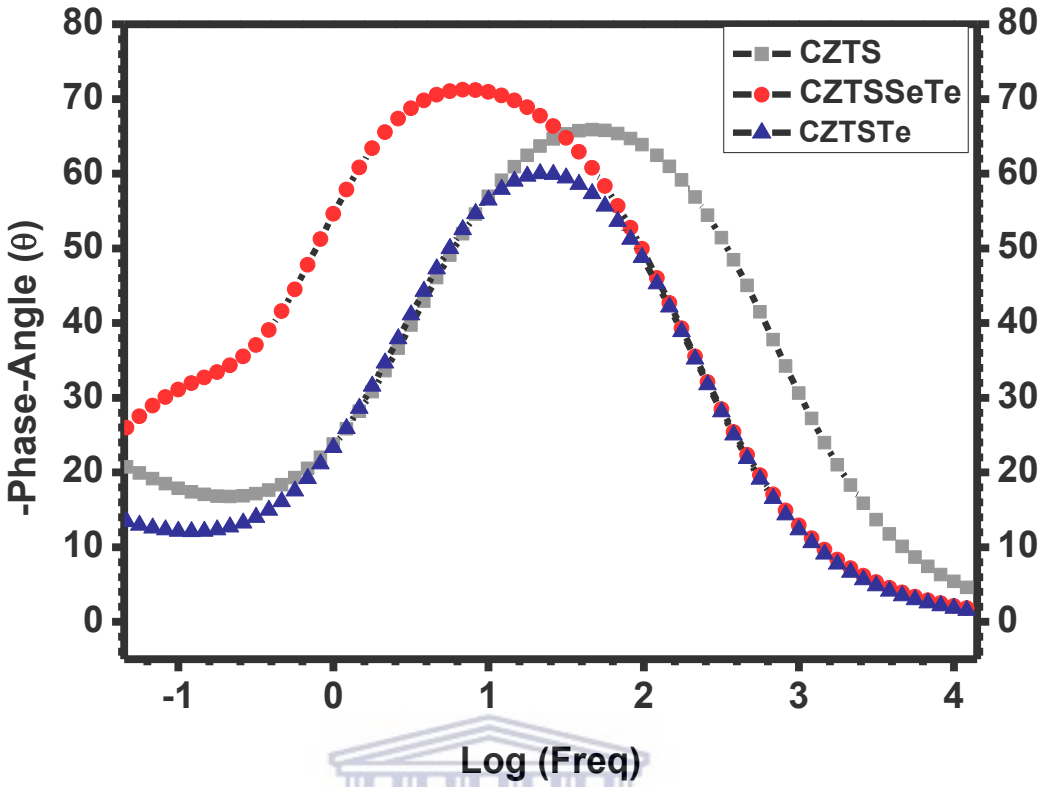

Figure 4. 24: Bode plot of the phase angle of the nanoparticles

The electrochemical behaviour observed in the nanoparticles from CV, SWV and EIS shows that with a lower ratio of tellurium as in the case of CZTSTe when compared to sulfur enhanced the peak current (oxidation and reduction) and conductivity but with addition of tellurium and selenium sharing same ratio with sulfur in the case of CZTSSeTe, the material became highly resistive. This resistive behaviour is due to metallic (cation) repulsion occurring in the structure of the nanoparticles as selenium and tellurium tend to act more metallic. With kesterite having more metallic elements; copper, zinc and tin, the addition of tellurium and selenium adds to like-charge repulsion in the structure thereby leading to the material being more resistive. Sulfur which is more electronegative does not have enough ratio to balance out the electropositive charge of the other constituent elements. This behaviour of CZTSSeTe showing a less conductive activity can also be attributed to its high crystallinity which can be seen from

the SAED micrograph obtained from HRTEM. Because it is highly crystalline, it means that the electrons are tightly held together in its lattice making it very hard to easily release electrons for current flow. The least crystalline of the three samples was CZTSTe as seen from the SAED image which is a contributing factor for the material to be the most conductivity due to the ease electron movement for current flow which due in part by its amorphous nature.

4.9.3 CURRENT-VOLTAGE (I-V) CURVE.

The I-V curve for the as-synthesized nanoparticles was obtained from EC-Lab software. as shown in figure 4.25. The I-V curve analysis of the synthesized nanoparticles was carried out in an electrolyte of 0.1M Lithium perchlorate and a three-electrode system was utilized where glassy carbon electrode was used as the working electrode and platinum wire was used as the counter electrode and Ag/AgCl was used as the reference electrode. This experiment was done in a potential window of -0.1 to 1.5 V and at a scan rate of 50 mV/s. The graph obtained when power was applied on the nanoparticles is given in figure 4.26 below:

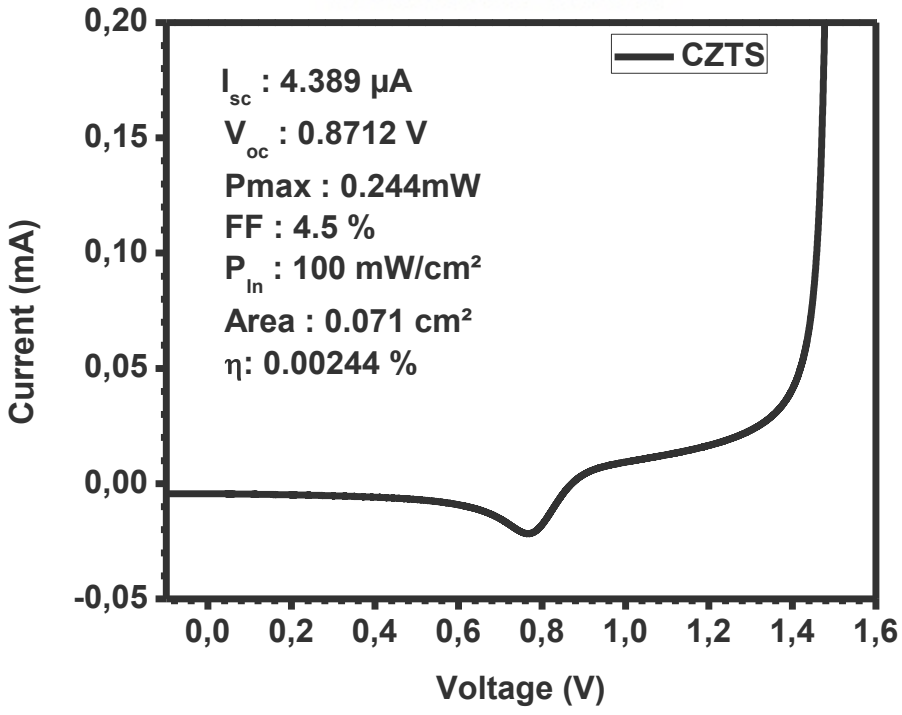

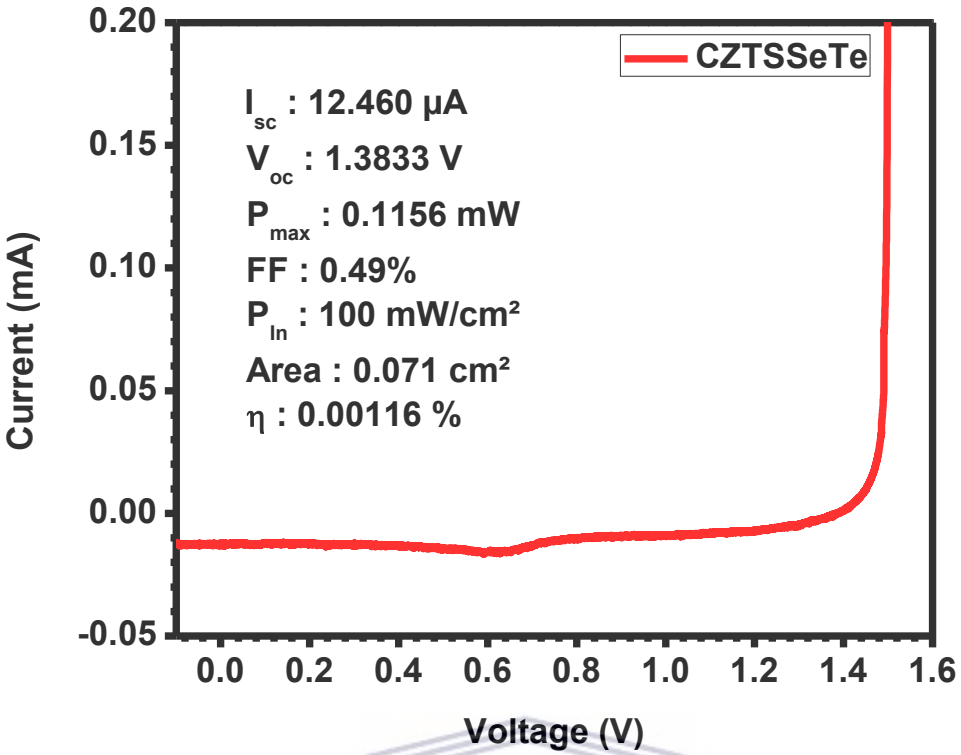

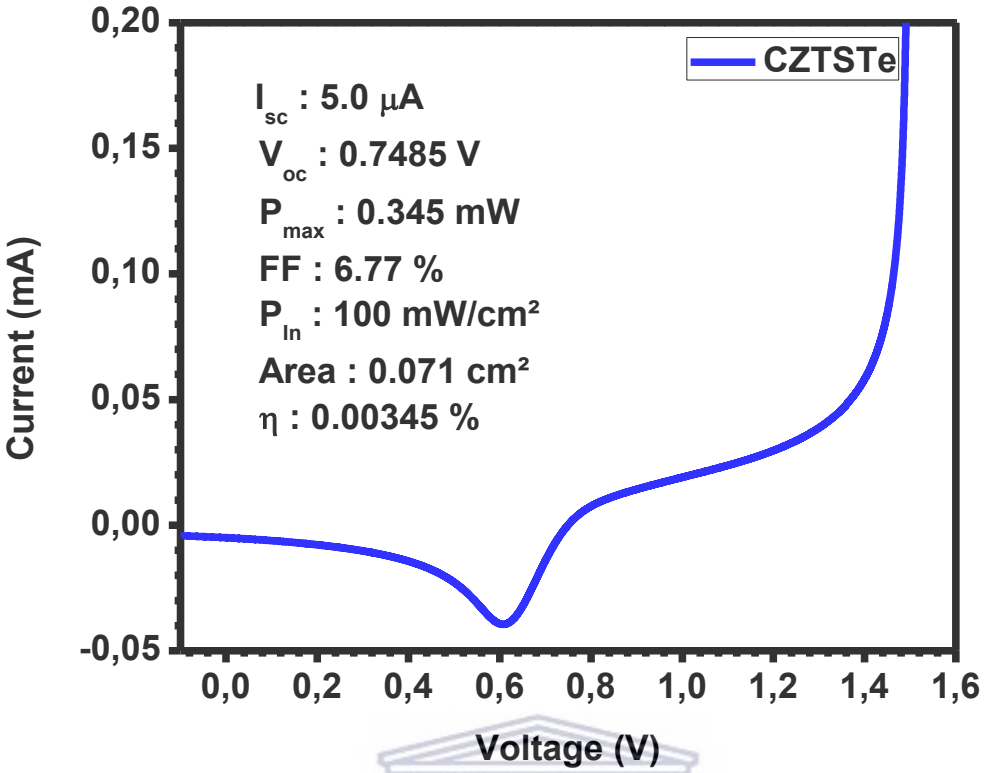

Figure 4.25 I-V curve of the as-synthesized nanoparticles of CZTS, CZTSSeTe and CZTSTe showing their PCE measured with EC-Lab Software.

From the I-V Curve graphs obtained for the nanoparticles in 0.1M Lithium perchlorate electrolyte, the efficiency of the nanoparticles was calculated and summarized in table 4.7 below:

Table 4 7 Parameters used for calculation of efficiency of the nanoparticles.

SAMPLE	J_{max} (mA/cm^2)	V_{max} (V)	Fill-Factor (%)	Efficiency (%)
CZTS	0.2999	0.7482	3.19	0.00224
CZTSSeTe	0.1219	0.9490	0.49	0.00116
CZTSTe	0.6165	0.5594	6.77	0.00345

The efficiency formula is given by:

$$\eta = \frac{FF \times V_{oc} \times J_{sc}}{P_{In}} \times 100\% \quad \textbf{(4.5)}$$

Where Fill-Factor (FF) is given as

$$FF = \frac{J_{max} \times V_{max}}{J_{sc} \times V_{oc}} \quad \textbf{(4.6)}$$

But maximum power P_{max} is given as

$$P_{max} = J_{max} \times V_{max} \quad \textbf{(4.7)}$$

Therefore, efficiency (η) is given as

$$\eta = \frac{P_{max}}{P_{in}} \times 100\% \quad \textbf{(4.8)}$$

The value for the efficiency of the nanoparticles as seen above followed the trend obtained in the other electrochemical techniques, where CZTSTe had a higher maximum current density produced and therefore had the highest efficiency of 0.00345 % while CZTS had an efficiency of 0.00224 % and CZTSSeTe had the least maximum current density produced with the least efficiency of 0.00116 % [53]. From the short circuit current I_{sc} and V_{oc} *obtained* for the various materials, it can be seen that CZTSSeTe had the highest values with I_{sc} value of 12 µA and V_{oc} value of 1.3833 V, agreeing with the optical band-gap obtained where it had the best optical bandgap of 1.06 eV. The high values of the I_{sc} and V_{oc} shows that it is able to absorb greater amount of energy than the other nanoparticles, but it fell short to convert the energy efficiently into usable current as its J_{max} value (0.1219 mA/cm^2) was the least amongst the three nanomaterials which follows the same trend observed in CV, SWV and EIS. It also exhibited the least fill-factor of 0.49 %. Although CZTSSeTe shows a greater potential of absorbing light than the other synthesized nanoparticles, it fell short to convert it efficiently into electrical current which is due to the high metallic composition as earlier stated given that selenium and tellurium act metallic and coupled with the electropositive metal constituents of the kesterite nanoparticle (copper, zinc and tin). This high metallic composition causes a repulsion in the electrochemical behaviour of the CZTSSeTe, resulting in the nanoparticle being more resistive and hence has a low power conversion efficiency. On the other hand, CZTSTe which started off with relatively high short circuit current 5.0 µA when compared to CZTS, maintained a high maximum current density J_{max} of 0.5594 mA/cm^2 and subsequently had the highest power conversion efficiency of 0.00345 %. This is the case as the optical band gap obtained showed the ability of the nanoparticle to absorb substantial amount of light incident on it with band-gap value of 1.62 eV when compared to CZTS with band-gap value of 1.73 eV. It was able to convert to substantial amount of current when compared to CZTSSeTe and CZTS which follows the very trend observed for the other electrochemical

characterizations. These results obtained show that although these materials had low power conversion efficiency, they demonstrated that they can be applied for photovoltaic cells.

REFERENCES

[1] C. Feldmann, "Polyol-Mediated Synthesis of Nanoscale Functional Materials," *Advanced functions material* 13 (2003) 101-107

[2] C. Kind, C. Feldmann, A. Quintilla and E. Ahlswede, "Citrate-capped $Cu_{11}In_9$ nanoparticles and its use for thin-film manufacturing of cis solar cells," *Chemistry of Materials* 23 (2011) 5269-5274

[3] Q.-B. Wei, P. Xu, X.-P. Ren and F. Fu, "Flower-like Cu_2ZnSnS_4 architectures synthetize and their visible-light catalytic properties," *Journal of Alloys and Compounds* 770 (2019) 424-432.

[4] S. Bahramzadeh, H. Abdizadeh, and M.R. Golobostanfard, "Controlling the morphology and properties of solvothermal synthesized Cu_2ZnSnS_4 nanoparticles by solvent type," *Journal of Alloys and Compounds* 642 (2015) 124–130.

[5] Q. Jiang, X. Chen, H. Gao, C. Feng and Z. Guo, "Synthesis of Cu_2ZnSnS_4 as Novel Anode material for Lithium-ion Battery," *Electrochimica Acta* 190 (2016) 703–712.

[6] Y. Guo, J. Wei, Y. Liu, T. Yang and Z. Xu, "Surfactant-Tuned Phase Structure and Morphologies of Cu_2ZnSnS_4 Hierarchical Microstructures and Their Visible-Light Photocatalytic Activities," *Nanoscale Research Letters* 12 (2017) 181.

[7] B. Patro, S. Vijaylakshmi and P. Sharma, "Rapid microwave-assisted solvothermal synthesis of Cu_2ZnSnS_4 (CZTS) nanocrystals for low-cost thin film photovoltaic: investigation of synthesis parameters and morphology control," *Journal of Materials Science: Materials in Electronics* 29 (2017) 3370–3380.

[8] M.Z. Ansari and N. Khare, “Rapid synthesis of flower shaped Cu_2ZnSnS_4 nanoparticles by microwave irradiation for solar cell application,” *AIP Conference Proceedings* 1728 (2016) 020563.

[9] B. Patro, S. Vijaylakshmi, R.K. Reddy, and P. Sharma, “Microwave-assisted solvothermal synthesis of Cu_2ZnSnS_4 (CZTS) nanocrystals for photovoltaic applications,” *Materials Today: Proceedings* 3 (2016) 2786–2794.

[10] V.A. Madiraju, K. Taneja, M. Kumar and R. Seelaboyina, “CZTS synthesis in aqueous media by microwave irradiation,” *Journal of Materials Science: Materials in Electronics* 27 (2015) 3152–3157.

[11] H. Schnablegger and Y. Singh, “The SAXS Guide: Getting acquainted with the principles,” *Anton Paar GmbH* 4 (2017) 1-163.

[12] H. Dong, T. Schnabel, E. Ahlswede and C. Feldmann, “Polyol-mediated synthesis of $Cu_2ZnSn(S,Se)_4$ kesterite nanoparticles and their use in thin-film solar cells,” *Solid State Sciences* 29 (2014) 52–57.

[13] D. Aldakov, A. Lefrançois and P. Reiss, “Ternary and quaternary metal chalcogenide nanocrystals: synthesis, properties and applications,” *Journal of Materials Chemistry C* 1 (2013) 3756.

[14] S. Chen, A. Walsh, X.-G. Gong and S.-H. Wei, “Classification of Lattice Defects in the Kesterite Cu_2ZnSnS_4 and $Cu_2ZnSnSe_4$ Earth-Abundant Solar Cell Absorbers,” *Advanced Materials* 25 (2013) 1522–1539.

[15] S. Jain, P. Chawla, S.N. Sharma, D. Singh, and N. Vijayan, “Efficient colloidal route to pure phase kesterite Cu_2ZnSnS_4 (CZTS) nanocrystals with controlled shape and structure,” *Superlattices and Microstructures* 119 (2018) 59–71.

[16] A.D. French and C.M. Santiago, “Cellulose polymorphy, crystallite size, and the Segal Crystallinity Index,” *Cellulose* 20 (2013) 583–588.

[17] M. Kumar, A. Dubey, N. Adhikari, S. Venkatesan, and Q. Qiao, “Strategic review of secondary phases, defects and defect-complexes in kesterite CZTS–Se solar cells,” *Energy and Environmental Science* 8 (2015) 3134–3159.

[18] R. Manivannan, D. Sahu, N. Selvaraju and S.V. Noyel, “Single Step Sonochemical Synthesis of Copper Zinc Tin Sulfide Nanoparticles,” *Journal of Scientific and Industrial research* 78 (2019) 102-105.

[19] A.G. Kannan, T.E. Manjulavalli and J. Chandrasekaran, “Influence of Solvent on the Properties of CZTS Nanoparticles,” *Procedia Engineering* 141 (2016) 15–22.

[20] B. Ananthoju, J. Mohapatra, D. Bahadur, N.V. Medhekar and M. Aslam, “Influence of the Cu_2ZnSnS_4 nanoparticles size on solar cell performance,” *Solar Energy Materials and Solar Cells* 189 (2019) 125–132.

[21] P.M. Kibasomba, S. Dhlamini, M. Maaza, C.-P. Liu, M.M. Rashad, D.A. Rayan, and B.W. Mwakikunga, “Strain and grain size of TiO_2 nanoparticles from TEM, Raman spectroscopy and XRD: The revisiting of the Williamson-Hall plot method,” *Results in Physics* 9 (2018) 628–635.

[22] D. Pareek, K.R. Balasubramaniam and P. Sharma, “Synthesis and characterization of kesterite $Cu_2ZnSnTe_4$ via ball-milling of elemental powder precursors,” *RSC Advances* 6 (2016) 68754–68759.

[23] T. J. Huang, X. Yin, C. Tang, G. Qi and H. Gong, “Influence of Ligands on the Formation of Kesterite Thin Films for Solar Cells: A Comparative Study,” *ChemSusChem* 9 (2016) 1032–1041.

[24] B. Pani, S. Pillai and U.P. Singh, “Kesterite based thin film absorber layers from ball milled precursors,” *Journal of Materials Science: Materials in Electronics* 27 (2016) 12412–12417.

[25] H.R. Jung, S.W. Shin, M.P. Suryawanshi, S.J. Yeo, J.H. Yun, J. H. Moon and J.H. Kim, “Phase evolution pathways of kesterite Cu_2ZnSnS_4 and $Cu_2ZnSnSe_4$ thin films during the annealing of sputtered Cu-Sn-Zn metallic precursors,” *Solar Energy* 145 (2017) 2–12.

[26] X. Chai, H. Qing, T. Shen, S. Sun and Y. Zhu, “A Rapid and Low-Cost Synthesis of Kesterite Cu_2ZnSnS_4 Microparticles by Microwave Irradiation,” *Advances in Analytical Chemistry* 8 (2018) 33-38.

[27] R.A. Wibowo, “Powder-to-film approach for fabricating critical raw material-free kesterite $Cu_2ZnSn(S,Se)_4$ thin film photovoltaic: A review,” *Solar Energy* 176 (2018) 157–169.

[28] S.-J. Lin, J.-M. Ting and Y.-S. Fu, “Single-phase, high-purity Cu_2ZnSnS_4 nanoparticles via a hydrothermal route,” *Ceramics International* 44 (2018) 4450–4456.

[29] S.M. Robati, M. Imani and A. Tadjarodi, “Ultrafast synthesis of crystalline Cu_2ZnSnS_4 nanoparticles by solid state microwave heating technique and study of their electrochemical behavior,” *Materials Letters* 225 (2018) 9–12.

[30] S. Hong and C. Kim, “Residual Stress Analysis of a Cu_2ZnSnS_4 Thin Film,” *IEEE 7th World Conference on Photovoltaic Energy Conversion* 7 (2018) 1-4.

[31] M. Bellardita, A. Di Paola, B. Megna and L. Palmisano, “Determination of the crystallinity of TiO_2 photocatalysts,” *Journal of Photochemistry and Photobiology A: Chemistry* 367 (2018) 312-320.

[32] X. Fontane, L. Calvo-Barrio, V. Izquierdo-Roca, E. Saucedo, A. Perez-Rodriguez, J.R. Morante, D.M. Berg, P.J. Dale and S. Siebentritt, "In-depth resolved Raman scattering analysis for the identification of secondary phases: Characterization of Cu_2ZnSnS_4 layers for solar cell applications," *Applied Physics Letters* 98 (2011)181905.

[33] M. Valdés, M.F. Pascual-Winter, A. Bruchhausen, W. Schreiner and M. Vázquez, "Cross-Section Analysis of the Composition of Sprayed Cu2 ZnSnS4 Thin Films by XPS, EDS, and Multi-Wavelength Raman Spectroscopy," *Physica Status Solidi (a)* 215 (2018) 1800639

[34] M. Grossberg, J. Krustok, J. Raudoja, K. Timmo, M. Altosaar and T. Raadik, "Photoluminescence and Raman study of $Cu_2ZnSn(Se_xS_{1-x})_4$ monograins for photovoltaic applications," *Thin Solid Films* 519 (2011) 7403-7406.

[35] V. Uvarova, "The influence of X-ray diffraction pattern angular range on Rietveld refinement results used for quantitative analysis, crystallite size calculation and unit-cell parameter refinement," *Journal of Applied Crystallography* 52 (2019).

[36] S. Das, I. Alam, J. Raiguru, B.V.R.S. Subramanyam and P. Mahanandia, "A facile method to synthesize CZTS quantum dots for solar cell applications," *Physica E: Low-dimensional Systems and Nanostructures* 105 (2019) 19-24.

[37] W. Wang, M.T. Winkler, O. Gunawan, T. Gokmen, T.K. Todorov, Y. Zhu and D.B. Mitzi, "Device Characteristics of CZTSSe Thin-Film Solar Cells with 12.6% Efficiency," *Advanced Energy Material* (2014) 1301465.

[38] D.J. Milliron, D.B Mitzi, M. Copel and C.E. Murray, "Solution-Processed Metal Chalcogenide Films for p-Type Transistors," *Chemistry of Materials* 18 (2006) 587-590.

[39] V.A. Akhavan, B.W. Goodfellow, M.G. Panthani, C. Steinhagen, T.B. Harvey, C.J. Stolle and B.A. Korgel, "Colloidal CIGS and CZTS nanocrystals: A precursor route to printed photovoltaics," *Journal of Solid-State Chemistry* 189 (2012) 2-12.

[40] A. Redinger, D.M. Berg, P.J. Dale, S. Siebentritt, "The Consequences of Kesterite Equilibria for Efficient Solar Cells," *Journal of American Chemical Society* 133 (2011) 3320-3323.

[41] A. Weber, R. Mainz and H.W. Schock, "On the Sn loss from thin films of the material system Cu–Zn–Sn–S in high vacuum," *Journal of Applied Physics* 107 (2010) 013516.

[42] D. Aldakov, A. Lefrancois and P. Reiss, "Ternary and quaternary metal chalcogenide nanocrystals: synthesis, properties and applications," *Journal of Materials Chemistry C* 1 (2013) 3756

[43] S. Chen, A. Walsh, X.G. Gong and S.H. Wei, "Classification of Lattice Defects in the Kesterite Cu_2ZnSnS_4 Earth-Abundant Solar Cell Absorbers," *Advanced Materials* 25 (2013) 1522-1539

[44] A. Fairbrother, X. Fontané, V. Izquierdo-Roca, M. Espindola-Rodriguez, S. López-Marino, M. Placidi, J. López-García, A. Pérez-Rodríguez and E. Saucedo, "Single-Step sulfo-selenization Method to Synthesize $Cu_2ZnSn(S_ySe_{1-y})_4$ absorbers from Metallic Stack Precursors," *ChemPhysChem* 14 (2013) 1836-1843

[45] Q. Guo, G.M. Ford, W.C. Yang, B.C. Walker, E.A. Stach, H.W. Hillhouse, R. Agrawal, "Fabrication of 7.2% Efficient CZTSSe Solar Cells Using CZTS Nanocrystals" *Journal of American Chemical Society* 132 (2010) 17384-17386.

[46] C.M. Fella, Y.E. Romanyuk and A.N. Tiwari, "Technological status of $Cu_2ZnSn(S,Se)_4$ thin film solar cells," *Solar Energy Materials and Solar Cells* 119 (2013) 276-277.

[47] A. Popescu, V. Constantin, A. Cojocaru and M. Olteanu, “Electrochemical Behaviour of Copper (II) Chloride in Choline Chloride-urea Deep Eutectic Solvent” *Revista De Chimie (Bucharest)* 62 (2011) 206-211

[48] S. Jain, S. Verma, S.P. Singh and S.N. Sharma, “An electrochemical biosensor based on novel butylamine capped CZTS nanoparticles immobilized by uricase for uric acid detection,” *Biosensors and Bioelectronics* 127 (2019) 135-141.

[49] S. Azmi, M. Nohair, M. El Marrakchi, E.M. Khoumri and M. Dabala, “Effect of the Complexing Agents on the Properties of Electrodeposited CZTS Thin Films,” *7th International Conference on Renewable Energy Research and Applications* 7 (2018).

[50] K.M. Lee, P.Y. Chen, C.Y. Hsu, J.H. Huang, W.H. Ho, H.C. Chenc and K.C. Ho, “A high-performance counter electrode based on poly (3, 4-alkylenedioxythiophene) for dye-sensitized solar cells,” *Journal of Power Sources* 188 (2009) 313-318.

[51] S.G. Hashmi, T. Moehl, J. Halme, Y. Ma, T. Saukkonen, A. Yella, F. Giordano, J.D. Decoppet, S.M. Zakeeruddin, P. Lund and M. Grätzel, “A durable SWCNT/PET polymer foil-based metal free counter electrode for flexible dye-sensitized solar cells,” *Journal of Materials Chemistry A* 2 (2014) 19609-19615.

[52] Y. Xie, C. Zhang, F. Yue, Y. Zhang, Y. Shi and T. Ma, “Morphology dependence of performance of counter electrodes for dye-sensitized solar cells of hydrothermally prepared hierarchical Cu2ZnSnS4 nanostructures,” *RSC Advances* 3 (2013) 23264-23268.

[53] J.M. Ferreira, K.P. Souza, F.M. Queiroz, I. Costa and C.R. Tomachuk, “Electrochemical and chemical characterization of electrodeposited zinc surface exposed to new surface treatments,” *Surface Coating Technology* 294 (2016) 36-46.

CHAPTER FIVE

FABRICATION OF DEVICE

5.1 MATERIALS

The following materials were used for the fabrication process of the kesterite solar cell and all the reagents were of analytical grade and no further purification was performed: Hellmanex III (Sigma Aldrich), isopropanol (Sigma Aldrich), Al-doped ZnO (Sigma Aldrich), cadmium nitrate tetrahydrate (Sigma Aldrich), thiourea (Sigma Aldrich), methanol (Sigma Aldrich), Deionized water was prepared with Millipore filtration system (Millipore-Sigma), and ITO coated glass.

5.2 DEVICE FABRICATION LAYERS

As has been stated earlier, fabrication of the kesterite photovoltaic cell involves deposition techniques which include vacuum and non-vacuum deposition techniques [1-5]. In this study we used the non-vacuum deposition technique, especially the ink deposition method [6,7]. The deposition involved dissolving the different layers in a suitable solvent and spin coating them unto the glass following layer by layer process and subsequently heating the glass to evaporate the solvent leaving behind the different layer on the glass used. For the fabrication of our kesterite photovoltaic cell, the following architecture was followed:

- ITO-coated glass
- Kesterite (CZTS and CZTSTe) absorber layer
- Cadmium sulfide buffer layer
- Al-doped zinc oxide window layer
- Ag cathode layer.

5.2.1 ITO-COATED GLASS PREPARATION

The process involved in the cleaning of the ITO-coated glass before deposition is as follows:

- The glass was sonicated for 5 minutes in a hot Hellmanex III solution
- After five minutes, the glass was removed and rinsed twice in hot de-ionized water.
- Subsequently the glass was sonicated for another 5 minutes in isopropanol after which it was rinsed thoroughly twice in hot de-ionized water.
- Finally, the glass was dried using N_2 gas gun and kept for deposition.

5.2.2 KESTERITE ABSORBER LAYER PREPARATION

The synthesized nanoparticles of CZTS, CZTSTe were prepared into ink in readiness for deposition process. The following procedure was observed in the preparation of the kesterite absorber ink:

- 150 mg of the synthesized nanoparticles of CZTS and CZTSTe were weighed on a weighing balance and poured into glass vials and properly labelled to distinguish both nanoparticles.
- 1 ml of Isopropanol was added to each of the nanoparticles (CZTS and CZTSTe) and was sonicated for about 15 minutes to allow for a homogenous dispersion of the nanoparticles in the solvent.
- The final dark ink obtained was kept ready for deposition on the ITO-coated glass.

5.2.3 CADMIUM SULFIDE BUFFER LAYER PREPARATION

The cadmium sulfide buffer layer was prepared through solution-based process and was subsequently spin coated following after the deposition of the kesterite absorber layer. The conventional method of preparing this layer is through chemical bath deposition where the already deposited kesterite absorber layer on the glass is dipped into a solution containing cadmium salt as the cadmium source and thiourea as the sulfur source in ammonia solution as solvent. This solution is heated to a temperature of 65 ˚C for 25 minutes allowing the layer of the cadmium sulfide to form on the glass. This method was not followed in this study as the necessary parameter were not available. The procedure used for the preparation of the cadmium buffer layer is as follows:

- 0.1 M of Cadmium nitrate tetrahydrate and 0.1 M thiourea was dissolved in methanol.
- 1 ml of deionized water was added to the solution to stabilize the solution.
- The solution was stirred at room temperature for 15 minutes until a clear transparent and homogeneous mixtures was obtained.
- The solution was kept and used for deposition of the layer.

5.2.4 ALUMINIUM DOPED ZINC OXIDE WINDOW LAYER PREPARATION

The window layer of Al: ZnO was prepared by sol-gel method which involved dissolving 6% aluminum dopant-ZnO nanoparticles in isopropanol. The sol-gel solution formed was then kept for deposition.

5.3 DEVICE LAYER DEPOSITION

All the layers of the device were spin coated and dried on a hot plate to evaporate the solvents. The already prepared kesterite nanoparticle (CZTS and CZTSTe) ink was spin coated on the already cleaned ITO-coated glass at the speed of 1500 rpm for 30 seconds. After spin-coating, the substrates are dried at 200 ˚C for 5 minutes on a hot plate. This was repeated five times to obtain a good thickness for the absorber layer. Subsequently the coated substrate was annealed at 400 ˚C for 1.5 hrs. in an inert condition [6].

After annealing the absorber layer, the glass was allowed to cool down and the cadmium sulfide solution was spin-coated onto the absorber layer at 1000 rpm for 30 seconds and was later annealed at 200 ˚C in air for 5 minutes. This was repeated 5 times to obtain a desirable thickness of the film [6].

The Al- doped ZnO window layer already prepared in isopropanol was spin-coated at 1000 rpm for 30 secs and was dried at 250 ˚C for 5 minutes in air using a hot plate [6].

Finally, the Ag cathode layer was deposited on the window layer of the device through chemical vapor deposition method. After the deposition of the cathode layer, the kesterite device (CZTS and CZTSTe) power conversion efficiency was obtained by I-V curve diode measurement. The final architecture of the prepared kesterite device is shown in figure 5.1 below

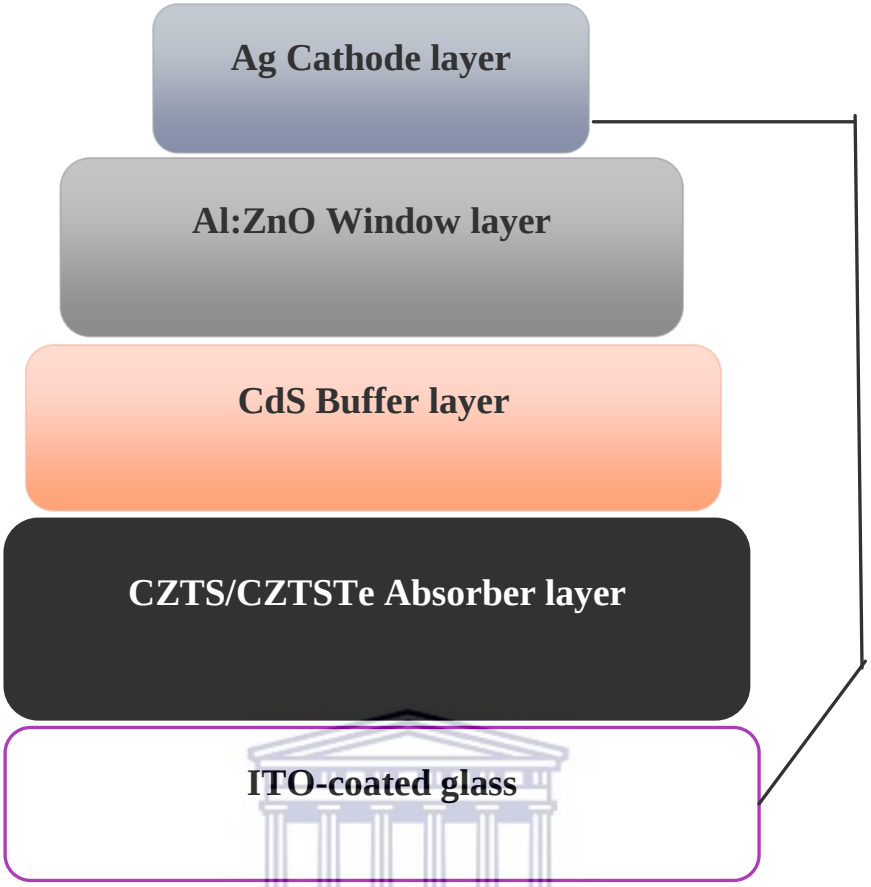

Figure 5. 1 Device architecture of the prepared kesterite (CZTS and CZTSTe) PV cells.

5.4 DEVICE MEASUREMENT (EFFICIENCY)

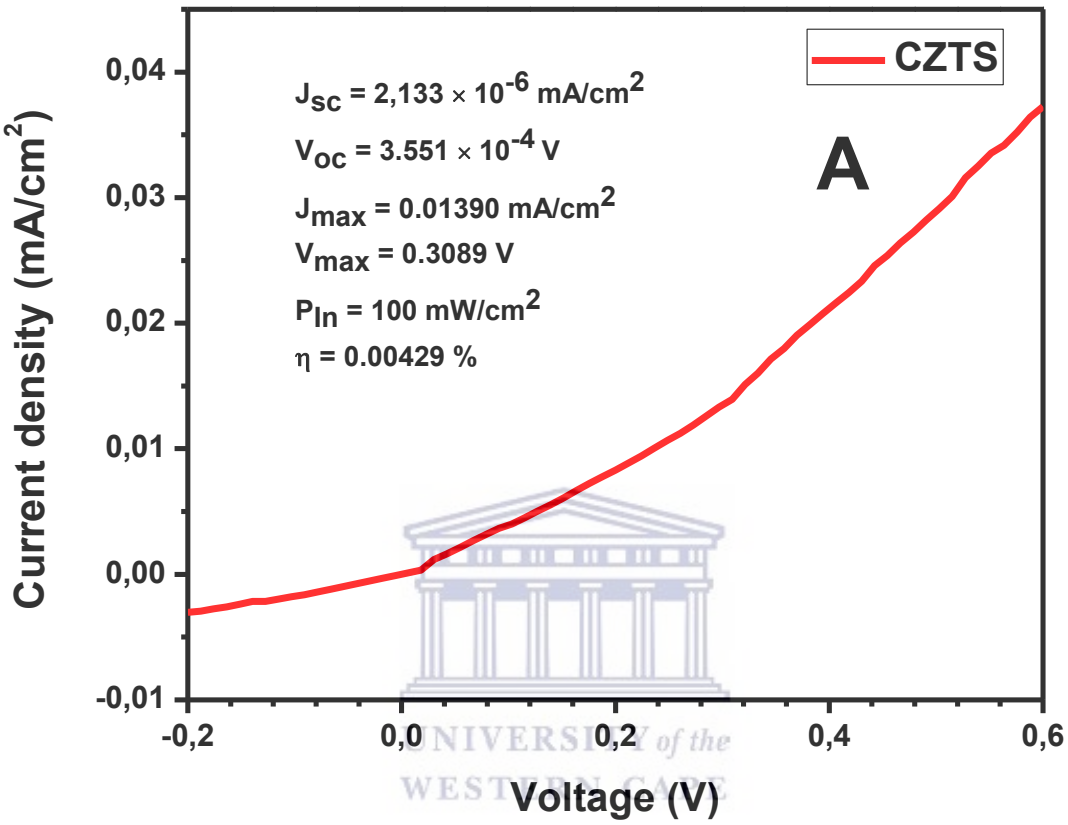

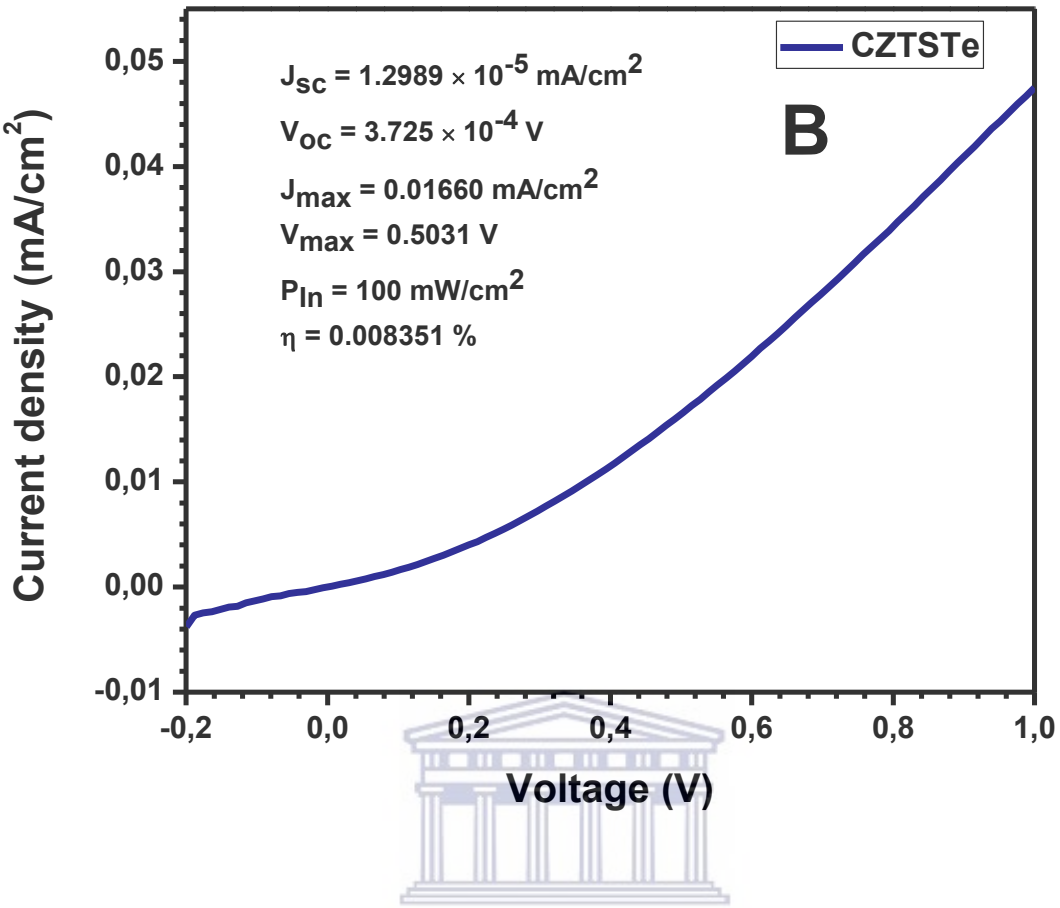

Figure 5. 2 J-V Curve showing the power conversion efficiency of (A) CZTS and (B) CZTSTe kesterite photovoltaic cell.

the efficiency of the kesterite device was calculated using the formula:

$$\eta = \frac{FF \times V_{oc} \times J_{sc}}{P_{In}} \times 100\% \quad \textbf{(5.1)}$$

Where Fill-Factor (FF) is given as

$$FF = \frac{J_{max} \times V_{max}}{J_{sc} \times V_{oc}} \quad \textbf{(5.2)}$$

But maximum power P_{max} is given as

$$P_{max} = J_{max} \times V_{max} \quad \textbf{(5.3)}$$

Therefore, efficiency (η) is given as

$$\eta = \frac{P_{max}}{P_{in}} \times 100\% \quad \textbf{(5.4)}$$

The J-V curve parameters obtained for the CZTS and CZTSTe kesterite photovoltaic cell is summarized in table 5.1 below:

Table 5. 1 Parameters for the calculating the power conversion efficiency of the prepared devices.

SAMPLE	J_{max} (mA/cm^2)	V_{max} (V)	Efficiency (%)
CZTS	0.01390	0.3089	0.00429
CZTSTe	0.01660	0.5031	0.00835

The efficiency obtained from the J-V curve shows that CZTSTe had a better photovoltaic application having an efficiency of 0.00835 % when compared to CZTS which had an efficiency of 0.00429 %. The efficiency obtained for CZTSTe shows that the addition of small ratio of tellurium to the kesterite structure improved its photovoltaic application. Given that the efficiency obtained for the devices were low, this is the case because the devices were not optimized. It is worthy to mote that the low efficiency obtained from the nanoparticles can be improved on through various optimization techniques as well as further and advance research strategies. This is the case as the kesterite CZTS when initially tested for PV cell application

through vacuum deposition method had a low power conversion efficiency of 0.66% [8] but at the moment with improved research procedure and new advances, the efficiency has improved to 8.4% [9], 11.6 % for CZTSe [10] and 12.6% in the case of CZTSSe [11]. In 2018, Hao X. et al were able to fabricate a device of CZTS with a power conversion efficiency of over 10% by heterojunction heating treatment process to reduce heterojunction recombination [12]. It is worthy to note that conventionally kesterite solar cell devices are fabricated on molybdenum coated solar lime glass which has been researched to be of immense advantage for the cell integration of kesterite solar cells [13] but due to the available facility during our device fabrication, ITO-coated glass was the best option available for use. The use of ITO-coated glass factors into the low efficiency obtained for the devices.

REFERENCES

[1] K.C. Sekhar, S.L. Abhilasha, S.R. Bhat, N.U. Raj, K. Srikrishna, R.G.K. Urs and R. Nagapadma, "Deposition of nano-structured multilayer coatings of Cu_2ZnSnS_4 (CZTS) thin films by vacuum thermal evaporation method," *IOP Conference Series: Materials Science and Engineering* 402 (2018) 012138.

[2] S. Abdelhaleem, A.E. Hassanien, R. Ahmad, M. Schuster, A.H. Ashour, M. Distaso and P.J. Wellmann, "Tuning the Properties of CZTS Films by Controlling the Process Parameters in Cost-Effective Non-vacuum Technique," *Journal of Electronic Materials* 47 (2018) 7085-7092.

[3] S. Das, K. Sa, P.C. Mahakul, J. Raiguru, I. Alam, B.V.R.S. Subramanyam and P. Mahanandia, "Synthesis of quaternary chalcogenide CZTS nanoparticles by a hydrothermal route," *IOP Conference Series: Materials Science and Engineering* 338 (2018) 012062.

[4] B.K. Rajwar and S.k. Sharma, "Structural and optical properties of Cu_2ZnSnS_4 synthesized by ultrasonic assisted sol-gel method," *Physica B: Condensed Matter* 537 (2018) 111–115.

[5] S. Das, I. Alam, J. Raiguru, B.V.R.S. Subramanyam and P. Mahanandia, "A facile method to synthesize CZTS quantum dots for solar cell applications," *Physica E: Low-Dimensional Systems and Nanostructures* 105 (2019) 19-24.

[6] K. Tanaka, M. Oonuki, N. Moritake and H. Uchiki, "Cu_2ZnSnS_4 thin film solar cells prepared by non-vacuum processing," *Solar Energy Materials and Solar Cells* 93 (2009) 583–587.

[7] E.P. Subramanian, G. Rajesh, N. Muthukumarasamy, M. Thambidurai, V.S. Asokan and D. Velauthapillai, "Solar cells of Cu_2ZnSnS_4 thin films prepared by chemical bath deposition method," *Indian Journal of Pure and Applied physics* 52 (2014) 620-624.

[8] H. Katagiri, N. Sasaguchi, S. Hando, S. Hoshino, J. Ohashi and T. Yokota, “Preparation and evaluation of Cu_2ZnSnS_4 thin films by sulfurization of e- evaporated precursors,” Solar Energy Materials and Solar Cells 49 (1997) 407–414.

[9] B. Shin, O. Gunawan, Y. Zhu, N.A. Bojarczuk, S.J. Chey and S. Guha, “Thin film solar cell with 8.4% power conversion efficiency using an earth- abundant Cu_2ZnSnS_4 absorber,” Progress in Photovoltaics: Research and Applications 21 (2013) 72–76.

[10] Y.S. Lee, T. Gershon, O. Gunawan, T.K. Todorov, T. Gokmen, Y. Virgus and S. Guha, “$Cu_2ZnSnSe_4$ thin-film solar cells by thermal co-evaporation with 11.6% efficiency and improved minority carrier diffusion length,” *Advanced Energy Materials* 5 (2015) 1401372.

[11] W. Wang, M.T. Winkler, O. Gunawan, T. Gokmen, T.K. Todorov, Y. Zhu and D.B Mitzi, “Device characteristics of CZTSSe thin-film solar cells with 12.6% efficiency,” *Advanced Energy Materials* 4 (2014) 1301465.

[12] C. Yan, J. Huang, K. Sun, S. Johnston, Y. Zhang, H. Sun, A. Pu, M. He, F. Liu, K. Eder, L. Yang, J.M. Cairney, N.J. Ekins-Daukes, Z. Hameiri, J.A. Stride, S. Chen, M.A. Green and X. Hao, “Cu_2ZnSnS_4 solar cells with over 10% power conversion efficiency enabled by heterojunction heat treatment,” *Nature Energy* 3 (2018) 764–772.

[13] K. Wang, O. Gunawan, T. Todorov, B. Shin, S. Chey, N. Bojarczuk, D. Mitzi and S. Guha,

“Thermally evaporated Cu_2ZnSnS_4 solar cells,” Applied Physics Letters 97 (2010) 143508–143508–3

CHAPTER SIX

CONCLUSION AND RECOMMENDATION

6.1 CONCLUSION

Materials which are able to harness the energy from the sun are researched to effectively improve energy in the world. Solar cells are able to absorb energy from the sun and convert it to electrical energy. Progress has been made in this regard as materials have been fabricated that are able to absorb sun energy and convert it to electrical and other useful energies. Silicon solar cells has been an example of the remarkable breakthrough in relation to solar cell, but due to the high cost involved in its production process, attention has been shifted towards finding materials which are cheaper to produce, non-toxic and are made of readily available materials. Kesterite which is an alloy of copper zinc tin and sulfur (CZTS) has attracted so much attention over the years due to its direct and tunable band gap of 1.5 eV making it a good semiconductor material and also made up of elements that are earth abundant. Although with these advantages, its efficiency in converting solar energy to electrical energy has not reached the marketable stage as the highest power conversion efficiency recorded for the material is 12.6%. Another advantage that kesterite material has in terms of application to solar cell is that its band-gap can be tuned, altered and improved. The purpose of this work was to incorporate tellurium into the kesterite structure of CZTS to reduce its band-gap which subsequently improves its photovoltaic efficiency. I was able to synthesize CZTS, CZTSSeTe and CZTSTe through anion hot-injection method and diethylene glycol (DEG) as solvent. The synthesized nanoparticles were easily dispersed into alcohol (ethanol or isopropanol) and analyzed to determine their properties.

Firstly, Cu_2ZnSnS_4 kesterite nanoparticles (CZTS) were prepared through polyol-controlled method according to literature. In this work, diethylene glycol was used for the synthesis

which allowed controlling the particle size and to minimize particle agglomeration. In order to reduce the chalcogens to go into reaction faster, sodium borohydride was used as a reducing agent for the anion precursor preparations. Then, CZTSSeTe and CZTSTe were successfully synthesized using the same method as that of CZTS. The surface condition of the synthesized nanoparticles was investigated through FTIR and the spectrum obtained reveals the presence of some functional group such as O-H stretching, C-C stretching, C-O stretching and C-H stretching. All these bands were attributed to the solvent used during synthesis and during washing and centrifugation but most importantly to the solvent used during synthesis. The presence of this solvent on the nanoparticles have been reported not to pose any problem during fabrication as they can be easily removed during annealing. The optical band gap of the synthesized nanoparticles was obtained from Tauc-plot by using the UV-vis data obtained for the materials. The band-gaps were 1.73 eV for CZTS, 1.06 eV for CZTSSeTe and 1.62 eV for CZTSTe. The reduced band-gap obtained for the tellurium containing nanoparticles shows a successfully outcome of the introduction of tellurium into the kesterite structure. This further confirms the logic behind the thesis where we postulated that the introduction of tellurium to the structure of the kesterite nanoparticle will reduce its bandgap which is expected to lead to a better efficiency when fabricated into a PV cell. This assertion stems from the fact that tellurium as an element is regarded as a good semiconductor element and also it is a better conductor material when compared to sulfur and selenium in their chalcogen family of group 16 in the periodic table. The morphology of the synthesized nanoparticles from SEM gave the expected flower-like appearance mostly reported for kesterite nanoparticles and the TEM micrographs as well as the SAXS plot of shape revealed that the nanoparticles were polydispersed due to slight agglomeration of the particles. The TEM micrograph also revealed the presence of a covering on the surface of the nanoparticle which we can confirm from the FTIR spectrum to be attributed to the solvent used during synthesis. The particle size of the

nanoparticles was obtained through SAXS plot of size distribution which confirm that the synthesized particle was of small size radius in nanoscale. The particle size obtained were 10 nm for CZTS, 15 nm for CZTSSeTe and 36 nm for CZTSTe. The crystal size of the nanoparticles was obtained using Debye-Scherrer equation from XRD data of the nanoparticles. The crystal size obtained for the CZTS is 11 nm, CZTSSeTe is 15 nm and that of CZTSTe is 31 nm. The crystal sizes obtained from XRD were close to the particle size gotten from SAXS. The crystallinity of the nanoparticles was examined through XRD and SAED. The plot of the XRD data revealed the presence of the kesterite phase in all the synthesized nanoparticles. The peaks obtained in the XRD were further confirmed by the SAED micrograph. Raman Spectroscopy was performed on the nanoparticles to validate the presence of the kesterite phase. The spectra obtained for CZTS showed a little shift of the kesterite phase due to the solvent which acted as a capping agent on the surface and presence of secondary phases (ZnS and SnS) while the other nanoparticles (CZTSSeTe and CZTSTe) maintained the value of the kesterite phase. The electroactivity of the materials was evaluated through CV and EIS. The CV results obtained showed high peak current in both oxidation and reduction for CZTSTe nanoparticles and showed low peak current in both oxidation and reduction for CZTSSeTe. Although this was not the behaviour that was desired however the high crystalline nature of CZTSSeTe nanoparticles as observed from the SAED micrograph supports why this behaviour is encountered as the nanoparticles due to their high crystalline nature have its electron strongly held up in the lattice making it difficult for its electrons to go into solution faster thereby making it less conductive. The EIS spectrum obtained for both Nyquist and Bode plots followed the same trend that was observed in the CV analysis where after utilizing ZView to simulate the date and generate equivalent circuit, the results of the *R*ct values obtained for the nanoparticles showed that CZTSTe had the least *R*ct value of 3.9 kΩ where CZTSSeTe had the highest *R*ct value of 67.9 kΩ. The low *R*ct value of CZTSTe shows

that the material is least resistive and so will conduct better which is observed from the high peak current values as well as the high diffusion coefficient value. CZTSSeTe with a high *R*ct value means that it is more resistive than all synthesized nanoparticles which means that it is less conductive which was due to its high crystallinity as seen from SAED micrograph and also corroborated by the CV results and it had the least diffusion coefficient value. I-V curve for the synthesized nanoparticles of CZTS, CZTSSeTe and CZTSTe in lithium perchlorate prepared in acetonitrile was evaluated to check the photovoltaic capability of the nanoparticles. The value for the efficiency of the nanoparticles as seen from the results, followed the trend obtained in the other electrochemical techniques, where CZTSTe had a higher maximum current density produced and therefore had the highest efficiency of 0.00345 % while CZTS had an efficiency of 0.00224 % and CZTSSeTe had the least maximum current density produced with the least efficiency of 0.00116 %. From the short circuit current I_{sc} and V_{oc} *obtained* for the various materials, it can be seen that CZTSSeTe had the highest values with I_{sc} value of 12 µA and V_{oc} value of 1.3833 V, agreeing with the optical band-gap obtained where it had the best optical bandgap of 1.06 eV. The high values of the I_{sc} and V_{oc} shows that it is able to absorb greater amount of energy than the other nanoparticles, but it fell short to convert the energy efficiently into usable current as its J_{max} value (0.1219 mA/cm^2) was the least amongst the three nanomaterials which follows the same trend observed in CV and EIS. It also exhibited the least fill-factor of 0.49 %. Although CZTSSeTe shows a greater potential of absorbing light than the other synthesized nanoparticles, it fell short to convert it efficiently into electrical current which is due to the high metallic composition as earlier stated given that selenium and tellurium act metallic and coupled with the electropositive metal constituents of the kesterite nanoparticle (copper, zinc and tin). This high metallic composition causes a repulsion in the electrochemical behaviour of the CZTSSeTe, resulting in the nanoparticle being more resistive and hence has a low power conversion efficiency. On the other hand,

CZTSTe which started off with relatively high short circuit current 5.0 µA when compared to CZTS, maintained a high maximum current density J_{max} of 0.5594 mA/cm2 and subsequently had the highest power conversion efficiency of 0.00345 %. This is the case as the optical band gap obtained showed the ability of the nanoparticle to absorb substantial amount of light incident on it with band-gap value of 1.62 eV when compared to CZTS with band-gap value of 1.73 eV. It was able to convert to substantial amount of current when compared to CZTSSeTe and CZTS which follows the very trend observed for the other electrochemical characterizations. These results obtained show that although these materials had low power conversion efficiency, they demonstrated that they can be applied for photovoltaic cells.

The device fabrication was performed, unfortunately the J-V curve obtained for CZTSSeTe gave a straight line indicating a resistance behaviour instead of a diode behaviour. The result reported in the thesis were for CZTS and CZTSTe kesterite PV cells performed under light. The analysis performed from the data obtained from the J-V curve of the devices shows that the incorporation of tellurium into the kesterite structure improved its photovoltaic efficiency when compared to the convention CZTS kesterite device that was tested. The efficiency of 0.00835 % was obtained for CZTSTe while CZTS had an efficiency of 0.00429 %. These efficiencies are very low compared to the already established efficiencies for kesterite solar cell device with value of 12.8 %. The low efficiency values obtained are due to the fact that there was no optimization carried out during device fabrication. Some of the optimization techniques that can be employed to better the performance of the kesterite nanomaterials are:

- Chemical bath etching which will remove the presence of secondary phases in the kesterite absorber layer. These secondary phases are not good for the device performance as they can cause shunting of the cell.
- Varying the ratio of the materials as it has been studied and found that kesterite solar cells with slight high zinc ratio perform better.

- Temperature studies are important during synthesis. By taking account of various temperature parameters, the kesterite solar cell can be improved as these temperatures will help determine the best temperature that yield an optimal device.
- The thickness of the various layers in the device architecture must be studied to ensure adequate volume of the layers available for absorbing and converting light to useful energy, thereby enhancing the efficiency.

6.2 RECOMMENDATION

Given the phase problem usually encountered in kesterite nanoparticles, more enhanced environment like glove-box is advised for use during synthesis of the nanoparticles. It is also important to make sure that during synthesis especially if the powder form of the chalcogens are to be used and is required to be reduced, proper studies are done to ensure that they were properly reduced so as to have them properly incorporated in the kesterite phase thereby reducing the formation of secondary phases. Chemical bath etching of the kesterite absorber layer should be carried out in order to remove the secondary phases if present and temperature studies also is important in preventing presence of secondary phases. Optimization studies should be done during fabrication so as to obtain improved PCE for the novel nanoparticles. The right amount of concentration of the precursor materials as well as suitable solvents should be examined so as to avoid agglomeration of the nanoparticles. Although, it has been reported to be an expensive procedure, vacuum deposition method can deliver better results and should be used to fabricate kesterite thin-film photovoltaic cells as the process through sputtering of the constituent metals reduces the presence of secondary phase formation in the PV cell.